Ab initio studies of extrinsic spin-orbit coupling effects in graphene and quantum Monte Carlo simulations of phosphorene

DISSERTATION

zur Erlangung des Doktorgrades
der Naturwissenschaften (Dr. rer. nat.)
der Fakultät für Physik
der Universität Regensburg

vorgelegt von

Tobias Frank

aus Regensburg

im Jahr 2018

Promotionsgesuch eingereicht am: 22.01.2018
Die Arbeit wurde angeleitet von: Prof. Dr. Jaroslav Fabian

Prüfungsausschuss:

Vorsitzender:	Prof. Dr. Jascha Repp
Erstgutachter:	Prof. Dr. Jaroslav Fabian
Zweitgutachter:	Prof. Dr. Ferdinand Evers (im Kolloquium vertreten durch: Prof. Dr. Milena Grifoni)
weiterer Prüfer:	Prof. Dr. Gunnar Bali (im Kolloquium vertreten durch: Prof. Dr. Vladimir Braun)

Termin Promotionskolloquium: 12.02.2019

Contents

Notation

Acronyms

ARPES	angle-resolved photoemission spectroscopy
BSE	Bethe–Salpeter equation
B3LYP	Becke 3-parameter (exchange), Lee, Yang and Parr exchange-correlation functional
CVD	chemical vapor deposition
DFT	density functional theory
DMC	diffusion Monte Carlo
DOS	density of states
GGA	generalized gradient approximation
HF	Hartee–Fock
HOMO	highest occupied molecular orbital
HWF	hybrid Wannier function
LDA	local density approximation
LUMO	lowest unoccupied molecular orbital
PAW	projector augmented wave
PBE	Perdew–Burke–Ernzerhof exchange-correlation functional
PIA	pseudospin inversion asymmetry
PL	photoluminescence
PLE	photoluminescence excitation spectroscopy
PLDOS	partial local density of states
RSDFT	relativistic spin-density functional theory
SOC	spin-orbit coupling
STM	scanning tunneling microscopy
STS	scanning tunneling spectroscopy
TMDC	transition metal dichalcogenide
QHE	quantum Hall effect
QAHE	quantum anomalous Hall effect
QMC	quantum Monte Carlo
QSHE	quantum spin Hall effect
QSHS	quantum spin Hall state
QVSHS	quantum valley spin Hall state
VMC	variational Monte Carlo
WCC	Wannier charge center

Constants

Constant	Value	Description
a_0	$0.529177\,\text{Å}$	Bohr radius
e	$-1.602177 \cdot 10^{-19}$ C	Electron charge
Ry	13.605693 eV	Rydberg energy
Ha	27.211386 eV	Hartree energy
m_e	$9.109383 \cdot 10^{-31}$ kg	Electron mass

Symbols

Symbol	Description
$\tilde{a}$	projector augmented wave pseudo-quantity
$\mathbf{A}$	magnetic vector potential
$\mathbf{B}$	magnetic field
e	absolute electron charge
$E,\ \varepsilon$	energy
η	four-spinor component
$f(r)$	function
$f[n]$	functional
$\hat{H}$	Hamiltonian operator
$\hat{\mathcal{H}}$	model Hamiltonian
$\mathbf{k}$	reciprocal space vector
$\mathbf{L}$	orbital angular momentum
m	mass
n	particle density, band index
N	particle number
$\hat{\mathbf{p}}$	momentum operator
Ψ	many-body wave function
ψ	single-particle wave function
ϕ	partial waves, atomic wave function
$\mathbf{r}$	real space vector
$\mathbf{S}$	spin angular momentum
σ, s	Pauli matrix or (pseudo) spin component
t, τ	time
$\hat{T}$	kinetic energy operator
u	periodic part of Bloch wave function
U	unitary matrix
V, v, φ	potential

1 Introduction

The field of two-dimensional (2D) materials offers a rich playground to study new physics and concepts for device applications [1]. Starting with the discovery of graphene [2], the field has seen intense research activity, with interest peaking also in terms of other 2D materials, for example the insulating transition metal dichalcogenides (TMDCs) [3], or superconducting and magnetic materials. Technologically, most of them are very promising, but considerable amount of scientific research centers still around graphene, owing to its peculiar dispersion relation [4] and recent advancements in device preparation quality [5].

One goal of research is to assess graphene's qualification for spintronics applications. Spintronics (shorthand for spin-based electronics) [6, 7] aims to utilize the spin degree of freedom of electrons for new forms of information storage and logic devices, using effects from magnetization and spin-orbit coupling. Spin-orbit coupling is an important ingredient for spintronic phenomena and devices such as the spin Hall effect, for spin relaxation, spin transistors and many more. On the other hand, in graphene, spin-orbit coupling and nuclear-spin–electron-spin coupling is relatively weak [8]. Therefore, along with its exceptional charge transport properties, it is expected to be a good material for transporting spin currents. Spin transport in graphene is limited by imperfections through external sources [8], e.g., by the specific growth mechanism, sample fabrication, underlying substrates, and atomic residuals, by induced magnetism and spin-orbit coupling. Therefore, it is important to study the origin of these extrinsic effects. One part of this thesis is dedicated to quantify spin-orbit coupling introduced by copper atoms and the copper substrate, because copper is a popular material for surface synthesis of high-quality graphene [5].

Another reason to study the effects of spin-orbit coupling in graphene is to actually control the spin degree of freedom. This can be achieved by proximitizing the material with other surfaces [9], ideally leaving the Dirac dispersion of graphene unaffected, for example by forming an interface with TMDCs [10]. TMDCs possess strong spin-orbit coupling, facilitating spin-valley coupling. It relates the spin degree of freedom to one of the two reciprocal-space K points (valleys), which make those systems very interesting from the optics point of view. These properties turn out to be transferable to graphene, resulting in orbital and spin-orbital proximity effects [11]. We will study these proximity effects in terms of continuum and tight-binding Hamiltonians.

With its linearly dispersed electrons, behaving effectively as Dirac particles, graphene demonstrates a so-called emergent (relativistic) effect, i.e., that a system consisting out of quasi-free quadratically dispersed particles can show emergent physical properties expected from other energy scales or other theories. Strangely enough, another emergent effect was discovered in a graphene model system [12]. Intrinsic spin-orbit coupling in principle is able to introduce a topological gap (which destroys the Dirac dispersion), just to give rise to Dirac dispersed edge states in one dimension lower, the

so-called quantum spin-Hall states. These edge states are protected by time-reversal symmetry and as long as scatterers at the edges preserve this symmetry, particles in this state cannot scatter back. Such dissipationless states would be very interesting for on-chip interconnects to decrease the electrical power consumption. The special type of spin-orbit coupling needed to induce these effects in graphene is intrinsically very small and needs to be enlarged by external means. It could potentially be inherited from a suitable substrate, which is another reason to study graphene/TMDC hybrid systems. The combination of different monolayer materials is a very topical research field [1]. It offers a way to find new materials with well designed properties, because the stacking nowadays can be controlled at will and performed in a very clean way. Graphene is an ideal starting point to design artificial dispersion, as it offers a gapless linear band structure. Engineering a linearly dispersed band structure into a gapped one by breaking symmetries is easier achieved than closing a gap. The effective low energy electrons can be studied in terms of tight-binding Hamiltonians [13], which then permit to explore edge state physics in proximitized graphene systems, which is a third point of this study.

From a technological point of view, graphene is not always the best material for some applications, such as field effect transistors [14]. Even with the breaking of symmetries it possesses a band gap which is very small, not suitable for optical devices in the infrared to ultraviolet scale. This is where other family members come into play, such as the aforementioned TMDCs or black phosphorus [15]. Black phosphorus is a very promising material, because it offers a way to tune its band gap by the number of layers that it is composed of [16]. The monolayer building block of black phosphorus is called phosphorene, which possesses a direct band gap. In order to understand the optical properties of the composed system, we need to understand the single layer first. Experimental and theoretical consensus on the fundamental gap of phosphorene is not found yet. Conventional theoretical methods to determine the band gap may fail or are harder to converge, when dealing with systems in which Coulomb interactions are strong as it is the case in open 2D systems. Not only is it important to gain more quantitative understanding of simulations obtained with conventional *ab initio* calculations, but also to apply new methods to the class of 2D systems. This is why we employ quantum Monte Carlo (QMC) simulations to study the fundamental gap of phosphorene.

The thesis starts with an introduction to relativistic spin-density functional theory and the quantum Monte Carlo method. The research part can be subdivided into two main topics. The first three chapters are devoted to density functional theory (DFT) and tight-binding studies of extrinsic spin-orbit coupling effects in graphene. In the first chapter, we discuss the effect of copper atom adsorption onto graphene and its consequences for the local spin-orbit coupling. The second chapter deals with orbital and spin-orbit coupling proximity effects induced by a copper surface into the electronic states of graphene, combining DFT calculations with an effective low-energy Hamiltonian. This effective Hamiltonian plays also an important role in the third chapter, where more general graphene proximity spin-orbit coupling induced phenomena are studied by means of tight-binding calculations. In particular, we explore edge state physics associated with different forms of graphene spin-orbit coupling. The last chapter deals with the many-body calculation of the fundamental gap of phosphorene.

2 Theoretical foundations and methodologies

2.1 Overview

This chapter introduces the theoretical concepts and methodologies, used to study the two-dimensional materials presented in this thesis. To explore the systems at hand, starting from a many-body description, several approximations need to be applied in order to make calculations tractable on the computer.

The title of this thesis carries the term *ab initio*, i.e., studies from first principles, given physical laws and constants as input parameters; this one could call *strong ab initio*. Although there are different opinions regarding which calculations are to be considered *ab initio*, we understand it in the sense that we are allowed to fine-tune the method to be in agreement with experiments (e.g., with the band gap), such that we can predict a quantity that is not known to us (e.g., spin-orbit coupling), calling it *weak ab initio*. The tuning is justified, because *ab initio* methods are known to sometimes have systematic deviations from experiments.

The purpose of this chapter is to introduce DFT and how it can be used to study relativistic effects like spin-orbit coupling, and to show the connection of DFT to many-body quantum Monte Carlo (QMC) methods. Figure 2.1 gives a guideline of theorems and effective descriptions that are explained later in this chapter. All of our investigations start from a many-body Hamiltonian, which is mapped to an effective noninteracting auxiliary picture [17, 18]. Constraining the auxiliary system to have the same ground state density as the original many-body interacting system, this leads to the Kohn–Sham approach to DFT, which can be tackled numerically (see Sec. 2.2). A similar mapping also holds in a fully relativistic context [19, 20]. In this thesis, however, we restrict ourselves to relativistic particles, where the relativistic treatment is done for the kinetic energy only. In both, nonrelativistic and relativistic DFT descriptions, approximations have to be made to the interaction term, that are briefly listed in Sec. 2.2.2. Standard DFT not always gives the best description for our classes of systems and known deficiencies have to be corrected. We consider the treatment of d orbitals with the Hubbard U correction, or the binding energy of van der Waals coupled systems, with empirical potentials (as discussed in Secs. 2.2.2 and 2.2.2, respectively). To deal with the difficulties of steep nuclei potentials, yet another mapping has to be imposed via the projector augmented wave (PAW) method [21], explained in Sec. 2.2.3. After discussion of basic properties and the nonrelativistic limit of the single-particle Dirac equation in Sec. 2.3, the relativistic extension of PAW [22] within the context of relativistic spin-density functional theory is described in Sec. 2.4. From this formulation of DFT, for a given system, one then can construct low-energy

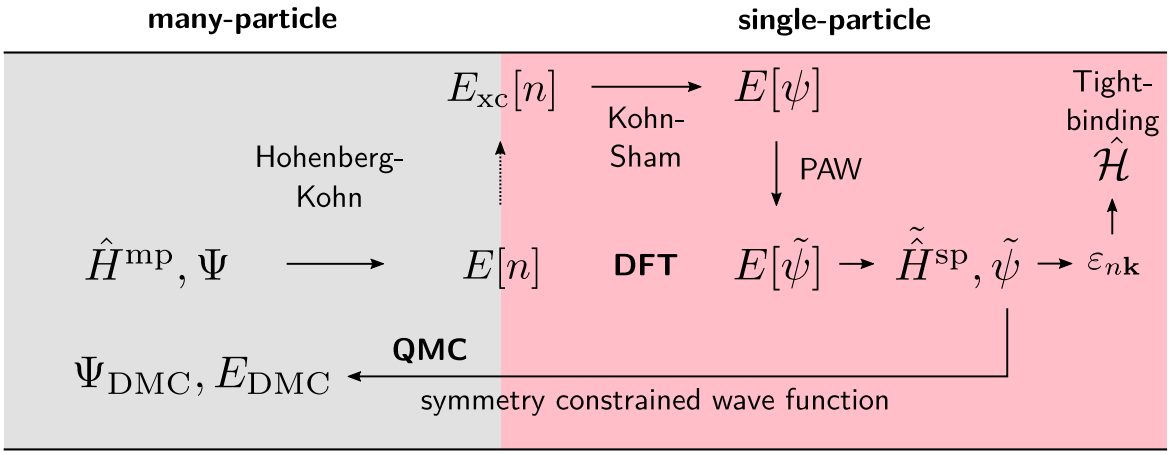

Figure 2.1: Overview of the many- and single-particle theories encountered in this thesis. The many-particle Born–Oppenheimer Hamiltonian $\hat{H}^{\mathrm{mp}}$ with many-particle wave function Ψ is associated with total energy functionals of the particle density n via the Hohenberg–Kohn theorems. By mapping to single-particle wave functions, the exchange-correlation energy functional $E_{\mathrm{xc}}[n]$ has to be separated out from the total energy functional, for which a reasonable approximation needs to be made. The single-particle Kohn–Sham states ψ are then linearly transformed via the PAW formalism to pseudo wave functions $\tilde{\psi}$ to be able to describe quantities in the atomic regions using a plane-wave basis. The total energy functional can then be varied with respect to $\tilde{\psi}$ to derive a single-particle Hamiltonian $\hat{H}^{\mathrm{sp}}$. Wave functions obtained from the single-particle Hamiltonian are used to construct trial wave functions for quantum Monte Carlo (QMC) methods [such as diffusion Monte Carlo (DMC)]. The dispersion relation $\varepsilon_{n\mathbf{k}}$ received from solving the single-particle Kohn–Sham problem is employed to extract effective tight-binding matrix elements for low-energy Hamiltonians $\hat{\mathcal{H}}$.

effective tight-binding Hamiltonians subject to lattice symmetry constraints, to extract the strength of effective-orbital spin-orbit coupling by fitting to the band structure and spin splittings obtained by DFT calculations.

A different branch of *ab initio* calculations are wave function based QMC methods, evaluated on the full nonrelativistic many-body Born–Oppenheimer Hamiltonian (see Sec. 2.5). In form of the variational Monte Carlo (VMC) and diffusion Monte Carlo (DMC) algorithms one is able to calculate ground and excited state energies of the interacting system without approximating (except for Ewald interactions) the many-body Hamiltonian. The main hurdle to make the method truly exact is that the symmetry of the wave functions needs to be constrained by the shape of DFT orbitals via trial wave functions. After variational optimization of the trial wave function with the help of VMC (see Sec. 2.5.1), the ground state (or excited state) subject to that symmetry constraint can be obtained by DMC (see Sec. 2.5.3).

2.2 Density functional theory

2.2.1 Nonrelativistic density functional theory

The many-body Hamiltonian of N nonrelativistic Coulomb-interacting electrons in a nonmagnetic external potential of N_a atom cores can be expressed as

$$\hat{H} = \hat{T} + \hat{V} + \hat{V}_\mathrm{ext}(\{\mathbf{R}\}), \tag{2.1}$$

with

$$\hat{T} = -\sum_{i=1}^{N} \frac{\nabla_{\mathbf{r}_i}^2}{2}, \tag{2.2}$$

$$\hat{V} = \frac{1}{2}\sum_{i=1}^{N}\sum_{j\neq i}^{N} \frac{1}{|\mathbf{r}_i - \mathbf{r}_j|}, \tag{2.3}$$

$$\hat{V}_\mathrm{ext}(\{\mathbf{R}\}) = -\sum_{i=1}^{N}\sum_{j=1}^{N_\mathrm{a}} \frac{Z_i}{|\mathbf{r}_i - \mathbf{R}_j|} + \frac{1}{2}\sum_{i=1}^{N_\mathrm{a}}\sum_{j\neq i}^{N_\mathrm{a}} \frac{Z_i Z_j}{|\mathbf{R}_i - \mathbf{R}_j|}. \tag{2.4}$$

This Hamiltonian is given in the Born–Oppenheimer approximation, where ions are assumed to be static. Hartree atomic units ($e = \frac{1}{4\pi\varepsilon_0} = \hbar = m_\mathrm{e} = 1$) are used. The first term is the many-particle kinetic energy operator $\hat{T}$, composed out of single-particle kinetic energy operators $\hat{T}^\mathrm{sp} = -\nabla^2/2$ acting on the electron coordinates $\mathbf{r}_i$. The third term, $\hat{V}$, describes the Coulomb interaction between electrons. The external potential $\hat{V}_\mathrm{ext}(\{\mathbf{R}\})$ comprises the interaction of electrons with the nuclei (of charge Z_i) at positions $\mathbf{R}_i$ and a constant term representing the electrostatic energy of the ions. In this approximation, the Hamiltonian has a parametric dependence on the positions of the atom cores, entering the external potential $\hat{V}_\mathrm{ext}(\{\mathbf{R}\}) = \hat{V}_\mathrm{ext}$.

It is of our interest to find the ground-state solution Ψ_0, with ground-state energy E_0, to the eigenvalue problem,

$$\hat{H}\Psi = E\Psi \tag{2.5}$$

involving the many-particle wave function Ψ and total energy E. In principle, this problem can be solved by a variational ansatz,

$$E_0 = \min_{\Psi_\mathrm{T}} \frac{\langle\Psi_\mathrm{T}|\,\hat{H}\,|\Psi_\mathrm{T}\rangle}{\langle\Psi_\mathrm{T}|\,\Psi_\mathrm{T}\rangle}, \tag{2.6}$$

via the so-called Ritz method, which states that the ground-state energy can be found by minimizing the energy expectation value by inserting trial wave functions Ψ_T. Each trial wave function will give a higher energy than the true ground-state energy, except if the trial wave function is the ground state. This approach is not very practical, but with enough flexibility in the trial wave function, Eq. (2.5) can be transformed into a matrix eigenvalue problem. A possible basis may consist of Slater determinants, composed of Hartree–Fock (excited) orbitals. This approach is known as the configuration interaction method. The method works for small systems, comprising on the

order of ten electrons, however, for many electrons, one hits an exponential wall due to the very large number of degrees of freedom involved. The required number of variational parameters would exceed by far the amount of memory and computational power available today [23].

Importantly, an alternate approach was developed by Pierre Hohenberg and Walter Kohn. They were able to reduce the degrees of freedom of the problem from the many-particle wave function with $3N$ coordinates (excluding spin) to the scalar electron density, which only depends on 3 coordinates. Their famous theorems, found in 1964 [17], together with the findings of Kohn and Sham later in 1965 [18], led to a breakthrough in electronic structure theory.

Hohenberg and Kohn proved in their first theorem that there is a one-to-one correspondence between the ground-state density of a system of N interacting electrons $n_0(\mathbf{r}) = \langle \sum_{i=1}^{N} \delta(\mathbf{r} - \mathbf{r}_i) \rangle_{\Psi=\Psi_0}$ and the external potential $\hat{V}_{\text{ext}}$ (up to a constant). An immediate consequence is that the ground-state expectation value of any observable $\hat{A}$ is a unique functional of the exact ground-state electron density

$$\langle \Psi_0 | \hat{A} | \Psi_0 \rangle = A[n_0], \tag{2.7}$$

including the ground-state energy $E_0 = E[n_0] = \langle \Psi_0 | \hat{H} | \Psi_0 \rangle$. This holds, because the ground-state density determines $\hat{V}_{\text{ext}}$ and thus the complete Hamiltonian. In turn, this fixes the ground state of the system and therefore the expectation value can be evaluated, making it a functional of the ground state density.

In their second theorem, they show that the total energy density functional $E[n]$ for a fixed external potential and density $n(\mathbf{r}) = \langle \sum_{i=1}^{N} \delta(\mathbf{r} - \mathbf{r}_i) \rangle_{\Psi}$ is of the form

$$\begin{aligned} E_{\text{HK}}[n] &= \langle \Psi | \hat{T} + \hat{V} | \Psi \rangle + \langle \Psi | \hat{V}_{\text{ext}} | \Psi \rangle \\ &= T[n] + V[n] + \int \mathrm{d}^3 r \; n(\mathbf{r}) V_{\text{ext}}(\mathbf{r}) \\ &= F_{\text{HK}}[n] + V_{\text{ext}}[n], \end{aligned} \tag{2.8}$$

where the Hohenberg–Kohn density functional $F_{\text{HK}}[n]$ is universal for any N many-electron system. This deals with the fact that kinetic and electron-electron Coulomb terms of Eq. (2.1) do not specify details about the system, which only enter via $\hat{V}_{\text{ext}}$. Importantly, $E[n]$ reaches its minimal value, equal to the ground-state total energy, for the ground-state density corresponding to $\hat{V}_{\text{ext}}$. From Eq. (2.3), the single-particle external potential is given by

$$V_{\text{ext}}(\mathbf{r}) = -\sum_{j=1}^{N_{\text{a}}} \frac{Z_i}{|\mathbf{r} - \mathbf{R}_j|} + \frac{1}{2N} \sum_{i=1}^{N_{\text{a}}} \sum_{j \neq i}^{N_{\text{a}}} \frac{Z_i Z_j}{|\mathbf{R}_i - \mathbf{R}_j|}. \tag{2.9}$$

Proofs of the theorems will not be given here, they can be found in Refs. [17, 24]. The big advantage of this approach is that all the information about the system's ground state is encoded in an easier to handle quantity, the electron density, rather than a complicated many-particle wave function with $3N$ degrees of freedom. The second theorem also provides a hint on how to obtain the ground state energy, yet

the exact form of the functional $F_{\mathrm{HK}}[n]$ is unfortunately unknown and limits practical applicability.

The next big step towards the minimization of the energy functional in Eq. (2.8) was achieved in 1965 by Kohn and Sham [18], applying a Hartree–Fock-like theory to the Hohenberg–Kohn total energy functional (here after Refs. [24, 25]). The ground state of a noninteracting many-electron system Ψ_0^{nonint} of N electrons[1] in an external potential can be represented with an antisymmetric Slater determinant

$$\Psi_0^{\mathrm{nonint}}(\mathbf{r}_1, \mathbf{r}_2, \ldots, \mathbf{r}_N) = \frac{1}{\sqrt{N!}} \begin{vmatrix} \psi_1(\mathbf{r}_1) & \psi_1(\mathbf{r}_2) & \ldots & \psi_1(\mathbf{r}_N) \\ \psi_2(\mathbf{r}_1) & \psi_2(\mathbf{r}_2) & \ldots & \psi_2(\mathbf{r}_N) \\ \vdots & \vdots & \ddots & \vdots \\ \psi_N(\mathbf{r}_1) & \psi_N(\mathbf{r}_2) & \ldots & \psi_N(\mathbf{r}_N) \end{vmatrix}, \tag{2.10}$$

consisting out of the N lowest-energy (nondegenerate) single-particle solutions $\psi_i(\mathbf{r})$ to the single-particle Schrödinger equation

$$\hat{H}^{\mathrm{sp}}\psi_i(\mathbf{r}) = \left[\hat{T}^{\mathrm{sp}} + v(\mathbf{r})\right] \psi_i(\mathbf{r}) = \varepsilon_i \psi_i(\mathbf{r}), \tag{2.11}$$

with the single-particle potential $v(\mathbf{r})$ in this case being represented by $V_{\mathrm{ext}}(\mathbf{r})$.

The kinetic energy can then be evaluated as

$$\langle \Psi_0^{\mathrm{nonint}} | \, \hat{T}^{\mathrm{sp}} \, | \Psi_0^{\mathrm{nonint}} \rangle = \sum_{i=1}^{N} \int \mathrm{d}^3 r \, \psi_i^*(\mathbf{r}) \left(-\frac{\nabla^2}{2} \right) \psi_i(\mathbf{r}) = T^{\mathrm{sp}}[n], \tag{2.12}$$

the external potential energy is given by

$$\langle \Psi_0^{\mathrm{nonint}} | \, \hat{V}_{\mathrm{ext}} \, | \Psi_0^{\mathrm{nonint}} \rangle = \int \mathrm{d}^3 r \, n(\mathbf{r}) V_{\mathrm{ext}}(\mathbf{r}) = V_{\mathrm{ext}}[n], \tag{2.13}$$

with the particle density

$$n(\mathbf{r}) = \sum_{i=1}^{N} \psi_i^*(\mathbf{r}) \psi_i(\mathbf{r}). \tag{2.14}$$

The kinetic energy of the particles can be expressed as a functional of the density, $T^{\mathrm{sp}}[n]$, because also in the case of noninteracting electrons a Hohenberg–Kohn theorem holds [24]. The brilliant idea of Kohn and Sham was to introduce auxiliary single-particle wave functions, obtained from an effective single-particle Hamiltonian, that would lead to the same density of interacting system. They replaced the original problem of interacting particles with independent auxiliary particles. Moreover, they could establish a way how to obtain this effective single-particle Hamiltonian and facilitate actual calculations.

The total energy functional of Eq. (2.8) contains the unknown functionals $T[n]$ and $V[n]$. In the Kohn–Sham formalism, they are in a first step approximated by the

[1] We restrict ourselves to spinless electrons here.

single-particle kinetic energy functional $T^{\mathrm{sp}}[n]$ of Eq. (2.12) and the Hartree energy

$$E_H[n] = \frac{1}{2} \int \mathrm{d}^3 r \, \mathrm{d}^3 r' \, \frac{n(\mathbf{r}) n(\mathbf{r}')}{|\mathbf{r} - \mathbf{r}'|}, \tag{2.15}$$

respectively. The Hartree energy represents the Coulomb interaction of a many-electron density with itself. It also contains interactions of electrons with themselves, a self-interaction which is unphysical and often is a source of errors in common DFT approximations. This replacement results in the total energy functional

$$E_{\mathrm{KS}}[n] = T^{\mathrm{sp}}[n] + E_{\mathrm{H}}[n] + V_{\mathrm{ext}}[n] + E_{\mathrm{xc}}[n], \tag{2.16}$$

where the error introduced by the substitutions are formally cured by the exchange-correlation energy $E_{\mathrm{xc}}[n]$. The replacement by the single-particle kinetic energy and Hartree energy has the advantage that these terms offer closed expressions in form of the single-particle wave functions and the density. These quantities are also known to be a reasonable approximation to the energy within Hartree–Fock theory. Furthermore, the second and third terms of Eq. (2.16) represent a charge neutral grouping. The exchange-correlation energy is given by $E_{\mathrm{xc}}[n] = (V[n] - E_{\mathrm{H}}[n]) + (T[n] - T^{\mathrm{sp}}[n])$ and must be a unique functional of the density, as all the other quantities are too [24]. It contains the name "exchange", as it has to cure the self-interaction error in the Hartree energy, which in Hartree–Fock theory is taken care of by the exchange interaction. Correlation energy is generally defined as the difference between the true ground state energy and the Hartree–Fock ground state solution. Equation (2.16) so far is formally exact by construction, with respect to Eq. (2.8). The exact functional $E_{\mathrm{xc}}[n]$, however, is unknown and needs to be approximated in practice (see Sec. 2.2.2).

Because one knows the explicit dependence of the total energy functional $E_{\mathrm{KS}}[n]$ on the single-particle wave functions ψ_i (except for the exchange-correlation part), one can use the method of Lagrange multipliers (ε_{lm}) to optimize the total energy with respect to the wave functions subject to the condition of wave function orthogonality $\langle \psi_l \,|\, \psi_m \rangle = \delta_{lm}$ and a density of N electrons, Eq. (2.14),

$$\begin{aligned} \frac{\delta}{\delta \psi_i^*(\mathbf{r})} \left[E_{\mathrm{KS}}[n] - \sum_{lm} \varepsilon_{lm} \int \mathrm{d}^3 r' \; [\psi_l^*(\mathbf{r}') \psi_m(\mathbf{r}') - \delta_{lm}] \right] \\ = \left[-\frac{\nabla^2}{2} + V_{\mathrm{H}}[n](\mathbf{r}) + V'_{\mathrm{ext}}(\mathbf{r}) + V_{\mathrm{xc}}[n](\mathbf{r}) \right] \psi_i(\mathbf{r}) \\ - \sum_m \varepsilon_{im} \psi_m(\mathbf{r}) \stackrel{!}{=} 0. \end{aligned} \tag{2.17}$$

We define the Hartree potential as

$$V_{\mathrm{H}}[n](\mathbf{r}) = \frac{\delta E_{\mathrm{H}}[n]}{\delta n(\mathbf{r})} = \int \mathrm{d}^3 r' \; \frac{n(\mathbf{r}')}{|\mathbf{r} - \mathbf{r}'|}. \tag{2.18}$$

The exchange-correlation potential is given by

$$V_{\mathrm{xc}}[n](\mathbf{r}) = \frac{\delta E_{\mathrm{xc}}[n]}{\delta n(\mathbf{r})}, \tag{2.19}$$

and the ion-ion interaction term of Eq. (2.9) dropped out in $V'_{\mathrm{ext}}(\mathbf{r})$. The matrix of Lagrange multipliers in Eq. (2.17) can be diagonalized by a unitary transformation of the wave functions [21] to result in the single-particle Kohn–Sham Eq. (2.11) with the Kohn–Sham potential

$$v(\mathbf{r}) = v[n + n^Z, n](\mathbf{r}) = V_{\mathrm{H}}[n + n^Z](\mathbf{r}) + V_{\mathrm{xc}}[n](\mathbf{r}), \tag{2.20}$$

where the external potential $V'_{\mathrm{ext}}(\mathbf{r})$ was incorporated into the Hartree potential by the ion density $n^Z(\mathbf{r}) = \sum_{i=1}^{N_{\mathrm{a}}} Z_i \delta(\mathbf{r} - \mathbf{R}_i)$.

Equation (2.20) is the final result of the work of Kohn and Sham. The solution of the many-body Schrödinger Eq. (2.5) was boiled down to a solution of an auxiliary single-particle Schrödinger equation, which is quite remarkable. The Kohn–Sham potential depends on the density of the auxiliary system, therefore the Kohn–Sham equation has to be solved self-consistently. Section 2.2.3 is devoted to the practical solution of the equation in terms of the projector augmented wave method. The only quantity which is still to be determined is the exchange-correlation density functional, for which approximations are discussed in the next section.

2.2.2 Exchange and correlation functionals and correction schemes

As discussed in Sec. 2.2.1, a universal functional $F_{\mathrm{HK}}[n]$ exists, which describes the many-body interaction of electrons in terms of their density. To find an approximation, this functional is rewritten in terms of known quantities as the Hartree energy and single-particle kinetic energy. All the unknown parts are then shifted into the exchange-correlation energy functional $E_{\mathrm{xc}}[n]$. With knowledge of the exact exchange-correlation functional, DFT would provide the exact description of nondegenerate ground states [26]. In practice however, one needs to use approximations for $E_{\mathrm{xc}}[n]$ and the results are only as good as the approximation for the exchange-correlation functional.

Local density approximation

The first approximation to be used for the exchange-correlation functional was the so-called local density approximation (LDA),

$$E_{\mathrm{xc}}^{\mathrm{LDA}}[n] = \int \mathrm{d}^3 r \; n(\mathbf{r}) \varepsilon_{\mathrm{xc}}(n(\mathbf{r})), \tag{2.21}$$

where $\varepsilon_{\mathrm{xc}}(n(\mathbf{r}))$ is the exchange-correlation energy per particle of a uniform electron gas of density $n(\mathbf{r})$ at the point $\mathbf{r}$. Surprisingly, this approximation gives qualitatively correct results not only in metals but also in covalently bonded insulators in most cases. LDA is nonempirical as the exchange energy part is analytically known. The

correlation part can be parametrized by fitting to *ab initio* diffusion Monte Carlo calculations of the homogeneous electron gas [27]. Its shortcomings are that binding energies are overestimated by about 1 eV/bond, giving rise to too short bond lengths in molecules and solids [26].

Generalized gradient approximation

To overcome the disadvantages of LDA, gradients of the density were incorporated into the exchange-correlation energy functional, which takes changes of the local density into account, i.e., it is a semi-local functional

$$E_{\mathrm{xc}}^{\mathrm{GGA}}[n] = \int \mathrm{d}^3r \; n(\mathbf{r})\, \varepsilon_{\mathrm{xc}}^{\mathrm{GGA}}\left(n(\mathbf{r}), |\nabla n(\mathbf{r})|, \nabla^2 n(\mathbf{r})\right). \tag{2.22}$$

This approximation is known as the so-called generalized gradient approximation (GGA). GGA has no unique form and in general there exist functionals whose parameters are either fit to (numerical) experiments or derived from exact conditions of quantum mechanics. One of the latter is the so-called Perdew–Burke–Ernzerhof exchange-correlation functional (PBE) functional [28], which currently is the most used exchange-correlation functional in solid state systems [26] and also the primarily used functional in this thesis.

In comparison with LDA, GGAs tend to improve total energies, atomization energies, energy barriers and structural energy differences [28]. GGAs expand and soften bonds, an effect that sometimes corrects and sometimes overcorrects the LDA prediction. Typically, GGAs favor density inhomogeneity more than LDA does [28].

Hybrid functionals

The last clear advance in development of exchange-correlation functionals came in the 90s with the so-called hybrid functionals [29]. The main idea is to replace a fraction a of the exchange energy $E_{\mathrm{x}}^{\mathrm{GGA}}$ of GGAs by Hartree–Fock exchange (also called exact exchange)

$$E_{\mathrm{xc},a}^{\mathrm{hybrid}} = aE_{\mathrm{x}}^{\mathrm{HF}} + (1-a)E_{\mathrm{x}}^{\mathrm{GGA}} + E_{\mathrm{c}}^{\mathrm{GGA}}, \tag{2.23}$$

with

$$E_{\mathrm{x}}^{\mathrm{HF}} = -\frac{1}{2}\sum_{\sigma}\sum_{ij}^{N}\int \mathrm{d}^3r \int \mathrm{d}^3r' \; \frac{\psi_{i\sigma}^*(\mathbf{r})\psi_{j\sigma}(\mathbf{r})\psi_{j\sigma}^*(\mathbf{r}')\psi_{i\sigma}(\mathbf{r}')}{|\mathbf{r}-\mathbf{r}'|}, \tag{2.24}$$

containing also the spin label σ, and leaving the original GGA correlation energy $E_{\mathrm{c}}^{\mathrm{GGA}}$. In this work besides PBE also the Becke 3-parameter (exchange), Lee, Yang and Parr exchange-correlation functional (B3LYP) [30] will be used, which is the most popular exchange-correlation functional in chemistry [26]. In the B3LYP, the fraction of exact exchange is 20%.

B3LYP is a not anymore a functional of the density only, but also of the Kohn–Sham orbitals ψ, which is why this class of theory is called orbital-dependent DFT. B3LYP is an empirical functional, which dependents on experimental fitting parameters. These were obtained by fitting to a set of atomization energies, ionization potentials, proton affinities, and total atomic energies. Kohn–Sham gaps predicted by hybrid functionals

are typically in better agreement with experimental band gaps than those obtained by PBE and LDA [31]. The downside of hybrid functionals is the increased computational cost and cumbersome convergence behavior in low-dimensional solid state systems when plane waves are used.

Hubbard U correction

In this thesis at some points usage of the so-called Hubbard U correction (also called DFT+U) is made. LDA and GGA are known to sometimes fail in systems where correlation effects are important [32, 33] as for example in transition metal oxides, which are wrongly predicted to be metals, but are insulators in reality. Motivated by the Hubbard model, where interactions of localized electrons are modeled by on-site Coulomb repulsion, a correction to the DFT total energy functional was proposed [32] and later refined in a simplified and rotationally invariant form [33]

$$\begin{aligned} E_U[\{n^{I\sigma}_{mm'}\}] &= E_{\mathrm{Hub}}[\{n^{I}_{mm'}\}] - E_{\mathrm{DC}}[\{n^{I\sigma}\}] \\ &= \frac{U}{2} \sum_I \sum_{m,\sigma} \left(n^{I\sigma}_{mm} - \sum_{m'} n^{I\sigma}_{mm'} n^{I\sigma}_{m'm} \right) \\ &= \frac{U}{2} \sum_I \sum_{\sigma} \mathrm{Tr}\left[n^{I\sigma}(1 - n^{I\sigma}) \right] . \end{aligned} \tag{2.25}$$

The correction to the total energy functional consists out of the Hubbard term E_{Hub} and a double counting term E_{DC}, which subtracts the interactions already described by the exchange-correlation functional. The energy correction involves spin-dependent local orbital occupation matrix elements $n^{I\sigma}_{mm'} = \sum_n f_n \langle \psi^\sigma_n | p^I_m \rangle \langle p^I_{m'} | \psi^\sigma_n \rangle$, which uses projectors on localized orbitals $p^I_m(\mathbf{r})$ centered around atom I and weighted by occupation numbers f_n.

The localized orbitals could for example be spherical harmonics with m being the magnetic quantum numbers of a certain angular momentum channel of interest. The choice of projectors is somewhat arbitrary and differs from implementation to implementation [33]. Spin-dependent atomic occupations are given by $n^{I\sigma} = \sum_m n^{I\sigma}_{mm}$ and total atomic occupations by $n^I = \sum_\sigma n^{I\sigma}$.

The effect of Eq. (2.25) is a penalty for partial occupation of electronic levels residing on a chosen atom for which the U correction is applied to (usually d or f states). It therefore leads to a partitioning into fully occupied and completely empty orbitals and thus is able to produce an insulating state for example in transition metal oxides.

To understand how Kohn–Sham orbitals are affected by the correction, one can derive by variation of Eq. (2.25) with respect to Kohn–Sham states the corresponding single-particle potential

$$V^\sigma_U = \sum_{Im} U \left(\frac{1}{2} - n^{I\sigma}_m \right) |p^I_m\rangle \langle p^I_m| . \tag{2.26}$$

From Eq. (2.26) it becomes apparent that Kohn–Sham orbitals, which carry the char-

acter of the local orbitals will be shifted towards lower energies if they are occupied and shifted towards higher energies if they are unoccupied for a positive value of U.

Empirical van der Waals corrections

Van der Waals forces are particularly important in systems with large surface areas. They are in detailed balance with electrostatic and exchange-repulsion interactions, and together they control for example binding distances in layered two-dimensional systems as for example in graphite. Common GGA functionals are semi-local in the electronic density and therefore cannot account for long-range electron correlations, which are responsible for van der Waals forces.

In this work semiempirical long-range dispersion corrections (DFT-D2) are employed, which come at low computational cost and work reasonably well for a broad range of systems [34]. Van der Waals interactions can be taken into account by adding long-range potentials to the Kohn–Sham total energy functional E_{KS}

$$E_{\mathrm{DFT-D2}} = E_{\mathrm{KS}} - s_6 \sum_{i<j}^{N_{\mathrm{at}}} \frac{C_6^{ij}}{R_{ij}^6} f(R_{ij}). \tag{2.27}$$

Here, a pairwise attractive interaction energy between atoms i and j is added (N_{at} number of atoms), which decreases quickly with interatomic distance as R_{ij}^{-6}. This form is motivated by the London formula for dispersion, which takes into account the instantaneous polarization of atoms and molecules and results in a weak attractive force for large distances. C_6^{ij} are dispersion coefficients for an atom pair ij, which are fixed parameters of the method [34]. The overall scaling factor s_6 depends on the exchange-correlation functional used. To avoid singularities, a damping factor $f(R_{ij})$ is multiplied to only correct for dispersion effects at interatomic distances larger than the sum of van der Waals radii of the atom pair (typically larger than 2 Å). At shorter distances only the Kohn–Sham total energy then contributes to the binding energy. Addition of Eq. (2.27) to the total energy functional has no direct consequences for the electron density, but gives additional forces in the atom relaxation procedure.

2.2.3 Projector augmented wave method

As we have seen, Coulomb interactions between electrons pose a severe challenge for studying many-body systems. This challenge can be overcome by mapping the interacting particles to fictitious noninteracting particles that move in an effective potential created by other particles as seen in the Kohn–Sham approach in the previous sections. Practically, the Kohn–Sham equation (2.11) together with the effective potential of Eq. (2.20) needs to be expanded in some basis.

In a periodic lattice the most natural choice is a plane-wave expansion. The expan-

sion also nicely connects to Bloch's theorem,

$$\psi_{n\mathbf{k}}(\mathbf{r}) = e^{i\mathbf{k}\mathbf{r}} u_{n\mathbf{k}}(\mathbf{r}) = \sum_{\mathbf{G}=\mathbf{0}}^{\mathbf{G}_{\mathrm{cut}}} e^{i(\mathbf{k}+\mathbf{G})\mathbf{r}} u_{n\mathbf{k},\mathbf{G}}, \tag{2.28}$$

$$\psi_{n\mathbf{k}}(\mathbf{r}+\mathbf{R}) = e^{i\mathbf{k}\mathbf{R}} \psi_{n\mathbf{k}}(\mathbf{r}), \tag{2.29}$$

where states can be assigned a band index n and crystal momentum $\mathbf{k}$. The cell-periodic part of the Bloch wave function $u_{n\mathbf{k}}(\mathbf{r})$ is decomposed into Fourier components $u_{n\mathbf{k},\mathbf{G}}$ in terms of reciprocal lattice vectors $\mathbf{G}$ to the real space lattice vectors $\mathbf{R}$. Plane waves form a complete and orthogonal basis. In a calculation, the basis set has to be limited by a momentum cutoff $\mathbf{G}_{\mathrm{cut}}$. Plane waves have the advantage of being systematically improvable by increasing the cutoff.

Not only the Coulomb interactions among the electrons are a problem to *ab initio* calculations, but also the interaction of the Kohn–Sham states with the nuclei. The steep potentials around the atom cores lead to a high kinetic energy, which makes the wave functions vary strongly. These short variations around the atom cores would need a prohibitively large amount of plane waves to describe the wave function accurately, about on the order of 10^8 plane waves [35], posing high demands on memory and computational time.

The problem of highly oscillating wave functions in the core region has historically been treated in many different ways. Available methods distinguish the core from the interstitial regions, reminiscent of a muffin tin (choosing specific atom radii for the separation). The strategy can either be to change the basis set within the muffin tin spheres, by matching atomic orbitals at the sphere boundary with plane waves, or in a second strategy to change the atomic potential itself to result in smooth so-called pseudopotentials, excluding the deep core states. The pseudopotentials are chosen such that the resulting wave functions are nodeless within the core region, but still reproduce the correct behavior in the interstitial region, where bonding takes place.

Here a different, relatively new approach, the so-called PAW method [21] is described, which is a mixture of both methods. The advantage of the PAW method is that all-electron wave functions are still accessible if needed and that the replacement is exact when the method specific basis expansion is increased, i.e., it does not suffer from energy and charge transferability problems like pseudopotentials. Furthermore, the PAW method is computationally efficient as it operates mainly on plane waves with low momentum cutoffs $\mathbf{G}_{\mathrm{cut}}$. Being the theoretical basis for pseudopotentials, PAW unifies the all-electron and pseudopotential approaches [21].

Transformation theory

The idea of the PAW method is to transform from a wave function picture with strongly varying character around the atom cores to a picture of smooth pseudo wave functions via a linear transformation (this section is heavily inspired by Refs. [21, 36, 37]). Inversely, this can be expressed by the transformation

$$\psi_n = \hat{\mathcal{T}} \tilde{\psi}_n, \tag{2.30}$$

with ψ_n being a single-particle wave function (e.g., in the Kohn–Sham sense) and $\tilde{\psi}_n$ the smooth pseudo single-particle wave function. The idea is then, if such a linear transformation exists, to express the total energy functional of Eq. (2.16),

$$E = E[n[\psi_n]] = E[n[\hat{\mathcal{T}}\tilde{\psi}_n]], \tag{2.31}$$

in terms of the pseudo wave functions and obtain a single-particle Schrödinger-like equation by variation of the total energy with respect to the pseudo wave functions subject to orthogonality constraints

$$\frac{\delta E}{\delta \tilde{\psi}_n^*(\mathbf{r})} = \left(\hat{\mathcal{T}}^\dagger \hat{H} \hat{\mathcal{T}} - \hat{\mathcal{T}}^\dagger \hat{\mathcal{T}} \varepsilon_n\right) \tilde{\psi}_n(\mathbf{r}) = 0, \tag{2.32}$$

similarly as in the end of Sec. 2.2.1.

The PAW transformation is given by [21]

$$\hat{\mathcal{T}} = \mathbb{1} + \sum_j \left(|\phi_j\rangle - |\tilde{\phi}_j\rangle\right) \langle p_j| \,, \tag{2.33}$$

which involves two types of so-called *partial waves*, the *atomic partial waves* ϕ_j and the *pseudo partial waves* $\tilde{\phi}_j$, augmented with projector functions p_j. The index j is a composed index $\{n, l, m_l, R\}$, with n the shell number, l angular momentum quantum number and magnetic quantum number m_l. Each atom, indexed with R, has its own set of partial waves and projectors located at the position of the atom.

The ϕ_j are wave functions obtained by solving all-electron DFT for isolated atoms, from which, by virtue of a pseudization recipe [36], smooth pseudo partial waves $\tilde{\phi}_j$ can be generated. The pseudo partial wave construction is not unique, but the common goal of these recipes is to smoothen the strongly varying wave function parts closeby the atom core. The pseudo partial waves are generated such, that they coincide outside a certain core radius with the atomic partial waves. The $\tilde{\phi}_j$ thereby define then also the projector functions p_j which are constrained to fulfill an orthogonality relation $\langle p_j|\tilde{\phi}_i\rangle = \delta_{ij}$. They are located within the core radius [21] and optimized to be representable by a small number of Fourier coefficients.

Why does the transformation of Eq. (2.30) achieve a smooth behavior of $\tilde{\psi}_n$? The effect of the replacement is best seen when acting on pseudo partial waves

$$\hat{\mathcal{T}} |\tilde{\phi}_i\rangle = |\tilde{\phi}_i\rangle + \sum_j \left(|\phi_j\rangle - |\tilde{\phi}_j\rangle\right) \underbrace{\langle p_j|\tilde{\phi}_i\rangle}_{=\delta_{ij}} = |\phi_j\rangle \,. \tag{2.34}$$

The transformation takes the smooth parts of pseudo wave function and replaces them with the strongly varying part. Conversely, an effective description within the pseudo wave function picture involves very smooth wave functions, because strongly varying parts were removed from ψ_n, which makes them representable with a Fourier series as in Eq. (2.28).

The behavior of the PAW transformation can also be seen from the example of a p-σ molecular orbital of Cl_2 in Fig. 2.2 [37]. It shows the decomposition of the wave

function in terms of

$$\langle \mathbf{r}|\psi\rangle = \langle \mathbf{r}|\hat{\mathcal{T}}\tilde{\psi}\rangle = \langle \mathbf{r}|\tilde{\psi}\rangle + \underbrace{\sum_j \langle \mathbf{r}|\phi_j\rangle \langle p_j|\tilde{\psi}\rangle}_{\langle \mathbf{r}|\psi^1\rangle} - \underbrace{\sum_j \langle \mathbf{r}|\tilde{\phi}_j\rangle \langle p_j|\tilde{\psi}\rangle}_{\langle \mathbf{r}|\tilde{\psi}^1\rangle} \tag{2.35}$$

and illustrates that in order to receive the full wave function ψ, one has to add a spiky atomic partial waves ψ^1 and remove the smooth pseudo partial waves $\tilde{\psi}^1$ from the smooth pseudo wave function $\tilde{\psi}$.

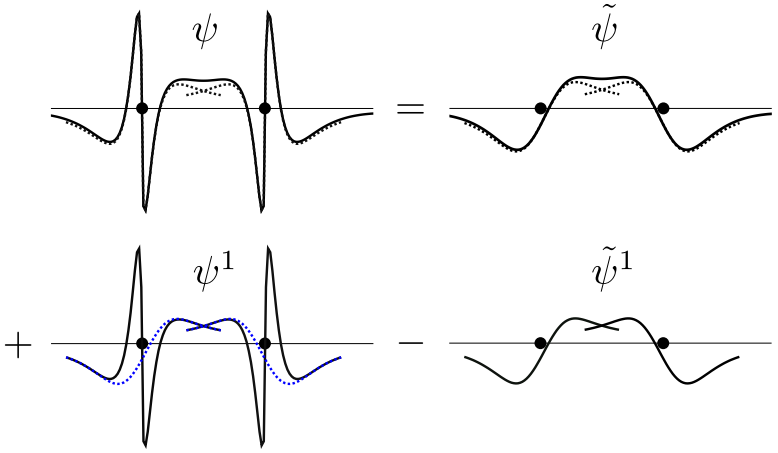

Figure 2.2: PAW transformation example from the p-σ orbital (ψ) of the Cl_2 molecule and its decomposition into pseudo wave function ($\tilde{\psi}$) and the two one-center expansions (ψ^1 and $\tilde{\psi}^1$) of Eq. (2.35), represented by solid lines. The dashed curves in the upper row are the lower row functions, for comparison. The blue dashed line is the same curve as $\tilde{\psi}^1$ to indicate that ψ^1 and $\tilde{\psi}^1$ coincide outside a certain radius measured from the atom, which are located at the dots. Adapted from Ref. [37].

Auxiliary Hamiltonian

In order to obtain the total energy functional, expressed in terms of the pseudo wave functions $\tilde{\psi}_n$, expectation values of single-particle operators $\hat{A}$ have to be translated into the pseudo picture $\hat{\tilde{A}}$

$$\langle \hat{A}\rangle = \sum_n \langle \psi_n|\, \hat{A}\, |\psi_n\rangle = \sum_n \langle \tilde{\psi}_n|\, \hat{\tilde{A}}\, |\tilde{\psi}_n\rangle\,. \tag{2.36}$$

The explicit form of $\hat{\tilde{A}}$ is given by

$$\begin{aligned}\hat{\tilde{A}} &= \hat{\mathcal{T}}^\dagger \hat{A} \hat{\mathcal{T}} \\ &= \hat{A} + \sum_{i,j} |p_i\rangle \left(\langle \phi_i | \hat{A} | \phi_j \rangle \right) - \langle \tilde{\phi}_i | \hat{A} | \tilde{\phi}_j \rangle \langle p_j | .\end{aligned} \tag{2.37}$$

Expectation values then commonly are separated into three parts

$$\begin{aligned}\langle \tilde{\psi}_n | \hat{\tilde{A}} | \tilde{\psi}_n \rangle =& \langle \tilde{\psi}_n | \hat{A} | \tilde{\psi}_n \rangle \\ &+ \sum_{i,j} \langle \tilde{\psi}_n | p_i \rangle \langle \phi_i | \hat{A} | \phi_j \rangle \langle p_j | \tilde{\psi}_n \rangle \\ &- \sum_{i,j} \langle \tilde{\psi}_n | p_i \rangle \langle \tilde{\phi}_i | \hat{A} | \tilde{\phi}_j \rangle \langle p_j | \tilde{\psi}_n \rangle \\ =& \tilde{A} + A^1 - \tilde{A}^1,\end{aligned} \tag{2.38}$$

defining plane-wave part $\tilde{A}$, and two-center parts A^1 and $\tilde{A}^1$.

In this formulation, the expectation value of the single-particle density operator $\hat{\rho} = |\mathbf{r}\rangle \langle \mathbf{r}|$ yields the electron density

$$n(\mathbf{r}) = \sum_n \langle \tilde{\psi}_n | \hat{\tilde{\rho}} | \tilde{\psi}_n \rangle = \tilde{n}(\mathbf{r}) + n^1(\mathbf{r}) - \tilde{n}^1(\mathbf{r}). \tag{2.39}$$

It is important to note that within the pseudo picture, the overlap operator $\hat{O} = \mathbb{1}$ is not a unit matrix anymore

$$\hat{\tilde{O}} = \mathbb{1} + \sum_{i,j} |p_i\rangle \left[\langle \phi_i | \phi_j \rangle - \langle \tilde{\phi}_i | \tilde{\phi}_j \rangle \right] \langle p_j | . \tag{2.40}$$

In a similar way the total energy functional separates into three contributions [21]

$$E = \tilde{E} + E^1 - \tilde{E}^1. \tag{2.41}$$

Variation of Eq. (2.41) subject to orthogonality constraints [Eq. (2.40)] with respect to pseudo wave functions leads to PAW Kohn–Sham equations

$$\hat{\tilde{H}} | \tilde{\psi}_n \rangle = \varepsilon_n \hat{\tilde{O}} | \tilde{\psi}_n \rangle \tag{2.42}$$

for the pseudo wave functions, representing a generalized eigenvalue problem with the overlap operator $\hat{\tilde{O}}$.

The pseudo Kohn–Sham Hamiltonian is then given as [21]

$$\begin{aligned}\hat{\tilde{H}} = &-\frac{1}{2}\nabla^2 + \tilde{v}[\tilde{n}+\hat{n},\tilde{n}](\mathbf{r}) \\ &+ \sum_{i,j} |p_i\rangle \left[\langle\phi_i| - \frac{1}{2}\nabla^2 + v^1[n^1+n^Z, n^1](\mathbf{r})\,|\phi_j\rangle\right]\langle p_j| \\ &- \sum_{i,j} |p_i\rangle \left[\langle\tilde{\phi}_i| - \frac{1}{2}\nabla^2 + \tilde{v}^1[\tilde{n}^1+\hat{n},\tilde{n}^1](\mathbf{r})\,|\tilde{\phi}_j\rangle\right]\langle p_j|\,, \end{aligned} \tag{2.43}$$

where again, the operator separates into plane-wave and one-center parts. The effective potentials v are given in the same form as in Eq. (2.20); the first argument in the functional brackets of the effective potentials $\tilde{v}$, v^1, and $\tilde{v}^1$ indicate the charge densities with which the Hartree potential is evaluated. The exchange-correlation potential is evaluated with the second argument, e.g., for $\tilde{v}$:

$$\tilde{v}[\tilde{n}+\hat{n},\tilde{n}](\mathbf{r}) = \frac{\delta E}{\delta\tilde{n}(\mathbf{r})} = \int \mathrm{d}^3\mathrm{r}'\,\frac{\tilde{n}(\mathbf{r}')+\hat{n}(\mathbf{r}')}{|\mathbf{r}-\mathbf{r}'|} + V_{\mathrm{xc}}[\tilde{n}](\mathbf{r}). \tag{2.44}$$

A compensation charge $\hat{n}$ has been introduced in Eq. (2.43) such that one can separate the Hartree contributions into plane-wave and partial-wave expansions [21].

The second and third term of Eq. (2.43) remind of nonlocal pseudopotential operators and in fact both, norm-conserving and ultrasoft pseudopotential formulations can be derived from the PAW theory [21, 37]. These nonlocal parts are not static as in the mentioned pseudopotential formalisms, but adapt to the instantaneous electronic environment through the densities n^1, $\tilde{n}^1$, and $\hat{n}$ [37].

From a numerical point of view the first part of the matrix elements of Hamiltonian (2.43) is evaluated in Fourier representation due to the smooth behavior of the resulting potential $\tilde{v}$. The terms in brackets in the second and third terms of Eq. (2.43) can be efficiently evaluated on a radial grid. The projector functions p_i were optimized in such a way that they are representable in terms of compact Fourier decompositions, such that the projection onto the pseudo wave function is possible in Fourier space.

Usually, only valence states are considered as a degree of freedom in the expansion for the density in Eq. (2.39), and core electrons are kept frozen. Nonlinear core corrections are applied to cure the nonlocal behavior in the separation of the core and valence density of the exchange-correlation energy [38]. Further errors are typically introduced due to the truncations in the plane-wave basis set as well as the truncation in the partial wave expansions in Eq. (2.30) [21]. The convergence parameter of the kinetic energy cutoff in the plane-wave expansion is comparable to ultrasoft pseudopotentials, with a very low cutoff energy of about 30 Ry. Reasonable PAW partial wave sets have a good accuracy and transferability with about 1–2 partial waves per angular momentum and site [21].

Before discussing the relativistic spin-density formulation of the PAW method, we first introduce the single-particle Dirac equation in the next section.

2.3 Effects from the relativistic kinetic energy

Since this thesis is devoted partly to graphene and relativistic effects, a short qualitative discussion of relativistic effects will be given and the Dirac equation will be discussed, to see where spin-orbit coupling (SOC) originates from. This section on the qualitative relatvistic effects [39] and the derivation of the nonrelativistic limit of the Dirac equation (can also be found in Ref. [40]) was heavily inspired by the talk "Introduction to noncollinear magnetism and spin-orbit coupling in `Quantum Espresso`" by Andrea Dal Corso (Sissa and Democritos, Trieste).

That relativistic effects may be relevant to the states in atoms or the dispersion of electrons in solids, can be expemlified by the following argument [39]. The relativistic mass of an electron is given by

$$m = \frac{m_\mathrm{e}}{\sqrt{1 - \frac{v^2}{c^2}}}, \tag{2.45}$$

with m_e the rest mass and v the average velocity of the electron. The mass m increases when the velocity becomes comparable to the speed of light c. The associated Bohr radius of an electron bound to a proton is

$$a_0 = \frac{\hbar^2}{me^2}, \tag{2.46}$$

which is reduced by an increased mass. In atomic units, the electron velocity expectation value in an hydrogenic atom is $v = Z$, with Z being the atomic number. The speed of light in atomic units is $c \approx 137$ and if one inserts the atomic number of mercury, for instance, $Z = 80$ one obtains $v/c = 0.58$.

In such an atom the Bohr radius is reduced by 23%. The increase of relativistic mass leads to a contraction of orbitals that are in the vicinity of the nucleus with large speeds. These are usually the inner s and p orbitals, while d and f orbitals expand due to the screening of the nuclear charge by the s and p orbitals. This effect is important for topological insulators, as the mechanism can lead to an inversion of s and p valence states (together with spin-orbit coupling). This was only a very qualitative example of a relativistic effect in an atom. To have a more microscopic insight, we need to look at the Dirac equation.

2.3.1 Single-particle Dirac equation

A general theory for the description of a relativistic electron in the hydrogen atom was found by Paul Dirac in 1928. For a free spin-1/2 particle with mass m the Dirac equation reads [41, 42]

$$i\hbar\frac{\partial\psi(\mathbf{r},t)}{\partial t} = \hat{H}_\mathrm{D}\psi(\mathbf{r},t) = \left(c\hat{\boldsymbol{\alpha}}\cdot\hat{\mathbf{p}} + \hat{\beta}mc^2\right)\psi(\mathbf{r},t) \tag{2.47}$$

$$= \left(\hat{T}_\mathrm{D} + mc^2\right)\psi(\mathbf{r},t), \tag{2.48}$$

where $\boldsymbol{\alpha}$ and β are 4×4 matrices and $\hat{\mathbf{p}} = -i\hbar\nabla$. The relativistic kinetic energy is given by $\hat{T}_{\mathrm{D}} = c\hat{\boldsymbol{\alpha}} \cdot \hat{\mathbf{p}} + (\hat{\beta} - 1)mc^2$. One possible representation of $\boldsymbol{\alpha}$ and β is given in terms of the Pauli matrices

$$\sigma_0 = \begin{pmatrix} 1 & 0 \\ 0 & 1 \end{pmatrix}, \sigma_x = \begin{pmatrix} 0 & 1 \\ 1 & 0 \end{pmatrix}, \sigma_y = \begin{pmatrix} 0 & -i \\ i & 0 \end{pmatrix}, \sigma_z = \begin{pmatrix} 1 & 0 \\ 0 & -1 \end{pmatrix} \tag{2.49}$$

as

$$\alpha_i = \begin{pmatrix} 0 & \sigma_i \\ \sigma_i & 0 \end{pmatrix}, \beta = \begin{pmatrix} \sigma_0 & 0 \\ 0 & -\sigma_0 \end{pmatrix}. \tag{2.50}$$

The eigenfunctions of the Dirac equation then are four-component spinors

$$\psi(\mathbf{r}, t) = \begin{pmatrix} \psi_1(\mathbf{r}, t) \\ \psi_2(\mathbf{r}, t) \\ \psi_3(\mathbf{r}, t) \\ \psi_4(\mathbf{r}, t) \end{pmatrix} = \begin{pmatrix} \psi^{\mathrm{A}}(\mathbf{r}, t) \\ \psi^{\mathrm{B}}(\mathbf{r}, t) \end{pmatrix}, \tag{2.51}$$

where ψ^{A} and ψ^{B} represent two-component spinors, named large and small component, respectively.

The interaction of an electron and an electromagnetic field, characterized by the scalar and vector potentials $\varphi(\mathbf{r})$ and $\mathbf{A}(\mathbf{r})$, are incorporated via minimal coupling $\hat{\mathbf{p}} \to \hat{\mathbf{p}} + e\mathbf{A}(\mathbf{r}) = \hat{\boldsymbol{\pi}}$ and $E \to E + e\varphi(\mathbf{r})$, where e is the absolute of the electron charge.

The time-independent Dirac equation can be obtained if $\varphi(\mathbf{r})$ and $\mathbf{A}(\mathbf{r})$ are time-independent by the ansatz $\psi(\mathbf{r}, t) = \exp(-iEt/\hbar)\psi(\mathbf{r})$, resulting in the equations

$$c\hat{\boldsymbol{\sigma}} \cdot \hat{\boldsymbol{\pi}}\psi^{\mathrm{B}}(\mathbf{r}) + \left[mc^2 - e\varphi(\mathbf{r}) - E\right]\psi^{\mathrm{A}}(\mathbf{r}) = 0, \tag{2.52}$$

$$c\hat{\boldsymbol{\sigma}} \cdot \hat{\boldsymbol{\pi}}\psi^{\mathrm{A}}(\mathbf{r}) - \left[E + mc^2 + e\varphi(\mathbf{r})\right]\psi^{\mathrm{B}}(\mathbf{r}) = 0. \tag{2.53}$$

2.3.2 Nonrelativistic limit of the Dirac equation

Defining the reduced energy $E' = E - mc^2$, one can rewrite Eq. (2.53) in the form

$$\psi^{\mathrm{B}}(\mathbf{r}) = \frac{c\hat{\boldsymbol{\sigma}} \cdot \hat{\boldsymbol{\pi}}\psi^{\mathrm{A}}(\mathbf{r})}{E' + 2mc^2 + e\varphi(\mathbf{r})} \approx \frac{1}{2mc}\hat{\boldsymbol{\sigma}} \cdot \hat{\boldsymbol{\pi}}\psi^{\mathrm{A}}(\mathbf{r}). \tag{2.54}$$

In the last step the denominator was expanded in a Taylor series in the small parameter $[E' + e\varphi(\mathbf{r})]/2mc^2$ and terms of order $(v/c)^2$ were ignored. From Eq. (2.54) it can be seen that $\psi^{\mathrm{B}}(\mathbf{r})$ is of order v/c $\psi^{\mathrm{A}}(\mathbf{r})$, because the canonical momentum expectation value is about $\langle\hat{\boldsymbol{\pi}}\rangle \propto v$.

If the expression for $\psi^{\mathrm{B}}(\mathbf{r})$ is inserted back in the equation for $\psi^{\mathrm{A}}(\mathbf{r})$, one obtains the Pauli equation

$$\left[\frac{1}{2m}(\hat{\boldsymbol{\sigma}} \cdot \hat{\boldsymbol{\pi}})(\hat{\boldsymbol{\sigma}} \cdot \hat{\boldsymbol{\pi}}) - e\varphi(\mathbf{r}) - E'\right]\psi^{\mathrm{A}}(\mathbf{r}) = 0. \tag{2.55}$$

The expansion

$$(\hat{\boldsymbol{\sigma}} \cdot \hat{\boldsymbol{\pi}})(\hat{\boldsymbol{\sigma}} \cdot \hat{\boldsymbol{\pi}}) = \hat{\boldsymbol{\pi}}^2 + e\hbar\hat{\boldsymbol{\sigma}} \cdot \nabla \times \mathbf{A}(\mathbf{r}), \tag{2.56}$$

leads to the Pauli equation in the more familiar form

$$\left[\hat{H}^{\mathrm{Pauli}} - E'\right] \psi^{\mathrm{A}}(\mathbf{r}) = \left[\frac{\hat{\boldsymbol{\pi}}^2}{2m} + \frac{e\hbar}{2m}\hat{\boldsymbol{\sigma}} \cdot \mathbf{B}(\mathbf{r}) - e\varphi(\mathbf{r}) - E'\right] \psi^{\mathrm{A}}(\mathbf{r}) = 0. \tag{2.57}$$

This was an important result of Dirac, showing the electron to possess a magnetic moment due to its spin angular momentum $\mu_{\mathrm{B}}\boldsymbol{\sigma}$, with $\mu_{\mathrm{B}} = e\hbar/2m$ the Bohr magneton, justifying Pauli's addition of a spin degree of freedom to the Schrödinger equation.

If one retains terms up to order $(v/c)^2$ in the Taylor series, one obtains the equation $\hat{H}\psi = E'\psi$ for a two-component spinor ψ, where the Hamiltonian is [40]

$$\hat{H} = \hat{H}^{\mathrm{Pauli}} - \frac{\hat{\mathbf{p}}^4}{8m^3c^2} - \frac{e\hbar^2}{8m^2c^2}\nabla \cdot \nabla\varphi(\mathbf{r}) - \frac{e\hbar}{4m^2c^2}\hat{\boldsymbol{\sigma}} \cdot [\nabla\varphi(\mathbf{r}) \times \hat{\mathbf{p}}]\,. \tag{2.58}$$

The first and second corrections to the Pauli Hamiltonian are the scalar-relativistic mass-velocity and Darwin terms. The mass-velocity term is a second order kinetic energy correction and is responsible for orbital contraction. The Darwin term leads to energy shifts in s-like states. The third term of Eq. (2.58) is the spin-orbit coupling. The largest energy scale in Eq. (2.58) is provided by the potential energy, about 10 eV, spin-Zeeman energy is about 0.1 meV. The scalar relativistic energy corrections of mass-velocity and Darwin term are typically as large as 0.01 meV. Spin-orbit coupling ranges mostly between 1 to 100 meV for valence electrons [40].

Spin-orbit coupling is an important ingredient for this thesis and can be rewritten in case of a spherical potential $\varphi(\mathbf{r}) = \varphi(r)$ as

$$\hat{H}_{\mathrm{soc}} = -\frac{e\hbar}{4m^2c^2}\frac{\partial\varphi(r)}{r\partial r}\hat{\boldsymbol{\sigma}} \cdot (\hat{\mathbf{r}} \times \hat{\mathbf{p}}) = -\frac{e}{2m^2c^2}\frac{\partial\varphi(r)}{r\partial r}\hat{\mathbf{L}} \cdot \hat{\mathbf{S}}, \tag{2.59}$$

with orbital angular momentum $\hat{\mathbf{L}} = \hat{\mathbf{r}} \times \hat{\mathbf{p}}$ and spin angular momentum $\hat{\mathbf{S}} = \hbar\hat{\boldsymbol{\sigma}}/2$.

Spin-orbit coupling leads to the lifting of the $2(2l+1)$ degenerate levels $|n\,l\,m_l\,m_s\rangle$ with shell number n, orbital angular momentum quantum number l, magnetic quantum number m_l and spin-z quantum number m_s. It splits the states into two groups, one with degeneracy $2l+2$ in which spin and angular momentum are parallel ($j = l + 1/2$) and one with degeneracy $2l$ where spin and angular momentum are antiparallel ($j = l - 1/2$). Eigenstates of spin-orbit coupling are usually denoted as $|n\,l\,j\,m_j\rangle$, where j and m_j are quantum numbers of total angular momentum $\hat{\mathbf{J}} = \hat{\mathbf{L}} + \hat{\mathbf{S}}$ and its projection onto a chosen axis.

The behavior of energy level splitting in a hydrogen-like atom with core charge Z subject to spin-orbit coupling can be obtained as [40]

$$\Delta E_{\mathrm{soc}} = \frac{Z^4\alpha}{n^3}\frac{1}{l(l+1)}\,\mathrm{Ry}, \tag{2.60}$$

with fine structure constant $\alpha \approx 1/137$. One expects strong spin-orbit coupling for heavy elements and smaller splittings for valence states.

2.4 Relativistic spin density functional theory

In the following, we briefly discuss the relativistic spin density functional theory formulation of the PAW method, following Refs. [19, 20, 22, 36] to indicate which approximations have been made and how finally relativistic effects enter the problem in form of a PAW Kohn–Sham Hamiltonian.

In the notion of relativistic quantum electrodynamics, the generalization of the density and the external electric potential is the four current and the four potential. In a generalized Hohenberg–Kohn theorem it can be shown that (after fixing a gauge) the ground state is uniquely determined by the four current [19]. Further it can be established, that the total energy as a functional of the four current is minimized by the four current associated with the ground state.

This fully relativistic approach needs to be simplified in order to carry out practical calculations. Specifically, contributions from orbital currents as well as retardation effects and magnetic interactions (e.g., Breit interaction) between the electrons are neglected [36]. What remains in the so-called relativistic spin-density functional theory (RSDFT) formulation are relativistic effects from the kinetic energy, giving rise to scalar relativistic quantities and spin-orbit coupling, see Eq. (2.58).

In order to derive the relativistic PAW Kohn–Sham equations, one starts with the total energy functional of RSDFT [19, 20, 22],

$$E_{\mathrm{RSDFT}} = \sum_{n,\eta_1,\eta_2} \langle \psi_n^{\eta_1} | \, \hat{T}_{\mathrm{D}}^{\eta_1,\eta_2} \, | \psi_n^{\eta_2} \rangle + E_{\mathrm{xc}}[n, \mathbf{m}] + E_{\mathrm{H}}[n + n^Z], \tag{2.61}$$

where the possibility of a magnetization density $\mathbf{m}(\mathbf{r})$ in the system is not excluded, even in the absence of an external magnetic field. This functional is very similar as in the nonrelativistic formulation of Eq. (2.16), except for the substitution of the kinetic energy with the relativistic kinetic energy $\hat{T}_{\mathrm{D}} = c\hat{\boldsymbol{\alpha}} \cdot \hat{\mathbf{p}} + (\hat{\beta} - 1)mc^2$. Again, as in the Kohn–Sham formalism, it is assumed that the problem of interacting Dirac particles can be mapped to noninteracting Dirac particles described by the wave functions ψ_n^η, which now carry a spinor index η. The noninteracting particles are constrained in such a way, that they reproduce the density $n(\mathbf{r}) = \sum_{n,\eta} \langle \psi_n^\eta | \mathbf{r} \rangle \langle \mathbf{r} | \psi_n^\eta \rangle$ and the magnetization density $\mathbf{m}(\mathbf{r}) = \mu_{\mathrm{B}} \Sigma_{\eta_1,\eta_2} \langle \psi_n^{\eta_1} | \mathbf{r} \rangle \langle \mathbf{r} | \psi_n^{\eta_2} \rangle (\hat{\beta}\hat{\boldsymbol{\sigma}})_{\eta_1,\eta_2}$ of the interacting system. The exchange-correlation functional, in principle, can contain also relativistic corrections beyond the Coulomb interactions [20], but those are usually neglected as mentioned earlier. The magnetization density $\mathbf{m}(\mathbf{r})$ needs to be allowed to change its direction in space, because due to spin-orbit coupling, s_z is not a good quantum number anymore and therefore the spin density can rotate.

Using the PAW transformation, Eq. (2.30) supplemented with spinor indices, one can arrive at the relativistic PAW Pauli-type Kohn–Sham equation [22]

$$\sum_{\sigma_2} \hat{\tilde{H}}^{\sigma_1,\sigma_2} \, |\tilde{\psi}_n^{\sigma_2}\rangle = \varepsilon_n \sum_{\sigma_2} \hat{\tilde{O}}^{\sigma_1,\sigma_2} \, |\tilde{\psi}_n^{\sigma_2}\rangle \,, \tag{2.62}$$

with the Hamiltonian

$$\begin{aligned}\hat{\tilde{H}}^{\sigma_1,\sigma_2} =& \frac{\hat{\mathbf{p}}^2}{2}\delta_{\sigma_1,\sigma_2} + \tilde{v}_{\sigma_1,\sigma_2} \\ &+ \sum_{ij} |p_i^{\sigma_1}\rangle \left[\sum_{\eta_1,\eta_2} \langle \phi_i^{\eta_1}| \hat{T}_{\mathrm{D}}^{\eta_1,\eta_2} + v_{\eta_1,\eta_2}^1 |\phi_i^{\eta_2}\rangle \right] \langle p_j^{\sigma_2}| \\ &- \sum_{ij} |p_i^{\sigma_1}\rangle \left[\sum_{\sigma_1',\sigma_2'} \langle \tilde{\phi}_i^{\sigma_1'}| \frac{\hat{\mathbf{p}}^2}{2} + \tilde{v}_{\sigma_1',\sigma_2'}^1 |\tilde{\phi}_i^{\sigma_2'}\rangle \right] \langle p_j^{\sigma_2}| \,, \end{aligned} \tag{2.63}$$

in close analogy to Eqs. (2.42) and (2.43).

The main feature of the Hamiltonian in Eq. (2.62) is that it operates only on the large components σ of the spinor indices η of the pseudo wave functions $\tilde{\psi}_n^\sigma$. Although it is not obvious from Eq. (2.63), this approach corresponds to calculating the relativistic kinetic energy [compare Eq. (2.48)] within the atomic region and neglecting small-component contributions in the interstitial regions, introducing an error on the order of $(v/c)^2 \approx 5 - 10 \times 10^{-5}$ [22]. The Hamiltonian (2.63) was brought in a form, such that it contains only nonrelativistic kinetic energy operators in the pseudo wave function and pseudo partial wave parts. This is very convenient as the kinetic energy operator is diagonal in the plane-wave basis. Another approximation is the neglect of contributions to the (magnetization) densities from the small components in the interstitial region. In a platinum atom for example, the charge density due to these terms is about 10^{-5} electrons [22]. The effect of this approximation is that the overlap operator $\hat{\tilde{O}}$ and the effective potentials in the pseudo sector can be made dependent only on the large spin components, introducing an error on the order of $1/c^2$ (for technical details see Ref. [22]). This significant reduction of degrees of freedom in the pseudo wave function decreases the computational cost at the expense of an error, which is still acceptable, because it is comparable to the transferability error usually encountered in nonrelativistic PAW [22].

The partial waves ϕ and $\tilde{\phi}$ are constructed by solving fully relativistic DFT for an isolated atom. The partial waves then carry a composed index $i = \{n, l, j, m_j, R\}$, which indicates the atom and quantum numbers of SOC eigenstates [22]. Only large components are used for projectors p and pseudo partial waves $\tilde{\phi}$. The result of the PAW transformation is that one gets an adaptive nonlocal pseudopotential distinguishing channels of different total angular momentum quantum numbers. The part where the full Dirac kinetic energy enters is the middle term of Eq. (2.63) for the atomic partial waves. The atomic partial waves can be identified with atomic orbitals, which have large kinetic energy in the core region. Therefore, this term is the main source of the relativistic effects, including spin-orbit coupling. Pre-generated pseudopotentials include partial waves and pseudo partial waves, ϕ_i^η, $\tilde{\phi}_i^\sigma$, respectively, as well as the projector functions p_i^σ. Pseudopotentials are constructed in such a way that they reproduce the fully relativistic valence spectrum of an atomic calculation exactly on a radial grid, including the spin-orbit coupling splittings. An example of the evaluation of a copper pseudopotential in terms of plane waves is discussed in Sec. 3.2.3.

2.5 Quantum Monte Carlo

The solution of the stationary many-electron Hamiltonian in Eq. (2.1) represents a formidable task to electronic structure theory. In this section we describe how variational Monte Carlo (VMC) and diffusion Monte Carlo (DMC) [summarized as QMC methods] can be used to calculate accurate ground state energies instead of, but with the help of DFT. The main ideas are condensed from an elaborate review of Foulkes et al. [43].

One of the main advantages of the QMC methods is that they explicitly treat the full many-body Hamiltonian in Eq. (2.1) with direct use of many-body correlated wave functions and are able to calculate ground state properties of atoms, molecules, and solids [43]. Although QMC methods are very expensive in computational time, they show favorable scaling with the number of electrons N as N^3, compared to the N^5–N^7 scaling of other correlated wave function methods. Their algorithms are nearly trivially parallelizable with a minimal amount of communication. Therefore, QMC methods are able to efficiently exploit the architecture of modern supercomputers with nearly linear scaling in the number of cores, which themselves can nowadays reach up to thousands. The QMC methods have already been applied to a variety of systems with impressive accuracy. QMC can predict cohesive energies, binding energies, and electronic gaps with only 1–3% deviation compared to experimental values [44]. Benchmark calculations on the G2 molecule set showed that on average 95% of the correlation energy can be recovered [45].

One milestone in electronic structure theory was the calculation of the ground state of the homogeneous electron gas by DMC [27], which underlies the local density approximation of DFT. The most widely used method for electronic structure calculations, DFT, is conversely very relevant to QMC. The accuracy of QMC relies on the quality of trial wave functions, which are usually generated by DFT. Even when using best available approximate exchange-correlation functionals DFT results are typically an order of magnitude less accurate than good QMC results [43]. Nevertheless, DFT is less computationally demanding, which is the reason why it is more widely applied than QMC. Typically, DFT delivers less accurate descriptions for van der Waals bound systems or strongly correlated systems. QMC is able to cure these shortcomings provided the trial wave function already describes the system qualitatively.

The workflow of a QMC calculation is as follows. In the first step, a DFT calculation is carried out. Secondly, the Kohn–Sham orbitals of the DFT calculations are used to construct a Slater determinant. A trial wave function is then formed by multiplying an additional Jastrow factor (discussed in Sec. 2.5.2), which contains variational parameters. In VMC (Sec. 2.5.1) the energy of this wave function is evaluated by Monte Carlo integration. Afterwards, the parameters in the Jastrow factor are optimized, to find the minimal total energy. Finally, the optimized trial wave function is treated within the DMC method (Sec. 2.5.3), which projects out the ground state subject to the nodal structure of the optimized trial wave function.

2.5.1 Variational Monte Carlo

The first QMC method we discuss here, is the variational Monte Carlo method [43]. As the name suggests, it is based on the Ritz principle, in which a many-electron trial wave function Ψ_T is used to evaluate the energy of a Hamiltonian $\hat{H}$ [see Eq. (2.1)]. The principle states that any wave function, which is not the ground state, will have a higher energy than the ground state,

$$\begin{aligned}\langle \hat{H} \rangle_\mathrm{VMC} &= \frac{\langle \Psi_\mathrm{T} | \, \hat{H} \, | \Psi_\mathrm{T} \rangle}{\langle \Psi_\mathrm{T} | \Psi_\mathrm{T} \rangle} = \frac{\int \Psi_\mathrm{T}^2(\mathbf{R}) [\Psi_\mathrm{T}^{-1}(\mathbf{R}) \hat{H} \Psi_\mathrm{T}(\mathbf{R})] \, \mathrm{d}\mathbf{R}}{\int \Psi_\mathrm{T}^2(\mathbf{R}) \, \mathrm{d}\mathbf{R}} \\ &= \int \mathcal{P}(\mathbf{R}) E_\mathrm{L}(\mathbf{R}) \, \mathrm{d}\mathbf{R} \geq E_0. \end{aligned} \tag{2.64}$$

Here, $\mathbf{R} = (\mathbf{r}_1, \mathbf{r}_2, \ldots, \mathbf{r}_N)$ stands for the N electron positions. The integral for the expectation value is performed over $3N$ electron coordinates. For traditional evaluation of this integral, for example by Simpson's rule, the error scales as $M^{-4/d}$, where M is the number of mesh points and d the dimension of the integral. If d gets increased, the error falls off increasingly slowly. Here is where stochastic methods are employed to solve the problem more efficiently. When the integral is sampled with randomly generated points $\mathbf{R}$, the statistical error decreases as the square root of the number of sampling points, regardless of dimensionality, which is a consequence of the central limit theorem [43].

In Eq. (2.64) the integral is further expressed in terms of a probability density $\mathcal{P}(\mathbf{R}) = \Psi_\mathrm{T}^2(\mathbf{R})$ and the local energy $E_\mathrm{L}(\mathbf{R}) = \Psi_\mathrm{T}^{-1}(\mathbf{R}) \hat{H} \Psi_\mathrm{T}(\mathbf{R})$. The local energy is a function of electron coordinates and becomes constant, when the trial wave function is an eigenstate of H. The final form of the integral can then be evaluated by so-called importance sampling. Instead of drawing random positions (also called configurations), a set of M positions $\{\mathbf{R}_m\}$ is picked, which is distributed according to the probability density $\mathcal{P}(\mathbf{R})$. The set $\{\mathbf{R}_m\}$ preferentially resides at the positions, at which the integrand is large, which leads to a more efficient evaluation of the integral. The VMC energy can finally be estimated by averaging over the local energy

$$E_\mathrm{VMC} = \frac{1}{M} \sum_{m=1}^{M} E_\mathrm{L}(\mathbf{R}_m). \tag{2.65}$$

The variance of the local energy σ_E^2 is given by

$$\begin{aligned}\sigma_E^2 &= \int \mathcal{P}(\mathbf{R}) [E_\mathrm{L}(\mathbf{R}) - E_\mathrm{VMC}]^2 \, \mathrm{d}\mathbf{R} \\ &\approx \frac{1}{M-1} \sum_{m=1}^{M} \left[E_\mathrm{L}(\mathbf{R}_m) - \frac{1}{M} \sum_{n=1}^{M} E_\mathrm{L}(\mathbf{R}_n) \right]^2, \end{aligned} \tag{2.66}$$

which leads to the standard error of the mean

$$\sigma = \frac{\sigma_E}{\sqrt{M}} \tag{2.67}$$

in the estimate of E_{VMC}. As the computational time scales linearly in M, the error decreases as inverse square root of the computational time. This is why a low σ_E is desirable to reduce the computational effort. If the trial wave function Ψ_{T} is an exact eigenfunction of the Hamiltonian, the local energy becomes constant and independent on the electron positions. Therefore, for the exact ground state a zero variance principle holds, as apparent from Eq. (2.66).

Metropolis Algorithm Given an analytical expression for a trial wave function $\Psi_{\mathrm{T}}(\mathbf{R})$, how can one generate a statistically independent set of configurations $\{\mathbf{R}_m\}$ which are distributed according to $\mathcal{P}(\mathbf{R}) = \Psi_{\mathrm{T}}^2(\mathbf{R})$, to carry out the integration in Eq. 2.64? This can be achieved with the help of the Metropolis rejection algorithm [43, 46]. The crucial steps are:

1. Start configurations (also called walkers) at random positions $\{\mathbf{R}\}$.

2. For every walker, propose a trial move to a new position $\mathbf{R}' = \mathbf{R} + d\mathbf{R}$. The proposal step $d\mathbf{R}$ is drawn from a Gaussian distribution $\mathcal{P}_{\mathrm{G}}(d\mathbf{R}) = (2\pi\tau)^{-3N/2} \exp\left[-(d\mathbf{R})^2/2\tau\right]$ with mean $\mathbf{0}$ and variance τ in each dimension. The probability to end up at $\mathbf{R}'$ given the starting point $\mathbf{R}$, $T(\mathbf{R}' \leftarrow \mathbf{R})$, is symmetric $[T(\mathbf{R} \leftarrow \mathbf{R}') = T(\mathbf{R}' \leftarrow \mathbf{R})]$ and constitutes a random walk.

3. Accept the trial move to $\mathbf{R}'$ with probability

$$A(\mathbf{R}' \leftarrow \mathbf{R}) = \min\left[1, \frac{T(\mathbf{R} \leftarrow \mathbf{R}')\mathcal{P}(\mathbf{R}')}{T(\mathbf{R}' \leftarrow \mathbf{R})\mathcal{P}(\mathbf{R})}\right] = \min\left[1, \frac{\mathcal{P}(\mathbf{R}')}{\mathcal{P}(\mathbf{R})}\right], \tag{2.68}$$

   i.e., draw a number w from a uniform probability distribution $\mathcal{P}_{[0,1]}(w)$ and accept the trial move if $w < A(\mathbf{R}' \leftarrow \mathbf{R})$. If the move was accepted, update the walker position to $\mathbf{R} = \mathbf{R}'$.

4. Measure the quantity of interest [e.g., the local energy $E_{\mathrm{L}}(\mathbf{R})$] and return to step two.

In this random walk, where walkers have no knowledge of previous actions besides their positions, the walker's trial moves will be accepted with a higher probability if the absolute value of the trial wave function $\mathcal{P}(\mathbf{R}')$ is larger at the new position, governed by the form of $A(\mathbf{R}' \leftarrow \mathbf{R})$. Therefore, there exists a bias towards regions in $\mathbf{R}$ of larger values of $\mathcal{P}(\mathbf{R})$. After an equilibration phase where walkers diffuse away from the initial random distribution, the walker density $n(\mathbf{R})$ reaches a steady-state. The Metropolis rejection algorithm thereby is designed to ensure a detailed balance condition, meaning that the flow of walkers from one volume element $d^{3N}\mathbf{R}$ at $\mathbf{R}$ to $d^{3N}\mathbf{R}'$ at $\mathbf{R}'$ is balanced by a flow of walkers from $d^{3N}\mathbf{R}'$ to $d^{3N}\mathbf{R}$. One can then show that

$$\frac{n(\mathbf{R})}{n(\mathbf{R}')} = \frac{\mathcal{P}(\mathbf{R})}{\mathcal{P}(\mathbf{R}')}, \tag{2.69}$$

i.e., that the walker density $n(\mathbf{R})$ is proportional to $\mathcal{P}(\mathbf{R})$ [43]. The parameter τ is used to control the trial step size and is an adjustable parameter. It is regulated such that

on average 50% of the trial steps are accepted to make the algorithm most efficient. In calculations, several independent walkers are distributed over parallel computing processes. As the random walks can proceed independently, the algorithm is trivially parallelizable. Only in the end of the calculation the measured data has to be collected and averaged according to Eq. (2.65).

2.5.2 Trial wave functions

The accuracy and efficiency of VMC and DMC calculations severely depend on the quality of the supplied trial wave functions. The great advantage of VMC is the flexibility regarding the form of many-body trial wave functions that can be used. In quantum chemistry calculations, these are usually Slater determinants, which are products of single-particle orbitals, functions which individually depend only on one electron coordinate. Due to the multidimensionality of the energy expectation integral one is often dependent on factorization of the wave function to calculate it. In VMC, however, one has the freedom to use wave functions which can depend on *electron coordinate differences*. This freedom can be used to correlate the electrons in the so-called Slater–Jastrow form [43, 47]

$$\Psi(\mathbf{X}) = D(\mathbf{X}) \exp\left[J(\mathbf{X})\right]. \tag{2.70}$$

Here, $\mathbf{X} = (\mathbf{x}_1, \ldots, \mathbf{x}_N) = (\mathbf{r}_1, \sigma_1, \ldots, \mathbf{r}_N, \sigma_N)$ is a composed index of electron position and spin coordinates, where $\sigma_i = \pm 1$. The Slater determinant $D(\mathbf{X})$ takes care for antisymmetry and the second term, which is positive definite, contains the Jastrow factor $\exp\left[J(\mathbf{X})\right]$.

In practice, the determinantal part is separated into spin-up and spin-down parts for computational efficiency,

$$\Psi(\mathbf{R}) = D^{\uparrow}(\mathbf{r}_1, \ldots, \mathbf{r}_{N_\uparrow}) D^{\downarrow}(\mathbf{r}_{N_\uparrow+1}, \ldots, \mathbf{r}_N) \exp\left[J(\mathbf{X})\right] \tag{2.71}$$

and the electron coordinates are ordered by spin (they carry an implicit spin-index). Although the wave function in Eq. (2.71) is not antisymmetric under exchange of spin-up and spin-down electrons, it gives the same expectation values for spin-independent operators compared to the nonseparated wave function of Eq. (2.70) [43].

A commonly used function in the Jastrow factor is [43]

$$J(\mathbf{X}) = \sum_{i=1}^{N} \chi(\mathbf{x}_i) - \frac{1}{2} \sum_{i=1}^{N} \sum_{j=1, j\neq i}^{N} u(\mathbf{x}_i, \mathbf{x}_j). \tag{2.72}$$

It incorporates the one-body term χ, which depends implicitly on nuclei and explicitly on electron positions, and describes electron–nuclear correlations. The second term u is a two-body term and it depends on pairs of electron coordinates. In parametrizations, these terms depend only on the *distances* of electrons and nuclei, and electrons and electrons, respectively.

The physically most important term is the u term [43]. Starting from the Slater determinant alone, it is known that the Slater determinant with the lowest energy

corresponds to the Hartee–Fock (HF) solution. Hartree–Fock theory is an effective noninteracting single-particle theory and contains by definition no correlations. The Hartree–Fock method incorporates automatically the Pauli principle via the assumption of an antisymmetric Slater determinant wave function ansatz. In the Hartree–Fock solution of the homogeneous electron gas, the Pauli principle manifests in the pair correlation function. Given a spin-up electron at a certain position, it is unlikely to find another electron with spin-up in the vicinity as the occupation of same quantum numbers has to be avoided. For electrons with opposite spins, the pair correlation function is constant [43]. If unlike-spin electrons can be found close, Coulomb repulsion is not optimally accounted for. This behavior is among others modified by u such that the pair correlation is suppressed at small distances and consequentially the Coulomb energy is decreased.

Another related way to motivate the Jastrow factor can be given in the example of the hydrogen atom. The ground state solution of the hydrogen $\phi_0(r) \propto \exp(-\alpha r)$ exhibits a cusp at $r = 0$. In order for the local energy $\phi_0(r)^{-1}\hat{H}\phi_0(r)$ to be constant, the kinetic energy of the cusplike wave function compensates the diverging Coulomb potential at $r = 0$. These electron–nuclei cusps are usually well described by HF and DFT contrary to the electron–electron cusps [43]. In the case of electron–electron Coulomb interaction, similar cusps arise and they need to be taken into account by the Jastrow factor. The parametrization of the u functions incorporate analytically known cusp conditions [43, 48, 49]

$$\frac{\partial u(r_{ij}, \sigma_i, \sigma_j)}{\partial r_{ij}}\Big|_{r_{ij}=0} = \begin{cases} 1/4 & \text{if } \sigma_i = \sigma_j \\ 1/2 & \text{if } \sigma_i \neq \sigma_j \end{cases}, \tag{2.73}$$

with $r_{ij} = |\mathbf{r}_i - \mathbf{r}_j|$.

The functions χ and u are parametrized by a linear combination of functions [49]

$$\chi(\mathbf{x}_i) = \sum_{I=1}^{N_{\text{atoms}}} \sum_{\beta} a_\beta^\chi f_{\text{Padé}}(r_{iI}, \beta), \tag{2.74}$$

$$u(\mathbf{x}_i, \mathbf{x}_j) = f_{\text{cusp}}(r_{ij}, \sigma_i, \sigma_j, \gamma) + \sum_{\beta} a_\beta^u f_{\text{Padé}}(r_{ij}, \beta). \tag{2.75}$$

The electron–nuclei distance is denoted as $r_{iI} = |\mathbf{r}_i - \mathbf{r}_I|$ and γ and a_β are variational parameters. The summation over β in our case is done for a set of 10 fixed values in the interval $[-1, 5]$, to increase the flexibility of the polynomial Padé basis functions $f_{\text{Padé}}$.

The cusp function is given by

$$f_{\text{cusp}}(r_{ij}, \sigma_i, \sigma_j, \gamma) = C_{\sigma_i,\sigma_j}\left[\frac{x - x^2 + x^3/3}{1 + \gamma(x - x^2 + x^3/3)} - \frac{1}{\gamma + 3}\right]. \tag{2.76}$$

The variable $x(r) = r/r_{\text{cut}}$ and r_{cut} defines the scale on which the cusp function and polynomial Padé functions decay to zero. The scale is usually chosen to be on the order of the lattice constant, such that the functions do not overlap for periodically

repeated atoms. For the derivative of the cusp function one obtains $f'_{\text{cusp}}(0) = C_{\sigma_i,\sigma_j}$, with $C = 1/4$ for electrons with same spins and $C = 1/2$ for electrons with opposite spins, fulfilling Eq. (2.73). The one-body term doesn't include the cusp term, as the cusps are already enforced by the Slater determinant resulting from the DFT orbitals.

Both, u and χ contain terms of combinations of polynomial Padé functions

$$f_{\text{Padé}}(r, \beta) = \frac{1 - x^2(6 - 8x + 3x^2)}{1 + \beta x^2(6 - 8x + 3x^2)}, \tag{2.77}$$

which have the property of $f_{\text{Padé}}(0) = 1$ and $f'_{\text{Padé}}(0) = 0$ to not alter the cusp, which was set by f_{cusp}. The β values set the curvature of these functions (for more details see Ref. [49]).

The Jastrow parametrization used in this work ensures a small number of variational parameters, typically on the order of 10^1–10^2 per atom. Yet, Slater–Jastrow wave functions are able to restore between about $75 - 85\%$ of the correlation energy and the VMC energy variance σ_E^2 is greatly lowered compared to Slater-determinant-only wave functions [43, 44]. The role of VMC in the QMC framework is to reduce the fluctuations in the local energy σ_E for the subsequent, more computationally intense, DMC calculation. The energy obtained from DMC is not influenced by the specific Jastrow factor, however the error bars are, as the number of Monte Carlo steps needed for a certain error σ scales with σ_E^2 [see Eq. (2.67)]. Therefore, wave function optimization is of great importance.

2.5.3 Diffusion Monte Carlo

The method building upon the optimized trial wave function received from VMC is the DMC method [43, 50, 51]. DMC is a Green's function based projector method, which evolves a starting wave function to the ground state by solving the imaginary-time Schrödinger equation

$$-\frac{\partial \Psi(\mathbf{R}, t)}{\partial t} = (\hat{H} - E_{\text{T}})\Psi(\mathbf{R}, t). \tag{2.78}$$

Here, t is a real variable and measures imaginary time. A constant energy shift of E_{T} was applied, which acts as a reference energy. In its integral form, the solution of Eq. (2.78) may be written as

$$\Psi(\mathbf{R}, t + \tau) = \int G(\mathbf{R}, \mathbf{R}', \tau)\Psi(\mathbf{R}', t)\, d\mathbf{R}', \tag{2.79}$$

with the Green's function

$$G(\mathbf{R}, \mathbf{R}', \tau) = \langle \mathbf{R}| \exp[-\tau(\hat{H} - E_{\text{T}})] \, |\mathbf{R}'\rangle \,, \tag{2.80}$$

fulfilling the same Eq. (2.78) as $\Psi(\mathbf{R})$ with the initial condition $G(\mathbf{R}, \mathbf{R}', 0) = \delta(\mathbf{R} - \mathbf{R}')$.

By spectral expansion we can express $\exp(-\tau\hat{H}) = \sum_i |\Psi_i\rangle \exp(-\tau E_i) \langle\Psi_i|$, in terms of Ψ_i and E_i, which are many-body eigenstates and corresponding eigenvalues of the time-independent Schrödinger equation. Then, the longtime-evolution of an initial

state Ψ_I is given by acting on it with the time evolution-operator

$$\begin{aligned}
&\lim_{\tau\to\infty} \langle \mathbf{R}| \exp[-\tau(\hat{H} - E_\mathrm{T})] \, |\Psi_\mathrm{I}\rangle \\
&= \lim_{\tau\to\infty} \int G(\mathbf{R}, \mathbf{R}', \tau)\Psi_\mathrm{I}(\mathbf{R}') \; d\mathbf{R}' && (2.81)\\
&= \lim_{\tau\to\infty} \sum_i \Psi_i(\mathbf{R}) \exp[-\tau(E_i - E_\mathrm{T})] \, \langle \Psi_i|\Psi_\mathrm{I}\rangle && (2.82)\\
&\overset{E_\mathrm{T}\approx E_0}{=} \lim_{\tau\to\infty} \Psi_0(\mathbf{R}) \exp[-\tau(E_0 - E_\mathrm{T})] \, \langle \Psi_0|\Psi_\mathrm{I}\rangle \\
&\propto \Psi_0(\mathbf{R}),
\end{aligned}$$

where the spectral expansion was used in the second step. From Eq. (2.81), one can see that by evolving the initial wave function $\Psi_\mathrm{I}(\mathbf{R})$ with the imaginary time Green's function, one projects onto the ground state, provided the overlap $\langle \Psi_0|\Psi_\mathrm{I}\rangle$ is finite and the reference energy is $E_\mathrm{T} \approx E_0$. The latter condition leads to the fact that higher-energy components of the initial state are exponentially suppressed in Eq. (2.82).

DMC can also be viewed from an alternative perspective [43]. The imaginary-time Schrödinger equation (2.78) reads

$$-\frac{\partial}{\partial t}\Psi(\mathbf{R}, t) = -\frac{1}{2}\sum_{i=1}^{N} \nabla_i^2 \Psi(\mathbf{R}, t) + [V(\mathbf{R}) - E_\mathrm{T}] \, \Psi(\mathbf{R}, t). \tag{2.83}$$

If only the kinetic energy part is present, this constitutes a diffusion equation in $3N$ dimensional space. Provided $\Psi(\mathbf{R}, t) \geq 0$ (a condition, which is not true in general), $\Psi(\mathbf{R}, t)$ can be interpreted as a distribution of Brownian particles at positions $\{\mathbf{R}\}$. A Brownian particle at $\mathbf{R}'$ before a time step will be found at $\mathbf{R}$ after a time step τ with probability

$$G_\mathrm{D}(\mathbf{R}, \mathbf{R}', \tau) = (2\pi\tau)^{-3N/2} \exp\left[-\frac{(\mathbf{R} - \mathbf{R}')^2}{2\tau}\right]. \tag{2.84}$$

In this way, an initial distribution of particles, centered at some point, will spread in space over time. The potential term in Eq. (2.83) however, will act as a *source or sink*, which forces a stationary distribution, if E_T is chosen correctly. The time evolution in Eq. (2.81) can then be interpreted in the same way as for the Brownian diffusion of particles, in terms of a time evolution of random walkers subject to sources and sinks.

The short-time Green's function of Eq. (2.83) is given by [43]

$$\begin{aligned}
G(\mathbf{R}, \mathbf{R}', \tau) &= \langle \mathbf{R}| \, e^{-\tau(\hat{T}+\hat{V}-E_\mathrm{T})} \, |\mathbf{R}'\rangle && (2.85)\\
&= (2\pi\tau)^{-3N/2} \exp\left[-\frac{(\mathbf{R} - \mathbf{R}')^2}{2\tau}\right] && (2.86)\\
&\quad \times \exp\left[-\tau[V(\mathbf{R}) + V(\mathbf{R}') - 2E_\mathrm{T}]\right] + \mathcal{O}(\tau^3) && (2.87)\\
&= G_\mathrm{D}(\mathbf{R}, \mathbf{R}', \tau) \times G_\mathrm{B}(\mathbf{R}, \mathbf{R}', \tau) + \mathcal{O}(\tau^3).
\end{aligned}$$

Because the kinetic and potential energy operators do not commute, the exponent

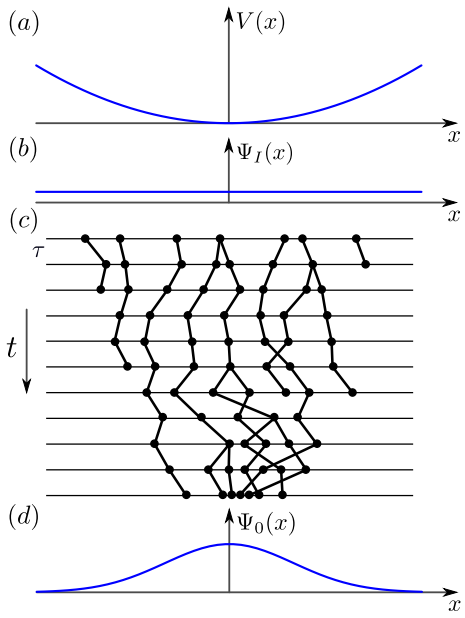

Figure 2.3: Illustration of the DMC algorithm. (a) Potential energy of the problem, (b) initial distribution of walkers Ψ_I, (c) imaginary time propagation of the walkers with time step τ. Walkers will diffuse to a position, where the potential is low as branching happens more often where the potential is low. Walkers die out, where the potential is high. (d) Final distribution of walkers, representing the ground state wave function Ψ_0.

in Eq. (2.85) has to be approximated by the Trotter–Suzuki formula $\mathrm{e}^{-\tau(\hat{A}+\hat{B})} = \mathrm{e}^{-\tau\hat{B}/2}\mathrm{e}^{-\tau\hat{A}}\mathrm{e}^{-\tau\hat{B}/2} + \mathcal{O}(\tau^3)$, which introduces an error proportional to τ^3. The error can be remedied by choosing a short time step ($\tau \approx 0.01$ au).

The two parts of the short-time Green's function are now interpreted as a diffusion process G_D, Eq. (2.86), and a probability reweighting process G_B, Eq. (2.87), respectively. Often this is also referred to as a branching or birth/death process. Numerically, this is mapped onto a set of random walkers $\{\mathbf{R}\}$ initially distributed according to $\Psi_\mathrm{I}(\mathbf{R})$. For each walker a series of M short time step propagations is carried out and positions of random walkers are sampled with alternating diffusion and birth/death processes by

$$\begin{aligned} &G(\mathbf{R}_M, \mathbf{R}_{M-1}, \tau) \cdots G(\mathbf{R}_2, \mathbf{R}_1, \tau)\Psi_\mathrm{I}(\mathbf{R}_1) = \\ &G_\mathrm{D}(\mathbf{R}_M, \mathbf{R}_{M-1})G_\mathrm{B}(\mathbf{R}_M, \mathbf{R}_{M-1}, \tau) \cdots G_\mathrm{D}(\mathbf{R}_2, \mathbf{R}_1, \tau)G_\mathrm{B}(\mathbf{R}_2, \mathbf{R}_1, \tau)\Psi_\mathrm{I}(\mathbf{R}_1). \end{aligned} \tag{2.88}$$

A schematic representation of this sampling process for a single particle in a parabolic potential, represented by several walkers, is given in Fig. 2.3. Each of the walkers performs a random walk with time step τ. After the walk, it will be decided whether the walker is allowed to survive or not. If $G_\mathrm{B} < 1$, it survives with probability G_B, else it is replicated with probability $G_\mathrm{B} - 1$. The total number of walkers can be controlled by the value of E_T (typical number of walkers 10^2–10^4) and is dynamically adjusted such that the total number of walkers is constant over time. In this way, walkers will accumulate where the potential is low as there the probability to survive is high according to Eq. (2.87). After a large number of steps, the walker distribution will approach a steady-state and the walkers are distributed according to the ground state wave function Ψ_0.

The method discussed so far will only work, if the wave function is positive and can itself be interpreted in terms of a probability distribution function. This, however, breaks down when several fermionic particles are considered, because due to the Pauli

principle, the wave function has to be antisymmetric. In turn, this implies regions in space, where the wave function is negative and it cannot represent a distribution function. This problem is called the *Fermion sign problem* [43].

For many-body systems, the Fermion sign problem in DMC is circumvented by the *fixed node approximation*. The essence of this approach is to constrain the walkers to regions in space (so-called nodal pockets), which are defined by regions in which the sign of a previously known wave function $\Psi_\mathrm{T}(\mathbf{R})$, e.g., obtained from VMC, is constant. Walkers are then not allowed to go from one region to another. The boundaries of these regions are the $3N-1$ dimensional hypersurfaces in $\mathbf{R}$-space where $\Psi_\mathrm{T}(\mathbf{R})=0$; those are called the *nodal surfaces*. The fixed node approximation can be achieved by multiplying Eq. (2.78) from the right with $\Psi_\mathrm{T}(\mathbf{R})$, as pointed out in the next arguments [43]. Instead of solving the Schrödinger equation for the state $\Psi(\mathbf{R},t)$, one solves for $f(\mathbf{R},t)=\Psi(\mathbf{R},t)\Psi_\mathrm{T}(\mathbf{R})$. This solves the Fermion sign problem, as now $f(\mathbf{R},t)\geq 0$ can be interpreted as a probability distribution function. As a remark, we consider our wave functions to be real-valued here, which is allowed due to the time-reversal symmetry of the systems considered by us. The trial wave function $\Psi_\mathrm{T}(\mathbf{R})$ will constrain the function $\Psi(\mathbf{R},t)$ to have the same sign structure in $\mathbf{R}$-space as $\Psi_\mathrm{T}(\mathbf{R})$ and their nodal surfaces coincide. In each of the nodal pockets, the wave function will reach its pocket ground state and therefore has an input bias. This approximation gives the exact ground state energy only if Ψ_T is the ground state. The error in the calculated energy can be shown to be of second order in the nodal surface error in Ψ_T [43].

One can then show [43] that the transformed Green's function for the new problem, $\tilde{G}(\mathbf{R},\mathbf{R}',\tau)=\Psi_\mathrm{T}(\mathbf{R})G(\mathbf{R},\mathbf{R}',\tau)/\Psi_\mathrm{T}(\mathbf{R}')$, takes the form $\tilde{G}=\tilde{G}_\mathrm{D}\times\tilde{G}_\mathrm{B}$ with

$$\tilde{G}_\mathrm{D}(\mathbf{R},\mathbf{R}',\tau)=\exp\left[-[\mathbf{R}-\mathbf{R}'-\tau\nabla_\mathbf{R}\ln\Psi_\mathrm{T}(\mathbf{R}')]^2/2\tau\right] \tag{2.89}$$

and

$$\tilde{G}_\mathrm{B}(\mathbf{R},\mathbf{R}',\tau)=\exp\left[-\tau(E_\mathrm{L}(\mathbf{R})+E_\mathrm{L}(\mathbf{R}')-2E_\mathrm{T})/2)\right]. \tag{2.90}$$

The diffusion process, Eq. (2.89), has now acquired an additional drift term. This drift term $[-\tau\nabla_\mathbf{R}\ln\Psi_\mathrm{T}(\mathbf{R}')]$ leads to a force acting on the walkers pointing towards regions where $\Psi_\mathrm{T}(\mathbf{R})$ is large. This helps to enforce the nodal constraint, since this force pushes walkers away from the nodal surfaces (if a wave function near a node is linear $\Psi\propto x$, then $\partial_x\ln\Psi=1/x$ and the drift velocity diverges at the nodal surface).

Further, the birth/death process fluctuates now less, since the local energy $E_\mathrm{L}(\mathbf{R})=\Psi_\mathrm{T}(\mathbf{R})^{-1}H\Psi_\mathrm{T}(\mathbf{R})$ assumes a much smoother behavior (a constant for an exact trial wave function), compared to the Coulomb potentials in Eq. (2.87), which greatly decreases the statistical noise [43].

In the limit of large M, $\tilde{G}(\mathbf{R}_M,\mathbf{R}_{M-1},\tau)\cdots\tilde{G}(\mathbf{R}_2,\mathbf{R}_1,\tau)\Psi_\mathrm{I}(\mathbf{R}_1)\Psi_\mathrm{T}(\mathbf{R}_1)$ samples the distribution $\Psi_\mathrm{T}(\mathbf{R})\Psi_0(\mathbf{R})$, called the *mixed distribution*. The initial distribution $\Psi_\mathrm{I}\Psi_\mathrm{T}$ is typically taken as Ψ_T^2, such that it can be generated with the Metropolis algorithm outlined in Sec. 2.5.1. The mixed distribution can be directly used to evaluate the

DMC ground state energy as

$$E_0 = \frac{\langle\Psi_0|\hat{H}|\Psi_\mathrm{T}\rangle}{\langle\Psi_0|\Psi_\mathrm{T}\rangle} = \frac{\int \Psi_0(\mathbf{R})\Psi_\mathrm{T}(\mathbf{R})\Psi_T^{-1}(\mathbf{R})\hat{H}\Psi_\mathrm{T}(\mathbf{R})\ d\mathbf{R}}{\int \Psi_0(\mathbf{R})\Psi_\mathrm{T}(\mathbf{R})\ d\mathbf{R}} \tag{2.91}$$

$$= \lim_{\tau\to\infty} \frac{\int f(\mathbf{R},\tau)E_\mathrm{L}(\mathbf{R})\ d\mathbf{R}}{\int f(\mathbf{R},\tau)\ d\mathbf{R}} \approx \frac{1}{M}\sum_{m=1}^{M} E_\mathrm{L}(\mathbf{R}_m) = E_\mathrm{DMC}. \tag{2.92}$$

Diffusion Monte Carlo algorithm We want to recapitulate how such an algorithm works in practice. The fixed-node DMC algorithm assumes to be given a trial wave function $\Psi_\mathrm{T}(\mathbf{R})$ and evaluates the ground state energy up to the fixed node error.

1. Sample an initial distribution of walkers $\{\mathbf{R}\}$ according to $|\Psi_\mathrm{T}(\mathbf{R})|^2$, using the Metropolis algorithm of VMC (see Sec. 2.5.1) and initialize the reference energy E_T to E_VMC.

2. Evaluate the drift velocity $\nabla \ln \Psi_\mathrm{T}(\mathbf{R})$ for each walker.

3. Propose new positions $\mathbf{R}' = \mathbf{R} + d\mathbf{R} + \tau\nabla \ln \Psi_\mathrm{T}(\mathbf{R})$, where $d\mathbf{R}$ is drawn from vectors with normally distributed entries with variance τ and zero mean.

4. Reject the move if the walker has crossed a nodal surface. This can be checked by comparing the signs of $\Psi_\mathrm{T}(\mathbf{R})$ and $\Psi_\mathrm{T}(\mathbf{R}')$.

5. Accept the trial move to $\mathbf{R}'$ with probability

$$A(\mathbf{R}' \leftarrow \mathbf{R}) = \min\left[1, \frac{\tilde{G}_\mathrm{D}(\mathbf{R},\mathbf{R}')\Psi_\mathrm{T}^2(\mathbf{R}')}{\tilde{G}_\mathrm{D}(\mathbf{R}',\mathbf{R})\Psi_\mathrm{T}^2(\mathbf{R})}\right], \tag{2.93}$$

   else set $\mathbf{R}'$ to $\mathbf{R}$.

6. For each walker, calculate how many walkers will be left at the new position by evaluating

$$N_\mathrm{new} = \lfloor \eta + \exp\left[-\tau[E_\mathrm{L}(\mathbf{R}) + E_\mathrm{L}(\mathbf{R}') - 2E_\mathrm{T}]/2\right]\rfloor, \tag{2.94}$$

   where η is a number drawn from a uniform distribution $\mathcal{P}_{[0,1]}(\eta)$.

7. If the calculation has ended the equilibration phase, accumulate the local energy.

8. Return to step 2.

The implementation of the DMC algorithm is very similar to the VMC algorithm, with the addition of the birth/death process and that the time step τ is significantly smaller. The parameter E_T is adjusted such that it is close to the local energy average and can be slightly tuned to control the total number of walkers to balance the workload in a parallel setup. With DMC typically 90–95% of the correlation energy can be restored, while simultaneously exhibiting scaling as $\mathcal{O}(N^{2-3})$ [43].

2.6 Employed Programs

In this thesis a multitude of foreign codes were used. To appreciate the work of their authors, a short list and description of the codes is presented.

Atomic simulation environment [52] (`ASE`) is a set of tools and Python modules for setting up, manipulating, running, visualizing and analyzing atomistic simulations.

Crystal 14 [53] is a commercial DFT code based on Gaussian type basis sets, which is able to treat extended systems. It therefore is suitable to handle particularly well quantum chemistry methods like Hartree–Fock or DFT with hybrid functionals.

Quantum Espresso [54] is a DFT code for extended systems based on plane waves and pseudopotentials. Further, it implements the PAW method also in the relativistic case. It can be used to carry out molecular dynamics, as well as noncollinear magnetic calculations.

Qwalk [44] is a quantum Monte Carlo code, which is able to take inputs from several DFT codes to calculate variational Monte Carlo and diffusion Monte Carlo ground state energies for molecules and extended systems.

Vesta [55] is a 3D visualization program for structural models, volumetric data such as electron/nuclear densities, and crystal morphologies.

Wien2k [56] allows to perform electronic structure calculations of solids using DFT. It is based on the full-potential (linearized) augmented plane-wave plus local orbitals method. `Wien2k` contains an all-electron scheme and can be viewed as the reference implementation concerning relativistic effects.

Xcrysden [57] is a crystalline and molecular structure visualisation program aiming at display of isosurfaces and contours, which can be superimposed on crystalline structures and interactively rotated and manipulated.

Z2Pack [58] is a code for calculating topological properties of systems described in terms of continuous $\mathbf{k} \cdot \mathbf{p}$ models, tight-binding models, and *ab initio* calculations. It can be used to identify Chern, $\mathbb{Z}_2$, and crystalline topological insulators as well as topological semimetals.

3 Copper adatoms on graphene: theory of orbital and spin-orbital effects

3.1 Extrinsic effects of spin-orbit coupling in graphene due to adsorbates

Spintronics aims to utilize the spin degree of freedom of electrons to realize new forms of information storage and logic devices [6–8]. In order to implement such devices one is in search of suitable materials exhibiting long coherence and spin-diffusion lengths as well as high spin-lifetimes. Graphene was anticipated to have these properties due to a vanishing nuclear-spin-spin coupling (in C^{12} isotopes) as well as with very low values of spin-orbit coupling [4, 59]. Dyakonov–Perel and Elliot–Yafet spin relaxation mechanisms lead to estimates of spin-relaxation times of $\tau_s \approx 10^{-6}$ s [8] in graphene. In experiments, however, spin-lifetimes were found to be in the range of τ_s =10 ps to 10 ns [8], at best a two orders of magnitude discrepancy compared to what is expected theoretically. Spin-diffusion lengths were found to be $l_s = 1 - 30$ μm, which is suitable for devices.

It is an ongoing topic of research to clarify the origin of spin-relaxation in graphene. The order of magnitude difference points to an extrinsic source of spin-relaxation [8, 60]. One possible source of spin relaxation can be ascribed to spin-orbit coupling induced by substrates. An example will be given in Chpt. 4, where graphene is placed on a Cu(111) surface. Another source can be unintentional graphene decoration. It was found that hydrogen atoms adsorbed on graphene could explain the spin physics. Hydrogen induces strong spin-orbit coupling [61, 62] and local magnetic moments of 1 μ_B [61, 63, 64] in graphene. The latter can give rise to a new spin-relaxation mechanism which is known under the name of resonant spin-relaxation [65]. In this phenomenon a conduction electron spends some time on a magnetic impurity and precesses in the local exchange field. When leaving the impurity its spin is randomized. This relaxation mechanism can efficiently account for spin-relaxation even if the concentration of adatoms is in the parts per million.

It is crucial to also understand the origin of extrinsic spin-orbit coupling in graphene in order to find the root for possible spin-relaxation mechanisms involving this interaction. Graphene's intrinsic spin-orbit coupling is only of small magnitude, about 12 μeV [59], owed to the p_z character of the low-energy states. Small admixtures of d states lead to a finite value of intrinsic spin-orbit coupling. The atomic spin-orbit splitting in the $2p$ orbitals of the carbon ion is 7.86 meV [66]. If the local bonding environment of the graphene atoms is reshaped from sp^2 to sp^3-type bonding, mini ripples are formed. It has been shown that these mini ripples lead to a hybridization of p_z and σ orbitals, which effectively transfers spin-orbit coupling into the low-energy

states, and for full sp^3 hybridization about 75% of the atomic spin-orbit coupling can be expected [60].

The mechanism of local spin-orbit coupling induction by hydrogen [61] follows the mechanism of mini ripples. When hydrogen is adsorbed onto graphene it pulls one carbon atom out of the plane and leads to sp^3 rehybridization. In both respects, hydrogen adsorption is an ideal toy model for inducing local magnetism as well as local spin-orbit coupling. Spin-orbit coupling induced in a controlled way offers further the possibility to fine tune graphene for spintronics applications. One of these applications is the spin-Hall effect [62]. In the spin-Hall effect, an applied longitudinal current leads to a transversal spin current. This may be used to generate spin currents, or to measure spin current with the inverse effect. In dilute hydrogen-decorated graphene the spin Hall effect was measured at room temperature with large nonlocal spin signals, hinting for spin-orbit coupling effects on the order of 2.5 meV [62]. To enable graphene for spintronics applications it is crucial to alter its properties and understand how spin-orbit coupling effects, induced by atomic or molecular adsorption, comes about.

After these discoveries other adsorbates were explored by us [67, 68]. Because organic residues are expected to be present after fabrication processes, we looked at spin-orbit coupling effects induced by a methyl (CH_3) adsorbate. Chemically, the methyl bonding behaves very much like hydrogen, which is attributed to the similar Pauling electronegativity of 2.28 and 2.20, respectively [68, 69]. Spin-orbit coupling and magnetic effects are found to be very similar. Another adsorbate candidate is fluorine, which binds in the top position (above a carbon atom), like hydrogen. Experimentally, high-density fluorination renders graphene insulating [70]. In the dilute limit, similarly as for hydrogen, it leads to giant local spin-orbit coupling values of about 10 meV [67]. The main source of spin-orbit coupling, though, stems from the fluorine p orbitals, different than in the hydrogenated case.

Induced spin-orbit coupling magnitudes cannot be extracted from DFT band structure calculations alone, since band splittings are simulation-cell size dependent. To overcome this problem, a tight-binding approach has to be employed. One constructs a local spin-orbit coupling model Hamiltonian and fits it to the calculated electronic structure. The so-extracted magnitudes of local spin-orbit coupling hopping matrix elements can range from 1 meV for hydrogen [61] or CH_3 [68], through 10 or so meV for fluorine [67, 71]. Even 100 meV for heavy adatoms such as Os [72], Au [73], Tl, and In [74], which prefer to sit in hollow positions, can be expected. The heavy adatoms can give rise to topological effects, [72, 74, 75] while light adatoms and especially organic molecules (whose presence on graphene is quite likely in ppm concentrations) can lead to resonant scattering and can strongly affect resistivity and spin relaxation [65, 76–79]. So far, there has been no investigation of the induced spin-orbit coupling due to adatoms in the bridge position, presumably as most of the adatoms prefer the top or hollow adsorption sites [80].

In recent years, Cu adatoms have emerged as important (unintended) functionalization elements, mainly due to the fact that large-scale graphene is grown by chemical vapor deposition (CVD) on Cu substrates [81]. It was shown experimentally (via the spin Hall effect) that CVD-grown graphene samples exhibit much lower conductivity and greater spin-Hall coefficients ($\gamma \approx 0.2$) than exfoliated graphene [82]. This all points to a possibly resonant character of the scattering of Dirac electrons off Cu

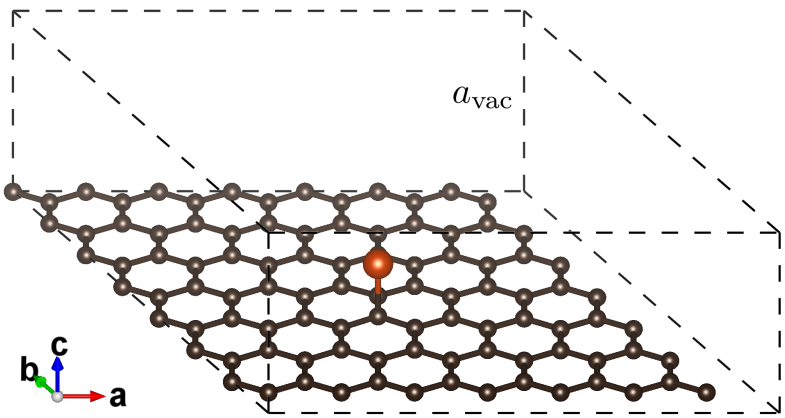

Figure 3.1: Supercell geometry for an isolated copper atom on graphene. Here, a 7×7 graphene supercell with a copper atom in the top position is shown. The simulation cell, indicated by dashed lines, has a slab geometry, with a vacuum distance of a_{vac}. (Supercell was rescaled in z direction due to space limitations here.)

adatoms (or clustered residues), similar to hydrogen, [65] as well as to a giant induced spin-orbit coupling in graphene due to Cu adatoms.

Here, we test if our intuition of a higher atomic number, implying larger local spin-orbit coupling effects, holds, by studying dilute graphene coverage with isolated Cu adatoms by DFT calculations. Methods and structures are described in Sec. 3.2. We simulate the adsorption of single copper atoms by embedding them into large graphene supercells and determine their adsorption sites. After analyzing the electronic structure in Sec. 3.3, we focus on explaining the origin of spin-orbit coupling with the help of a DFT+U study. This knowledge enables us to construct a minimal local spin-orbit coupling tight-binding Hamiltonians (Sec. 3.4), which we use to fit to the *ab initio* data and extract the tight-binding parameters. In the end of this section we compare the obtained parameters to other adsorbates. We will summarize and conclude our findings in Sec. 3.5.

3.2 Computational methods and system geometries

To model an isolated copper adatom on graphene, we consider different supercells of 5×5, 7×7, and 10×10 units of graphene containing one copper and 50, 98, and 200 carbon atoms, respectively, to avoid interactions of the periodic images of the copper adatoms. An exemplary simulation cell in the 7×7 case is shown in Fig. 3.1. We treat the system in a slab geometry, where vacuum is added into the perpendicular direction. The separating vacuum spacer a_{vac} perpendicular to the graphene plane was set to 15 Å, a compromise between computational cost and avoidance of interactions among the graphene sheets. The value of a_{vac} is well established in adsorbate calculations [61, 67, 68]. For information such as binding energies, density of states, atomic, and angular momentum spectral decompositions, and the Bader and Löwdin charges, we compute

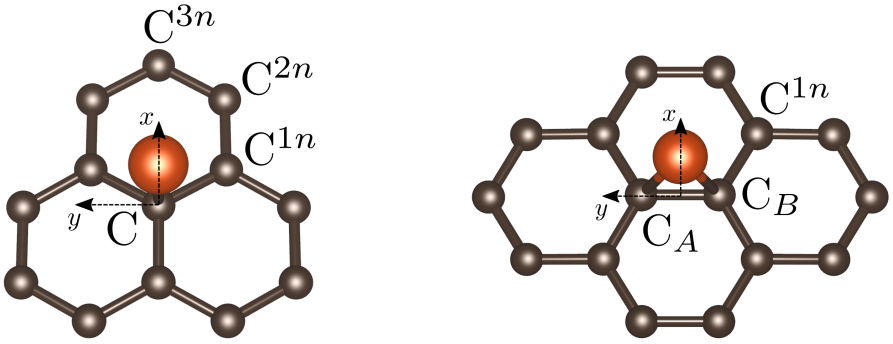

(a) top (b) bridge

Figure 3.2: Sketch of the local copper adsorption region on graphene: (a) adsorption in the top and (b) in the bridge position. The convention labeling the carbon atoms is indicated.

the quantities in the smaller 5×5, and 7×7 supercells, which are computationally less demanding. To study spin-orbit coupling effects, we use a 10×10 supercell to minimize the influence of periodic images.

3.2.1 Methods

We employ DFT implemented in the plane wave code `Quantum Espresso` [54] to compute ground state properties of the above specified systems. Our calculations for the graphene supercells are performed at a k point sampling equivalent to a k sampling of $40 \times 40 \times 1$ of a single graphene unit cell. We use Kresse–Joubert [83] relativistic PAW pseudopotentials [22] generated for, and used in connection with, the PBE functional [28]. The pseudopotentials incorporate eleven valence electrons for copper and four valence electrons for carbon atoms. We discuss the accuracy of spin-orbit coupling effects imprinted in the copper pseudopotential in Sec. 3.2.3. A plane wave energy cutoff of 40 Ry and a cutoff of 320 Ry for the Fourier representations of charge density and potential were found, to ensure converged results. Van der Waals interactions are taken into account by the empirical Grimme–D2 method [34] (see also Sec. 2.2.2). Hubbard U corrections [32] were applied for the copper d orbitals in the simplified rotational invariant formulation [33] as discussed in Sec. 2.2.2, to analyze the spin-orbit coupling contributions.

3.2.2 Absorption sites and structural relaxation

Copper adatoms are considered in the top and bridge position of graphene as shown in Fig. 3.2. The initial configuration of a copper atom adsorbed on a specific position on flat graphene was relaxed until the sum of Hellmann–Feynman forces acting on atoms were smaller than 0.001 $\mathrm{Ry/a_0}$, using the BFGS algorithm [84]. In particular, the relaxed structure with copper in the top position, has a copper-graphene distance of 2.13 Å and a local corrugation, measured as the distance between the graphene plane

and the pulled out functionalized carbon atom(s), of 0.08 Å. For the bridge position we found a copper–graphene distance of 2.16 Å and a local corrugation of 0.11 Å. The low corrugation indicates weak bonding as compared to for example a hydrogenated system with strong corrugation of about 0.36 Å [61]. We therefore do not optimize lattice constants of graphene, as we expect only tiny changes of the graphene host system with a lattice constant of multiples of 2.46 Å, depending on the supercell size. This approach was justified even in the covalently bonded hydrogen and fluorine cases on the level of 5×5 cells [61, 67].

The importance of nonlocal interactions to the bonding behavior of coinage metal atoms on graphene was pointed out by Amft et al. [85], who studied different approximations to van der Waals interactions. Exchange-correlation functionals including (or supplemented with) van der Waals interactions lead to a significant difference in binding energies of copper on graphene in different adsorption configurations [85]. For a 5×5 supercell we find that the top configuration, see Fig. 3.2(a), has about 225 meV lower ground state energy than the hollow configuration (copper adsorbed in the middle of a hexagonal ring). Furthermore the top position is just 1 meV lower in energy than the bridge position, see Fig. 3.2(b). Hence, in agreement with Ref. [85] we confirm that the top and bridge configurations—both very close in energy—are more favorable compared to the hollow position. For this reason we focus our analysis on these two configurations.

All our supercells and their reciprocal counterparts are hosted in a hexagonal lattice. However, they differ by the allowed point group symmetry operations. Namely, the point groups for the top and bridge adatom positions are C_{3v} (6 symmetry operations) and C_{2v} (4 symmetry operations), respectively, where the symmetry axis is defined by the graphene surface normal, penetrating through the copper atom. The symmetries have direct impact on the shapes of the irreducible wedges that are used to sample the Brillouin zone.

3.2.3 Error estimation for spin-orbit coupling in the copper atom

The p and d states of the copper atom will play an essential role in spin-orbit coupling effects. Here, we discuss the pseudization of the copper atom and its accompanied transferability error in the spin-orbit coupling splittings.

In Tab. 3.1 we show a comparison of a fully relativistic all-electron calculation of a copper atom on a radial grid to its pseudized PAW version in a box using plane waves, where in both calculations the PBE functional was used. The all-electron calculation is the output of the preparatory calculation for the PAW pseudopotential generation, using the `atomic` program included in the `Quantum Espresso` package [54]. The electronic configuration was constrained such that half an electron was additionally promoted from the d to the s shell (shown in Tab. 3.1), relative to the atomic ground state configuration. We used the parametrization of the pseudopotential as provided in the `pslibrary` [87][1]. When constrained to the same electronic configuration, the single-particle levels from the all-electron calculation matched very well by the PAW pseudopotential, better than 0.1 meV (not shown).

[1] `http://people.sissa.it/~dalcorso/pslibrary/`

State	j	E_{AE} [eV]	$E_{\mathrm{PAW}}^{\mathrm{box}}$ [eV]	Occ. AE	ΔE_{exp} [eV] [86]
3d	3/2	−7.268	−5.201	4.00	
Δ_d		0.282	0.269	-	0.253 (^2D $3d^9 4s^2$)
3d	5/2	−6.987	−4.932	5.50	
4s	1/2	−5.182	−4.655	1.50	
4p	1/2	−0.949	−0.934	0.00	
Δ_p		0.044	0.026	-	0.031 (^2P $3d^{10} 4p^1$)
4p	3/2	−0.905	−0.908	0.00	

Table 3.1: Comparison of energy levels and SOC splittings of an isolated copper atom of an all-electron (AE) calculation with a PAW calculation of an atom in a cubic box of length 20 Å. States with total angular momentum quantum number j are indicated. All-electron and PAW calculations are fully relativistic calculations. The forced occupation of the total angular momentum states in the AE calculation is indicated. We give the spin-orbit coupling splittings Δ_p/Δ_d of the p and d states. Experimental values of splittings (ΔE_{exp}) of corresponding terms are given (experimental errors are smaller than 0.01 meV) [66].

To estimate errors in transferability we compare the all-electron calculation to a calculation of an isolated copper atom in a cubic box with cell dimension of $a =$ 20 Å, plane-wave energy cutoff of 45 Ry and charge density cutoff of 320 Ry. The absolute values of energy levels of this calculation cannot be directly compared to the all-electron calculation, as the electronic configurations differ. The box calculation reproduces a copper atom in the natural ground state, therefore levels are shifted with respect to the all-electron calculation. The box calculation also assumes an array of repeating copper atoms in all directions and therefore depends strongly on the size of the box, representing the spacer between periodic images. Here, we just attempt to compare spin-orbit coupling splittings of single-particle levels, Δ_d and Δ_p to show how they transfer to an application in a practical calculation.

First, the all-electron calculation reproduces the experimental splittings [66] with relative errors of 10% for d levels and 30% for p levels. Second, we find that splittings of the box calculation are converged with respect to the box size and plane-wave cutoff better than 5 meV (not shown). The box calculation reproduces the all-electron splittings of the d levels better than p level splittings, with respective errors of 5% and 41%, which we take as error estimates. In Sec. 3.3.3, we show that in a worse case scenario p levels contribute with 65% to spin-orbit coupling and d states with 35%. Therefore, the relative error should propagate with

$$\Delta = \frac{\Delta_d \cdot 35\% \cdot 5\% + \Delta_p \cdot 65\% \cdot 41\%}{\Delta_d \cdot 35\% + \Delta_p \cdot 65\%} = 10\% \tag{3.1}$$

into the states of graphene. With all additional systematic errors, we estimate errors in values of spin-orbit coupling tight-binding parameters (obtained in sections 3.4.1 and 3.4.2) to be 20%.

3.3 Electronic structure

We first analyze the orbital occupations and charging of Cu sitting in the top and bridge positions in a non-spin-polarized calculation. The electronic configuration of the outer valence shells of a copper atom is $d^{10}s^1p^0$. Placing Cu on graphene, the Löwdin charge analysis [88] in the top position yields a total occupation of 10.94 e with an orbital occupation of (s, p, d) = (0.85, 0.26, 9.83) e. In the bridge case the total occupation is 11.01 e and (s, p, d) = (0.89, 0.29, 9.83) e. The s and d channels are redistributed to p states with a population of 0.3 e, which reflects the lowered local symmetries due to the directional bonding. Alternatively, the Bader charge analysis [89] determines the copper atom to possess a charge of 10.81 e for the top and 10.75 e for the bridge configuration. Charge analysis can be carried out in many different ways, because the definition of an atom in a molecule or solid is not unique. While the Löwdin analysis is a population analysis of the wave function, the Bader charge represents a partitioning of the electron density. Both analysis have in common, that the total charge transfer is rather small. The Bader charge analysis seems to be more consistent with a slight partial depopulation of the copper s level, discussed in Sections 3.3.1 and 3.3.2, and hints for a donation of fractions of electrons from copper to graphene.

We note that spin-polarized calculations for our systems result in magnetic ground states with magnetic moments of 1 μ_B for both studied adsorption configurations, in agreement with results in Refs. [90, 91]. The total energy gain is about 140 meV compared to the nonmagnetic ground state solution. The mechanism generating the magnetic state is different from that in hydrogenated graphene where hydrogen also binds in the top position [61, 65]. In the case of hydrogen, the sublattice imbalance of electron occupation of the graphene lattice leads to an extended magnetic moment distribution [92]. Here, it is the unpaired localized s state on the copper that forms the magnetic state [90, 91], in a very similar fashion as the copper doublet atomic state ^2S.

Although there are magnetic ground states, we stick to nonpolarized calculations as we are interested in spin-orbit coupling effects and want to separate them from potential magnetic effects here.

3.3.1 Copper in the top position

The low-energy band structure for a 10×10 supercell of graphene with copper adsorbed in the top position is shown in Fig. 3.3. Along with the DFT data we present also the tight-binding calculated band structure; the model itself is discussed later in Sec. 3.4.1. Weak bonding of the copper adatom to graphene reflects in the modest binding energy of 0.68 eV (determined by calculating the energy gain with respect to isolated components). The low binding energy points to physisorption, in which binding energies are typically lower than 0.8 eV/atom. A second sign of weak bonding is the existence of remnants of graphene's Dirac cone, which are visible from -1 to 0.75 eV, with respect to the Fermi level, mainly composed out of bands (a) and (c), denoted as the *valence* and *conduction* bands, respectively. At the Fermi level there is a flat band, which we call the *midgap* band (b). The hybridization gaps that open

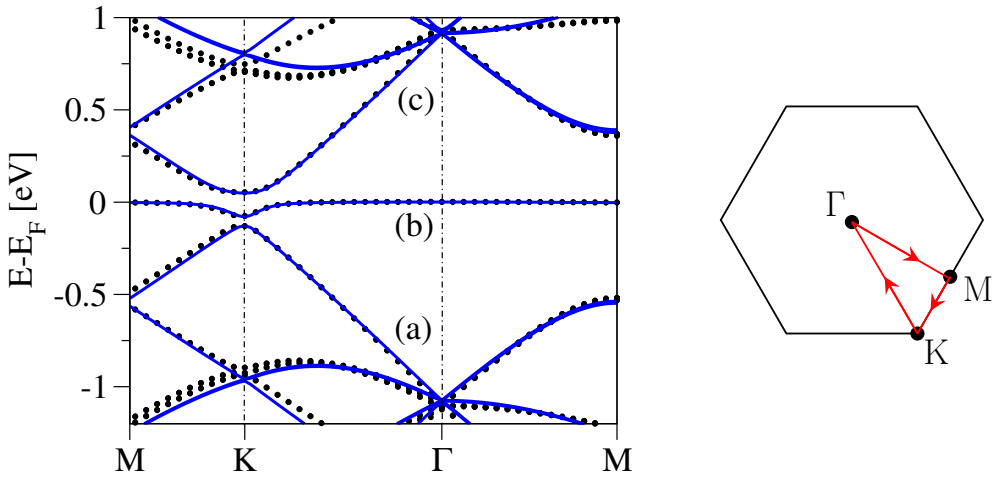

Figure 3.3: Electronic band structure along the high-symmetry lines in the first Brillouin zone (sketched in the right panel) for 10×10 graphene functionalized by copper in the top position. The (black) symbols are first-principles data and the (blue) solid lines correspond to the tight-binding model fit with the hybridization $\omega_t = 0.81$ eV and the on-site energy $\varepsilon_t = 0.08$ eV (discussed in Sec. 3.4.1). Fitting involved the valence (a), midgap (b) and conduction (c) bands around the Fermi level. Fitting and tight-binding caluclations were done by Susanne Irmer, from Ref. [93].

around the K point are a result of the copper–carbon bonding, which will become clear from the following density of states analysis. The Dirac energy, obtained by linearly interpolating bands (a) and (c) to the K point, is situated about 0.1 eV below the Fermi level, i.e., copper acts as a dopant in accordance with the above Bader charge analysis.

Fig. 3.4 displays the partial local density of states (PLDOS) with the atomic-site-resolved projections on states with different total angular momenta. We focus on copper (Cu), the functionalized carbon (C) and its neighboring atoms (C^{1n}, C^{2n}, and C^{3n}), as defined in Fig. 3.2(a). The PLDOS on Cu, see panel (a) in Fig. 3.4, is dominated by states with s character near the Fermi level. Small contributions from the s states are also present in the energy range from -2.5 to 1.5 eV. The PLDOS peak at the Fermi level arises from the flat midgap band (b) seen in Fig. 3.3. The s states of copper play an important role in bonding which can be seen from the hybridization gap in Fig. 3.3 and the overlap in the PLDOS with the electronic states that reside on the neighboring carbon atoms.

The d states extend in the range from -4 eV to -1 eV with respect to the Fermi level with a broad maximum contribution at -2 eV. The d states of copper with the total angular momentum $j = 3/2$ and $j = 5/2$ are split in energy by spin-orbit interaction of about 0.25 eV, which can be seen from the shifts of d levels at about -1.5 eV. This splitting is understandable in terms of the intra-atomic spin-orbit coupling of the isolated copper atom whose experimental value is 253 meV [86], see also Sec. 3.2.3. However, the weaker intra-atomic spin-orbit splitting of the Cu $4p$ states of 31 meV [86] is not visible in the PLDOS (partly due to numerical broadening). The PLDOS shows

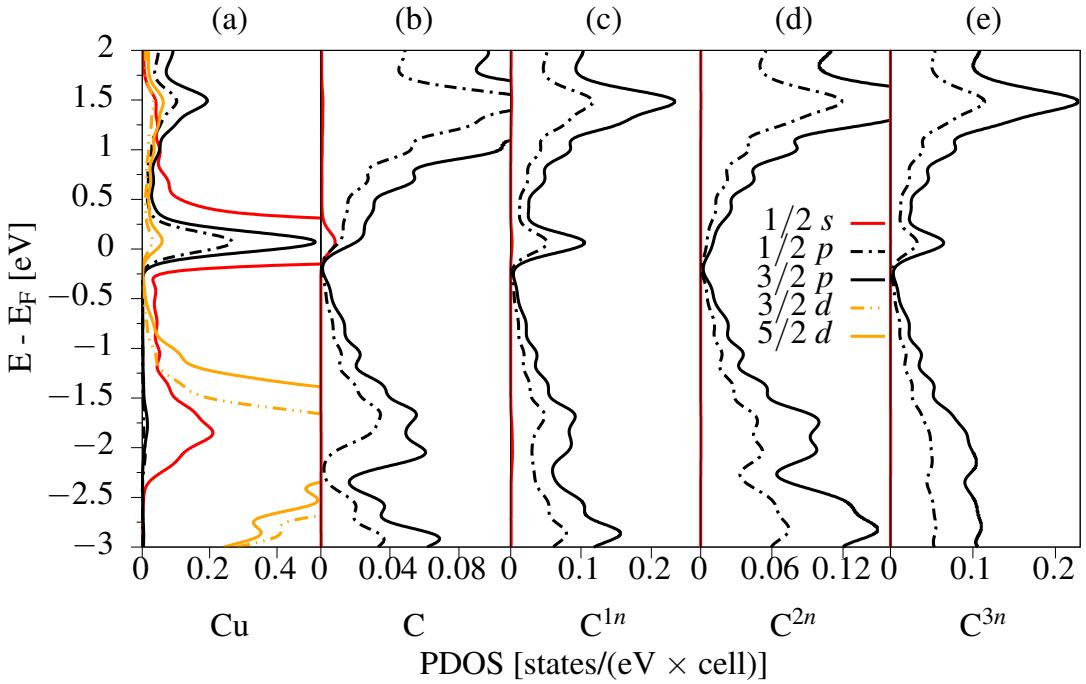

Figure 3.4: Partial local density of states for 7×7 graphene supercell with copper adsorbed in the top configuration. (a) Partial local density of states for the copper adatom, (b) for the functionalized carbon C and its (c) nearest-neighbor carbon C^{1n}, (d) second-nearest neighbor carbon C^{2n} and (e) third-nearest carbon C^{3n}. Projected densities are labeled by the total angular momentum j and the corresponding atomic orbital angular momentum quantum numbers s, p, d, respectively. The numerical Gaussian broadening is 130 meV.

that additionally to copper s states also p and d states are present directly at the Fermi energy, with a total p to d PLDOS ratio of 8.9. We also analyzed the PLDOS in terms of the orbital angular momentum states, which shows that the DOS around the Fermi energy consists mainly out of $m_z = 0$ states (not shown here). However, we find very small contributions of $m_z = \pm 1$, and ± 2 states at the Fermi energy, which should induce spin-orbit coupling.

The PLDOSs of the carbon atoms, see Fig. 3.4(b)–(e), exhibit approximate linear behavior for electron and hole branches, when ignoring the peaks at the Fermi level, most clearly seen for example in panel (d). This resembles the linear low-energy density of states of pristine graphene and gives again a hint for noninvasive and weak bonding of copper to graphene. The carbon p DOS shows about 2/3 of $m_j = 3/2$ and 1/3 of $m_j = 1/2$ contributions, which are understandable in terms of the absolute squares of Clebsch–Gordan coefficients of a p_z orbital ($|p_z, \uparrow\rangle = \sqrt{2/3}\,|3/2, \uparrow\rangle - \sqrt{1/3}\,|1/2, \uparrow\rangle$).

3.3.2 Copper in the bridge position

When a copper atom is placed in the bridge adsorption position, we obtain the band structure of Fig. 3.5. We also sketch the Brillouin zone with its irreducible wedge, the

interior of the trapezoid $\Gamma M_1 K_1 K_2 \Gamma$. The knowledge of electronic properties within this wedge is enough to reconstruct the whole Brillouin zone using lattice symmetries. By time-reversing and translating by a reciprocal lattice vector one can map K_1 to K_2 and hence the spectrum at those two points are identical (time-reversal implies only the opposite spin polarization for eigenstates). This is not the case for M_1 and M_2 points in the C_{2v} case. There does not exist a transformation combining time-reversal, reciprocal lattice translation and a C_{2v} point group operation that would map M_1 to M_2, contrary to the C_{3v} case. Therefore the spectra at M_1 and M_2 are in general distinct. The same holds also for other k points along the high-symmetry lines that are displayed in Fig. 3.5.

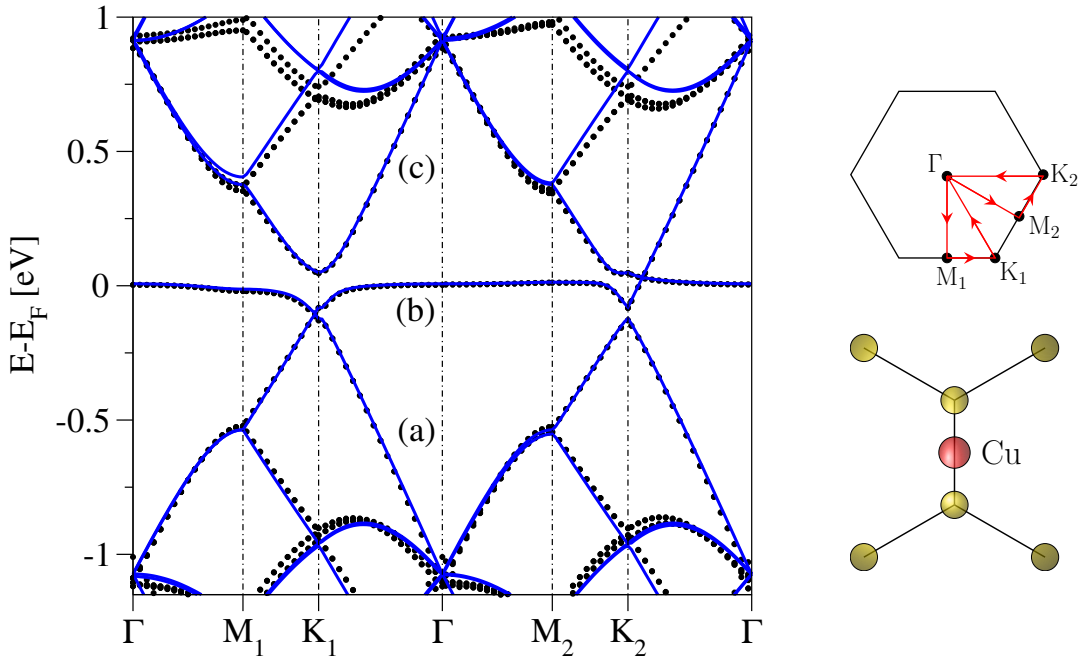

Figure 3.5: Electronic band structure along the high-symmetry lines in the irreducible wedge of the first Brillouin zone (sketched in the right panel) for 10×10 graphene functionalized by copper in the bridge position. The (black) symbols are first-principles data and the (blue) solid lines correspond to the tight-binding model fit with the hybridization $\omega_b = 0.54$ eV and the on-site energy $\varepsilon_b = 0.02$ eV (discussed in Sec. 3.4.2). Fitting involved the valence (a), midgap (b) and conduction (c) bands around the Fermi level. Lower sketch at right shows an excerpt of the unit cell around the bridge adatom; coordinate system directions of real and reciprocal lattices correspond to each other. Fitting and tight-binding caluclations were done by Susanne Irmer, from Ref. [93].

To examine those features we look at the band structure along the meandering high-symmetry path $\Gamma M_1 K_1 \Gamma M_2 K_2 \Gamma$ inside the irreducible wedge of the BZ in Fig. 3.5, which has C_{2v} symmetric structure. We recognize similarities of the band structure compared to the top case, with a flat state hybridizing with the Dirac cone. The low-energy bands can be again classified in three bands – valence (a), midgap (b), and

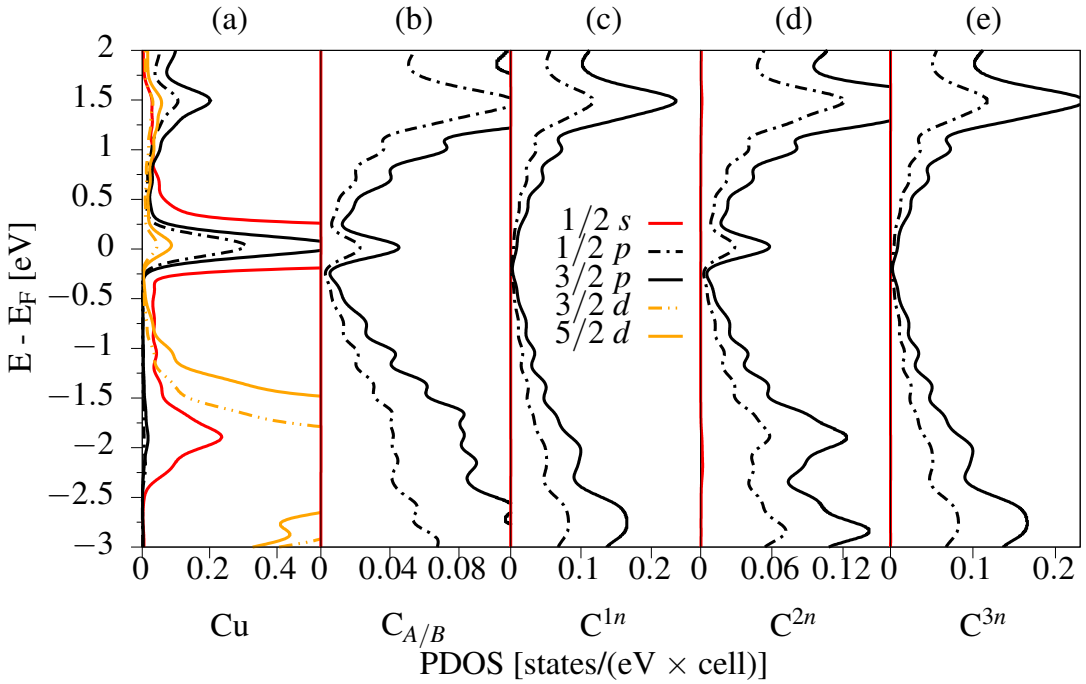

Figure 3.6: Partial local density of states for 7×7 graphene supercell with copper adsorbed in the bridge configuration. (a) Partial local density of states for the copper adatom, (b) for one (out of two) functionalized carbon $C_{A/B}$ and its (c) nearest-neighbor carbon C^{1n}, (d) second-nearest neighbor carbon C^{2n} and (e) third-nearest carbon C^{3n} atom. Projected densities are labeled by the total angular momentum j and the corresponding atomic orbital quantum numbers s, p, d, respectively. The numerical Gaussian broadening is 130 meV.

conduction (c) bands, as shown in Fig. 3.5. The difference compared to the top case lies in the observation that along k paths which are perpendicular to the carbon-copper bond (compare k paths ΓK_2 and M_1K_1 with the sketch of the local environment of the copper atom in Fig. 3.5) crossings appear, with degeneracies off the high-symmetry k points.

The PLDOS for graphene functionalized by copper at the bridge position, displayed in Fig. 3.6, is remarkably similar to the PLDOS analyzed above, given the very different symmetries of the systems. Therefore, we qualitatively and quantitatively expect the dominant physical mechanisms for spin-orbit coupling to be the same in both systems. For example, the states with s, p, and d character appear at the same energies as before, the PLDOS of copper p states at the Fermi energy is 6.9 times larger than the one for copper d states, which is not very different from the top case. The total angular momentum states of Cu with $j = 3/2$ and $j = 5/2$ are again split by 0.25 eV and the PLDOS peaks near the Fermi level are also built mainly from states with $m_z = 0$ (not shown here), which is important for the construction of tight-binding Hamiltonians.

Although both copper resolved PLDOSs are very alike, there are quantitative differences due to the local environment of the copper atom. Differences in the binding behavior are most apparent in the density of states of the neighboring carbon atoms.

For the top case, the copper s state hybridizes with the π states of graphene for carbon atoms in the opposite sublattice, which is analogous to hydrogen and fluorine [61, 67]. In the bridge case, one sees a larger hybridization between copper s states and the π states of carbon atoms $C_{A/B}$, which are nearest neighbors of copper, manifested in the peaks at the Fermi level in panel 3.6(b).

3.3.3 Origin of the local spin-orbit coupling

In order to construct an effective spin-orbit coupling Hamiltonian it is important to analyze its microscopic origin. Fig. 3.7 displays the spin-orbit splittings of the valence (a), midgap (b), and conduction (c) bands, for both the top and bridge adsorption configurations along the indicated high-symmetry paths for the 7×7 supercell.

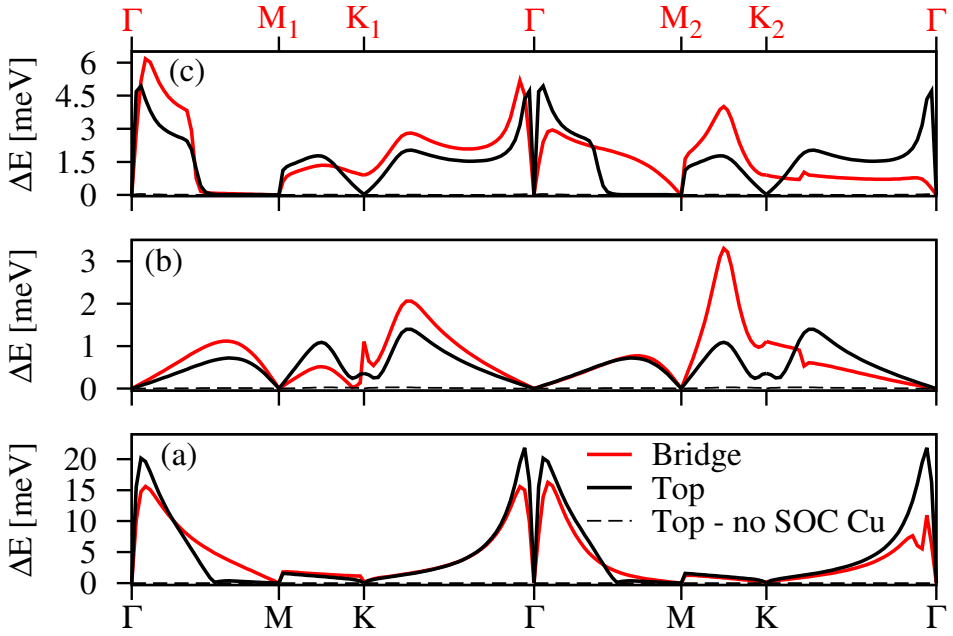

Figure 3.7: Spin-orbit induced coupling band splittings for the top (black solid) and bridge copper positions (red solid) in the 7×7 supercell for valence (a), midgap (b) and the conduction (c) band, respectively. Resulting splittings for the top case with turned off spin-orbit coupling on copper are shown as black dashed lines. High symmetry points are labeled for the top and bridge cases according to Figs. 3.3 and 3.5, respectively.

The band splittings again show qualitatively similar behavior for the top and bridge adsorption. Large splittings up to 20 meV are observed for the valence band, values of 1 meV for the midgap band and up to 4.5 meV in the conduction band. Splittings at Γ and M points vanish due to time-reversal symmetry. The midgap band at the K point is split significantly. For this band, the splitting in the top case is mostly lower than in the bridge configuration. The bridge case is especially interesting because it shows how the spin-orbit coupling splittings are affected by the interactions among the bands. Due to the broken symmetry, the k paths M_1K_1 and M_2K_2 are in general

different, which is manifested in the band structure and translates also into the band splittings. On different segments of the k path in Fig. 3.5 the hybridization between the midgap and either valence or conduction band has different intensity. Along the path M_2K_2, where the midgap and conduction bands are closer to each other, the spin-orbit splitting is greatly enhanced to 3 meV as opposed to the path along M_1K_1 where the spin-orbit coupling is reduced to 0.5 meV.

Figure. 3.7 also displays spin-orbit splittings for the top adsorption configuration when spin-orbit coupling on the copper adatom is turned off by replacing the relativistic copper pseudopotential by a nonrelativistic one. The splittings drop to very small values in the range of tens of μeV and they resemble in magnitude the spin-orbit splittings calculated for dilute hydrogenated graphene [61]. These residual spin-orbit splittings are due to contributions from sp^3 rehybridization of the carbon atoms in the presence of a small local out-of-plane distortion [60] caused by copper and are negligible. *We conclude that the origin of the local spin-orbit coupling in copper functionalized graphene is due to the intra-atomic spin-orbit coupling of the copper atom.* Note that the DFT band analysis of spin-orbit mediated splittings can give just a qualitative picture as the band splittings are supercell size dependent and vanish in the limit of large cells. The absolute values of spin-orbit coupling strengths can be only extracted from a realistic tight-binding model, as discussed in Sec. 3.4.

In what follows we look in more detail on spin-orbit coupling physics between copper and graphene. For practical reasons we take 5×5 supercells to reduce computational costs. We have checked that the orbital decomposition of bands close to the Fermi level changes marginally compared to larger cells and hence conclusions drawn from the smaller supercell analyses are valid also for larger 7×7 and 10×10 supercells.

To separate the spin-orbit coupling effects originating from d and p orbitals, we performed DFT+U calculations [32]. Figure 3.8 displays the band structures for copper in the top position with Hubbard $U = 0$ eV and $U = 2$ eV applied on the Cu d orbitals. The Hubbard U shifts the fully occupied d states to lower energies, as discussed in Sec. 2.2.2. Comparing the left and right panels in Fig. 3.8 we see that the shift of the d levels to lower energies starts to modify the band structure from -1.5 eV, while near the Fermi level the bands are hardly affected. This is understandable from our previous PLDOS analysis, Fig. 3.4: the d level contribution to states near the Fermi level for $U = 0$ eV is quite small and their onset at the K point lies at -1.75 eV. For Hubbard $U = 2$ eV the d state onset is located at -2.25 eV.

Fig. 3.9 shows the spin-orbit coupling band splittings of a copper atom in the top position of the 5×5 supercell for a subsequent series of Hubbard $U = 0, 2, 4$, and 8 eV. The shift of d levels towards lower energies affects the ratio between p and d density of states on the copper atom at the Fermi level (within the midgap band), which we determine to be $p/d = 10.0, 15.8, 23.4$, and 43.1, respectively. The p state contribution thereby remains unchanged. From Fig. 3.9 we see that diminishing the d orbital contributions with raising U, decreases the spin-orbit band splittings. This effect is most visible in the valence band since there is higher contribution from d states. The splittings in the midgap and conduction band, however, decrease less drastically. To quantify this behavior we take the maximum of the splitting for the midgap band Δ (located between M and K), and plot it against the ratio $r = d/p$ of d to p density of states (DOS) contributions at the Fermi level. The graph of Δ versus

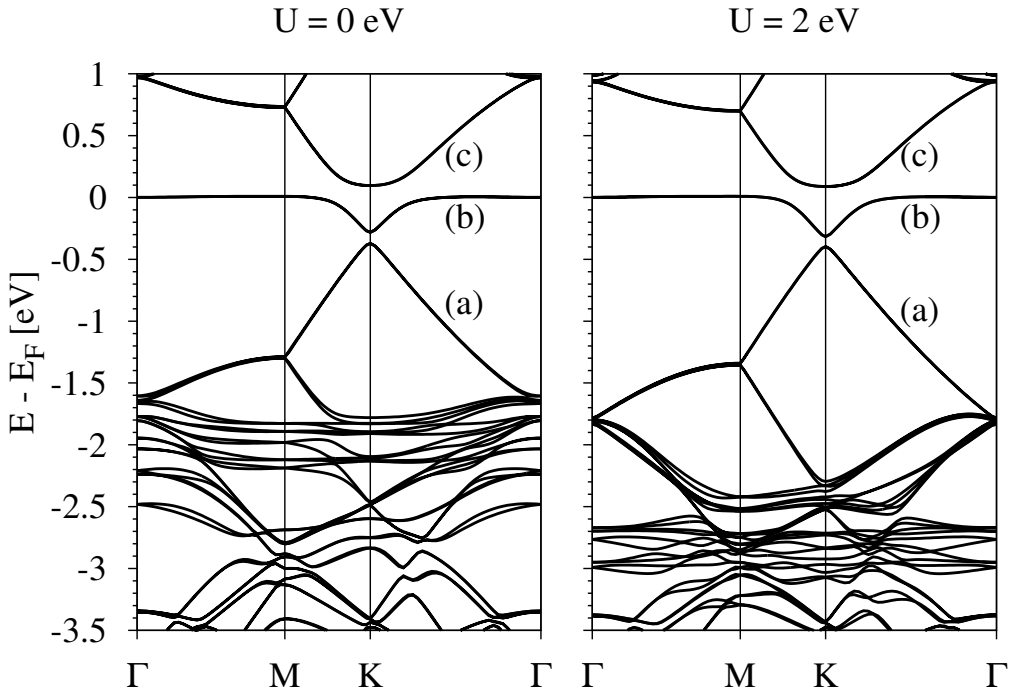

Figure 3.8: Calculated electronic band structure with Hubbard U for 5×5 supercell with copper in the top position. The left panel corresponds to $U = 0\,\mathrm{eV}$ and the right one to $U = 2\,\mathrm{eV}$. The effect of Hubbard U is seen on the copper d levels which are shifted down in energy for $U = 2\,\mathrm{eV}$.

r is shown in Fig. 3.10. We see that Δ scales linearly with r hence writing

$$\Delta(r) = \tilde{\Delta} \cdot r + \Delta_p \,, \tag{3.2}$$

we can extract $\tilde{\Delta} = 9.5$ meV and $\Delta_p = 0.51$ meV. Extrapolating $\Delta(r)$ for $r \to 0$, i.e., for no contributions from d orbitals, one would obtain a splitting of 0.51 meV, solely due to p contributions. Comparing that value with $\Delta(r \simeq 0.1) = 1.46$ meV, i.e., at $U = 0\,\mathrm{eV}$, we see that ca. 35% of the spin-orbit splitting (at the particular k point and band) stems from the p orbitals and 65% from their d state counterparts. A similar analysis can be carried out for the K point, see Fig. 3.10. Here, we extract Δ_p of 0.40 meV. Compared to the $U = 0$ eV case with $\Delta = 0.65$ meV we find a contribution of 62% from p orbitals. *Both, p and d orbitals contribute to spin-orbit coupling in nearly equal magnitude at low energies.* At first sight it seems odd that the maximal splitting at the Fermi level (midgap band) is by $\sim 50\%$ governed by the d orbitals whose spectral density at this energy is an order of magnitude smaller when compared to the p states (see, e.g., Fig. 3.4). But as we already noted in Sec. 3.2.3, the intra-atomic spin-orbit splitting of d levels of the isolated copper (253 meV) is an order of magnitude larger when compared to p states (31 meV), so both contributions reasonably compete.

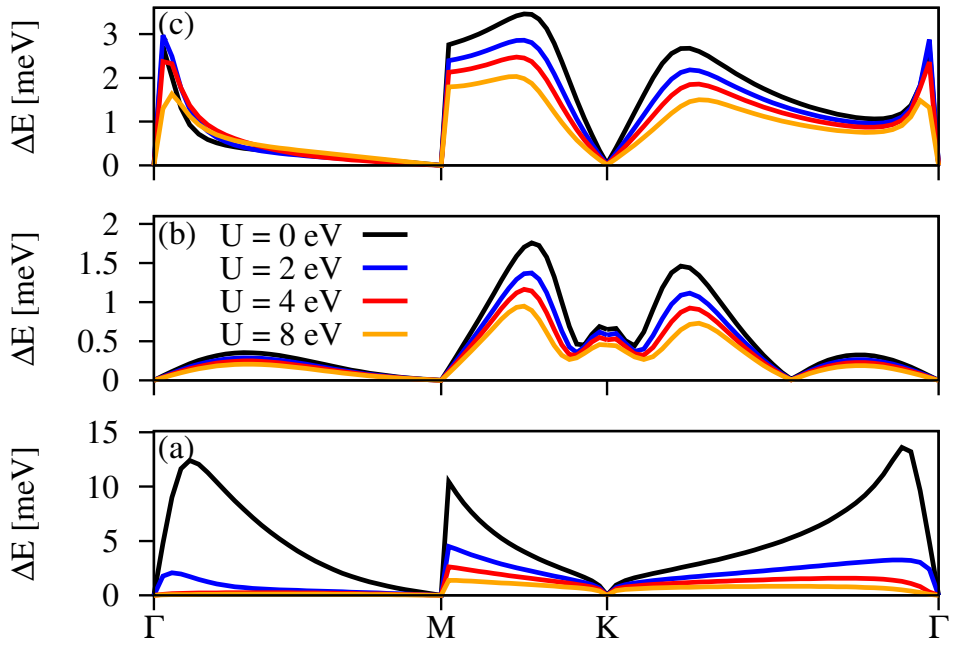

Figure 3.9: Evolution of the spin-orbit band splittings for a 5×5 supercell with copper in the top position for the valence (a), midgap (b) and conduction (c) bands, respectively, with respect to the strength of Hubbard U. Different colors correspond to Hubbard U of 0, 2, 4 and 8 eV, respectively.

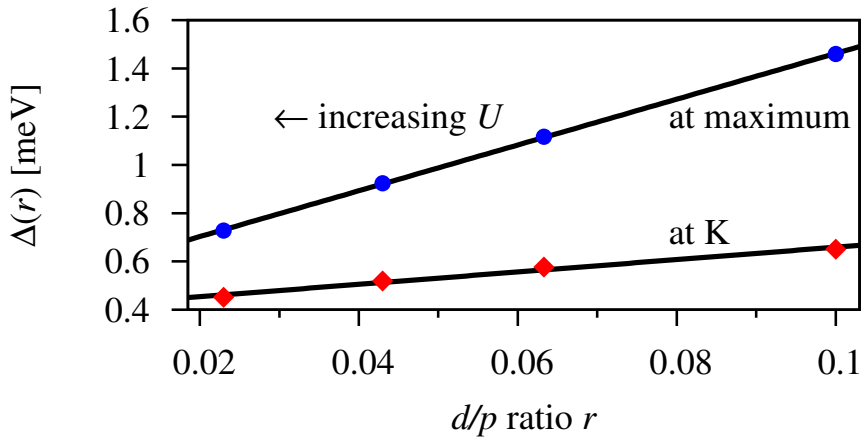

Figure 3.10: Spin-orbit splittings for the midgap band from Fig. 3.9 in the top position, versus the ratio $r = d/p$ between the d and p state densities at the Fermi energy—controlled by the strength of Hubbard U. Circles represent the extracted data for the maximal splitting, diamonds represent the extracted data at the K point for $U = 0$, 2, 4, 8 eV and the black lines are linear fits.

3.3.4 Spatial visualization of spin-orbit coupling

Copper adsorbed on graphene affects the low-energy graphene states via hybridization and induces spin-orbit coupling by small contributions to the electronic states from copper p and d states. Spin-orbit coupling in general manifests in the lifting of the degeneracy of bands when inversion symmetry is absent. Here, we show how spin-orbit coupling redistributes the density of, without SOC degenerate, Kohn–Sham states in real space. We compute the "spin-orbit coupling induced polarization density"

$$\Delta\varrho_n^{\mathbf{k}}(\mathbf{r}) = \left|\phi_{n,\sigma}^{\mathbf{k}}(\mathbf{r})\right|^2 - \left|\phi_{n,-\sigma}^{\mathbf{k}}(\mathbf{r})\right|^2, \tag{3.3}$$

where $\phi_{n,\sigma}^{\mathbf{k}}(\mathbf{r})$ is a Kohn–Sham wave function at momentum $\mathbf{k}$ with spin σ and band index n. The partner state is denoted by $-\sigma$, which is very close in energy and split off by spin-orbit coupling.

The polarization densities $\Delta\varrho_n^{\mathrm{K}}(\mathbf{r})$ for the midgap band states at the K point are shown in Fig. 3.11 for both adsorption configurations and two different unit cell sizes 7×7 and 10×10. The isosurface plots display the location where effects of spin-orbit coupling are largest. Although we cannot extract quantitative information from these plots, they give an intuition for which atoms and orbitals are contributing to the spin-orbit coupling physics of the system. In a sense it is a direct way to visualize the effects of spin-orbit coupling in real space. At the copper atom, redistribution effects are the largest. Moving away from the impurity $\Delta\varrho_n^{\mathrm{K}}(r)$ falls off rapidly, which is understandable since in pristine graphene spin-orbit effects are very small. This local behavior is remarkable because the separate densities of the states $\left|\phi_{n,\sigma}^{\mathbf{k}}(\mathbf{r})\right|^2$ and $\left|\phi_{n,-\sigma}^{\mathbf{k}}(\mathbf{r})\right|^2$ are spread *all over* the graphene sheet (not shown). We see that the isosurface profiles of the spin-orbit coupling induced polarization density nicely reflect the local point group symmetry, i.e., C_{3v} for top and C_{2v} for bridge. Moreover, we observe that the $\Delta\varrho_n^{\mathrm{K}}(r)$ profiles qualitatively stay the same when increasing the supercell size. Only the farther away carbon atoms loose their polarization. This indicates that in the 7×7 supercell still interference effects are present, whereas in the 10×10 cells the polarization seems much more localized, being only present on the four nearest neighbor carbon atom shells. This method could be applied to other situations, where inversion symmetry is broken, and one wants to analyze the local origin of spin-orbit coupling in more complex systems.

3.4 Tight-binding models and extraction of spin-orbit coupling parameters

The following important work of tight-binding model derivation and parameter extraction was done by Susanne Irmer. Figures produced by Susanne Irmer are marked with citation of Ref. [93]. Here, we describe the methodology and results for completeness as published together in Ref. [93].

To analyze spin-orbit coupling and orbital effects, we construct a tight-binding Hamiltonian of the form $\hat{\mathcal{H}} = \hat{\mathcal{H}}_0 + \hat{\mathcal{H}}_{\mathrm{orb}} + \hat{\mathcal{H}}_{\mathrm{soc}}$. This Hamiltonian includes the unperturbed graphene Hamiltonian $\hat{\mathcal{H}}_0$, orbital effects stemming from the copper atom $\hat{\mathcal{H}}_{\mathrm{orb}}$

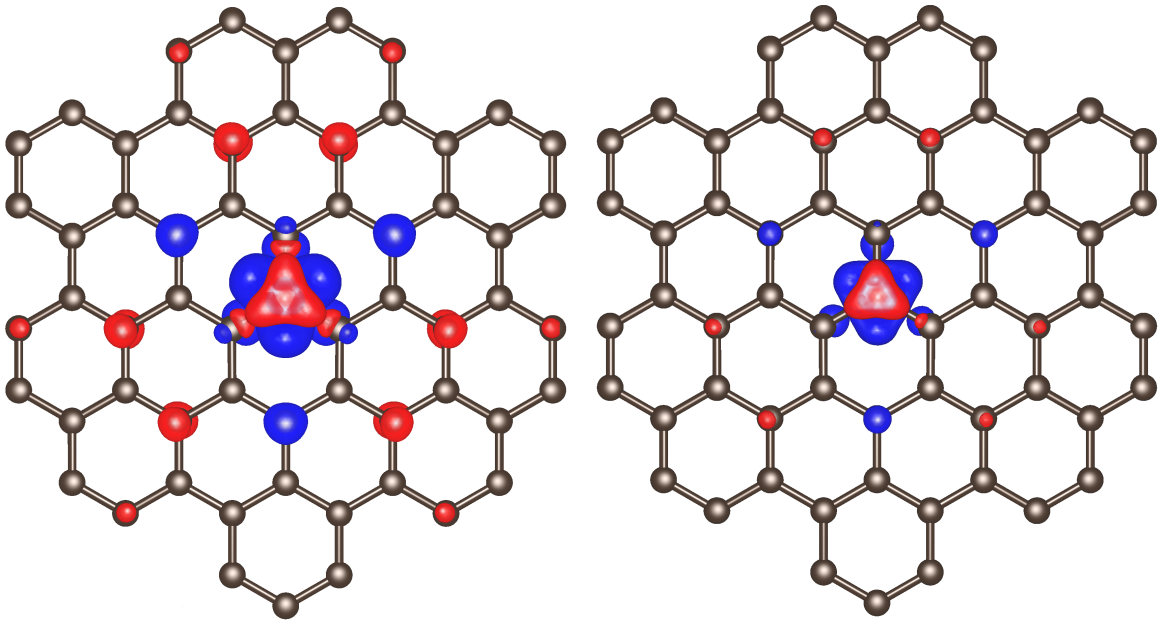

(a) 7×7 top

(b) 10×10 top

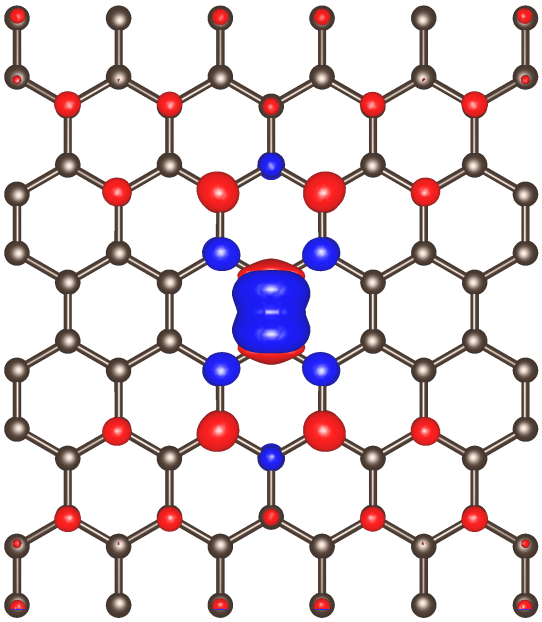

(c) 7×7 bridge

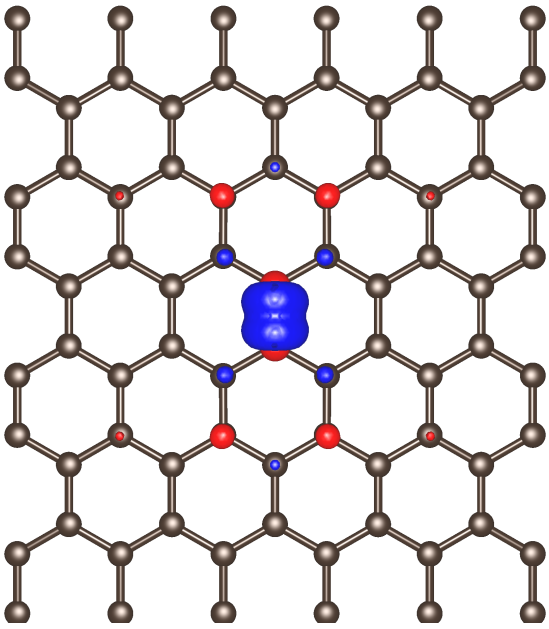

(d) 10×10 bridge

Figure 3.11: Spatial distribution of the spin-orbit coupling induced polarization density $\Delta\varrho_n^{\mathrm{K}}(\mathbf{r})$ in the vicinity of the copper atom for the midgap band at the K point. Displayed are different supercell sizes and adsorption positions as indicated. Isosurfaces of $\Delta\varrho_n^{\mathrm{K}}(\mathbf{r})$ for $+3 \cdot 10^{-6}\text{Å}^{-3}$ (red) and $-3 \cdot 10^{-6}\text{Å}^{-3}$ (blue) are shown.

with no dependence on the spin degree of freedom. The Hamiltonian $\hat{\mathcal{H}}_{\mathrm{soc}}$ describes the local spin-orbit coupling effects induced by the copper atom. This procedure is valuable, as it allows one to extract local hopping elements, which in the limit of large supercell sizes, are independent on the supercell size and describes the impurity locally.

The unperturbed graphene Hamiltonian reads

$$\hat{\mathcal{H}}_0 = -t \sum_{\langle i,j\rangle,s} \hat{c}^\dagger_{is}\hat{c}_{js} + \frac{i\lambda_{\mathrm{I}}}{3\sqrt{3}} \sum_{\langle\langle i,j\rangle\rangle,s,s'}{}' \nu_{ij} \left[\hat{\mathbf{s}}_z\right]_{ss'} \hat{c}^\dagger_{is}\hat{c}_{js'} \,. \tag{3.4}$$

The orbital hopping in the first term, is a nearest-neighbor hopping, indicated by the summation over $\langle i\,,j\rangle$, in the bipartite lattice of graphene [94] with sublattice degrees of freedom A and B. Creation $\hat{c}^\dagger_{is}$ and annihilation operators $\hat{c}_{is}$ represent carbon p_z orbitals located at site i with a spin-z quantum number of s. The hopping is parametrized by a value of $t = 2.6$ eV [4]. The second term represents the intrinsic SOC of graphene, which is a next-nearest neighbor hopping process [95] and is set to a value of $\lambda_{\mathrm{I}} = 12\,\mu$eV [59]. Intrinsic SOC is a spin-preserving second-nearest-neighbor hopping (indicated by $\langle\langle i,j\rangle\rangle$) as only the z component of the spin Pauli matrix vector $\hat{\mathbf{s}}$ enters. Locally, the copper atom changes the intrinsic graphene SOC hoppings, which is why the contribution to intrinsic SOC by the carbon atoms surrounding the copper atom is excluded from the summation, indicated by the prime. These excluded hoppings are then compensated for in $\hat{\mathcal{H}}_{\mathrm{soc}}$. The prefactor ν_{ij} has different signs of $+1$ (-1) if the hopping occurs along an anticlockwise (clockwise) path from site j to i via a common neighbor (see, e.g., [13]).

3.4.1 Top configuration

Orbital Hamiltonian We understand the copper atom as a monovalent impurity which at low energies is reduced to an s-like orbital (compare Sec. 3.3). The orbital is an effective one as it incorporates also p and d contributions such, that it is compatible with the local point group and time-reversal symmetries. The orbital part of the impurity Hamiltonian in the top position is formulated as

$$\hat{\mathcal{H}}_{\mathrm{orb}} = \varepsilon_t \sum_s \hat{X}^\dagger_s \hat{X}_s + \left(\omega_t \sum_s \hat{X}^\dagger_s \hat{C}_s + \mathrm{H.c.}\right) \,, \tag{3.5}$$

already developed for other systems with hydrogen, fluorine or methyl molecule adsorption [61, 67, 68]. The effective orbital with spin degree of freedom s on the copper atom is represented by operators $\hat{X}_s$ with an on-site energy of ε_t and a coupling to the carbon atom below via the hybridization parameter ω_t; for a graphical representation see Fig. 3.12(a).

We use $\hat{\mathcal{H}}_0$ and $\hat{\mathcal{H}}_{\mathrm{orb}}$ to fit the band structure of a copper atom in the top position of a 10×10 graphene supercell in a first step. Tight-binding fits with respect to the valence, midgap, and conduction bands in comparison with the DFT-computed band structure are shown in Fig. 3.3. The resulting fit parameters are $\varepsilon_t = 0.08\,\mathrm{eV}$ and $\omega_t = 0.81\,\mathrm{eV}$. The relative magnitudes of the fitting parameters with respect to other adsorption species are discussed later after spin-orbit coupling parameters have been

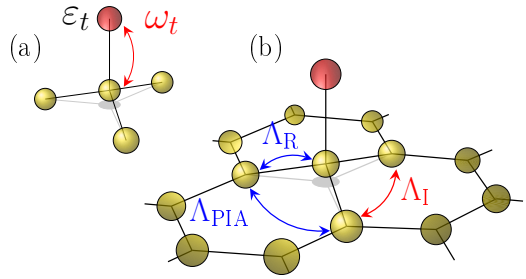

Figure 3.12: Graphical representation of the minimal orbital and SOC Hamiltonians $\hat{\mathcal{H}}_\mathrm{orb}$ and $\hat{\mathcal{H}}_\mathrm{soc}$, respectively, for the copper in top adsorption position. (a) hybridization hopping ω_t and the copper on-site energy ε_t, (b) local SOC mediated hoppings among the carbon atoms near the copper Λ_I, Λ_R and Λ_PIA. From Ref. [93].

extracted. With only two fitting parameters ε_t and ω_t one obtains an excellent fit over the complete MKΓM line. The parameters obtained from this fitting procedure are kept fixed in the following analysis of SOC.

Spin-orbital Hamiltonian The minimal C_{3v} and time-reversal invariant local SOC Hamiltonian reads [13, 61, 67, 68],

$$\begin{aligned}\hat{\mathcal{H}}_\mathrm{soc} = &\frac{i\Lambda_\mathrm{I}}{3\sqrt{3}} \sum_{\langle\langle i,j\rangle\rangle,s,s'} \hat{C}^{1n\dagger}_{is} \hat{C}^{1n}_{js'}\, \nu_{ij}\, [\hat{\mathbf{s}}_z]_{ss'} \\ &+ \frac{2i\Lambda_\mathrm{R}}{3} \sum_{j,s,s'} \hat{C}^{\dagger}_{s} \hat{C}^{1n}_{js'} \left[\left(\hat{\mathbf{s}} \times \mathbf{d}_{\mathrm{C}\mathrm{C}^{1n}_j}\right)_z\right]_{ss'} + \mathrm{H.c.} \\ &+ \frac{2i\Lambda_\mathrm{PIA}}{3} \sum_{\langle\langle i,j\rangle\rangle,s,s'} \hat{C}^{1n\dagger}_{is} \hat{C}^{1n}_{js'} \left[\left(\hat{\mathbf{s}} \times \mathbf{d}_{\mathrm{C}^{1n}_i\mathrm{C}^{1n}_j}\right)_z\right]_{ss'} .\end{aligned} \tag{3.6}$$

We keep the same SOC terminology as introduced in Ref. [61]. Λ_I represents the spin-conserving second-nearest neighbor hopping (intrinsic), Λ_R the spin-flipping nearest-neighbor hopping (Rashba), and Λ_PIA the spin-flipping second-nearest-neighbor hopping, referred to as pseudospin inversion asymmetry (PIA). The hopping terms can be more easily understood from a pictorial representation, see Fig. 3.12(b). The unit vector $\mathbf{d}_{\mathrm{C}_i,\mathrm{C}_j}$ lies in the graphene plane and connects the three carbon atoms around the occupied carbon atom and points from atom C_j to C_i. The site labeling in Hamiltonian (3.6) is the same as defined in Fig. 3.2(a). Since the Λ_R and Λ_PIA terms come as the z component of a cross product involving the Pauli spin vector $\hat{\mathbf{s}}$, only $\hat{\mathbf{s}}_x$ and $\hat{\mathbf{s}}_y$ matrices are involved. In contrast to the Λ_I term, the Λ_R and Λ_PIA terms therefore represent spin-flipping hopping processes.

The terms in Hamiltonian (3.6) were derived from symmetry arguments [13, 61, 67], which can tell about whether hopping terms are nonzero, real- or complex-valued, and how they can be grouped by geometrical factors ν and $\mathbf{d}$. Although symmetry allows also different local SOC terms in the vicinity of the adatom (see Refs. [61, 67, 68]), here the three parameters Λ_I, Λ_R, and Λ_PIA provide enough flexibility to effectively

describe the spectrum of the system.

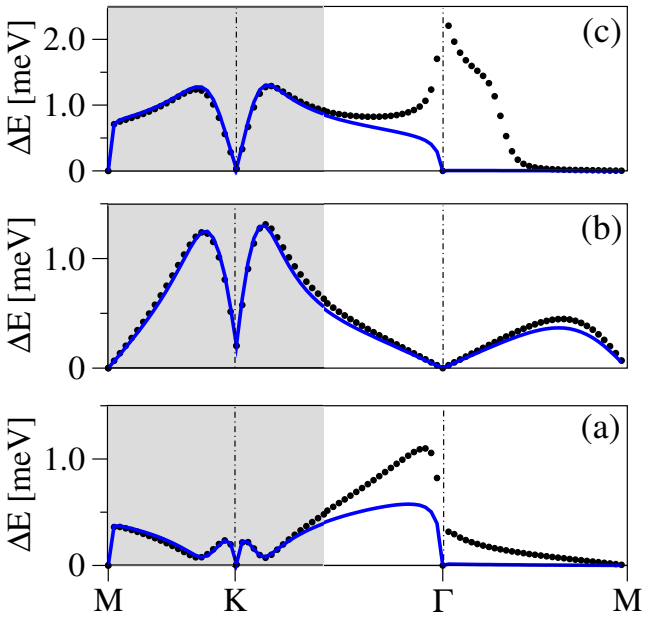

Figure 3.13: Spin splittings of the valence (a), midgap (b), and conduction band (c) for the copper on a 10×10 graphene supercell in the top position. First principle data (black symbols) are fitted by the tight-binding model Hamiltonian $\hat{\mathcal{H}}_0 + \hat{\mathcal{H}}_{\text{orb}} + \hat{\mathcal{H}}_{\text{soc}}$ for crystal momenta in the shaded regions. The model computed data is represented by solid (blue) lines. Fitting and tight-binding caluclations were done by Susanne Irmer, from Ref. [93].

To obtain the spin-orbit coupling hopping elements, we fit our model to the band splittings of valence, midgap and conduction bands, which are shown in Fig. 3.13 for a copper atom in the 10×10 supercell. The orbital parameters obtained above are kept fixed. The least-squares fit takes only information around the K point into account. The extracted parameters are $\Lambda_{\text{I}} = 9.0\,\text{meV}$, $\Lambda_{\text{R}} = 30.2\,\text{meV}$ and $\Lambda_{\text{PIA}} = -47.4\,\text{meV}$. Along the full MK line and about one-third of KΓ line the model excellently reproduces the DFT data. Approaching the Γ point the model strongly deviates for the valence and conduction bands from first principles, but still stays perfectly aligned within the midgap band. This is because at the Γ point the valence and conduction bands lie far away from the Fermi energy and other states contribute with different angular momenta (see Fig. 3.4). Our effective low-energy Hamiltonian assumes that all participating atomic orbitals transform with respect to C_{3v} as states with $m_z = 0$, which ceases to hold far away from the Fermi energy.

We compile comparable orbital and SOC parameters for the top-adsorbed cases of H, F, CH_3, and Cu in Tab. 3.2. Concerning the orbital parameters, the on-site energy of copper is relatively low, on the same level as the carbon p_z (of reference energy $\varepsilon_{p_z} = 0$ eV), hydrogen, and methyl orbitals, indicating low doping. However the hybridization energy is much lower compared to all other adsorbates, which is a sign of weak bonding. Comparing copper to hydrogen [61], fluorine [67], and methyl [68], we see that the present SOC parameters are an order or two orders of magnitudes larger.

Atom	ω_t[eV]	ε_t[eV]	$\Lambda_{\mathrm{I}}^{\mathrm{A}}$[meV]	$\Lambda_{\mathrm{I}}^{\mathrm{B}}$[meV]	$\Lambda_{\mathrm{PIA}}^{\mathrm{B}}$[meV]	Λ_{R}	$\overline{\lvert\Lambda\rvert}$[meV]
H [61]	7.5	0.16	−0.21		−0.77	0.33	0.55
F [67]	5.5	−2.2		3.3	7.3	11.2	7.3
CH_3 [68]	7.6	−0.19	−0.77	0.15	−0.69	1.02	0.62
Cu	0.81	0.08		9.0	−47.4	30.2	28.9

Table 3.2: Orbital and SOC tight-binding parameters for adatoms in the top position. In this work, Λ_{I} is equivalent to $\Lambda_{\mathrm{I}}^{\mathrm{B}}$ and Λ_{PIA} to $\Lambda_{\mathrm{PIA}}^{\mathrm{B}}$ of Refs. [61, 67, 68]. $\Lambda_{\mathrm{I}}^{\mathrm{A}}$ is the spin-conserving hopping from the decorated carbon orbital to its next-nearest neighbors. $\overline{\lvert\Lambda\rvert}$ is the averaged absolutes of spin-orbit coupling parameters.

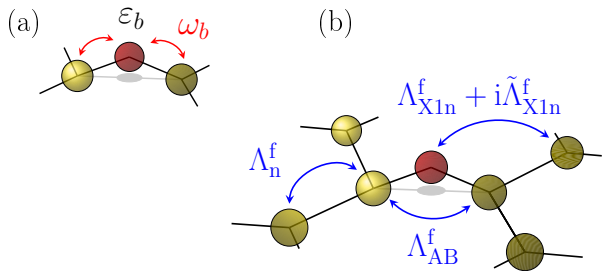

Figure 3.14: Graphical representation of the minimal orbital and SOC Hamiltonians $\hat{\mathcal{H}}_{\mathrm{orb}}$ and $\hat{\mathcal{H}}_{\mathrm{soc}}$, respectively, for the copper in bridge adsorption position. (a) Hybridization hopping ω_b and the copper on-site energy ε_b. (b) Local SOC mediated hoppings among the carbon atoms near copper $\Lambda^{\mathrm{f}}_{\mathrm{n}}$, $\Lambda^{\mathrm{f}}_{\mathrm{AB}}$, and $\Lambda^{\mathrm{f}}_{\mathrm{X1n}} + i\tilde{\Lambda}^{\mathrm{f}}_{\mathrm{X1n}}$. From Ref. [93].

We also calculated the average magnitude of SOC parameters $\overline{\lvert\Lambda\rvert}$. There seems to be a *linear* relationship between the atomic number of 1, 9, and 29 and size of SOC effects $\overline{\lvert\Lambda\rvert}$ in hydrogen, fluorine and copper decorated graphene, respectively. This is somewhat surprising as spin-orbit coupling energy splittings grow faster than linearly with respect to the atomic number. Methyl falls out of that trend, chemically it is behaving more like a hydrogen bond [68].

3.4.2 Bridge configuration

The local point group symmetry for the adatom binding in the bridge position is C_{2v}. Symmetry operations involve C_2 rotations around the principal axis and vertical reflections σ_v^{xz} and σ_v^{yz} (see Fig. 3.2(b)). To describe the local physics of the copper atom in the bridge system, the strategy is similar as in the top case. Assuming an effective orbital with angular momentum of $m_z = 0$ on the copper atom we construct a minimal orbital $\hat{\mathcal{H}}_{\mathrm{orb}}$ and spin-orbital $\hat{\mathcal{H}}_{\mathrm{soc}}$ low-energy tight-binding Hamiltonian respecting the local point group symmetries and time-reversal symmetry.

Orbital Hamiltonian In the spirit of Eq. (3.5), we formulate a similar orbital Hamiltonian for the bridge position

$$\hat{\mathcal{H}}_{\mathrm{orb}} = \varepsilon_b \sum_s \hat{X}_s^\dagger \hat{X}_s + \omega_b \left(\sum_s \left(\hat{X}_s^\dagger \hat{C}_{\mathrm{A}s} + \hat{X}_s^\dagger \hat{C}_{\mathrm{B}s} \right) + \mathrm{H.c.} \right) . \tag{3.7}$$

The energy offset of the effective copper orbital $\hat{X}_s$ of spin s with respect to the carbon p_z orbital is given by ε_b and the hopping strength to the two neighboring carbon atoms C_A and C_B is parametrized by the hybridization strength ω_b. A graphical representation of atom labeling is given in Fig. 3.2(b) and hoppings are visualized in Fig. 3.14.

Ignoring the SOC part of $\hat{\mathcal{H}}_0$, Eq. (3.4), we can fit $\hat{\mathcal{H}}_0 + \hat{\mathcal{H}}_{\mathrm{orb}}$ with respect to the DFT-computed band structure. As a result we obtain $\varepsilon_b = 0.02\,\mathrm{eV}$ and $\omega_b = 0.54\,\mathrm{eV}$. The comparison between the *ab initio* and tight-binding calculations is shown in Fig. 3.5. Over the whole high symmetry path $\Gamma\mathrm{M}_1\mathrm{K}_1\Gamma\mathrm{M}_2\mathrm{K}_2\Gamma$ a near-perfect orbital description is obtained, using only two parameters. The tight-binding calculation even reproduces perfectly all the crossings and anticrossings at the Fermi energy.

Spin-orbital Hamiltonian The reduced symmetry from C_{3v} to C_{2v} allows much more possible complex-valued spin-orbit coupling hoppings (see [13] for a comprehensive list). Not all of them are necessary to reproduce the spin-orbit coupling physics in the case of a copper atom on the bridge site. The minimal SOC Hamiltonian in the bridge position with real-valued parameters Λ and complying with the coordinate system in Fig. 3.2(b), reads

$$\begin{aligned}
\hat{\mathcal{H}}_{\mathrm{soc}} = {} & i\Lambda^{\mathrm{f}}_{\mathrm{AB}} \sum_{\langle i,j\rangle,s,s'} \hat{C}^\dagger_{\mathrm{A}s} \hat{C}_{\mathrm{B}s'} \left[\hat{\mathbf{s}}_x\right]_{ss'} + \mathrm{H.c.} \\
& + \Lambda^{\mathrm{f}}_{\mathrm{n}} \sum_{s,s'} \left(\sum_{j\in\mathrm{B}} \hat{C}^\dagger_{\mathrm{A}s} \hat{C}^{1n}_{js'} - \sum_{j\in\mathrm{A}} \hat{C}^\dagger_{\mathrm{B}s} \hat{C}^{1n}_{js'} \right) \nu_{\mathrm{XC}^{1n}_j} \left[\hat{\mathbf{s}}_y\right]_{ss'} + \mathrm{H.c.} \\
& + \sum_{s,s'} \left(\sum_{j\in\mathrm{A}} \hat{X}^\dagger_s \hat{C}^{1n}_{js'} - \sum_{j\in\mathrm{B}} \hat{X}^\dagger_s \hat{C}^{1n}_{js'} \right) \left(\Lambda^{\mathrm{f}}_{\mathrm{X1n}} \nu_{\mathrm{XC}^{1n}_j} \left[i\,\hat{\mathbf{s}}_y\right]_{ss'} + i\tilde{\Lambda}^{\mathrm{f}}_{\mathrm{X1n}} \left[\hat{\mathbf{s}}_x\right]_{ss'} \right) + \mathrm{H.c.}\,.
\end{aligned} \tag{3.8}$$

The schematic representation in Fig 3.14(b) eases the understanding of the three hopping parts. The first term, parametrized by $\Lambda^{\mathrm{f}}_{\mathrm{AB}}$, represents the spin-flipping hopping between the functionalized carbon sites C_A and C_B. The second term accounts for the spin-flipping hoppings between a functionalized carbon $\mathrm{C}_{A/B}$ and its two nearest neighbors C^{1n}. Those hoppings are parametrized by SOC strength $\Lambda^{\mathrm{f}}_{\mathrm{n}}$. The symbol $\nu_{\mathrm{X,C}^{1n}}$ has a similar meaning as in Eq. (3.4). Viewed from top, it encodes the hopping sense when going from Cu via $\mathrm{C}_{A/B}$ to C^{1n} and assumes values of $1(-1)$ for anticlockwise (clockwise) hopping. The third line represents the spin-flipping hoppings between the copper X and the four $C^{1\mathrm{n}}$ orbitals. The hopping is parametrized by the complex-valued parameter $\Lambda^{\mathrm{f}}_{\mathrm{X1n}} + i\,\tilde{\Lambda}^{\mathrm{f}}_{\mathrm{X1n}}$.

In Fig. 3.15 we show the fit of *ab initio* band splittings by the tight-binding model for valence, midgap and conduction bands. The full Hamiltonian $\hat{\mathcal{H}}_0 + \hat{\mathcal{H}}_{\mathrm{orb}} + \hat{\mathcal{H}}_{\mathrm{soc}}$

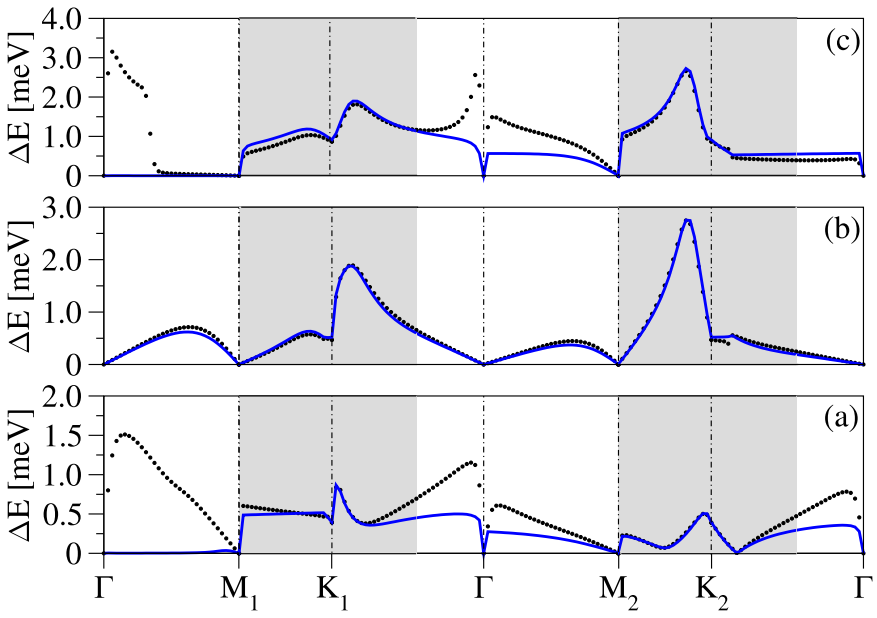

Figure 3.15: Spin splittings of the valence (a), midgap (b), and conduction band (c), for the copper atom on 10×10 graphene supercell in the bridge position. First principle data (black symbols) are fitted by the tight-binding model Hamiltonian $\hat{\mathcal{H}}_0 + \hat{\mathcal{H}}_{\text{orb}} + \hat{\mathcal{H}}_{\text{soc}}$ for momenta in the shaded regions, the model computed data is represented by solid (blue) lines. Fitting and tight-binding caluclations were done by Susanne Irmer, from Ref. [93].

is used to fit the regions about the two K points, indicated by the shaded areas. Parameters obtained are compiled in Tab. 3.3. The quality of the model Hamiltonian is very similar to the top one. Splittings of low-energy bands are very well described. Similarly as in the top case, the model is not expected to describe regions around the Γ point for valence and conduction bands, as the angular momenta of wave functions differ there from $m_z = 0$.

ω_b[eV]	ε_b[eV]	$\Lambda^{\text{f}}_{\text{AB}}$[meV]	$\Lambda^{\text{f}}_{\text{n}}$[meV]	$\Lambda^{\text{f}}_{\text{X1n}}$[meV]	$\tilde{\Lambda}^{\text{f}}_{\text{X1n}}$[meV]	$\overline{\lvert\Lambda\rvert}$[meV]
0.54	0.02	41.0	-7.5	1.4	8.4	14.6

Table 3.3: Orbital and SOC tight-binding parameters for Cu in the bridge position.

Overall, when compared to the top case parameters, the orders of magnitude are in the same range. The averaged magnitudes of SOC parameters $\overline{|\Lambda|}$ is only half as large in this case. However, the maximal amplitudes of hoppings are very similar of about 45 meV. The overall averaged values of spin-orbit coupling hopping elements correspond very well to an experimental estimate of spin-orbit coupling energy of 20 meV [82] measured in spin-Hall experiments in graphene with copper residuals.

3.5 Summary and conclusions

We determine the adsorption position of copper to be in the bridge and top position, both being energetically equivalent, with a total energy difference of just 1 meV. Although the symmetries of the local point groups (C_{3v} and C_{2v}) are very different, we find similar orbital physics, reflected in a flat s-type low-energy band, donated by the copper atom. The source of spin-orbit coupling is the presence of copper p and d levels. This result is obtained with the help of a DFT+Hubbard-U study, which lets one shift the copper d states away from the Fermi energy towards lower energies. Then, only copper p states are left and one can analyze their contributions to spin-orbit splittings. Contributions from copper d orbitals range between 35 to 65% and the rest is from copper p states. This is rather surprising, as the copper p states are by an order of magnitude more abundant than d states at low energies. However, the atomic spin-orbit coupling in the copper atom, about 250 meV for d states and 30 meV for p states also differs by about a factor of ten, which explains the balance. We further present a scheme to visualize the source of spin-orbit coupling in real space by plotting a polarization density of spin-orbit coupling-split Kohn–Sham partners.

Through the knowledge of the orbital structure of states at low energies, which are mainly composed out of $m_z = 0$ orbitals, we are able to propose a Hamiltonian with only two parameters, an on-site energy and a hybridization energy, for both the bridge and top cases. With the help of this Hamiltonian we can model the low-energy orbital band structure over the whole Brillouin zone. We demonstrate that a spin-orbit coupling model Hamiltonian derived for a hydrogen atom on graphene [61] is also useful to describe a top-adsorbed copper atom. This model allows us to extract model spin-orbit coupling values and compare to other systems like hydrogenated or fluorinated graphene. In addition, we provide a new tight-binding model for the bridge case, which yields a good description of the low-energy orbital and spin-orbit physics. In terms of magnitudes we find very large spin-orbit coupling values in the order of tens of meVs. This fulfills the expectation of larger spin-orbit coupling induced by heavier atoms, compared to, e.g., the fluorinated case. Our findings are in accordance with spin Hall measurements in graphene grown by CVD [82], which estimate spin-orbit coupling to be about 20 meV. We find a linear growth of spin-orbit coupling tight-binding parameters with respect to the atomic number, when looking at H, F, and Cu atoms.

Our tight-binding Hamiltonians are a starting point for further investigations. It can be shown for example that copper atoms act as resonant scatterers [93]. The models can also be used in quantum spin-transport simulations at large scale [78, 79, 96] to understand spin-relaxation or the spin-Hall effect [82].

4 Theory of electronic and spin-orbit proximity effects in graphene on Cu(111)

4.1 The hybrid system graphene–Cu(111)

Copper is an important material for graphene. Graphene–copper junctions are often encountered in technological applications [97, 98]. For example, graphene can be used to seal a copper surface to preserve its excellent plasmonic characteristics [99] or prevent it from corrosion [100].

The growth of graphene via chemical vapor deposition (CVD), i.e., the deposition of ethylene C_2H_4 on single-crystal Cu(111) surfaces, is amongst the most popular techniques to obtain large (poly)crystalline graphene [101]. In a novel process using dry delamination [5], graphene with mobilities as high as 350000 $cm^2V^{-1}s^{-1}$ can be grown, leaving the copper foil reusable. Even single-layer graphene grains of millimeter size as well as pyramid-like bi- and trilayer graphene, and hexagonal onion ring-like graphene grains can be synthesized on copper [102, 103]. Important to our study, graphene produced on a copper surface exhibits a giant spin Hall effect [82]. A likely source of this spin-orbit coupling (SOC) mediated effect is due to residual copper adatoms and ad-clusters.

Experimentally, graphene on the Cu(111) surface has been well studied by means of angle-resolved photoemission spectroscopy (ARPES) [104–110] and scanning tunneling microscopy (STM) [101]. Graphene's π states with their linear dispersion are found to be preserved. ARPES measurements of graphene on Cu(111) reveal electron doping in graphene [110], leading to a shift of the Dirac energy E_D, which we define as the average energy of the graphene's π states at K with respect to the Fermi energy E_F. Typically, E_D is found at about -0.3 eV [110], in good agreement with theoretical predictions [98]. The top of the d band edge of copper begins at -2 eV below the Fermi level. It is observed that a gap opens within the Dirac cone of graphene of about 50–180 meV [104, 106–110].

Spin-orbit coupling (SOC) effects in graphene on selected metal substrates were studied theoretically [111, 112], and experimentally [113, 114] and it was noticed that substrates can induce sizeable spin-orbit effects important for spintronics applications [6, 8]. Spin-resolved ARPES experiments [107] focused on the spin-orbit effects introduced by metallic surfaces in graphene, investigating the role of the atomic number of the substrate. It was found that the states of graphene can be split due to Rashba SOC by up to 100 meV in the case of Au and 10 meV in the case of Ni [112], respectively. Copper substrate induced spin-orbit splittings in graphene are expected to be substantially smaller [107]. They were measured at a temperature of 40 K, which gives the resolution limit and also the upper bound for the SOC effects of 3.4

meV. The mechanism introducing the spin-orbit interaction was identified to be the hybridization between the substrate's d and graphene's π states [107]. Our present work agrees with this conclusion, and predicts the values of the Rashba splitting to be about 2 meV for a reasonable distance between graphene and copper, just below the stated experimental resolution of Ref. [107].

To obtain accurate graphene–metal distances, it is crucial to consider van der Waals interactions. It was found [115–117] that the dispersive long-range interactions play an important role in binding, yielding graphene–copper distances of 2.91 to 3.58 Å.

Here, we focus on hybridization and proximity effects by means of density functional theory (DFT) calculations. By the application of an effective Hubbard U [32], we achieve a good agreement with experiment in terms of the ARPES emission spectra and the band structure features. We carry out an analysis of the orbital composition of the band structure, giving us hints for a model Hamiltonian including spin-orbit interactions, which can be used to describe graphene in combination with many other materials that yield a C_{3v} or higher symmetric system. We then fit the DFT data to the model Hamiltonian and extract parameters such as the staggered potential as well as SOC values. As the graphene–copper distance is not exactly known experimentally, and there is still a theoretical uncertainty in determining its magnitude, we carry out a distance-dependent study.

Our main finding is a strong graphene–Cu(111) distance-dependent SOC introduced in the graphene states. We use a model Hamiltonian to describe those states, for which we observe a Rashba SOC parameter which reaches values of a few meVs, while being absent in pristine graphene. The proximity induced intrinsic SOC is in the tens to hundreds of μeV range, a factor of up to ten times larger than in pristine graphene. We also observe a closing of the induced gap for a graphene–copper distance of 2.4 Å. This is accompanied by a peculiar reordering of spin and pseudospin states associated with a gap inversion at small distances.

This chapter is organized as follows. Section 4.2 deals with the computational methods used. Geometrical structure modeling is described in Sec. 4.3. In Sec. 4.4 we carry out the analysis of the electronic structure. In Sec. 4.5 we introduce our model Hamiltonian and fit it to the *ab initio* data in Sec. 4.6. Finally, in Sec. 4.7 we present our graphene–copper distance-dependent study with a discussion of the proximity induced effects.

4.2 Computational methods

In order to study the graphene–Cu(111) hybrid system, we use DFT implemented in the plane-wave code `Quantum Espresso` [54] to calculate its relativistic properties. The calculations are performed at a k point sampling of the Brillouin zone of 40×40, if not indicated otherwise. A slab geometry is applied, where we add a minimum of 15 Å of vacuum around the structure in z direction. We used the Kresse-Joubert ultrasoft (relativistic) PBE [28] projector augmented wave pseudopotentials [83] as described in Sec. 2.4. The plane-wave energy cutoff was set to 40 Ry and the charge density cutoff to 320 Ry to ensure converged results. Van der Waals interactions were taken into account using the empirical method of Grimme [34] (see also Sec. 2.2.2). To

cross check SOC calculations we also employed the all-electron, full potential linearized augmented plane-wave code `Wien2k` [56]. We found that SOC splittings were differing at most by 20%, which is our estimate of systematic error for the quantities extracted in this study (see also Sec. 3.2.3). For processing our distance dependent studies, the atomic simulation environment (`ASE`) [52] was used to generate the different unit cells and automate the DFT calculation process. Hellmann–Feynman forces in relaxed structures were decreased until they were smaller than 0.001 Ry/a_0. Calculations for graphene on Cu(111) included calculations adding the Hubbard U correction [33] (see also section 2.2.2).

4.3 Choice of simulation geometry

To clarify how the interface of graphene and Cu(111) should be modeled, several aspects have to be taken into account. The mismatch between the lattice constant of Cu(111)'s surface, of $3.61/\sqrt{2}$ Å [118], and graphene's lattice constant of 2.46 Å is 3.8%. The resulting moiré structures were observed by STM experiments [101] with different periodicities in epitaxially grown graphene on Cu(111); the most observed one (30% of the area) is a commensurate lattice configuration with a periodicity of 66 Å. Another experiment [104] found that 60% of graphene grains on Cu(111) are preferentially rotated by 3° with respect to the substrate. To accurately account for the lattice mismatch and such small rotations, this would give a unit cell containing hundreds of atoms, which is computationally too demanding. Therefore we model the system in a commensurate configuration using only a single graphene unit cell on the minimal Cu(111) surface unit cell as shown in Fig. 4.1, following the strategy of Refs. [97, 98]. We set the lattice constant of copper to be compatible with the experimental graphene lattice constant, to describe graphene as realistically as possible. A supporting fact to use graphene's lattice constant is that graphene is only van der Waals-bound to copper and its strong in-plane σ bonds remain intact [98]. Copper is then compressed with respect to its natural state. This will be cured by letting copper expand in the vertical direction, as described later.

In the vertical direction one distinguishes three nonequivalent Cu planes, see Fig. 4.1. We label the ABC stacked planes of the underlying fcc copper crystal from the surface towards bulk as top, hcp, fcc, and so on. We tested three different commensurate configurations named according to over which Cu atoms the two carbon atoms of graphene's unit cell sit. This gives rise to three possible graphene physisorbed positions named as top-fcc, top-hcp, and hcp-fcc configurations [98]. In Fig. 4.1, we show the top-fcc configuration, where one carbon atom (from sublattice B) resides on a top copper atom, while the other carbon (from sublattice A) is sitting on the fcc Cu layer.

To simulate a copper surface we use four layers of copper. We checked that the physics of the graphene low-energy states does not change drastically by removing the lower top layer, as shown later when band splittings are discussed. In addition, we find good agreement of the (copper) band structure with ARPES experiments [104–110], as discussed later.

In our studies we first relax the copper slab *alone* without applying van der Waals corrections, then fix its degrees of freedom and let just the carbon atoms relax in z

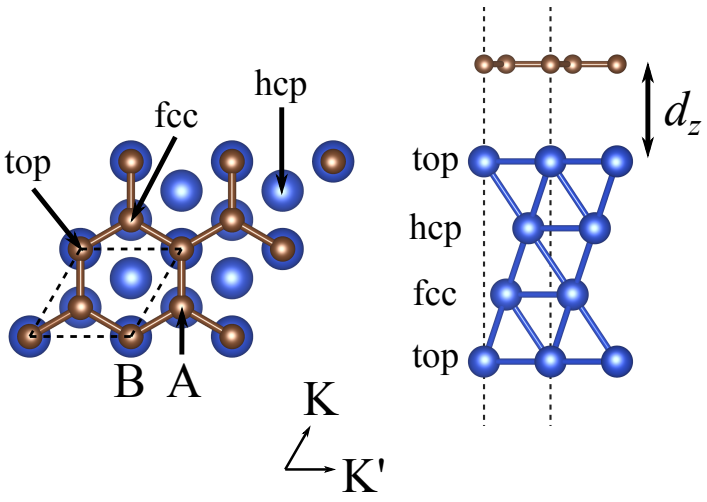

Figure 4.1: Structure: Top and side views of the unit cell, which is indicated as black dashed lines, repeated twice in each lateral direction. Blue (large) spheres indicate the copper atoms, brown (small) spheres the carbon atoms. The sublattice is depicted by labels A and B and the convention of K points is indicated. The copper layers are labeled by top, hcp and fcc, which also tag the adsorption positions.

direction including empirical van der Waals corrections [34] to determine the geometry with lowest energy. For the unrelaxed copper slab we start with strained copper such that its surface lattice constant $a_{\mathrm{Cu}}/\sqrt{2}$ is equal to the experimental graphene lattice constant of 2.46 Å yielding a bulk copper lattice constant of $a_{\mathrm{Cu}} = 3.48$ Å. This represents a compression of the copper slab by 3.8% with respect to the bulk value of 3.61 Å [118]. After letting the copper slab relax in z direction, the distance of copper atoms from plane to plane is 2.59 Å, corresponding to an *expansion* of 1.7% compared to bulk copper. This compensates to some extent for the compression in the xy plane.

Comparing the top-fcc configuration with the other commensurate configurations top-hcp and hcp-fcc we find slightly different graphene–Cu(111) distances d_z of 3.10 Å, 3.11 Å, and 3.12 Å, respectively. The distances are consistent with other calculations where values of 2.91 to 3.58 Å were found [97, 115–117]. The corrugation of the carbon atoms in z direction is less than 10^{-3} Å, expressing the weak nature of binding. The lowest energetic configuration is the top-fcc arrangement in agreement with Ref. [97], followed by the top-hcp, which is only 2.3 meV higher in energy per unit cell. The highest one in total energy with 12.3 meV compared to top-fcc is hcp-fcc, where the surface copper atom sits within the carbon ring. Therefore in the following we consider the top-fcc configuration as a case study.

4.4 Electronic structure and comparison with photoemission experiments

The orbital resolved electronic structure of graphene on Cu(111), for a copper–graphene distance of 3.10 Å, is shown in Fig. 4.2. An effective Hubbard U parameter [33] of $U = 1$ eV was set to act on the Cu $3d$ electrons. We want to predict the size of SOC induced by copper in the Dirac cone of graphene. Therefore it is crucial to describe the spectral overlap of graphene π states with the copper orbitals correctly. With standard generalized gradient approximation (GGA) functionals the strongly localized character of d states of metal atoms is sometimes poorly accounted for. In order to overcome this deficiency we fix the copper d levels such that their energy is in accordance with experiment. Although this is not an *ab initio* approach, we do not want to overestimate SOC parameters by having the d bands too close to the Dirac cone.

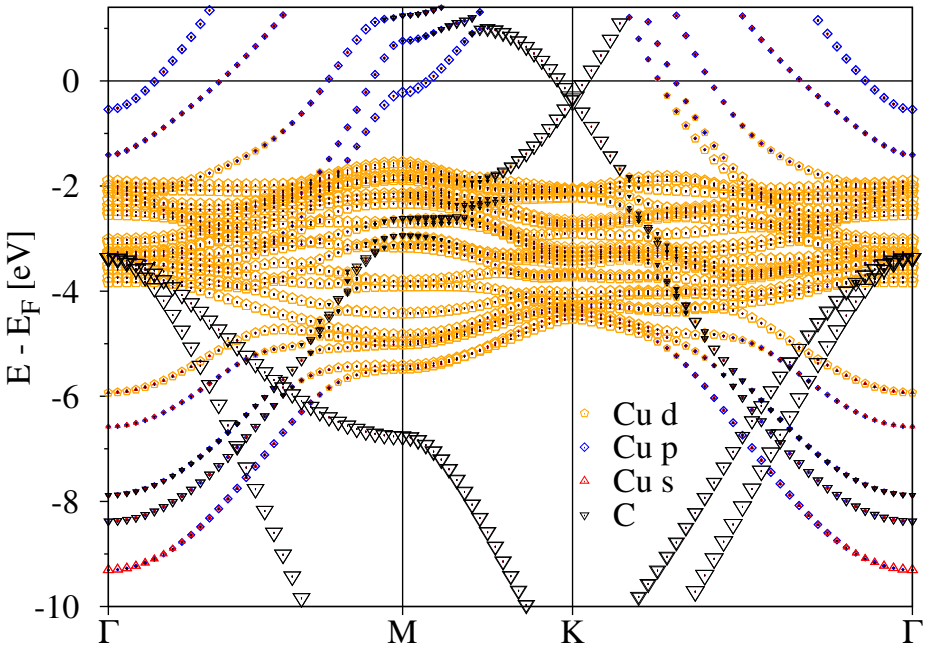

Figure 4.2: Calculated electronic structure of graphene/Cu(111) slab. The graphene distance from Cu(111) surface is 3.10 Å. The overlaying symbols indicate orbital resolved contributions to the eigenvalues. Orange pentagons show Cu d bands, red upward pointing triangles represent Cu s states, blue squares show Cu p states and black downward pointing triangles indicate graphene states. This band structure is remarkably similar to the one found by ARPES measurements [104].

In Tab. 4.1 several results of ARPES measurements are shown, for graphene either residing directly on the Cu(111) surface, or being attached to a Ni(111) surface with a layer of copper atoms intercalated. In experiments, copper d bands can be identified in the energy range from -2 to -5 eV with respect to the Fermi energy. The effect of the Hubbard U correction is a rigid shift of the filled copper d levels to lower energies, away

from the graphene π states, acting in our case as an on-site energy (see Sec. 2.2.2). We find for a mild Hubbard U correction of 1 eV to the copper d states, the onset of d states to be matched with experiments. Without Hubbard U, the d bands lie about 0.5 eV higher in energy. The copper d levels, which we obtain in our calculations are distributed in an energy range of -1.5 to -6 eV over the whole Brillouin zone, see Fig. 4.2. At K, the d bands have a sharp onset at -2 eV and a bandwidth of 2.5 eV, matching well with most of the experimental data presented in Tab. 4.1. The positions of d energy levels are also dependent on the compression of the copper slab. If the copper slab is not allowed to relax in the z-direction, the d levels lie closer to the Dirac cone by about 1 eV compared to the expanded slab.

Reference	System	E_{D} [meV]	d bands range [eV]	E_{gap} [meV]
[104]	Gr/Cu(111)	-371	-2 to -5	50
[105]	Gr/Cu(111)	-400	-2 to -4	< 200
[106]	Gr/Cu(111)	-350		100
[110]	Gr/Cu(111)	-300		250
[107]	Gr/Cu/Ni(111)	-400	-2 to -5	250
[108]	Gr/Cu/Ni(111)	-310		180
[109]	Gr/Cu/Ni(111)	-450	-1.5 to -4	150

Table 4.1: Experimental properties of the Gr/Cu(111) and Gr/Cu/Ni(111) intercalated surfaces found by ARPES measurements. The Dirac energy E_{D} is the average energy of the graphene-π states at K. The induced proximity gap within the π states at K is labeled by E_{gap}. E_{D} and the d band range are given with respect to the Fermi energy E_F.

From Fig. 4.2, it can be seen that the Dirac cone structure is preserved for energies higher than -2 eV. Below this energy region the graphene π states hybridize with the copper d states. This can be seen by the avoided crossings if one follows the π band towards the Γ point at -8.5 eV. On this way, at -6 eV the π states branch and strongly hybridize with a copper band consisting of p and s states. Those are states which are situated on the surfaces of the slab and whose degeneracy is broken due to the graphene lattice potential. The graphene σ states starting from -3.5 eV at the Γ point are mainly unaffected. The copper s and p states are present in the energy region between -9.5 eV and -6 eV as well as from -2 eV and upwards.

In accordance with other DFT calculations [97, 98], we find charge transfer from the Cu(111) surface to graphene. As a result, graphene gets n-doped. Although the work functions of $W = 4.5$ eV for graphene and about $W = 5.22$ eV for copper suggest the opposite behavior, the chemical interactions lead to a combined work function of $W = 4.4$ eV and to electron doping [98]. The doping strength can be quantified by the value of the Dirac energy E_{D}. We define the Dirac energy as the average value of the four graphene-π eigenvalues (including spin) at K with respect to the Fermi energy. The lower the value of E_D, the larger is the n doping.

We compared the effect of the relaxation of copper slabs in z-direction for the relaxed and nonrelaxed (bulk lattice constant of 3.48 Å) cases on the doping of graphene. For nonrelaxed (compressed) copper slabs the electron doping of graphene was significantly

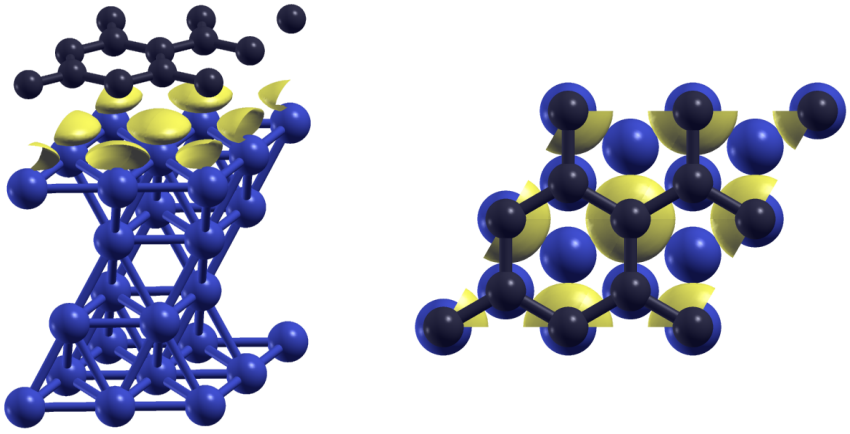

(a) side view (b) top view

Figure 4.3: Copper–graphene surface state. The state from the Γ point directly below the Fermi energy is situated between the copper surface and graphene below the B sublattice.

higher than for relaxed slabs due to the higher kinetic energy of electrons in nonrelaxed copper. For relaxed copper slabs we obtain $E_D = -330$ meV, which is comparable to experiment (see Tab. 4.1). It is therefore crucial to lower the kinetic energy of electrons in the artificially compressed copper slab by letting it relax in the z direction.

One prominent feature of the Cu(111) facet is its Shockley surface state [105]. Shockley states occur usually in metals when the potential sharply changes at the surface. These states, which are Bloch-like inside the bulk leak as an exponentially decaying tail into the vacuum. Shockley states are expected at the Γ point. In ARPES experiments, on the clean Cu(111) surface, the Shockley state is found at -0.4 eV and gets shifted towards a higher energy of -0.25 eV upon graphene synthesis [101, 105]. We find a surface state at the energy -0.54 eV, see the Γ point in the band structure Fig. 4.2. The probability density of this state is shown in Fig. 4.3. The main charge density is located in between the interface of graphene and copper and the state is localized below the B sublattice. Our theoretical values differ by about 0.3 eV compared to experiment, which could be due to the in-plane strained copper, or due to the small number of layers in the copper slab. In our calculations, for the copper slab without graphene, the surface state lies about 100 meV lower at an energy of -0.65 eV, which is in agreement with experiment that the Shockley state gets shifted towards higher energies, when graphene is adsorbed.

All in all we find good agreement of the orbital band structure with experiment [104]. The only shortcoming is the description of the graphene gap E_{gap} appearing in the Dirac cone, which is opening at the Dirac energy E_D. We find it to be about 20 meV (see Sec. 4.6), which is lower than the 50 to 250 meV stated in experiments (see also Tab. 4.1). This deviation is still unexplained and could be studied with more advanced methods like hybrid functionals or the *GW* method.

4.5 Graphene proximity model Hamiltonian

As we demonstrated above, DFT+U reasonably captures the electronic structure of graphene on the Cu(111) surface. Now, we use the DFT calculations to predict proximity induced effects of the copper surface on the SOC in graphene. For this purpose we study a low-energy Hamiltonian describing π states of graphene on Cu(111). Before presenting the low-energy model Hamiltonian, we discuss its underlying tight-binding description, which we will also make heavy use of in Chpt. 5.

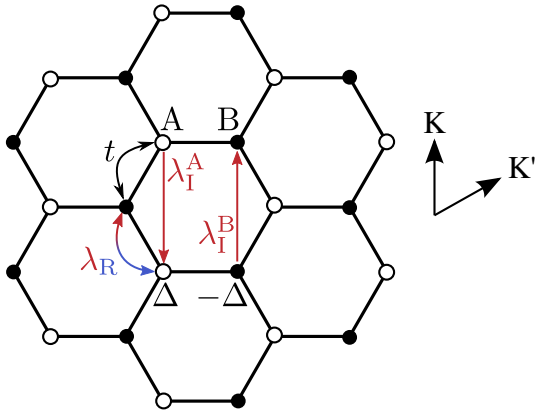

Figure 4.4: Visualization of the proximity SOC Hamiltonian, Eq. (4.1). Open circles denote sublattice A, filled circles sublattice B, whose on-site staggered potentials $\pm\Delta$ are shown. Hoppings are indicated by arrows. Spin-orbit coupling hoppings are color coded. Processes with one color conserve the spin in the case of next-nearest neighbor intrinsic SOC λ_{I} (here the spin-up case is shown) and the spin is flipped in the nearest-neighbor Rashba hopping λ_{R}. The convention of K points relative to the lattice is indicated.

The tight-binding Hamiltonian we use contains orbital and SOC parts and describes graphene whose symmetry group is lowered from D_{6h} (pure graphene) to C_{3v}. Such a Hamiltonian was introduced already in the context of hydrogenated graphene [61] in which the pseudospin symmetry gets broken explicitly by sublattice-selected hydrogenation. It was also found useful in graphene whose pseudospin is implicitly broken by placing it on spatially varying lattices such as transition metal dichalcogenides (TMDCs) [10]. In our case the pseudospin symmetry is broken explicitly as the two sublattices experience a different potential environment, because one carbon atom sits closer to a copper atom than the other, see Fig. 4.1.

This C_{3v}-symmetric real-space tight-binding Hamiltonian is given by [11, 13, 61]

$$\begin{aligned}\hat{\mathcal{H}} \;=\; & -\sum_{\langle i,j\rangle,s} t\,\hat{c}_{is}^{\dagger}\hat{c}_{js} + \sum_{i,s}\xi_i\,\Delta\,\hat{c}_{is}^{\dagger}\hat{c}_{is} \\ & + \frac{2i\lambda_{\mathrm{R}}}{3}\sum_{\langle i,j\rangle,s,s'}\left[(\hat{\mathbf{s}}\times\mathbf{d}_{ij})_z\right]_{ss'}\hat{c}_{is}^{\dagger}\hat{c}_{js'} \\ & + \frac{i}{3\sqrt{3}}\sum_{\langle\langle i,j\rangle\rangle,s,s'}\lambda_{\mathrm{I}}^{i}\,\nu_{ij}\left[\hat{\mathbf{s}}_z\right]_{ss'}\hat{c}_{is}^{\dagger}\hat{c}_{js'}\;. \end{aligned} \tag{4.1}$$

A visualization of the hopping terms is given in Fig. 4.4. Electrons in the graphene p_z orbitals are created and annihilated by operators $\hat{c}^\dagger$ and $\hat{c}$, respectively. Nearest-neighbor hopping t occurs between sites j and i, preserving spin s. The on-site staggered potential Δ has signs $\xi_i = 1$ and -1, for sublattice A and B, respectively. The staggered potential accounts for the different effective potentials the carbon atoms feel when placed on a substrate. Rashba SOC λ_R, which is a nearest-neighbor hopping, mixes states of opposite spins and sublattices. This is due to the fact that the z component of the cross product of the unit vector $\mathbf{d}_{ij}$, pointing from site j to i, and $\hat{\mathbf{s}}$, the vector of spin Pauli matrices, involves only s_x and s_y matrices. The last term is the sublattice-resolved intrinsic SOC, which is a next-nearest neighbor hopping. It couples same spins and depends on clockwise ($\nu_{ij} = -1$) or counterclockwise ($\nu_{ij} = 1$) paths along a hexagonal carbon ring from site j to i. This term distinguishes different sublattices with the parameter λ_I^i, where i stands for A or B.

By Fourier-transforming Hamiltonian (4.1) and linearizing around the K/K′ points, one arrives at the low-energy Hamiltonian, which is a sum of the following terms [13]

$$\hat{\mathcal{H}}_\mathrm{k} = \hbar v_\mathrm{F}(\kappa k_x \sigma_x - k_y \sigma_y) s_0 \ , \tag{4.2}$$

$$\hat{\mathcal{H}}_\Delta = \Delta\, \sigma_z s_0 \ , \tag{4.3}$$

$$\hat{\mathcal{H}}_\mathrm{R} = \lambda_\mathrm{R}(-\kappa \sigma_x s_y - \sigma_y s_x) \ , \tag{4.4}$$

$$\hat{\mathcal{H}}_\mathrm{I} = \frac{1}{2}\left[\lambda_\mathrm{I}^\mathrm{A}(\sigma_z + \sigma_0) + \lambda_\mathrm{I}^\mathrm{B}(\sigma_z - \sigma_0)\right] \kappa s_z \ . \tag{4.5}$$

The first term is recognized as the familiar graphene zero-mass Dirac Hamiltonian, where $v_\mathrm{F} = \sqrt{3}at/2\hbar$ is the Fermi velocity and $\kappa = 1(-1)$ labels the valley degree of freedom at K(K′). The Cartesian components of the electron wave vector, k_x and k_y, are measured from K(K′). The pseudospin Pauli matrices σ_x and σ_y act on the spinor space formed by the triangular sublattices of graphene. The real spin degree of freedom s is described by Pauli matrices, and the subscript "0" denotes the 2×2 identity matrix also in the case of σ. We imply a Kronecker product for combinations of matrices σ and s. The second term $\hat{\mathcal{H}}_\Delta$ introduces a mass gap in the spectrum by the staggered potential, which breaks the chiral symmetry of graphene [119]. Without other terms this opens up a gap of $2|\Delta|$. This gap is still present even when SOC is absent. As a consequence of adsorption to a substrate, graphene loses its horizontal reflection symmetry. This leads to the fact that s_z is not a good quantum number anymore, i.e., processes exist that couple both spins. This is realized in the graphene Rashba Hamiltonian $\hat{\mathcal{H}}_\mathrm{R}$ (which is similar to the Bychkov–Rashba Hamiltonian $\hat{\mathcal{H}}_\mathrm{BR} \propto (s_x k_y - s_y k_x)$ arising due to structural inversion asymmetry [59, 120]). Compared to intrinsic SOC in pristine graphene, see Sec. 3.4, "intrinsic" SOC is now allowed to be sublattice-resolved. As sublattice-resolved intrinsic SOC (later also referred to as intrinsic SOC) is a next-nearest neighbor hopping, it acts solely on a given sublattice. If $\lambda_\mathrm{I}^\mathrm{A} \neq \lambda_\mathrm{I}^\mathrm{B}$, the spin degeneracy gets lifted, reflecting the loss of space inversion symmetry. The intrinsic SOC can also be interpreted as local spin-dependent magnetic fields [119], however, preserving time-reversal symmetry.

As a remark, throughout this thesis we follow the convention as defined in Ref. [13]. In the original publication [121] as well as in Ref. [11], where parameters for graphene on TMDCs were extracted, a different convention was chosen. To translate the pa-

rameters from these publications (indicated as overlined symbols) to the convention used here, one needs to transform

$$\kappa = -\bar{\kappa} \ , \tag{4.6}$$
$$t = -\bar{t} \ , \tag{4.7}$$
$$\lambda_{\mathrm{I}}^{\mathrm{A}} = -\bar{\lambda}_{\mathrm{I}}^{\mathrm{A}} \ , \tag{4.8}$$
$$\lambda_{\mathrm{I}}^{\mathrm{B}} = -\bar{\lambda}_{\mathrm{I}}^{\mathrm{B}} \ , \tag{4.9}$$

and otherwise keep the same parameters.

The four eigenvalues of the model Hamiltonian (4.2)–(4.5) at the K point ($\kappa = 1$, $k_x,\ k_y = 0$) read

$$\varepsilon_4 = \frac{1}{2}(\lambda_{\mathrm{I}}^{\mathrm{A}} + \lambda_{\mathrm{I}}^{\mathrm{B}}) + \sqrt{[\Delta - \frac{1}{2}(\lambda_{\mathrm{I}}^{\mathrm{A}} - \lambda_{\mathrm{I}}^{\mathrm{B}})]^2 + 4\lambda_{\mathrm{R}}^2} \ , \tag{4.10}$$
$$\varepsilon_3 = \Delta - \lambda_{\mathrm{I}}^{\mathrm{A}} \ , \tag{4.11}$$
$$\varepsilon_2 = -\Delta - \lambda_{\mathrm{I}}^{\mathrm{B}} \ , \tag{4.12}$$
$$\varepsilon_1 = \frac{1}{2}(\lambda_{\mathrm{I}}^{\mathrm{A}} + \lambda_{\mathrm{I}}^{\mathrm{B}}) - \sqrt{[\Delta - \frac{1}{2}(\lambda_{\mathrm{I}}^{\mathrm{A}} - \lambda_{\mathrm{I}}^{\mathrm{B}})]^2 + 4\lambda_{\mathrm{R}}^2} \ . \tag{4.13}$$

We ordered the eigenvalues by decreasing energies (ε_4 highest, ε_1 lowest), where we assumed $\Delta \gg \lambda_{\mathrm{R}} \gg \lambda_{\mathrm{I}}^{\mathrm{A}}, \lambda_{\mathrm{I}}^{\mathrm{B}}$. In this situation the eigenstates ε_2 and ε_3 always have spin-z expectation values of $\langle s_z/2\rangle_2 = 1/2$ and $\langle s_z/2\rangle_3 = -1/2$, and pseudospin expectation values of $\langle \sigma_z/2\rangle_2 = -1/2$ and $\langle \sigma_z/2\rangle_3 = 1/2$, i.e., they are localized on sublattice B and A, respectively. The eigenstates ε_1 and ε_4 in general are mixtures of sublattices and spin directions, but have almost $\langle s_z/2\rangle_1 \simeq -1/2$, $\langle \sigma_z/2\rangle_1 \simeq -1/2$ and $\langle s_z/2\rangle_4 \simeq 1/2$, $\langle \sigma_z/2\rangle_4 \simeq 1/2$ under the assumption $\Delta \gg \lambda_{\mathrm{R}} \gg \lambda_{\mathrm{I}}^{\mathrm{A}}, \lambda_{\mathrm{I}}^{\mathrm{B}}$.

In the model Hamiltonian there are four unknown parameters (without v_{F}). The equations for the eigenvalues provide three energy differences. To construct a set of independent equations we further take into account the spin-z expectation value for the first eigenstate denoted by $s_1^z = \langle s_z/2\rangle_1$, which we also evaluate from DFT. The model parameters thus can be expressed as follows

$$\Delta = \frac{1}{4}\left[-\varepsilon_2 + \varepsilon_3 + 2s_1^z(\varepsilon_1 - \varepsilon_4)\right] \ , \tag{4.14}$$
$$\lambda_{\mathrm{I}}^{\mathrm{A}} = \frac{1}{4}\left[\varepsilon_1 - 2\varepsilon_3 + \varepsilon_4 + 2s_1^z(\varepsilon_1 - \varepsilon_4)\right] \ , \tag{4.15}$$
$$\lambda_{\mathrm{I}}^{\mathrm{B}} = \frac{1}{4}\left[\varepsilon_1 - 2\varepsilon_2 + \varepsilon_4 - 2s_1^z(\varepsilon_1 - \varepsilon_4)\right] \ , \tag{4.16}$$
$$\lambda_{\mathrm{R}} = \frac{1}{4}\left(\varepsilon_1 - \varepsilon_4\right)\sqrt{1 - 4(s_1^z)^2} \ . \tag{4.17}$$

We note that special care has to be taken when associating the order of the DFT eigenvalues with respect to the model Hamiltonian eigenvalues. For every state we checked that the sublattice localization and spin-z expectation values of model and DFT calculations agree.

4.6 Parameter extraction and validation of the model

In Fig. 4.5 we compare low-energy graphene bands calculated from DFT with the model Hamiltonian. Model Hamiltonian parameters are listed in Tab. 4.2. The proximity effects, both, the orbital and SOC ones are significant. The staggered potential Δ dominates the energy scale. The value of $E_{\text{gap}} = \varepsilon_3 - \varepsilon_2 = 17.7$ meV$\approx 2|\Delta|$, is in agreement with the extracted staggered potential Δ of 8.95 meV via Eq. (4.14). The Rashba SOC parameter of 1.5 meV indicates a very strong effect of the space inversion asymmetry, which would correspond to an applied transverse electric field of 310 V/nm for bare graphene [59]. The intrinsic SOC parameters have opposite signs and especially $\lambda_{\text{I}}^{\text{A}}$ is significantly enhanced in comparison to the tens of μeV in bare graphene [59].

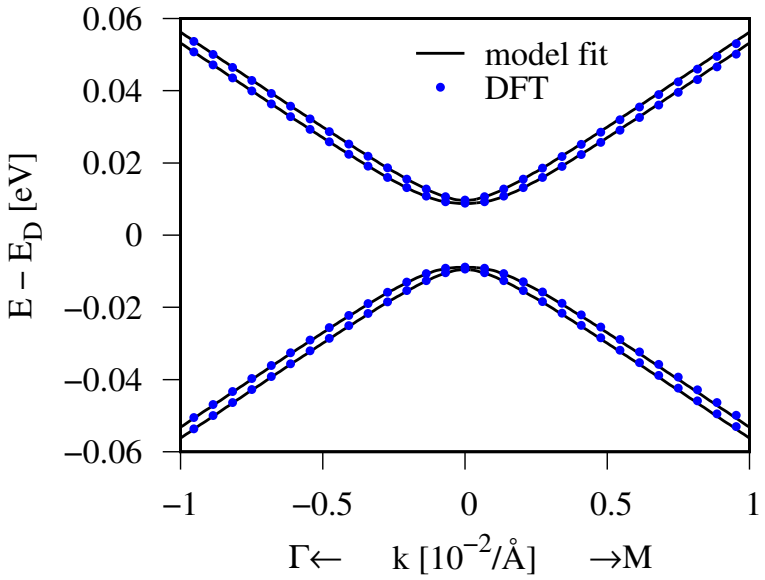

Figure 4.5: Comparison of DFT calculations with the model calculations for a graphene–copper distance of 3.10 Å around the K point. The energy is measured with respect to the Dirac energy E_{D}. The plot is centered at K ($k = 0$) and its left part corresponds to the k points pointing towards Γ and the right part towards the M point.

The Fermi velocity, which is another independent fit parameter, determines the slope away from the K point. We adjusted it to $v_{\text{F}} = 0.825 \cdot 10^6$ m/s, which is equivalent to a nearest neighbor hopping of $t = 2.55$ eV, such that a good fit along $\Gamma - \text{K}$ is achieved, see Fig. 4.5. We see that the band structure is rather isotropic in this range of k points and the model description agrees very well with the DFT data. We observe a good agreement up to energies ± 0.1 eV away from the Dirac energy. Only at more distant k points along the direction KM, we can observe a deviation of the linear model from the DFT band structure. This is a consequence of so-called trigonal warping [4]. Trigonal warping is encoded in the structure functions of graphene [13], the dispersion becomes direction-dependent via higher-order k terms our linearized model doesn't account for.

Cu layers	d_z [Å]	Δ [meV]	$\lambda_{\mathrm{I}}^{\mathrm{A}}$ [meV]	$\lambda_{\mathrm{I}}^{\mathrm{B}}$ [meV]	λ_{R} [meV]
3	3.1	8.85	0.17	−0.04	1.56
4	**3.1**	**8.95**	**0.17**	**−0.04**	**1.53**
4	2.5	2.71	0.88	−0.58	9.53
4	2.2	−8.24	2.57	−0.96	16.6

Table 4.2: Low-energy Hamiltonian parameters for different case studies. We indicate the number of Cu layers used in the copper slab; in the case of three layers the bottommost layer is removed. Different cases of graphene–Cu(111) distances d_z are listed. Numbers in boldface represent our main result.

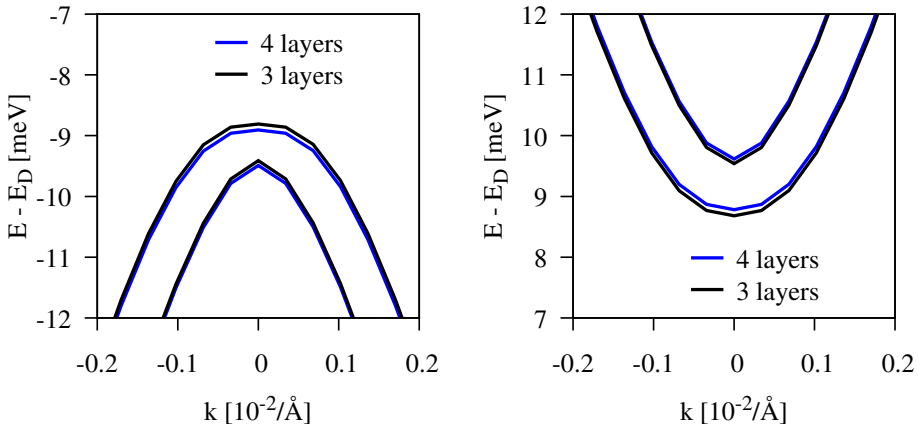

(a) valence bands

(b) conduction bands

Figure 4.6: Influence of the number of copper layers on the orbital and SOC proximity effects. The calculations correspond to band structures close to the K point comparing the case of three and four layers of copper. Energies are plotted with respect to the Dirac energy E_{D} (averaged energies of valence and conduction bands).

To further ensure that our results are independent of the number of copper layers, we provide a comparison between three layers and four layers. Zooms into the valence and conduction band extrema, shown in Fig. 4.6, reveal only a minor change in eigenvalues. The extracted model parameters in the three-layer case are listed in Tab. 4.2. We find the intrinsic SOC parameters to be converged. Only the Rashba and staggered potential values change by less than 2%, which indicates that four layers of copper represent a good approximation to the Cu(111) surface for our means.

Due to breaking of space inversion symmetry, bands become nondegenerate. We compare the band spin splittings obtained by DFT and the model calculations, for the valence and conduction bands, see Fig. 4.7. By construction, the splittings at K are recovered exactly. The model reproduces very well the narrowing of the band splittings for k points up to $\pm 1 \cdot 10^{-2}$/Å away from the K point, even though only information from the K point enters. As the model does not include SOC terms dependent on k, both the valence and conduction band splittings from the model

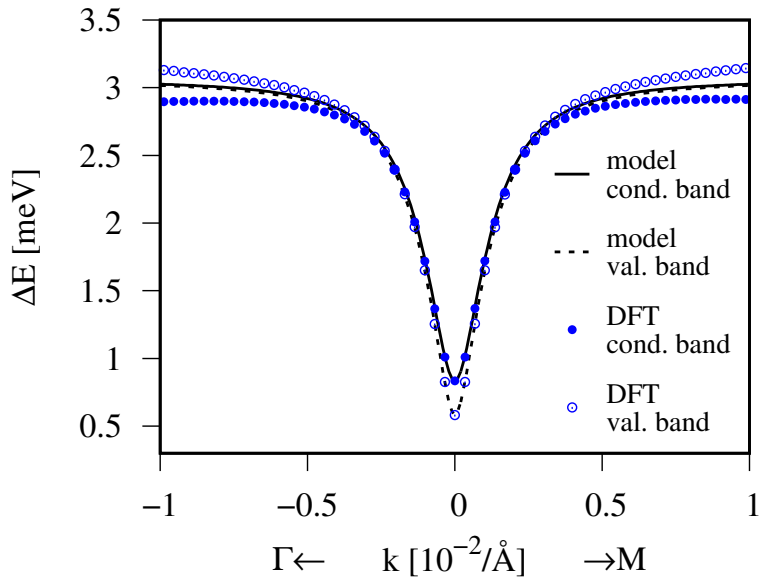

Figure 4.7: Calculated spin splittings of the valence and conduction bands. The DFT data is shown by symbols while the lines correspond to the model description. The distance between graphene and copper is 3.10 Å.

calculations saturate at a common value for larger k, at twice the value of Rashba SOC. To include k dependent contributions one needs to consider terms such as pseudospin inversion asymmetry (PIA) SOC [10, 61, 67], which can capture the k dependence of the splittings. In the DFT calculations we observe that the splittings for valence (conduction) bands increase (decrease) with larger distances from K as the interaction with copper d levels increases (decreases) and the induced spin-orbit effects are stronger (weaker) in a similar fashion as in Chpt. 3.

4.7 Graphene–copper distance study of proximity parameters

The local density approximation (LDA) as well as GGA cannot fully account for dispersive forces due to their (semi-)local nature. Different methods dealing with van der Waals interactions yield inconsistent results [97, 115–117] when trying to treat graphene on metal surfaces, with possible distances between $d_z = 2.91 - 3.58$ Å. Therefore, we conduct calculations of electronic properties for different graphene–Cu(111) distances. We use the Hubbard correction [33] with $U = 1$ eV for Cu d electrons. The relative coordinates of the atoms within the copper slab and within graphene are fixed and the graphene–copper distance d_z is varied. We apply the same analysis as in Sec. 4.5 for each distance configuration d_z and extract the total energy of the structure, the Dirac energy shift E_D, the staggered potential Δ, the Rashba and intrinsic SOC parameters as well as spin-z expectation values of the graphene states at the K point.

In Fig. 4.8(a) we show the total energy as a function of the graphene distance d_z from the Cu(111) surface. The curve is shifted with respect to the minimal total energy at

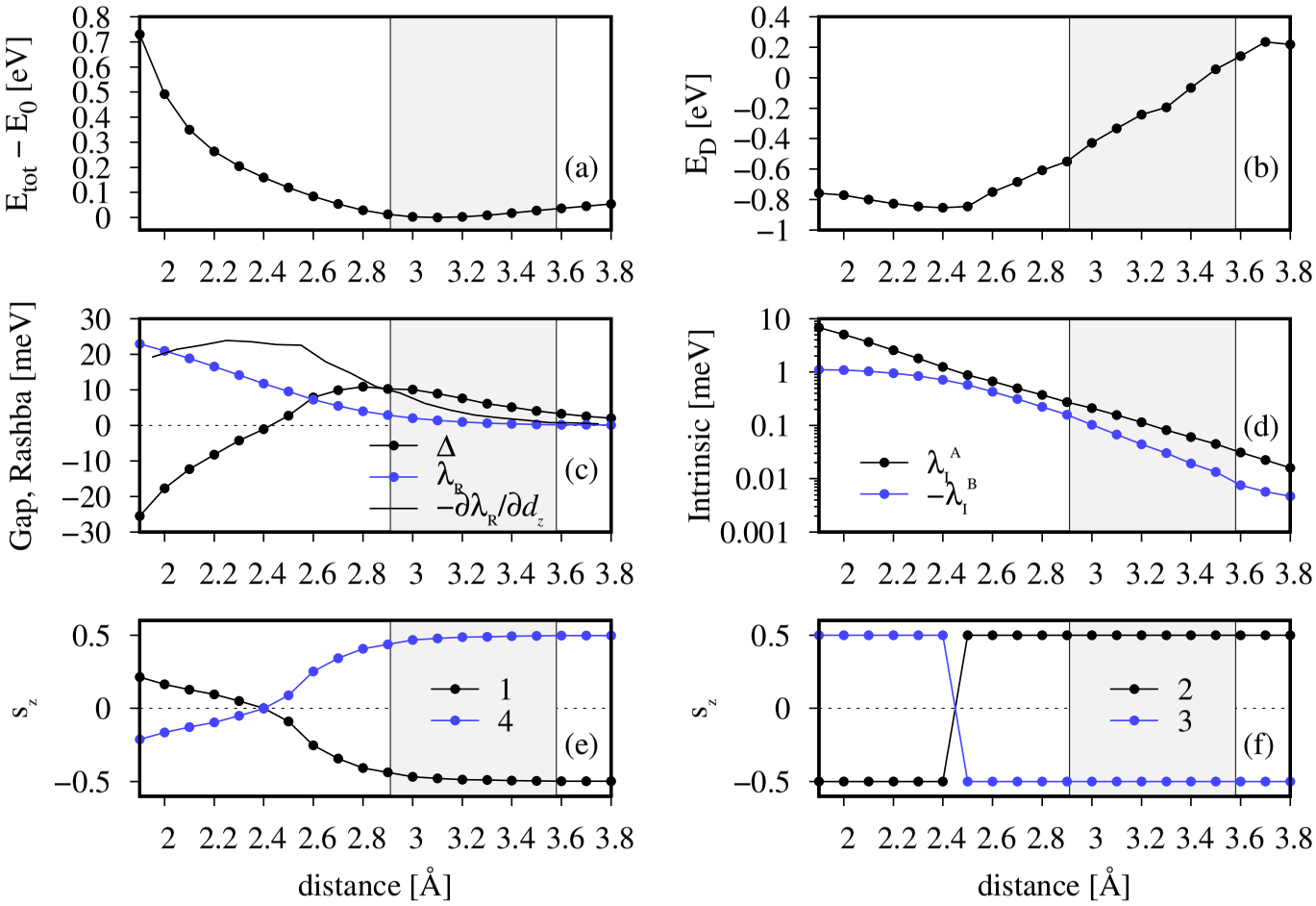

Figure 4.8: Calculations of low-energy properties of graphene on Cu(111) surface as a function of distance, with a Hubbard U of 1 eV. (a) Total energy with respect to the minimal total energy at 3.10 Å. (b) Dirac energy shift E_D with respect to Fermi level. (c) proximity induced potential Δ and Rashba SOC parameter λ_R, as well as the derivative of λ_R. (d) intrinsic SOC parameters $\lambda_\mathrm{I}^\mathrm{A}$ and $\lambda_\mathrm{I}^\mathrm{B}$. (e) spin s_z expectation values for the ε_1 and ε_4 graphene eigenvalues at the K point and (f) for the ε_2 and ε_3 eigenvalues. The shaded region indicates predicted distances from other theoretical references [115–117].

the distance of 3.10 Å. The energy dependence has a rather shallow minimum where the energy increases by just 54 meV when compared to graphene at a distance of 3.8 Å. This indicates weak van der Waals bonding with the substrate.

Figure 4.8(b) visualizes the shift of the Dirac energy E_D with respect to the Fermi level. We see that graphene stays n-doped for distances smaller than 3.5 Å. When surfaces of different materials are brought together, charge transfer is governed by their differences in work functions. Graphene and Cu(111) have work functions of 4.5 and 5.22 eV, respectively [98]. Therefore naively one would expect the electrons to be transferred from graphene to copper. This is true for larger separations ($d_z >$ 3.5 Å), as we confirm here, however there is orbital hybridization for smaller distances, which effectively lower the work function of the combined system to about 4.4 eV [98], which renders graphene electron doped in the equilibrium position. When graphene is approached to copper from 3.5 to 2.5 Å there is a linear behavior of doping towards more n-doping. For distances smaller than 2.5 Å the level of doping stays roughly constant with a tendency towards less n-doping. We attribute the overall behavior to a depopulation of the copper surface state of Sec. 4.4. The surface state gets shifted towards higher energies when graphene is brought closer and the depopulated electron density is transferred to graphene. At 2.5 Å the surface state crosses the Fermi energy and is unoccupied (we cross checked this with band structure calculations).

Figure 4.8(c) shows the values for the staggered potential Δ and the Rashba spin-orbit parameter λ_R. The Rashba parameter is increasing steadily with decreasing distance. We also plot the derivative of the Rashba parameter with respect to the distance $-\partial\lambda_\mathrm{R}/\partial d_z$. One sees that E_D and the change in the Rashba parameter are correlated. Both curves change their trend at 2.5 Å. We can see that the origin of the Rashba SOC is due to charge doping (determined by the Fermi energy shift E_D), leading to a built-in electric field, and due to the positioning of the graphene sheet in the electrostatic potential of the Cu(111) surface. At the distance of 2.5 Å the charge doping stops, and therefore the Rashba SOC increases at a lower pace. It remains increasing though, as the graphene sheet resides in a potential which becomes steeper as it gets closer to the nuclei of copper. Values of Rashba SOC can become very large in this system, of about tens of meV, which is an order of magnitude larger than graphene on TMDCs [11]. It is surprising that the staggered potential Δ, which first increases from larger to smaller distances, decreases, becomes zero at about 2.4 Å and then changes its sign. This means an inversion of the effective potential an electron feels in the sublattices and might be caused by hybridization effects.

To reach the regime of a negative staggered potential, the distance between graphene and the copper surface needs to be reduced. We estimate the pressure p one would have to exert on graphene as

$$p = \frac{\Delta E}{\Delta d_z \cdot A} = \frac{200\ \mathrm{meV}}{(3.10 - 2.40)\ \text{Å} \cdot (2.46\ \text{Å})^2 \cdot \sin 60^\circ} \tag{4.18}$$

$$= 8.7\ \mathrm{GPa}, \tag{4.19}$$

where ΔE is the total energy difference between the state at $d_z = 3.10$ Å and the state at $d_z = 2.40$ Å. Δd_z is their difference in distance and A is the area of the graphene unit cell. The bulk modulus of copper for comparison is 143 GPa [122].

The amplitudes of the intrinsic SOC parameters $\lambda_{\mathrm{I}}^{\mathrm{A}}$ and $\lambda_{\mathrm{I}}^{\mathrm{B}}$ strongly increase as graphene is pushed towards the Cu(111) surface, see Fig. 4.8(d). For large distances both parameters tend to values comparable in size as in pure graphene, on the order of tens of μeV. For smaller distances the sublattice asymmetry transfers to the parameters and $\lambda_{\mathrm{I}}^{\mathrm{A}}$ is much stronger affected due to the specific graphene sublattice positioning on Cu(111). $\lambda_{\mathrm{I}}^{\mathrm{A}}$ reaches values up to 7 meV, whereas $\lambda_{\mathrm{I}}^{\mathrm{B}}$ in magnitude stays smaller than 1 meV for all tested distances and tends to saturate at 1 meV when reaching a small distance of 1.9 Å. In this configuration, $\lambda_{\mathrm{I}}^{\mathrm{A}}$ stays positive and $\lambda_{\mathrm{I}}^{\mathrm{B}}$ negative. Opposite-sign induced intrinsic SOC parameters are also obtained in the case of adsorption of graphene on TMDCs [11]. A more qualitative model explanation for the intrinsic SOCs is given in the next section.

4.7.1 Geometry dependence of intrinsic spin-orbit coupling

What is the origin of the intrinsic SOC and can one explain the sign and relative magnitudes of $\lambda_{\mathrm{I}}^{\mathrm{A}}$ and $\lambda_{\mathrm{I}}^{\mathrm{B}}$? To get more insight, we carried out the distance-dependent study also for the other adsorption configurations top-hcp and hcp-fcc, see Fig. 4.1. The extracted parameters are shown in Fig. 4.9. In all adsorption geometries, the magnitudes of the parameters behave in a similar manner, their magnitude increases monotonically when graphene is brought closer to the Cu(111) surface. However, pronounced differences in signs and magnitudes occur. In the case of top-hcp, $\lambda_{\mathrm{I}}^{\mathrm{A}}$ has comparable behavior as in the top-fcc case but $\lambda_{\mathrm{I}}^{\mathrm{B}}$ parameter is reduced in magnitude. In the case of hcp-fcc, both parameters are comparable in magnitude to the $\lambda_{\mathrm{I}}^{\mathrm{A}}$ parameter of the top-fcc case and total induced SOC is strongest. Concerning the parameter signs, we find that in the top-hcp case both parameters are positive and in the hcp-fcc case both are negative.

In order to explain these findings, it is useful to visualize the three adsorption geometries' unit cells and hexagonal graphene carbon rings in Fig. 4.10. In Fig. 4.10(d) we see that an electron hopping within the A sublattice passes close-by a top atom, in contrast to within the B sublattice, where neighboring copper atoms are lying in a deeper layer. In all adsorption cases, when a top atom is close-by, intrinsic SOC is strongest. This can be explained by a virtual hopping process, where the electron first visits a copper orbital, picks up atomic SOC and then leaves to the target site. The process is similar to how intrinsic SOC is generated in bare graphene, where the intermediate orbital is a d orbital on the nearest neighbor carbon atom in the hopping path [123]. The strength of this process depends on the overlaps of the p_z orbital with the copper orbital, which decreases exponentially with distance. Therefore the effect of the top atom is strongest. Alternatively, this process can be interpreted in terms of the microscopic SOC Hamiltonian [see Eq. (2.58)],

$$\hat{H}_{\mathrm{so}} = \frac{\hbar}{4m^2c^2}\mathbf{s}\cdot(\nabla V(\mathbf{r})\times\mathbf{p}) \ , \tag{4.20}$$

which is an interplay between the effective crystal field gradient $\nabla V(\mathbf{r})$ and an electron's momentum $\mathbf{p}$ in form of a vector product and its projection onto the electron's spin $\mathbf{s}$. Taking the top-fcc case as an example, for a spin-up electron hopping (as-

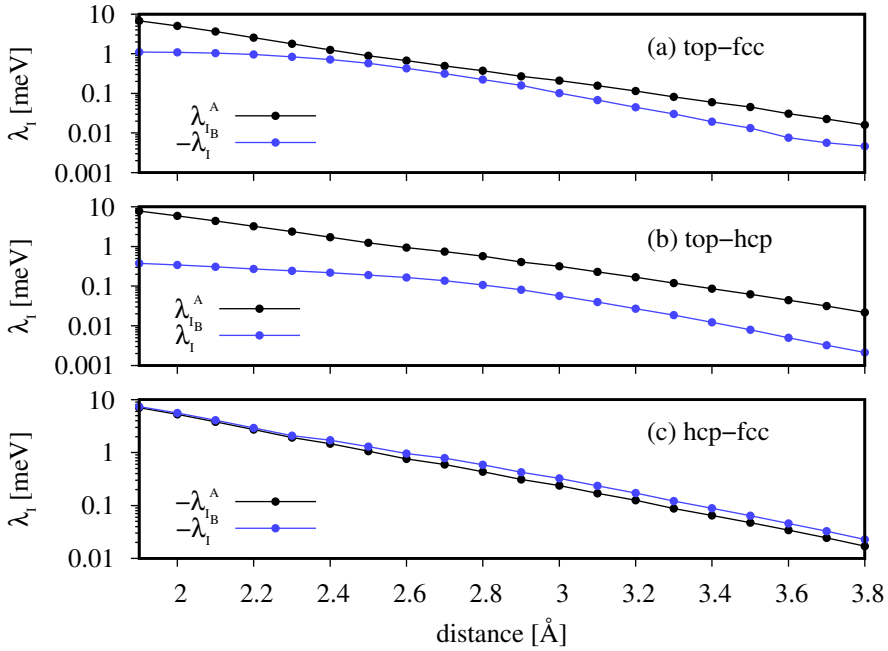

Figure 4.9: Extracted sublattice-resolved intrinsic SOC parameters of different adsorption configurations versus the graphene–copper distance. The intrinsic SOCs are plotted in logarithmic scale. Multiplication by -1 is indicated in the legends of the graphs.

sociated with momentum $\mathbf{p}$) in the B sublattice, $\lambda_{\mathrm{I}}^{\mathrm{B}}$ according to Hamiltonian (4.1) is defined for an anticlockwise path as indicated in Fig. 4.10(d). Due to symmetry breaking there is an in-plane component of the crystal field gradient perpendicularly to the hopping path, which can be seen from Fig. 4.10(g). We model copper atoms as partially unscreened ion cores due to charge transfer from copper to graphene. The potential gradient at the height of graphene then has a component from left to right, as the hcp copper atom is closer than the fcc atom. The top atom here is irrelevant for the crystal field gradient, as it does not break the symmetry. In general, we assume an in-plane crystal field gradient pointing from the lower copper atom towards the higher one (compare blue arrows in Fig. 4.10(d)–(f)). Consequently, the cross product of crystal field gradient and momentum points into the plane in the case of the B sublattice in Fig. 4.10(d). Projected on spin up, we get a negative value of $\lambda_{\mathrm{I}}^{\mathrm{B}}$. In the A sublattice, the crystal field gradient also points from left to right, but the hopping direction is reversed (looking at anticlockwise hopping). This also reverses the vector product, such that it points out of plane resulting in a positive $\lambda_{\mathrm{I}}^{\mathrm{A}}$.

This simple phenomenological picture can be applied also to the top-hcp case, which is very similar to top-fcc, with a sign change for $\lambda_{\mathrm{I}}^{\mathrm{B}}$ due to the opposite crystal field gradient. In the hcp-fcc case, sublattice symmetry is only slightly broken, with the top copper atom sitting in the middle of the hexagonal ring. In this situation both intrinsic hoppings occur close to the top atom and the proximity SOC effect is largest. The latter case is especially interesting as it generates the type of SOC ($\lambda_{\mathrm{I}}^{\mathrm{A}} = \lambda_{\mathrm{I}}^{\mathrm{B}}$) essential for the quantum spin Hall effect in graphene [12]. The induction of same-sign intrinsic

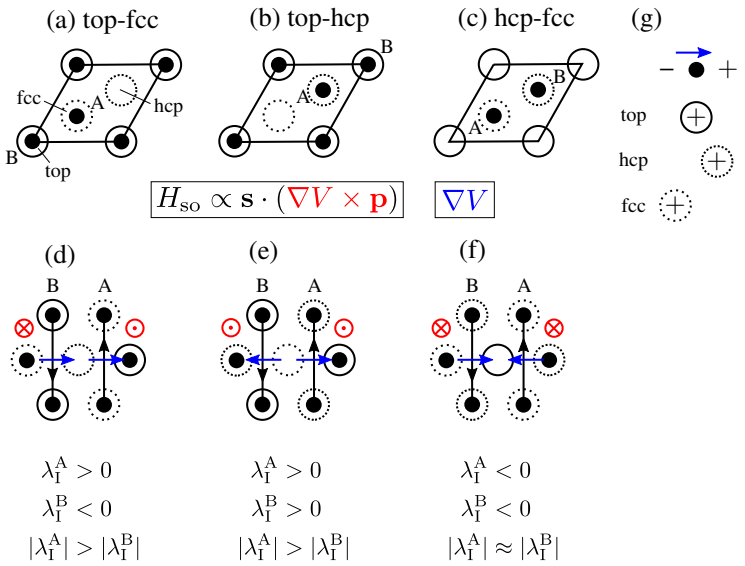

Figure 4.10: Visualization of different unit cells for the indicated adsorption geometries (a)–(c) and hexagonal carbon rings of graphene (d)–(f) with the relative positions of the copper atoms in the different layers. Each column represents one adsorption configuration. (g) Sketch of the in-plane component of the crystal field gradient, perpendicular to a hopping path. Copper atoms are indicated by open (dashed) circles and full dots denote the graphene lattice. Next-nearest neighbor hoppings with their directions are indicated by black arrows and crystal field gradients in the middle of the hopping paths are shown by blue arrows. The cross product of crystal field gradient and momentum is depicted by red symbols. We also show relative signs and magnitudes of the extracted λ_{I} parameters in the lower row, corresponding to Fig. 4.9.

SOC is also consistent with hollow adatom adsorption, where the quantum spin Hall effect was theoretically demonstrated [72, 74].

In experiments, due to the lattice mismatch of graphene and the Cu(111) surface, the adsorption geometry will not be fixed, but rather undergo a smooth transition between top-fcc, top-hcp, and hcp-fcc due to the formation of moiré patterns. It is likely that the SOC has to be averaged over the different regions. The effect of lattice mismatch and possibly a noncommensurate orientation of the lattices on the effective proximity induced SOC is still an open question.

4.7.2 Staggered potential sign change

Getting back to the top-fcc adsorption geometry in Sec. 4.7, we found that by pushing graphene towards the substrate, the staggered potential can change its sign. The similar configuration top-hcp (see Fig. 4.10) exhibits the same kind of sign change and spin and pseudospin flip as in the top-fcc case. For the energetically higher configuration hcp-fcc, the transition is absent at all studied distances from 1.9 to 3.8 Å.

To discuss the accompanied consequences of the sign change in the top-fcc system, we look at the spin-z expectation values of the graphene states in Fig. 4.8(e) and (f), where 1 labels the lowest energy and 4 the highest energy state. The outermost

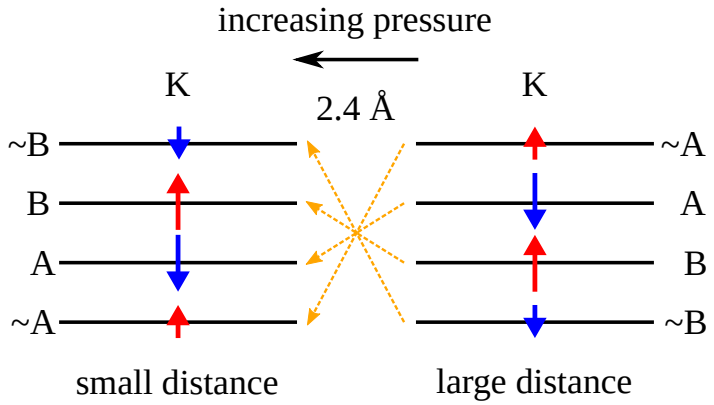

Figure 4.11: Scheme visualizing the transition of spin states at K with vertical pressure. Black solid lines indicate the energy levels, A and B stands for the sublattice. Arrows pointing upwards (downwards) represent spins pointing along z ($-z$), shorter arrows indicate spin mixture and their projection to the z direction.

expectation values of states 1 and 4 represent spin states of mixed spin. Values of spin 1/2 are only reached, when graphene is well separated from copper. Then, s_z is a good quantum number due to the absence of Rashba coupling. The spin expectation values of states 2 and 3 are quantized in the z direction. When the staggered potential vanishes, at 2.4 Å, we observe the signs of all spin expectation values to flip as exemplified in Fig. 4.11. When Δ changes sign, additionally to spin-reversal the sublattice is reversed. We checked this explicitly by plotting the Kohn–Sham state density, where we find indeed a change of sublattice population as indicated in Fig. 4.11. The pseudospin reversal is understandable, as a sign change in Δ switches the energetic roles of sublattices [see Eq. (4.3)]. In the absence of Rashba SOC, this would give just a pairwise exchange of the lowest two states with the highest two states (four permutations), preserving the spin ordering. Rashba SOC, however, is the dominant energy scale in this regime, and leads to a complete flip of all spins as indicated in Fig. 4.11 (six permutations). The lowest two and highest two states are exchanged, but in addition each pair of bands is twisted.

The behavior under sign change of Δ is further illustrated in Fig. 4.12, where we show the bands structures obtained from DFT calculations around K for distances of 2.2 and 2.5 Å, with the corresponding spin-z expectation values. The plot is consistent with Fig. 4.8(e) and (f). For 2.5 Å the band structure resembles the one in Fig. 4.5 and has spin up-down-up-down sequence, where the inner eigenstates have pure $s_z = \pm 1/2$ components. The spin-z character within the bands stays the same.

The band structure for 2.2 Å is qualitatively different. At the K point the inner eigenstates again have pure $s_z = \mp 1/2$ spin, but all signs are reversed with respect to the case at 2.5 Å. Furthermore, the spin-z character is not preserved within the bands. Our model is able to reproduce the spin-z behavior of Fig. 4.12 (not shown

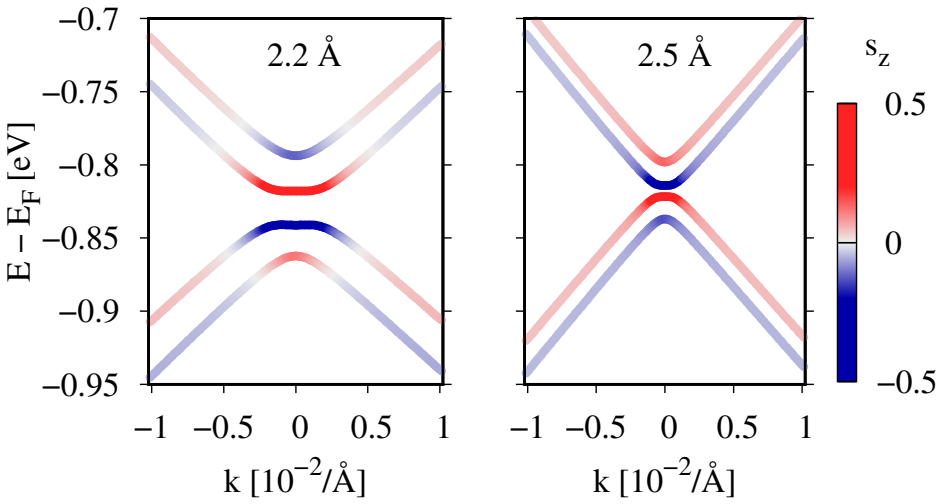

Figure 4.12: Band structure topologies of graphene on Cu(111) for 2.2 Å and 2.5 Å distances of graphene from the Cu(111) surface. The spin s_z expectation values for the states are encoded by the color scale, where red color denotes spin-z expectation value of $1/2$ and blue color denotes a spin-z expectation value of $-1/2$. The two band structures are qualitatively different.

here). The structure resembles a band inversion for the inner bands with a significant spin mixing in outermost bands.

A band inversion could have impact on the topology of the system, a transition to a quantum spin Hall phase might happen. However, in this system there are metallic states present due to copper, which prevent a classification in terms of trivial and topological insulating phases. Even if no metallic states would be present, neither system is a topological insulator, as in both regimes either Δ or λ_R is larger than λ_I^A or λ_I^B, which destroys a possible quantum spin Hall state induced by λ_I [124]. The two different regimes could however give rise to zero-line modes [125] when one goes spatially from a system with positive Δ to another one with negative Δ [126–128].

4.8 Summary and conclusions

In this study, we show that although there is a lattice mismatch of 3.8% of the Cu(111) and graphene surfaces, a commensurate stacking of minimal graphene and Cu(111) unit cells gives a good agreement between electronic structure calculations and ARPES measurements. To match the onset of d orbitals in experiment with respect to the Fermi energy, we have to apply a small Hubbard U correction of 1 eV. In our study, we identify the top-fcc adsorption configuration as the lowest energetic one with a graphene–copper distance of 3.1 Å, in agreement with other calculations. Graphene in contact to the metal surface becomes n-doped, where the Dirac energy lies about 330 meV below the Fermi energy, again in good agreement with ARPES measurements.

We find a hybridization of copper d states with the π states of graphene, which induces proximity SOC in graphene.

Introducing a low-energy C_{3v} symmetric Hamiltonian, which accounts for the broken D_{6h} symmetry of graphene by the substrate, we are able to extract effective proximity induced orbital and spin-orbital coupling parameters. We observe a significant effective staggered potential of 9 meV, breaking the chiral symmetry of graphene. The substrate gives also rise to a structural inversion asymmetry, leading to the induction of Rashba SOC of 1.5 meV, which is equivalent to a perpendicular applied electric field of 320 V/nm to bare graphene. We find sublattice-resolved intrinsic SOC of 40 and 170 μeV in the different sublattices, which is much larger than the value of 12 μeV in isolated graphene. In our calculations, four layers of copper yield already converged values of orbital and spin-orbital parameters. Our findings are experimentally verifiable with techniques such as spin-resolved ARPES, by increasing the resolution to resolve the meV and sub meV spectral ranges.

We take the theoretical uncertainty in the graphene–Cu(111) distance as a motivation to study the distance dependence of the aforementioned parameters. Pushing graphene towards the metal surface leads to an increase in induced SOC, with the parameters acquiring values in the meV range. By studying also the induced intrinsic SOC of the other adsorption configurations, top-hcp and hcp-fcc, we are able to explain magnitudes and signs thereof by an interpretation in terms of the microscopic SOC Hamiltonian. Increased proximity leads to even stronger n-type doping, where at a certain distance the staggered potential unexpectedly flips its sign. This sign change in combination with Rashba SOC gives rise to a complete flip of spins and pseudospins, which could have potential consequences for the system's topology. To reach the transition regime we estimate a pressure of 8.7 GPa, which has to be exerted on graphene. This could be realized for example by pressing a scanning tip onto graphene grown on a Cu(111) surface.

5 Protected pseudohelical edge states in $\mathbb{Z}_2$-trivial spin-orbit coupling proximitized graphene

5.1 Topological states and proximity effects in graphene

Graphene has extraordinary electronic properties [4], showing ultrahigh mobilities of up to several 100000 Vs/cm^2 [5], an ambipolar field effect [2] and exhibits a very clean quantum Hall effect (QHE) [129] probing the Dirac nature of its electronic structure. Together with its special mechanical and optical properties it is an ideal material to study experimentally.

The two-dimensional structure and the abovementioned characteristics let hope for a densely-packed integration in electronic circuits. To make graphene and other materials even more useful for low-power applications one seeks for dissipationless transport effects [125]. One of these effects is the QHE [130]. In the QHE, a strong applied magnetic field leads to a quantized Hall conductivity, which can be expressed via the TKNN formula $\sigma_{xy} = Ce^2/h$ [131], where C is the Chern number and e^2/h the quantum of conductance.

The application of very large magnetic fields is not very practical for integrated circuits and solutions for avoiding them were sought for. In 1988 Haldane came up with a proposal [119], where with the help of a two-dimensional honeycomb lattice model such a solution was found. In the nearest-neighbor tight-binding approximation, the Hamiltonian possesses a chiral (or sublattice) symmetry. This leads to a vanishing σ_z component of the pseudospin degree of freedom and the states remain degenerate at the K point. To induce topological edge conductivity, a nontrivial band gap has to be opened in the Dirac cones of graphene. A trivial gap can be opened by applying a so-called staggered potential $\Delta\sigma_z$, breaking the sublattice symmetry. This, however leads to a Chern number and Hall conductivity of zero, as Chern numbers of the different K valleys in time-reversal symmetric graphene, have opposite signs and sum up to zero. Time-reversal symmetry thus has to be broken to get a finite Hall conductivity. To open up a nontrivial gap, as Haldane showed, one can consider a time-reversal symmetry breaking next nearest-neighbor hopping, where a spinless electron picks up a phase depending on the hopping direction on the path. This can be realized by alternating magnetic fluxes, such that the total magnetic field penetrating the unit cell adds up to zero. The effective low-energy perturbation in the valleys of graphene, labeled by κ, is $\sigma_z\kappa$. This term is odd under time-reversal symmetry, which changes κ to $-\kappa$. It was then shown that under this perturbation, the Chern number acquires a nontrivial quantized value. In analogy to the anomalous Hall effect, the magnetic-

fieldless materialization of the Hall effect, this effect was called the quantum anomalous Hall effect (QAHE).

The approach by Haldane was considered to be hardly realizable. On the one hand it was thought that the two-dimensional honeycomb lattice is not realizable in the real world and on the other hand that the application of alternating fluxes would be too complicated in experiment.

However after the discovery of graphene in 2004 [2], research picked up the proposal by Haldane again. In 2005 Kane and Mele discovered [12, 124] that the role of the magnetic fluxes can be played by graphene's intrinsic spin-orbit coupling. They considered two time-reversed copies of the Haldane model such that the overall perturbation was respecting time-reversal symmetry with the term $\sigma_z \kappa s_z$, where the real spin Pauli matrix s_z was considered additionally. As time-reversal symmetry is respected with this term, the transversal conductivity still remains zero with a total Chern number of zero. Despite zero Chern number, for each spin sector the individual Chern numbers, called spin Chern numbers, are quantized by construction. Therefore, the spin Hall conductivity shows quantized values. Thus the term QSHE was coined. Intrinsically graphene would itself be a topological insulator, its small intrinsic spin-orbit coupling of some μeV [59] though limits an experimental observation.

Graphene as is, with its zero energy gap, offers an ideal starting point to create materials with different electronic properties. Being a two-dimensional material it has two surfaces, which can be covered by different materials. By bringing materials into proximity to graphene, its electronic properties can be influenced. These so-called proximity effects are a topical research field nowadays [132]. There are several types of proximity effects in graphene. First of all, they manifest in a breaking of symmetries. A substrate breaks the horizontal mirror symmetry and can also lead to a breaking of sublattice symmetry, as the carbon atoms from different sublattices see distinct electrostatic environments. Graphene can be doped by bringing it into contact with metal surfaces of different work functions to change the carrier character in graphene [97]. More exotic proximity effects are the induction of exchange interaction [68, 133] or superconductivity [134].

In the context of spintronics in graphene [6–8] it is important to control and increase spin-orbit coupling. This is also important to realize the quantum spin Hall state (QSHS) as mentioned. Materials for inducing proximity spin-orbit coupling in graphene cannot be taken arbitrarily. Heavy metal substrates with strong spin-orbit coupling often hybridize heavily with graphene and destroy the graphene Dirac dispersion [97]. One looks for insulators without reactive surface states. Ideal candidates are the transition metal dichalcogenides (TMDCs). They represent inert and well-defined chemical structures, which partly incorporate heavy metals like molybdenum or tungsten in combination with sulfide, selenium or tellurium. It turns out that the graphene Dirac cones lie inside the band gap of these materials when brought together and spin-orbit coupling can be enlarged [10].

These van der Waals coupled heterostructures can be relatively easily fabricated. Many experiments confirmed a strong proximity spin-orbit coupling effect in the system by exploring weak localization measurements [135–142], spin transport measurements [135, 141, 143], assigning SOC in the range of 1–10 meV.

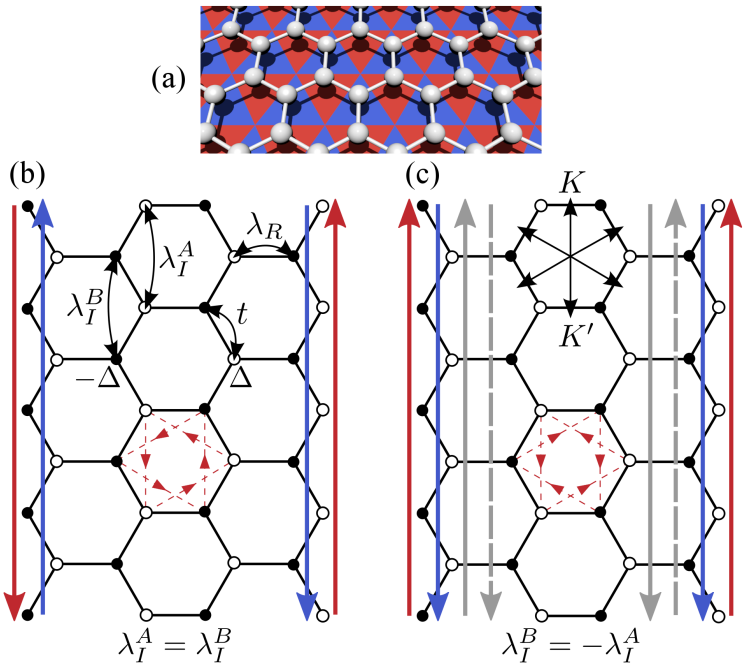

Figure 5.1: Schematics of proximity induced properties in graphene. (a) Graphene placed on a symmetry breaking substrate. Sublattice A is represented as empty, sublattice B as filled dots. Symbols colored in red (blue) denote spin-up (spin-down) characteristics. Panel (b) shows the hopping parameters used in our model. Dashed red lines encode spin-up intrinsic SOC hoppings (signs indicated by arrows), for the uniform case of $\lambda_\mathrm{I}^\mathrm{A} = \lambda_\mathrm{I}^\mathrm{B}$ within a hexagon. Helical states and their velocity directions are indicated by long arrows. Panel (c) shows reciprocal K and K′ directions with respect to the lattice. Intrinsic SOC spin-up hoppings are shown for staggered intrinsic SOC, $\lambda_\mathrm{I}^\mathrm{A} = -\lambda_\mathrm{I}^\mathrm{B}$ by red dashed lines. Solid (dashed) gray arrows indicate valley edge states located in the $\kappa = 1(-1)$ valley. Red and blue arrows show pseudohelical states carrying a finite spin current along the ribbon.

In the case of a generic substrate, when the sublattice symmetry of graphene is broken, intrinsic spin-orbit coupling can be sublattice-dependent, expressing itself as $\frac{1}{2}\left[\lambda_\mathrm{I}^\mathrm{A}(\sigma_z + \sigma_0) + \lambda_\mathrm{I}^\mathrm{B}(\sigma_z - \sigma_0)\right]\kappa s_z$ [61]. This spin-orbit coupling also includes the Kane–Mele case when $\lambda_\mathrm{I}^\mathrm{A} = \lambda_\mathrm{I}^\mathrm{B}$ (uniform intrinsic SOC). In graphene on TMDCs however, it is the other extreme, $\lambda_\mathrm{I}^\mathrm{B} = -\lambda_\mathrm{I}^\mathrm{A}$, the case of a so-called *valley Zeeman coupling* [10, 11, 138] or *staggered intrinsic SOC*. Interesting effects can be observed like a giant spin lifetime anisotropy of in-plane and out-of-plane spins [144–146], which tests and proofs the existence of staggered-sublattice resolved SOC. Further, heterostructures of TMDCs can be used to optically inject spins into graphene via spin-valley coupling of the TMDC [147, 148]. These heterostructures can also lead to an effective charge to spin conversion [149].

From a theoretical point of view, *ab initio* calculations of graphene in contact with TMDCs estimate induced spin-orbit coupling splittings on the order of meV [10, 11,

138, 140, 150]. Curiously, it was shown that within the low energy dispersion of graphene by spin-orbit coupling proximity effect, inverted band structure arises [11, 138, 140, 150, 151]. So far there is no consistent picture concerning the edge modes, which appear due to this inversion. The systems were reported to be topologically nontrivial ($\mathbb{Z}_2 = 1$) [138], which appears in line with the appearance of helical edge modes (termed quantum spin Hall states) [11], but inconsistent with the statement of having a trivial system ($\mathbb{Z}_2 = 0$) by Ref. [140].

Here, we aim to provide a unified picture of the topological nature of spin-orbit coupling proximity models and the existence and character of edge states. In Sec. 5.2, we introduce a modified Haldane model [119] with staggered intrinsic SOC to illustrate how edge states appear in models with two different limits of intrinsic SOC, same magnitude and signs in the sublattice [12] and same magnitude but different signs [11] in Sec. 5.3. In the different sign case, there are in general two pairs of edge states formed at each edge, pseudohelical and valley-like. This makes the bulk model trivial [140], which we prove and complement by the study of the $\mathbb{Z}_2$ phases within the intrinsic SOC space in Sec. 5.4. Can protected edge states arise in a $\mathbb{Z}_2$-trivial system? Yes, and the key is to gap out unwanted (valley) pair of states by finite size effects, which we explore in Sec. 5.5. This is realized in narrow ribbons, as we show. The remaining pair is protected against time-reversal scattering, just like the QSHS. But unlike helical states of the QSHS, our edge states are pseudohelical, being spin-up at one zigzag edge, and spin-down at the other. Finally we address the effect of onsite disorder for pseudohelical and helical edge states in Sec. 5.6.

5.2 Graphene spin-orbit coupling proximitized tight-binding Hamiltonian

The electronic structure of a bipartite hexagonal lattice with broken sublattice and horizontal reflection symmetries, such as graphene on a trigonal symmetric substrate, can be described by a C_{3v}-symmetric tight-binding Hamiltonian [10, 11, 13, 61, 121] that was introduced in Sec. 4.5, Eq. (4.1).

The essential hopping terms are depicted in Fig. 5.1(b). The orbital effects include the nearest-neighbor hopping t and the on-site staggered potential Δ. Spin-orbit coupling effects are incorporated by the sublattice-resolved, spin-preserving intrinsic spin-orbit couplings $\lambda_{\mathrm{I}}^{\mathrm{A}}$ and $\lambda_{\mathrm{I}}^{\mathrm{B}}$ as well as the nearest-neighbor spin-flipping Rashba spin-orbit coupling λ_{R}. For more details on the processes and how they arise in a realistic system, see Chpt. 4.

In this study, we focus on effects, when the sublattice-resolved intrinsic spin-orbit couplings are large compared to the parameters Δ and λ_{R}, as then topological effects may arise [124]. The distinction of sublattices in the intrinsic SOC is an extension of the models introduced earlier by Haldane [119] and by Kane and Mele [12], and by McClure and Yafet [95]. It makes the model experimentally more relevant, while also introducing new physics. The effective Hamiltonian is surprisingly flexible and can be applied to describe spin-orbit coupling effects in hydrogenated graphene [61], graphene on metal substrates as Cu(111) [121], or graphene on TMDCs [10, 11].

Following Ref. [12], for numerical examples in this work, we use values of $t = 1$, $\Delta = 0.1\ t$, $\lambda_\mathrm{R} = 0.075\ t$, and $\lambda_\mathrm{I}^\mathrm{A}, |\lambda_\mathrm{I}^\mathrm{B}| = \sqrt{27} \cdot 0.06\ t \approx 0.312\ t$ if not indicated differently. In the case of graphene on TMDCs, the magnitudes of $\lambda_\mathrm{I}^\mathrm{A}$ and $\lambda_\mathrm{I}^\mathrm{B}$ are the same within 20%, but their signs are different [11]. The relative magnitudes of the parameters are chosen to fulfill $\lambda_\mathrm{I}^\mathrm{A}, |\lambda_\mathrm{I}^\mathrm{B}| > \Delta > \lambda_\mathrm{R}$, such that topologically nontrivial regimes can be expected on the one hand [12] and the case of graphene on WSe_2 can be qualitatively reproduced on the other. In reality we expect weaker couplings from proximity effects [11], but here our goal is to demonstrate qualitative features of the models. We will also comment on what is expected in real samples in Sec. 5.5.3.

We implement the tight-binding Hamiltonian (4.1) in a Python code, defining the real-space hoppings. The Hamiltonians for 2D and 1D periodic structures are obtained by numerical Fourier transformation. Finite flakes were constructed using the real-space hopping matrix elements. To test the validity of our implementation we compared our numerically Fourier-transformed 2D tight-binding Hamiltonian to the analytic one of Ref. [13], which gave the same band structures for random parameters.

5.3 Ribbon physics: a comparison between the quantum spin Hall effect and sublattice-broken spin-orbit coupling systems

5.3.1 Special cases of intrinsic spin-orbit couplings

To illustrate the spin-orbit coupling physics of our model, we choose the two opposite limits $\lambda_\mathrm{I}^\mathrm{A} = \lambda_\mathrm{I}^\mathrm{B} = \lambda_\mathrm{I}$ as the *uniform*, and $\lambda_\mathrm{I}^\mathrm{B} = -\lambda_\mathrm{I}^\mathrm{A} = \lambda_\mathrm{I}$ as the *staggered* intrinsic SOC model cases. These two cases have been chosen to have a comparison between the known topologically nontrivial case of a Kane–Mele system (uniform) and the idealized limit of graphene on TMDCs (staggered).

For analysis it is useful to also know the low-energy form of the tight-binding Hamiltonian (4.1). It is given in Eqs. (4.2)–(4.5). The corresponding intrinsic part of the Hamiltonian, Eq. (4.5), for the cases we study are

$$\mathcal{H}_\mathrm{I}^\mathrm{uniform} = \lambda_\mathrm{I} \sigma_z \kappa s_z, \tag{5.1}$$

$$\mathcal{H}_\mathrm{I}^\mathrm{staggered} = \lambda_\mathrm{I} \sigma_0 \kappa s_z. \tag{5.2}$$

Pauli matrices σ and s act on pseudospin (sublattice) and spin space, respectively. The K/K′ points are addressed by the value of κ of ± 1. In literature the second term is often called a "valley Zeeman coupling" [140, 144], as it couples the spin-z degree of freedom with the valley sign.

5.3.2 Zigzag band structures

To discuss the physics and implications of Hamiltonian (4.1), we first calculate the band structure of a zigzag ribbon (compare scheme Fig. 5.1), where solely a staggered potential of $\Delta = 0.1\ t$ is applied. Its band structure is shown in Fig. 5.2. The width of ribbons in this chapter will be denoted by w. In this case it has a relatively large width of $w = 100\ a$. In a zigzag ribbon, the K and K′ points are backfolded along momenta

parallel to the zigzag ribbon. The K and K′ points fall onto different momenta and are well distinguishable. Subbands represent slices of the Dirac cones of bulk graphene and are referred to as bulk bands.

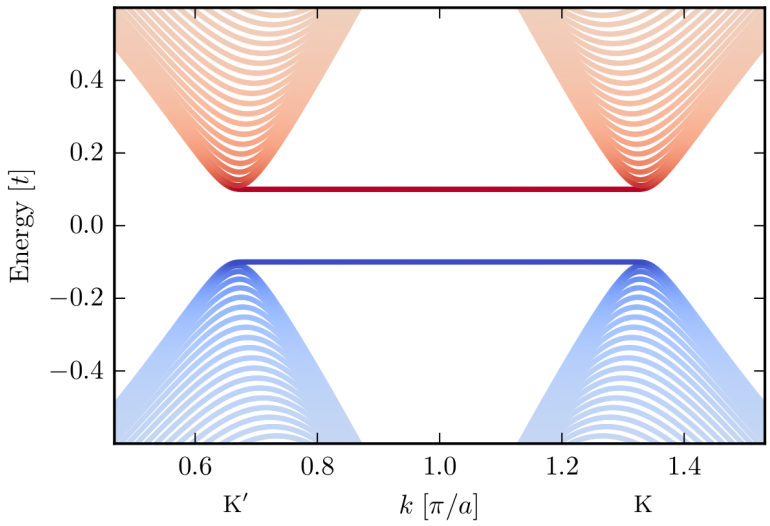

Figure 5.2: Spectrum of a wide zigzag ribbon with an applied staggered potential. The color code denotes the sublattice expectation value, red for sublattice A and blue for sublattice B. The Dirac cone of graphene is backfolded into momenta corresponding to K′ and K. The parameters are $w = 100\ a$, $t = 1$, $\Delta = 0.1\ t$.

The staggered potential $\Delta\,\sigma_z$ [see Eq. (4.3)] creates a gap of 2Δ, raising the energy of A sublattice states and lowering states of sublattice B by site-dependent local potentials. This leads to the pseudospin-valley state denoted as $(v\mathrm{K}, c\mathrm{K}; v\mathrm{K}', c\mathrm{K}') = (\mathrm{B}, \mathrm{A}; \mathrm{B}, \mathrm{A})$; here, c and v label the conduction and valence bands. Between valley maxima and minima, edge modes appear due to the chiral nature of graphene [119]. The state described here serves as a starting point for a further discussion of SOC effects. Here, we consider first spin-up electrons only, to exclude effects from the spin-mixing Rashba SOC. This can be achieved numerically by setting a very large on-site energy for spin-down electrons.

The dispersion relation of a zigzag ribbon with spin-up electrons is plotted in Figs. 5.3(a) and (b) for the uniform and staggered cases. The two valleys with bulk-like subbands and edge states are still well visible. The energetics of the spectra can be interpreted from simple considerations. We start from the case with small staggered potential, where valance and conduction states at K(K′) reside only in one sublattice, compare Fig. 5.2. For K electrons, the phase of the Bloch wave function on sublattice A/B rotates (increases by $2\pi/3$) counterclockwise/clockwise, see Fig. 5.4. For K′ electrons this behavior is reversed. We now add intrinsic SOC, which can be viewed as an action of a vector potential (Peierls phase) [119], whose rotation within the sublattices is sketched as well in Fig. 5.4. A spin-up electron hopping along the arrows on the hopping path picks up a phase of $\pi/2$, giving a factor i in the intrinsic SOC

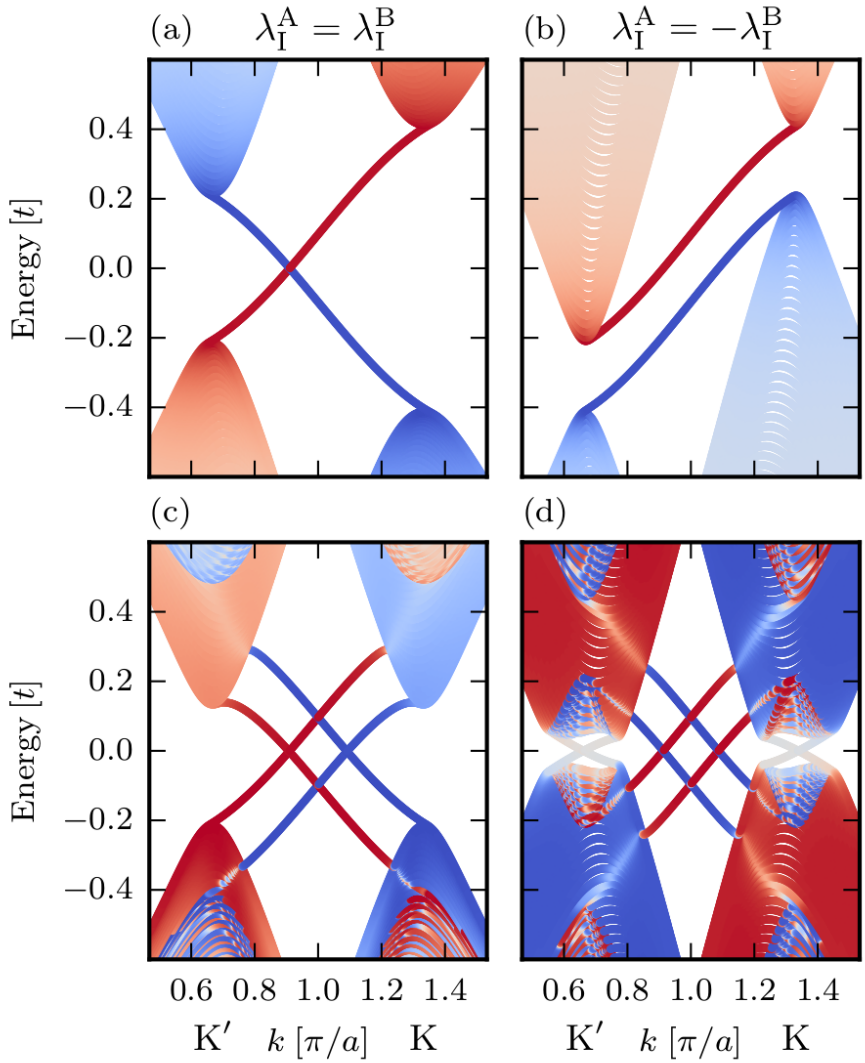

Figure 5.3: Spectra of wide zigzag ribbons comparing spinless and spinful cases. The color code in (a) and (b) for the spinless case denotes the sublattice expectation value, red for sublattice A, and blue for sublattice B. The spectrum of the spinful case with additional Rashba SOC in (c) and (d) is color coded with the spin expectation value, red for spin-up, and blue for spin-down. The left column shows the uniform case, $\lambda_{\mathrm{I}}^{\mathrm{A}} = \lambda_{\mathrm{I}}^{\mathrm{B}}$, right column the staggered case, $\lambda_{\mathrm{I}}^{\mathrm{B}} = -\lambda_{\mathrm{I}}^{\mathrm{A}}$. The parameters are $w = 100\ a$, $t = 1$, $\Delta = 0.1\ t$, $\lambda_{\mathrm{R}} = 0.075\, t$, $\lambda_{\mathrm{I}}^{\mathrm{A}}, |\lambda_{\mathrm{I}}^{\mathrm{B}}| = \sqrt{27} \cdot 0.06\, t$.

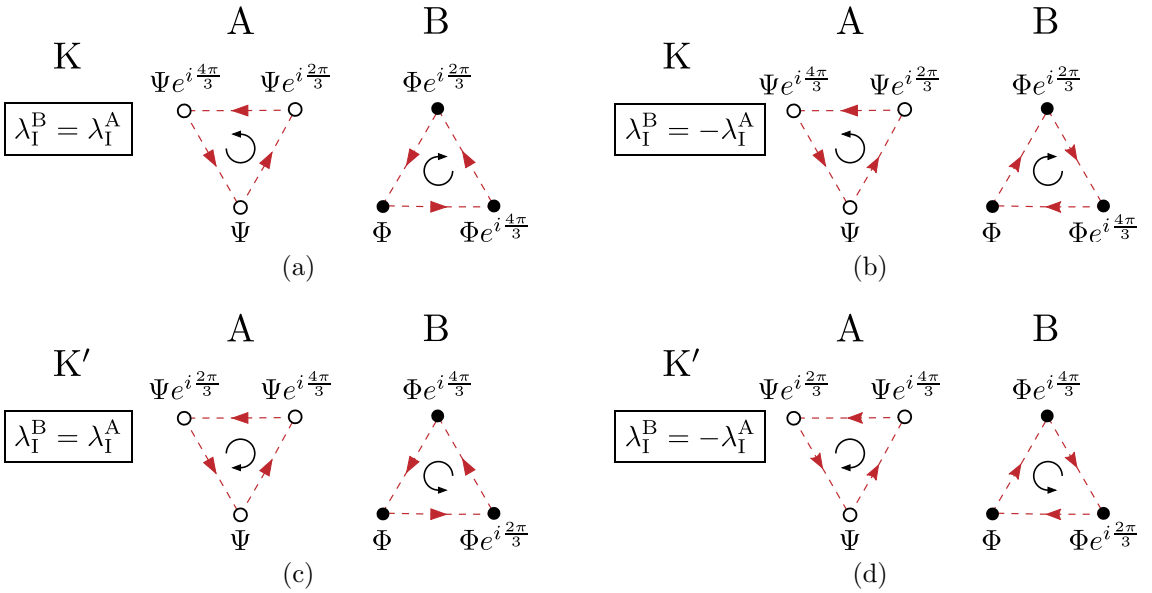

Figure 5.4: Interplay of wave function phase rotation at the K and K′ points with the intrinsic SOC hopping phases in the different sublattices. The wave function values and their phases picked up by a lattice translation ($\psi_{\mathbf{k}}(\mathbf{r}+\Delta\mathbf{r}) = \psi_{\mathbf{k}}(\mathbf{r})e^{i\mathbf{k}\Delta\mathbf{r}}$) are indicated. Circulating arrows denote the rotation sense of the wave function's phase inside the sublattice. Dashed lines with arrows denote the sign of intrinsic SOC hoppings, ν_{ij}, for an electron with spin-up, + for hopping along the arrow, − when hopping against, compare Hamiltonian (4.1).

part of Hamiltonian (4.1). A spin-up electron hopping against it picks up a phase of $-\pi/2$, giving a factor of $-i$. This shows the connection to the Haldane model [119], where we have sublattice resolved hoppings, but the special case of $\phi = \pi/2$, leading to time-reversal symmetry breaking for a single spin species.

If the Bloch phase rotation has the same sense as the rotation of the vector potential, the energy of the state increases. If the rotations are opposite with respect to each other, the energy is decreased. This is analogous to a system with an orbital momentum in a magnetic field.

In the uniform case, the vector potential rotates counterclockwise [Figs. 5.4(a) and 5.4(c)] so that at K-electrons in sublattice A can be found at higher and electrons in sublattice B at lower energies. The opposite is true at K′, with the result seen in Fig. 5.3(a). This establishes the connection to Eq. (5.1), which is a valley-pseudospin Zeeman coupling (with $s_z = 1$ for spin-up electrons). Once the effective magnetic field λ_{I} overcomes the staggered potential Δ, the sublattice occupation becomes $(\mathrm{B},\mathrm{A};\mathrm{A},\mathrm{B})$, flipping A and B at K′, and a chiral state that crosses the gap develops, see Fig. 5.3(a). This is the well known case of a Chern insulator [119].

In the case of staggered intrinsic SOC, the intrinsic SOC phase and wave function rotations are aligned in each sublattice in the same way within the K valley [see Figs. 5.4(b) and (d)]. In the other valley, the rotations are anti-aligned. Consequently, energy levels shift in opposite directions in the two valleys, and the sublattice expec-

tation values remain (B, A; B, A), as seen Fig. 5.3(b). With this explanation in mind, we can see the connection to Eq. (5.2). If $\lambda_I \geq \Delta$, the system becomes metallic, as the conduction band in the K′ point in this case has lower energy than the valence band in the K point. Further, there are isolated propagating states which connect states of same sublattice expectation value from the different valleys. Unlike edge states from uniform SOC which carry opposite velocities, edge states from staggered SOC have same velocities, which produces current in the ground state. This is possible here, because time-reversal symmetry for a single spin species is broken.

Let us now reinstate both spins into the picture. The complete spectra for zigzag ribbons can be obtained by mirroring the spectra in Figs. 5.3(a) and (b) around the time-reversal invariant point π/a and assigning the opposite spin. If we also introduce Rashba SOC, we get additional spin mixing. The results are shown in Figs. 5.3(c) and (d). In the uniform case, the resulting band structure is additive, leading to two pairs of helical edge states, a manifestation of the QSHS [12]. Edge states with the same spin polarization travel in opposite directions on the different edges and at each edge, a time-reversed partner coexists with spin-down polarization [see Fig. 5.1(a)]. These edge states are also known as helical edge states, where spin is locked to the momentum. The effect of Rashba SOC is the mixing of spins in the bulk bands, most apparent in the conduction bands.

In the staggered case, Fig. 5.3(d), there are also what appear to be helical edge modes with spin-polarization present, like in the QSHS. We term them *pseudohelical*, for reasons motivated in Sec. 5.5.2. Contrary to the QSHS, the edge states with same spin on different edges travel along the *same* direction, see Fig. 5.1(c), leading to a net spin current. We note that a spin current which involves products of the spin operator $\mathbf{s}$ and current density $\mathbf{j}$ doesn't violate time-reversal symmetry as $\mathbf{s}$ and $\mathbf{j}$ are both odd under time-reversal symmetry. The bulk states, when mirrored around π/a, are overlapping energetically at the K points and create a metallic state. When Rashba spin-orbit coupling is applied, a gap in the overlapping region at the K points is opened, as shown in Fig. 5.3(d). This gap is inverted. Inside this Rashba gap two new edge states appear in each valley, with quenched spins. Each valley contributes one mode per edge with opposite velocities on the distinct boundaries [see Fig. 5.1(c) for a scheme]. We note that similarly to the case of the QSHS [124] $\lambda_R \gg \lambda_I$ destroys all edge states. Having both valley-centered and helical states, we term this the "quantum valley spin Hall state (QVSHS)"[1].

5.3.3 Armchair band structures

The existence or absence of edge states in an insulator can give insight into its topological nature via the bulk-edge correspondence. This correspondence states that at every interface of a nontrivial system with a trivial system (like vacuum) zero energy modes need to appear [153]. Besides the zigzag edges shown in Sec. 5.3.2, another natural graphene termination is the armchair one. The armchair edges play also an important role in the tunneling of the pseudohelical state discussed later in Sec. 5.5. Here, we contrast their behavior under the staggered and uniform cases of intrinsic

[1] A similar abbreviation was introduced in a graphene system with magnetic impurities [152]

SOC.

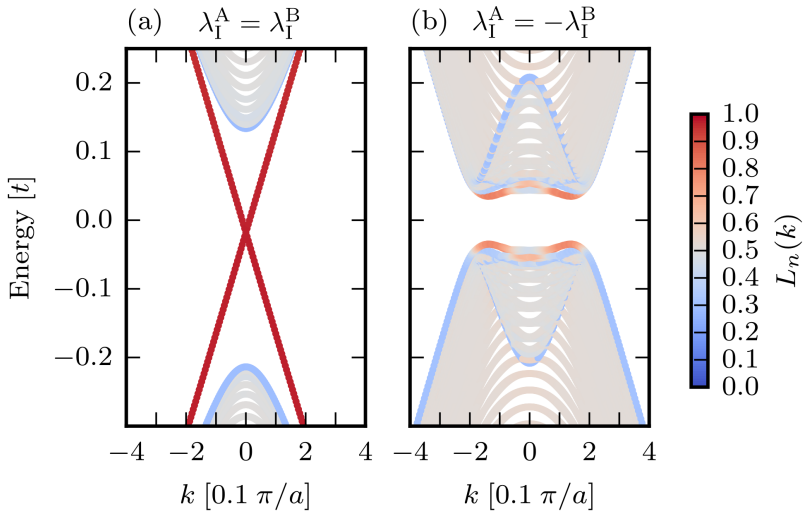

Figure 5.5: Low-energy band structures of wide armchair ribbons for (a) uniform and (b) staggered intrinsic SOC cases. Color code denotes localization $L_n(k)$, red for being localized at the edges, blue for having expectation value in the middle of the ribbon and grey being spread over the ribbon. The parameters are $w = 100\ a$, $t = 1$, $\Delta = 0.1\ t$, $\lambda_R = 0.075\,t$, $\lambda_I^A, |\lambda_I^B| = \sqrt{27} \cdot 0.06\,t$.

The band structures for armchair ribbons are shown in Fig. 5.5, where we also calculate the localization properties of the different states in the dispersion relation. The localization $L_n(k)$ of the states was determined with the formula

$$L_n(k) = \sum_c l(c) \sum_{i \in c} |\psi_{n,i}(k)|^2, \tag{5.3}$$

where c runs over the unit cells of the ribbon and $|\psi_{n,i}(k)|^2$ are the squared tight-binding coefficients of the wave functions with composed index i indicating spin and atom degrees of freedom inside the unit cell. We choose the weight function as

$$l(c) = \begin{cases} 1 - 2c/w & c \leq w/2 \\ 2c/w - 1 & w/2 < c \leq w, \end{cases} \tag{5.4}$$

i.e., a piecewise linear, even function around the center of the ribbon, where it has a value of zero and a value of 1 at the edges. This means, that a higher value of $L_n(k)$ indicates a stronger localization on either edge.

The resulting band structure in the uniform case, Fig. 5.5(a), shows, propagating edge modes within the bulk gap, as expected for a topological insulator, which are well localized at the edges of the system. We note that with the particular localization function chosen, the bulk band structure envelope is also highlighted, having values $L_n(k) \approx 0.3$, i.e., states which are centered in the middle of the ribbon. These states

are the ones interacting least with the boundaries, thus experiencing almost no shift in energy as compared to the other subbands.

In the staggered case, Fig. 5.5(b), the armchair band structure is gapped in the energy region of $\pm 0.034\ t$. We checked that the ribbon is already wide enough to exclude hybridization effects of possible edge states. Armchair edge states exhibit different metallic/insulating behavior depending on the width of the armchair ribbon. They fall into three classes C, which can be separated with the formula $C = w/a \mod 3$. We checked armchair ribbons of the different classes, all of them stayed gapped. Together with this finding and the existence of an even number of edge states per edge, we can conclude that the state must be a trivial insulator, as the bulk-edge correspondence does not hold. Curiously, states with pronounced edge localization are present also here at the borders of the band gap, less localized than in the uniform case. Also in this case bulk envelope bands can be recognized, where the band inversion is clearly observable.

5.4 Topological classification

In the previous section, we concluded that the staggered case represents a trivial insulator. In this section we calculate topological invariants and show where the transition between trivial and nontrivial states happens, when intrinsic SOC is away from the limiting cases of $\lambda_{\mathrm{I}}^{\mathrm{B}} = \pm\lambda_{\mathrm{I}}^{\mathrm{A}}$. The Hamiltonian in Eq. (4.1) possesses time-reversal symmetry, has broken particle-hole and sublattice symmetries, therefore it belongs to the class of AII Hamiltonians, see App. B. In two dimensions this leads to the possibility of a $\mathbb{Z}_2$ classification [154].

5.4.1 Intrinsic spin-orbit coupling phase space: bulk gap and topological invariant

For our sublattice-broken spin-orbit coupling model, we first calculate the bulk graphene gap, which is displayed in Fig. 5.5(a), in the space of the two sublattice intrinsic SOC parameters. This map shows four distinct regions separated by gap closings, where one can expect a change in topology. Analytic gap closing conditions at the K points are indicated as well in Fig. 5.5(a) coinciding very well with the numerical data. The analytic gap closing conditions can be found in App. C.

To calculate the $\mathbb{Z}_2$ invariant, we used the code `Z2Pack` [58]. With the help of tracking Wannier charge centers of the occupied bands over half of the Brillouin zone, one can determine the $\mathbb{Z}_2$ invariant of the system. The method is described in more detail in App. A. The results of the $\mathbb{Z}_2$ invariant calculation are displayed in Fig. 5.5(b) where the same phase space as in the previous section within the $\lambda_{\mathrm{I}}^{\mathrm{A}} - \lambda_{\mathrm{I}}^{\mathrm{B}}$ parameter space was chosen. We sampled the phase space by a 51×51 grid.

The calculated invariants in the $\lambda_{\mathrm{I}}^{\mathrm{A}} = \lambda_{\mathrm{I}}^{\mathrm{B}}$ corners show the expected behavior of $\mathbb{Z}_2 = \mathbb{1}$ in the QSHS. Hamiltonians in these phase space regions, which are separated by gap closings show nontrivial behavior. We find the staggered cases, located on the $\lambda_{\mathrm{I}}^{\mathrm{A}} = -\lambda_{\mathrm{I}}^{\mathrm{B}}$ diagonal, to have a trivial $\mathbb{Z}_2$ invariant as already expected in Sec. 5.3.3 and also reinforcing the statement of Ref. [140] of the system being a trivial insulator.

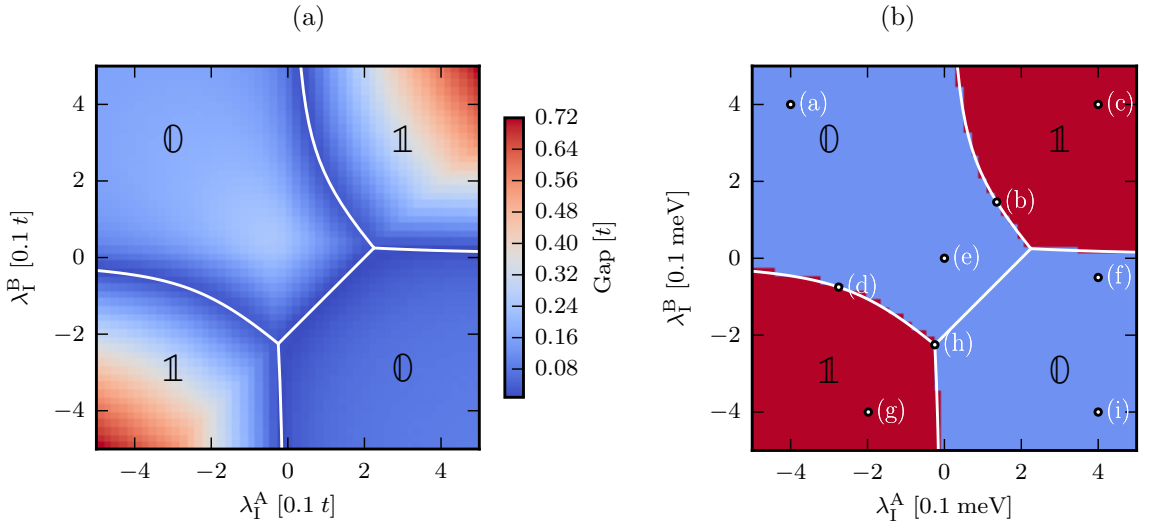

Figure 5.6: Graphene bulk gap and $\mathbb{Z}_2$ phase space in the $\lambda_I^A - \lambda_I^B$ plane. Solid lines are analytic expressions for a gap closing at the K points, which separate trivial ($\mathbb{0}$) and nontrivial ($\mathbb{1}$) phases from each other. (a) Calculated global graphene band gap as a function of intrinsic spin-orbit coupling. The color denotes the size of the gap in graphene. (b) Calculated $\mathbb{Z}_2$ invariant as a function of intrinsic spin-orbit coupling. Blue areas and red areas have trivial ($\mathbb{0}$) and nontrivial ($\mathbb{1}$) $\mathbb{Z}_2$ invariants, respectively. Labels (a)–(i) correspond to selected points for which band structures are shown in Fig. 5.7. The parameters are $t = 1$, $\Delta = 0.1\ t$, $\lambda_R = 0.075\, t$.

In the phase space of Fig. 5.5(a) there is also a gap closing between the two trivial phases, which corresponds to a change in the valley Chern number [151], which will be discussed in Sec. 5.4.3. We note here that not everywhere in this phase space zigzag edge states can be found. In the central region, where intrinsic SOC is small $\lambda_I \lesssim \Delta$ in both edge terminations (armchair and zigzag), states are absent within the gap.

5.4.2 Bulk low-energy band structure shapes

The Hamiltonian of Eq. (4.1) is very rich in possible band structure realizations. We selected special points from the intrinsic SOC phase space of Fig. 5.5(b) to illustrate which bulk band topologies one can expect and display them in Fig. 5.7. Bands for the staggered case are shown in panels 5.7(a) and (i), whereas panels 5.7(c) and (g) show the case of quantum spin Hall systems. Panel 5.7(b) presents the closing of the gap when going from the uniform SOC to the staggered SOC case. Panel 5.7(e) is taken from a point, where the intrinsic SOC is zero and is an example where also the zigzag ribbons are gapped and no edge states are present. The special point panel 5.7(d) shows the case of a gap closing with maximal mixture of spins in the valence bands. In panel 5.7(h), we point out the case of a triple degeneracy, which lies at a point where three gap closing lines meet each other (see also App. C.2 for the condition of triple points). A generic case for the inverted gap regime is shown in panel 5.7(f).

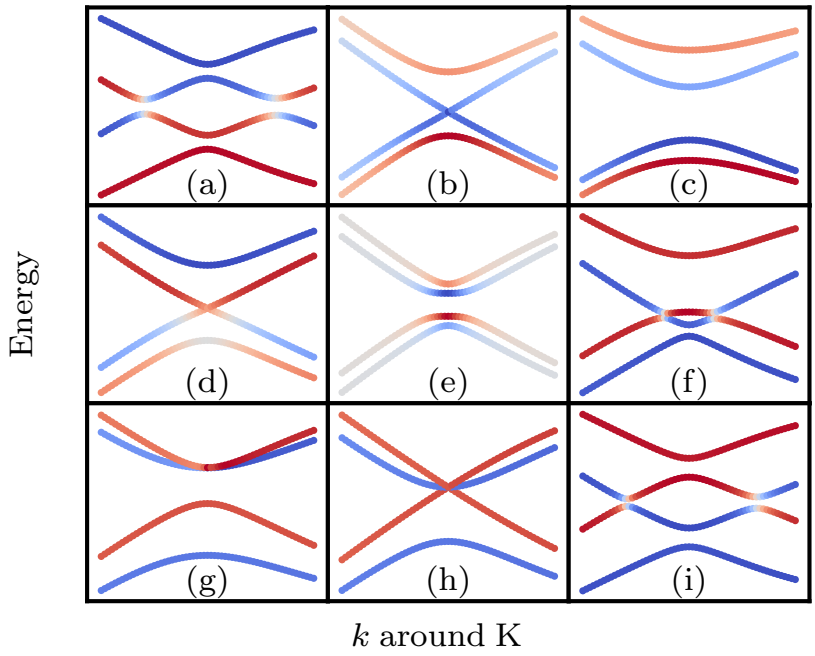

Figure 5.7: Graphene bulk low-energy band topologies around the K point for selected intrinsic SOC parameters. Color encodes spin-expectation values, red and blue stand correspondingly for spin-up and spin-down projections. Panel labeling (a)–(i) is in one-to-one correspondence with intrinsic SOC parameters displayed in Fig. 5.5(b). The other parameters are $t = 1$, $\Delta = 0.1\ t$, $\lambda_{\mathrm{R}} = 0.075\, t$.

5.4.3 Berry curvature in the staggered spin-orbit coupling case

To characterize the origin of the edge states in the staggered SOC case, we carried out the analysis of Berry curvatures,

$$\Omega_n(\mathbf{k}) = -2\mathrm{Im} \sum_{n' \neq n} \frac{\langle u_n^{\mathbf{k}} | \hat{v}_x^{\mathbf{k}} | u_{n'}^{\mathbf{k}} \rangle \langle u_{n'}^{\mathbf{k}} | \hat{v}_y^{\mathbf{k}} | u_n^{\mathbf{k}} \rangle}{(\omega_{n'}^{\mathbf{k}} - \omega_n^{\mathbf{k}})^2}, \tag{5.5}$$

as they can be used to calculate Chern numbers and tell about the existence of conducting edge channels. $\hat{v}_i = \partial\hat{\mathcal{H}}(\mathbf{k})/\hbar\partial k_i$ is the velocity operator in direction i, $\omega_n^{\mathbf{k}} = \varepsilon_{n\mathbf{k}}/\hbar$ with $\varepsilon_{n\mathbf{k}}$ being the energy eigenvalues of the Hamiltonian. The Berry curvatures for the staggered case of occupied bands at K/K′ points are shown in Fig. 5.8. The Berry curvature is calculated for a system which has a comparable band structure as in Fig. 5.7(i). The asymmetry of the Berry curvature stems from trigonal warping effects (different dispersion of bands along k paths KM and KΓ). The broader central peaks at the K/K′ points are responsible for the spin-polarized modes, where for example in the QSHS without Rashba SOC a spin Chern number can be defined [125]. At the gaps, which are opened due to the Rashba SOC at the Fermi energy [compare panel 5.7(i)], side peaks in the Berry curvature appear. This is reasonable, as the Berry curvature is usually high at small-gapped anticrossings, see Eq. (5.5).

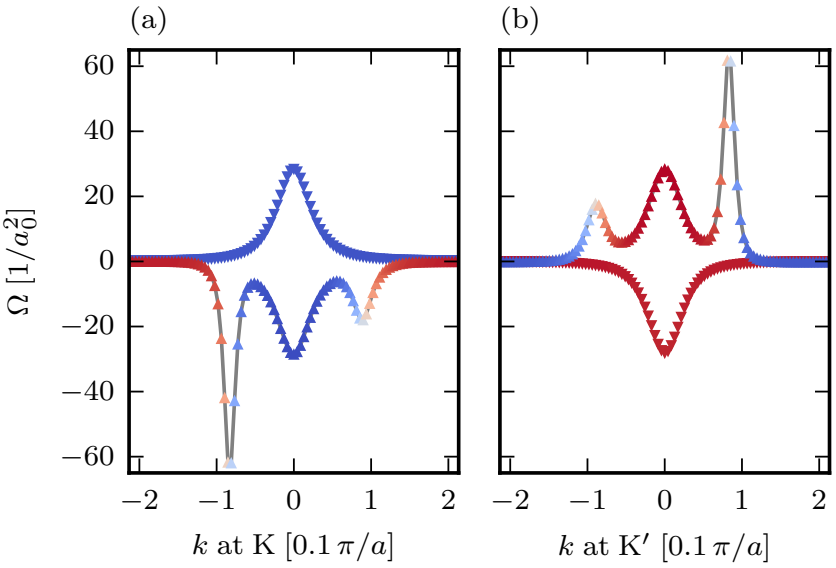

Figure 5.8: Berry curvature for the two low energy states of bulk graphene in the staggered case. Berry curvature is shown at K in (a) and K′ in (b). Downward pointing triangles denote the band lower in energy, upward pointing triangles indicate the band higher in energy. The color encodes the spin-expectation value, where red and blue stand for spin-up and spin-down, respectively. The parameters are $t = 1$, $\Delta = 0.1\ t$, $\lambda_\mathrm{R} = 0.075\,t$, $\lambda_\mathrm{I}^\mathrm{A} = -\lambda_\mathrm{I}^\mathrm{B} = \sqrt{27} \cdot 0.06\,t$.

The valley Chern number is defined as [125]

$$\mathcal{C}_v = \left(\mathcal{C}_\mathrm{K} - \mathcal{C}_\mathrm{K'}\right)/2, \tag{5.6}$$

with

$$\mathcal{C}_\mathrm{K} = \frac{1}{2\pi} \sum_n^{\mathrm{occ}} \int_{\mathbf{k}\in \mathrm{BZ}/2} d\mathbf{k}\ \Omega_n^z(\mathbf{k}). \tag{5.7}$$

The integration limit extends over half of the Brillouin zone belonging to the triangle around the K/K′ point.

We find the valley Chern number to be about 1, with $\mathcal{C}_\mathrm{K/K'} = \pm 1$ as found in Ref. [151] for the staggered case. We note that swapping of signs of $\lambda_\mathrm{I}^\mathrm{A}$ and $\lambda_\mathrm{I}^\mathrm{B}$ switches the signs of $\mathcal{C}_\mathrm{K/K'}$ and leads to a valley Chern number of -1 as also found in Ref. [151]. The calculated valley Chern number is independent of the size of Rashba SOC, which we checked by varying Rashba SOC by ±25%. On the other hand we note a slight sensitivity to the staggered potential, which was not mentioned by Ref. [151].

The valley Chern number is not a strict topological invariant, however it can be an indicator for the existence of valley edge states [125] like it is found here. We note that our system, regarding the valley-centered states, is very similar to bilayer graphene subject to a perpendicular electric field which shows a quantum valley Hall state [155]. This system represents twice a copy of ours with a valley Chern number of 2 due to

spin degeneracy, showing an absence of states in armchair ribbons as well. Valley Hall states are not topologically protected. They can give rise to quantized transport along zigzag edges, however they are sensitive to short range scattering [125] which occurs for example in armchair terminations.

5.5 Ribbon width effects and finite flakes

In the studies of graphene zigzag ribbons on TMDCs [11] only pseudohelical edge states were found at the Fermi energy and valley states were absent. This lead to the conclusion of having found "quantum spin Hall states", implicitly characterizing the system as a topological insulator. It turns out that the absence of valley states was due to finite size quantization, which we want to further explain here. More specifically we consider the study of narrow zigzag ribbons and finite flakes of graphene, where peculiar edge states can be found.

5.5.1 Zigzag edge state localization properties

Crucial for our further analysis is the localization behavior of the zigzag edge states found in the staggered case. Edge states are expected to be exponentially localized at the boundaries of a ribbon. The wave functions of valley-centered and pseudohelical states from the left edge of a wide zigzag ribbon are shown in Fig. 5.9(a). The states were selected close to the respective crossing points (at zero energy) in Fig. 5.3(d) from the lower energy edge state at momentum $k = 0.681\,\pi/a$ and $k = 0.917\,\pi/a$ for valley-centered and pseudohelical states, respectively.

To get the localization length, we fit $|\psi(y)|^2 \propto \exp(-y/\lambda)$, where y is measured from the edge. We find that pseudohelical edge states decay very quickly, over half a unit cell ($\lambda \approx 0.4\,a$), whereas valley states have a much longer localization length ($\lambda \approx 9\,a$). The localization of the valley-centered state depends strongly on the value of the Rashba SOC, see Fig. 5.9(b). The valley centered edge states live inside the Rashba gap. The larger the Rasbha gap, the more the edge states are energetically decoupled from the bulk states. This explains the larger localization length of valley-centered states with respect to the pseudohelical edge states, the former being energetically closer to bulk states.

5.5.2 Protected pseudohelical edge states

The different localization behavior of the two types of edge states indicates that for narrow ribbons, valley-centered states should be gapped due to hybridization with states from the other side of the ribbon, when the ribbon width is comparable to the localization length. A comparison of the band structures for zigzag ribbons of width of ten unit cells for uniform and staggered cases is shown in Figs. 5.10(a) and (b), respectively. Indeed, the valley states exhibit a gap in Fig. 5.10(b), explaining the sole occurrence of apparent quantum Hall states in Ref. [11]. In Ref. [11], much smaller values for SOC were used to study the ribbons and the respective valley state

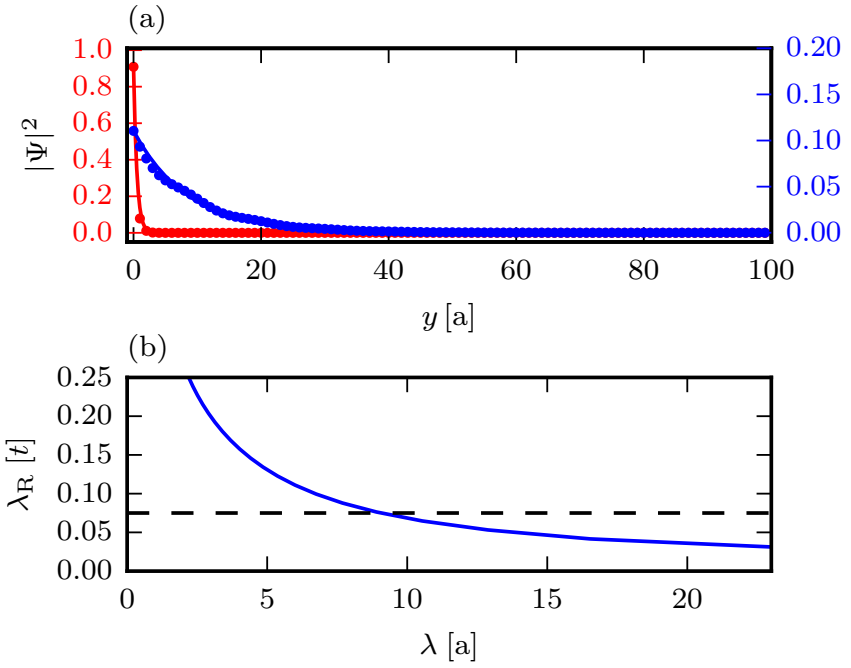

Figure 5.9: Localization behavior of pseudohelical and valley-centered edge states of a wide zigzag ribbon with staggered SOC parameters in the transversal ribbon direction y. Blue and red dots in panel (a) represent the normalized probabilities of finding the valley-centered or pseudohelical state in the yth unit cell, respectively, solid lines are the respective fits. Panel (b) shows the localization length λ of the valley-centered state versus the Rashba parameter. The standard Rashba parameter used here is indicated as dashed line. The parameters are $w = 100\,a$, $t = 1$, $\Delta = 0.1\,t$, $\lambda_\mathrm{R} = 0.075\,t$, $\lambda_\mathrm{I}^\mathrm{A} = -\lambda_\mathrm{I}^\mathrm{B} = \sqrt{27}\cdot 0.06\,t$.

localization length was far greater. This is why even in ribbons up to a width of about 1000 unit cell sizes, only pseudohelical states were seen.

With the valley states gapped out, we are left with a single pair of pseudohelical states at each edge inside the gap. What are these states and how do they compare to the helical modes of the QSHS? In particular, since the spin-up modes head in one direction along the two edges, how do the states meet in a finite flake? To clarify this question, we calculate wave functions of finite graphene flakes taking states from within the gaps as shown in Fig. 5.10(a) and (b). To simulate short-range scattering we removed one orbital from the left zigzag edge. Additionally we calculated spin and site expectation values as well as net probability bond currents [156],

$$\mathbf{J}_{(i,j)} = \frac{\mathbf{R}_i - \mathbf{R}_j}{i\hbar} \sum_{s,s'} \left(\psi_{sj}\psi^*_{s'i} \langle s'i|\mathcal{H}|sj\rangle - \psi_{s'i}\psi^*_{sj} \langle sj|\mathcal{H}|s'i\rangle \right), \tag{5.8}$$

between lattice points $\mathbf{R}_i$ and $\mathbf{R}_j$. The labels s and s' denote spins of orbitals and ψ_{sj} are the tight-binding coefficients. The matrix elements are the real-space hopping elements defined in Eq. (4.1).

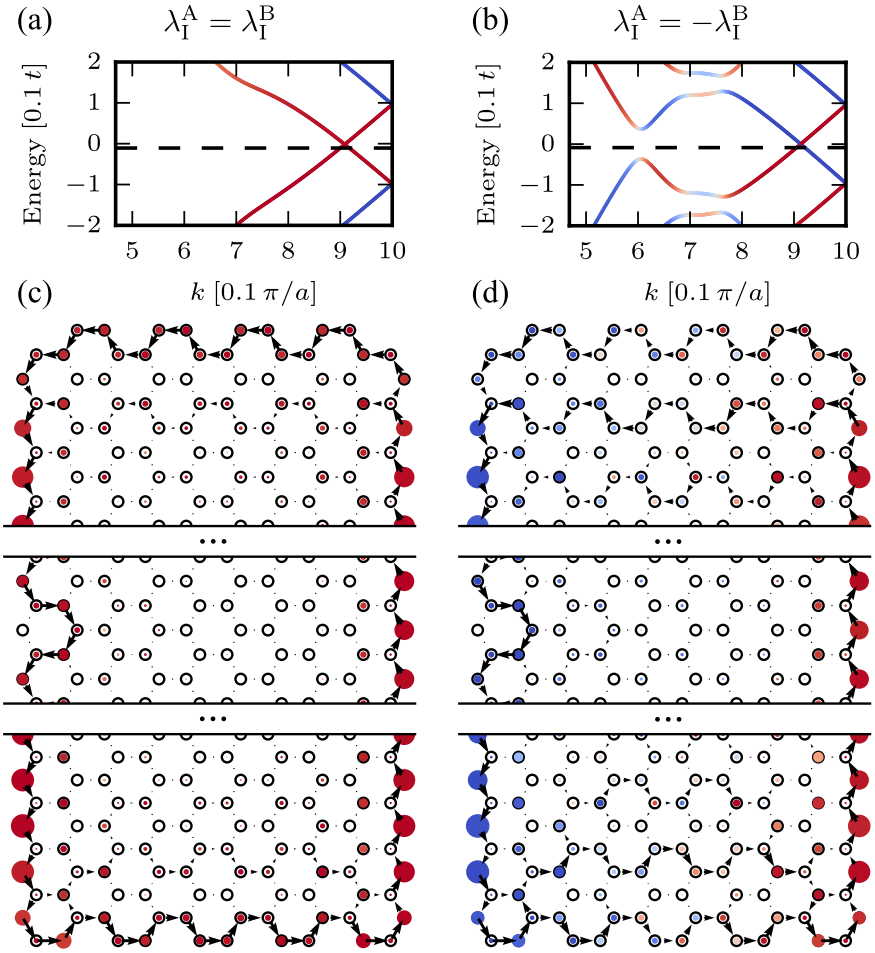

Figure 5.10: Finite sized zigzag ribbons and flakes of width of ten zigzag unit cells. Left column is for the case of $\lambda_{\mathrm{I}}^{\mathrm{A}} = \lambda_{\mathrm{I}}^{\mathrm{B}}$ and right column for $\lambda_{\mathrm{I}}^{\mathrm{B}} = -\lambda_{\mathrm{I}}^{\mathrm{A}}$. Panels (a) and (b) show the band structure of an infinite zigzag ribbon over half of the Brillouin zone with spin expectation values as color code (up in red, down in blue). Panels (c) and (d) show finite flakes of length of 100 zigzag cells and properties of a state that lies at energy indicated by dashed lines in panels (a) and (b), respectively. Empty dots denote the lattice, full dots indicate the site expectation value, color coded for spin polarization, and black arrows show probability bond currents. Orbitals in the middle area of panels (c) and (d) have been removed acting as short-range scatterers. Images of flakes have been cut due to size constraints. The parameters are $w = 10\ a$, $l = 100\ a$, $t = 1$, $\Delta = 0.1\ t$, $\lambda_{\mathrm{R}} = 0.075\, t$, $\lambda_{\mathrm{I}}^{\mathrm{A}}, |\lambda_{\mathrm{I}}^{\mathrm{B}}| = \sqrt{27} \cdot 0.06\, t$.

In the QSHS, Fig. 5.10(c), we find a true helical edge state flowing along the boundary, as expected, avoiding the short-range scatterer and preserving its spin along z. The time-reversal partner of this state has the opposite chirality and opposite spin polarization. The probability bond currents are well localized at the edges of the flake, as expected.

The edge states appearing in the finite-size gap of the QVSHS are presented in Fig. 5.10(d). They have several fascinating features. a) The probability bond current navigates around the short-range scatterer and *does not scatter back*. The reason is that there is only the time-reversal partner, $T\psi$ of the edge state ψ at this energy and, as for topologically protected states, backscattering is forbidden as long as the impurity V is nonmagnetic and scattering is elastic (mathematically, $\langle\psi|V|T\psi\rangle = 0$). b) Spin polarization is opposite on the two edges, which are formed by different sublattices. This is why we call these states *pseudohelical*—with pseudo describing either the pseudospin-spin locking or the "not-really-helical" character of the states. Net spin current flows in this state along the zigzag direction. Also, we explicitly checked that the out-of-plane g-factor of the pseudohelical states is nearly zero. We applied a small Zeeman magnetic field $\mathcal{H}_{\text{ex}} = g\mu_B B\sigma_0 s_z = g\lambda_{\text{ex}}\sigma_0 s_z$ with the exchange energy $\lambda_{\text{ex}} = 0.001\ t$ and found a value of $g = 0.0242$, for flakes of length of 100 unit cells. This low g factor is expected since, although the pseudohelical states are locally spin polarized, globally the pseudohelical states are spinless. c) Further, also at odds with true helical states which exist along the armchair edge, pseudohelical states exhibit reflectionless tunneling along the armchair boundary gradually changing their spin in Fig. 5.10(d) due to Rashba SOC. This tunneling connects protected modes at opposite edges by narrow channels, which could be termed wormholes, as in 3D topological insulators [157]. We discuss the transition to the bulk behavior of wider flakes in Sec. 5.5.4. d) We checked that the pseudohelical states are robust with respect to nonmagnetic onsite disorder up to strengths comparable to Rashba SOC (see Sec. 5.6).

5.5.3 Condition for the absence of valley edge states

The pseudohelical states found in the previous section are stabilized by geometric effects. The absence of valley states is crucial for their protection. If they would be existent, (back)scattering of pseudohelical states into valley states would be possible. To quantify the behavior of valley states under the change of ribbon width, it is helpful to look at the band structure of a narrow ribbon in Fig. 5.11. Panel (a) shows the interplay of intrinsic SOC and staggered potential creating a gap inversion analogously to the one in Fig. 5.3(d), but without Rashba SOC. One can recognize the valence band maximum and conduction band minimum whose distance defines the inverted gap E_{g}. From these valence and conduction extremal points, the pseudohelical states originate and meet at the Brillouin zone boundary $k = \pi/a$. If Rashba SOC is added, see Fig. 5.11(b), it splits spin-up and -down bands of different sublattices. The pseudohelical edge states are not affected as they are spatially decoupled and Rashba SOC is a nearest-neighbor hopping process.

The narrow ribbon can also be viewed as a finite quantum well with hard wall boundaries, where bulk-like subbands are separated by a constant energy of ΔE, as indicated in Fig. 5.11(a). We find this level spacing to follow the expected formula

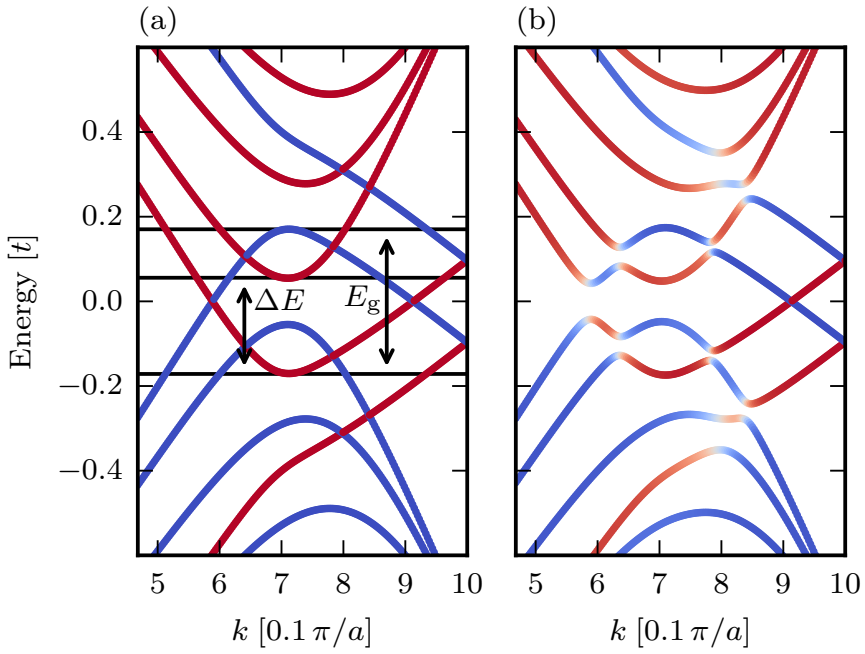

Figure 5.11: Finite size and Rashba coupling influence on zigzag ribbon band structures. Size of the ribbons is 13 zigzag unit cells. Panel (a) is without Rashba SOC (vice versa for (b)). Color encodes the spin-expectation value, where red and blue stand for spin-up and spin-down, respectively. The finite size level spacing ΔE and the inverted gap size E_g are indicated. The parameters are $w = 13\ a$, $t = 1$, $\Delta = 0.1\ t$, $\lambda_\mathrm{R} = 0.075\,t$, $\lambda_\mathrm{I}^\mathrm{A} = -\lambda_\mathrm{I}^\mathrm{B} = \sqrt{27} \cdot 0.06\,t$.

$\Delta E \approx \pi\hbar v_\mathrm{F}/w$ [158]. If the following condition is fulfilled

$$\Delta E > \frac{E_\mathrm{g}}{2}, \tag{5.9}$$

the first subbands do not touch at zero energy at K, as it is the case in Fig. 5.11(a). Because Rashba SOC opens a gap in the remaining crossing pair of states at $k = 0.6\ \pi/a$, see Fig. 5.11(b), no other states than the pseudohelical ones are present at zero energy. The inverted gap is assumed to be independent on the width of the ribbon, which is true for not too small ribbons. Inserting $v_\mathrm{F} = \sqrt{3}at/2\hbar$ into the equation one gets

$$\frac{w}{a} \lesssim \sqrt{3}\pi \frac{t}{E_\mathrm{g}}, \tag{5.10}$$

which is the condition for w for *absence* of valley states in narrow ribbons. For the staggered case we get a critical value of $w \approx 13\,a$, inserting a gap of $E_\mathrm{g} \approx 2\lambda_\mathrm{I} - 2\Delta = 0.424\,t$. For more realistic gaps (e.g., WSe_2, Ref. [11]) of $E_\mathrm{g} = 1.32\,\mathrm{meV} = 0.53 \cdot 10^{-3}\,t$ one would expect ribbons of width smaller than $10266\,a$ (about 2.5 μm), where one can still expect only pseudohelical states to be present at the Fermi level. For narrow ribbons, to observe pseudohelical states, one should reside within the Rashba gap to

the left of the K point, see Fig. 5.11(b). This gap increases with the ribbon width, as observed in Ref. [11], with a power law dependence. In the limit of infinitely wide ribbons, it saturates at twice the Rashba parameter value.

In this subsection we discussed finite size effects on the band structure of zigzag ribbons. To see how the valley states emerge we attached an animation[2]. This video shows the same data as in Fig. 5.9, varying the width of the ribbon. With increasing width, ΔE decreases due to finite size quantization and without Rashba coupling the states within the inverted gap become increasingly dense. Rashba coupling then acts among this densely sampled space and leaves back the valley states.

5.5.4 Emergence of pseudohelical states in finite flakes

Graphene, subject to a staggered potential, staggered intrinsic, and Rashba SOC is an insulating material which only exhibits conducting modes at the zigzag edges. Nevertheless, pseudohelical states from narrow flakes are able to tunnel in a reflectionless manner through the armchair part of the flake. Here, we explore how this tunneling breaks down, when the width of the flake is increased.

To study the breakdown we calculated the low-energy local density of states by summing the site probabilities $\sum_s |\psi^n_{si}|^2$ of state n at lattice position $\mathbf{R}_i$ in the energy interval $[-0.02\ t,\ 0.02\ t]$,

$$D(\mathbf{r}_i) = \frac{\sum_n \sum_s |\psi^n_{si}|^2}{\sum_{n,i} \sum_s |\psi^n_{si}|^2}. \tag{5.11}$$

This normalized quantity summarizes the localization behavior better than looking at the states individually, since for wider flakes, other types than pseudohelical states can contribute to the low-energy spectrum.

Starting from the narrow flake shown in Fig. 5.12(a), we obtain the same result as in Sec. 5.5.2. Pseudohelical states are localized at the zigzag edge, which are able to cross the armchair edge. The crossing is possible, because the state presumably tunnels into the localized states of the armchair ribbon, see Sec. 5.3.3. The flake of intermediate width, shown in Fig. 5.12(b) is wider than the critical width of 13 graphene unit cells (compare Sec. 5.5.3). The local density of states contributes to the inner region of the flake, driving it metallic. At this size, subbands cross at zero energy and contribute as delocalized states. When increasing the width ($w \geq 40\ a$), the density of states shows the expected behavior of the bulk limit, where the system is insulating and states at the armchair edge are absent (see Sec. 5.3.3). The density of states now represents standing waves localized along the zigzag boundaries, with a slow (valley states-like) exponential decay into the inner regions, as discussed in Sec. 5.5.1.

The transition from the pseudohelical regime to the insulating one is rather oscillating than continuous. As the width increases, different pairs of subbands cross at zero energy and lead to a metallic behavior until this mechanism becomes continuous (see also the animation).

[2] `http://www.physik.uni-regensburg.de/forschung/fabian/media/supp_valley_emergence.mp4`

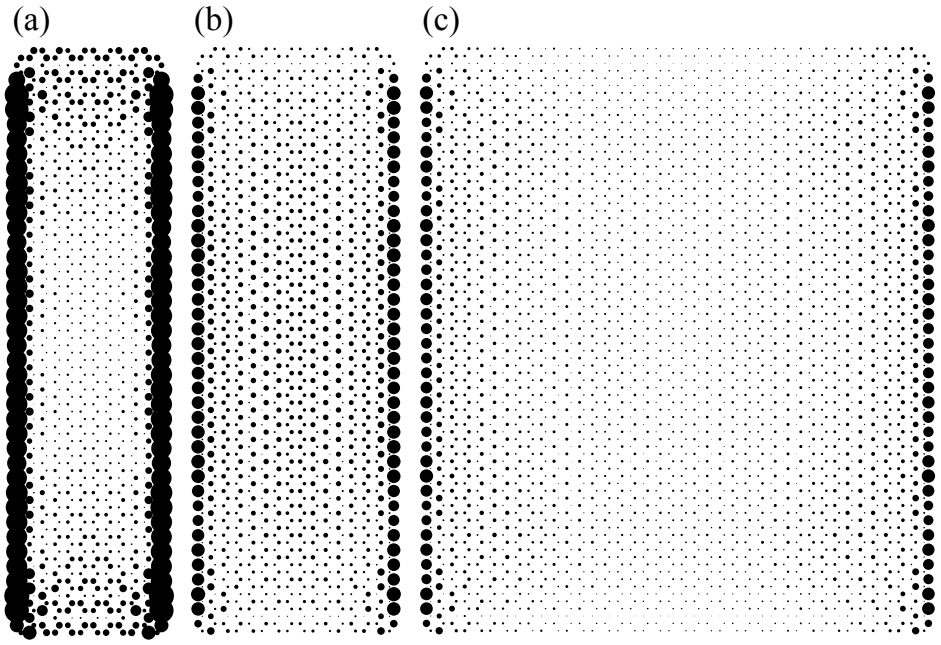

Figure 5.12: Low-energy local density of states for different widths of flakes. Circles indicate low-energy local density of states $D(\mathbf{r}_i)$ for states lying in the energy interval of $-0.02\,t$ to $0.02\,t$, where the area of circles scales linearly with magnitude of the local density of states. The parameters are $w = 12/16/40\ a$, $l = 40\ a$, $t = 1$, $\Delta = 0.1\ t$, $\lambda_\mathrm{R} = 0.075\,t$, $\lambda_\mathrm{I}^\mathrm{A} = -\lambda_\mathrm{I}^\mathrm{B} = \sqrt{27} \cdot 0.06\,t$.

5.6 Effect of uniform onsite disorder on edge states

The case of staggered SOC is topologically trivial, however it is possible to have protected edge states due to only one pair of time-reversal partners at each edge. Are the quantum spin Hall states of the topological uniform case more protected than the pseudohelical states in the staggered case? Here, we add random onsite disorder on each lattice site, being the same for each spin, i.e., preserving time-reversal symmetry. The onsite disorder is randomly drawn from a uniform distribution within the interval $[-W, W]$ with the disorder strength W.

The effect of onsite disorder is shown in Fig. 5.13. The flakes are 80 graphene cells long and 10 cells wide. We visualize the amplitudes of the highest occupied states color coded by spin-expectation values. The states are doubly degenerate due to time-reversal symmetry. In order to be able to compare them, we chose states with similar spin expectation values from the Kramers doublet and varied the disorder strength. The case of uniform intrinsic SOC, Fig. 5.13(a) shows the evolution for disorder strengths of $W = 0.1,\ 0.5,\ 1.0,\ 1.5\ t$. One can see that the state is quite robust under disorder, where effects of disorder are clearly visible at $W = 1.0\ t$ and localization effects set in. This critical disorder strength is about three times the size of the intrinsic SOC. The staggered intrinsic SOC case is shown in 5.13(b) for disorder strengths $W = 0.01,\ 0.1,\ 0.3,\ 0.5\ t$. Localization effects set in earlier at about $W = 0.3\ t$, i.e., about three times the Rashba SOC energy scale or comparable

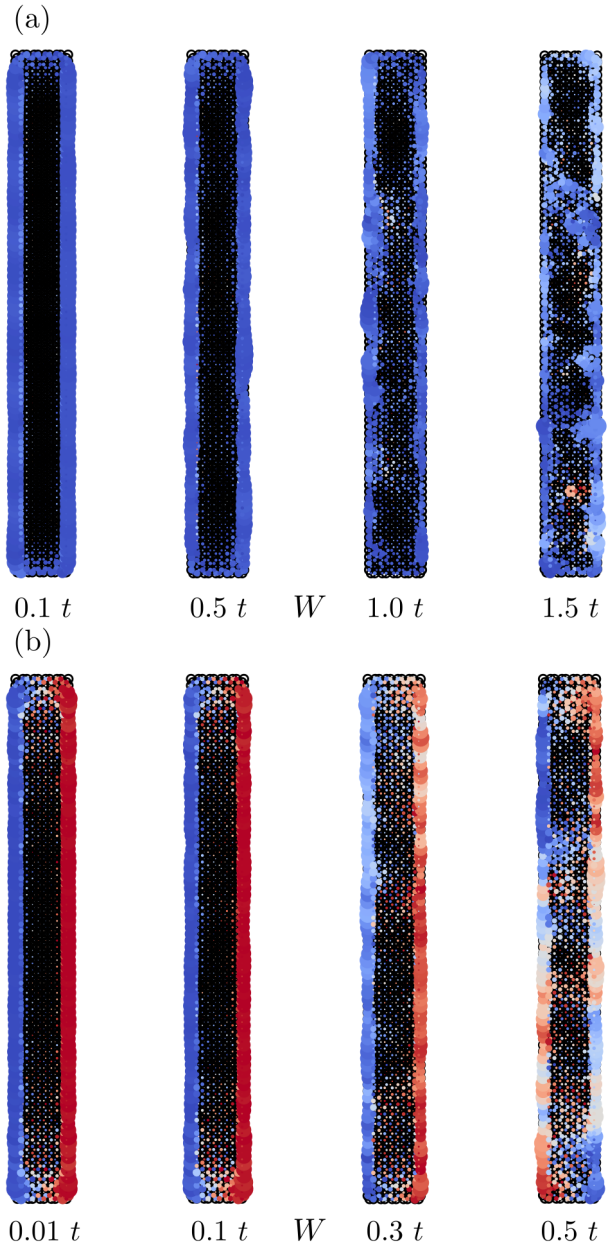

Figure 5.13: Effect of onsite disorder on the edge states of graphene flakes of the uniform (a) and staggered (b) cases. Shown are amplitudes of wave functions of highest occupied levels with similar spin expectation value, color coded red for spin-up and blue for spin-down. The flake length is 80 and width is 10 graphene unit cells. The value for the disorder strength W is shown below the flakes. The parameters are $w = 80\,a$, $l = 10\,a$, $t = 1$, $\Delta = 0.1\,t$, $\lambda_\mathrm{R} = 0.075\,t$, $\lambda_\mathrm{I}^\mathrm{A}, |\lambda_\mathrm{I}^\mathrm{B}| = \sqrt{27} \cdot 0.06\,t$.

to the intrinsic SOC. The energy scale determining the resilience to disorder in the staggered case is likely the Rashba SOC strength as the edge states live inside the Rashba gap of about 0.1 t, compare Fig. 5.10(b).

In conclusion, helical states from the uniform case are more robust compared to pseudohelical states. This however is not too surprising as helical states reside inside a larger energy gap (determined by the size of λ_{I}) than pseudohelical states. The energy gap in the staggered case is determined by Rashba SOC, which has to be smaller than intrinsic SOC, a condition to see pseudohelical states.

5.7 Summary and conclusions

To conclude, we provide an explanation of edge state physics for a general class of graphene spin-orbit coupling proximity Hamiltonians. By comparing to the quantum spin Hall state, we show that the staggered case of intrinsic spin-orbit coupling, which is a realistic realization of proximity spin-orbit coupling in graphene [144, 145], is $\mathbb{Z}_2$-trivial. This clarifies the contradictory findings in literature [11, 138, 140] of triviality/nontriviality. We show that what seem to be quantum spin Hall states in Ref. [11] are in fact pseudohelical states that remain when other valley-centered edge states are gapped out by finite size effects. We explore in this work, how the absence of valley-centered states depends on the width of the zigzag ribbons and provide a formula to estimate the critical width, Eq. (5.10).

By explicit tight-binding calculations of graphene flakes, we are able to show the general properties of what we call pseudohelical states. They are protected by time-reversal symmetry from short-range scattering in analogy to the quantum spin Hall case. This is special, since the hosting system is a trivial insulator. The pseudohelical states carry an intrinsic spin current and have similar properties with respect to onsite disorder as compared to helical states of the quantum spin Hall system.

These findings are interesting on a theoretical level on the one hand, as analogous states could exist in trivial 3D counterparts. From an experimental view, graphene on substrates such as TMDCs or other surfaces, which provide strong spin-orbit coupling could show these pseudohelical modes. As the atomically precise growth of (zigzag) ribbons is possible [159], we expect pseudohelical states to be observable in experiment, provided the spin-orbit coupling induced by the substrate is strong enough and that the substrate is insulating. Ribbons need to be smaller than a critical width, which we estimate to be in the micrometer regime for realistic inverted gaps.

There are several interesting open questions, the behavior of states under Coulomb interaction for example. The magnetic coupling in graphene [63] could give rise to antiferromagnetic/ferromagnetic ground states of zigzag ribbons [160]. Similarly as for the quantum spin Hall states this symmetry breaking could lead to the destruction of the edge states. In this case, it would be interesting to see which energy scale dominates, Coulomb interactions or proximity spin-orbit coupling. Another path to pursue is the question of different types of perturbations, like magnetic impurities or orbital magnetic fields.

6 Many-body quantum Monte Carlo study of phosphorene

6.1 Introduction to phosphorene

Since the discovery of graphene, interest in 2D materials has increased tremendously. The family of 2D materials now also includes insulators like hexagonal boron nitride (hBN) [161] and transition metal dichalcogenides (TMDCs) [3], which enhance and extend the functional possibilities of graphene [10, 11]. The large-gap material hexagonal boron nitride, for example, is a perfect capping material for graphene [5], which shields it from the environment and improves its electronic quality. The TMDCs, whose band gaps lie in the infrared to visible spectrum between 1.5–2.5 eV [14], are known for their circular dichroism; that is, individual K valleys of the hexagonal Brillouin zone can be addressed by circularly polarized light, holding promise for optical and valleytronics applications [10].

Recently, another material was added to the 2D materials, black phosphorus [14–16]. Very much like graphite, it is a single-elemental layered material consisting out of phosphorus atoms, appearing in a puckered quasi-hexagonal form with four atoms per rectangular unit cell, see Fig. 6.1. Phosphorus has a valence configuration of $3s^2\ 3p^3$ and exhibits three-bond coordination. Black phosphorus is a low gap insulator, and was demonstrated to be a suitable material for future high-performance thin-film field-effect transistors, operating in the multi-gigahertz frequency range [15]. Devices may show a good trade-off between relatively high charge carrier mobility of 1000 $\mathrm{cm}^2/\mathrm{Vs}$ and high current on/off switching ratios of about $10^4 - 10^5$ [15, 162], which makes the material interesting for high-speed flexible electronics [14]. Graphene, in contrast, is limited to radio frequency electronics only, due to its low on/off ratio. The trade-off between mobility and on/off ratio in black phosphorus is also even better than in TMDCs [15]. Another feature of the black phosphorus lattice is its anisotropy. The main system directions can be distinguished by the orthogonal zigzag and armchair directions, see Fig. 6.1. It was recognized that the carrier mobility shows anisotropy in the different lattice directions. Higher conductivity and mobility can be found in the armchair direction [14, 16]. The lattice anisotropy can also have consequences for spin relaxation, which is different for armchair and zigzag directions due to anisotropic spin-orbit coupling [163].

Black phosphorus and its multilayers can be used in plasmonic devices [164] and are anticipated to be highly efficient thermoelectrics [14, 16]. The most severe disadvantage of the material is its reactiveness when exposed to ambient conditions. As black phosphorus has a lone-pair orbital taking part in the bonding, it is reactive to oxygen and therefore degrades when exposed to air. This can be circumvented by capping it

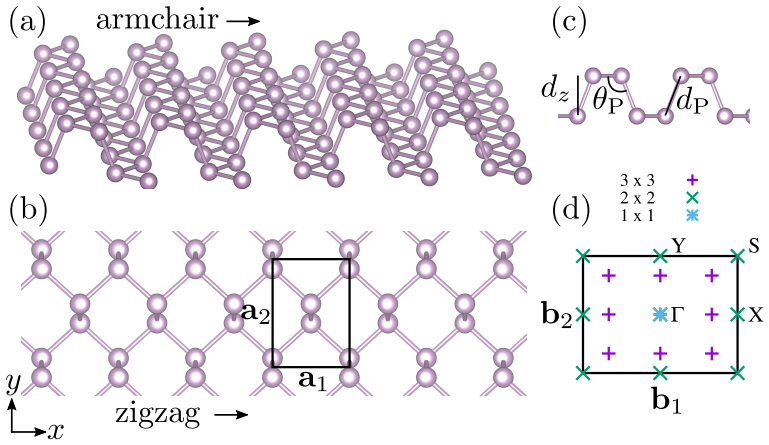

Figure 6.1: Lattice of single layer black phosphorus – phosphorene. The side view in (a) shows the puckered structure arising in the armchair direction. In the top view (b), the zigzag direction is indicated. The rectangular unit cell with the lattice vectors $\mathbf{a}_{1/2}$ are shown. In (c), the inter-plane bond length d_P and bond angle θ_P are labeled. In (d), we show reciprocal cell quantities with reciprocal lattice vectors $\mathbf{b}_{1/2}$ and high-symmetry points Γ, X, Y, and S. The different symbols indicate points in the 1×1 Brillouin zone, which fold back to the Γ point, if different supercell sizes $2 \times 2/3 \times 3$ are concerned.

with other materials [14]. Another important challenge, black phosphorus applications face is the invention of large-area fabrication methods.

The most interesting property of black phosphorus is related to its direct gap at the Γ point, which appears in all multilayers in contrast to TMDCs, where only the monolayer possesses this property. Additionally, the material offers several ways to alter the gap. First, the gap changes with respect to the number of layers [165, 166] from 0.3 eV to about 2 eV from bulk to the monolayer limit [16, 167]. This energy range bridges the gap between graphene and the TMDCs and is important for mid-infrared optoelectronic, photovoltaic, photocatalytic, and thermal imaging applications, as well as for fiber optic telecommunications [16]. Interestingly, extinction Fourier transform infrared spectra (FTIR) can be used to unambiguously characterize the different multilayers by fingerprinting side-band peaks in the spectra [165], which occur due to the repetition of layers. The second way of tuning the gap is by the application of strain [168, 169]. Monolayer phosphorene can sustain large in-plane compressive/tensile strain of up to 10%, compared to 2% in bulk [170]. The gap in black phosphorus is predicted to show a large dependence on strain [171]. In bilayer black phosphorus, recent experiments demonstrate a ten percent change of the gap when 1% uniaxial strain is applied, irrespective of the zigzag or armchair direction [165]. The third way of manipulating the gap is by changing the dielectric constant of the substrate or capping. In two-dimensional materials the screening of the Coulomb interaction is very weak and the gap is expected to depend strongly on the dielectric constant of the neighboring material [162, 168, 172, 173]. The gap values can be further changed by alloying with arsenic, such that even lower values than 0.3 eV can be reached [14].

Ref.	T/E	Method	ε (substr.)	$a_1/a_2/a_3$ [Å]	Δ_f [eV]	Δ_o [eV]	Δ_b [eV]
	T	PBE	1	3.31/4.38/500	**0.80**		
[174]	T	PBE	1	3.34/4.57/15	0.84		
[174]	T	HSE06	1	3.34/4.57/15	1.52		
	T	B3LYP	1	3.31/4.38/500	**1.88**		
[175]	T	G_0W_0@PBE	1	3.31/4.38/25	1.6		
[176]	T	GW_0@PBE	1	3.31/4.38/25	1.85		
[177]	T	GW_0@PBE	1	3.31/4.52/18	1.94		
[178]	T	G_0W_0@PBE	1	3.31/4.63/15	2.03		
[178]	T	GW_0@PBE	1	3.31/4.63/15	2.29		
[179]	T	GW_0@HSE06	1	3.30/4.50/15	2.41		
[180]	T	BSE@G_0W_0@PBE	1	–/–/30	1.83	1.32	0.51
[167]	T	BSE@G_0W_0@PBE	1		2.0	1.2	0.8
[181]	T	BSE@G_0W_0@PBE	1	3.30/4.59/25	2.1	1.3	0.8
[182]	T	BSE@GW_0@PW91	1	3.32/4.62/30	2.26	1.43	0.83
[183]	T	DMC@model	1				0.744
[183]	T	DMC@model	3.8				0.405
[168]	T	numerical@model	1				0.76
	T	DMC@B3LYP@cluster	1	3.31/4.38	**2.36(14)**	*1.72(10)*	*0.64(4)*
	T	DMC@PBE@periodic	1	3.31/4.38/50	**2.54(15)**	*1.85(11)*	*0.69(4)*
	T	DMC@B3LYP@periodic	1	3.31/4.38/50	**2.68(14)**	*1.96(10)*	*0.72(4)*
[177]	E	STS	bulk-BP		2.05		
[184]	E	PLE	SiO_2		2.2(1)	1.3(0.02)	0.9(0.12)
[162]	E	PL	SiO_2-Si		*1.98*	1.45	
[165]	E	PL	SiO_2		*2.29*	1.67	
[185]	E	OA	Al_2O_3/hBN		*2.37*	1.73	
[186]	E	PL	SiO_2-Si		*2.40*	1.75(0.04)	
[172]	E	PL	SiO_2		*2.74*	2.0(0.04)	
[172]	E	PL	Si		*2.88*	2.1(0.02)	

Table 6.1: Theoretical (T) and experimental (E) values of fundamental (Δ_f) and optical (Δ_o) gaps, as well as exciton binding energies ($\Delta_b = \Delta_f - \Delta_o$) in phosphorene. In the rows for theoretical studies, we list DFT calculations by indicating the exchange-correlation functional. Kohn–Sham gaps are listed in the fundamental gap column. In *GW* calculations, we indicate which type of *GW* was used and on which functional it is based on. Theory solving the Bethe–Salpeter equation to calculate electron-hole binding are indicated by BSE. Model studies [168, 183] solve effective center-of-mass Hamiltonians with a Keldysh potential for the interaction term. Values appearing in italic are estimates using the scaling Eqs. (6.1) and (6.2) [180]. Lattice constants with vacuum thickness (a_3) in theoretical approaches are listed. The column ε reports on the dielectric constant of the substrate or on the material used as substrate and encapsulation in the case of Al_2O_3/hBN. The experimental method abbreviations are as follows: STS – scanning tunneling spectroscopy, PLE – photoluminescence excitation spectroscopy, PL – photoluminescence, OA – optical absorption. The results of this work appear in bold and without reference.

A vast amount of theoretical and experimental studies concerning the optical properties of phosphorene is available, see Tab. 6.1. When referring to the gap, it is important to distinguish the fundamental gap from the optical gap. The latter is experimentally more accessible and corresponds to the minimal energy a photon needs to have in order to get absorbed by the solid. The optical gap is related to the formation of an electron-hole pair, while the fundamental gap represents the quasiparticle gap (for a more detailed discussion see Sec. 6.2). The optical spectra from experiments in Tab. 6.1 are measured with optical absorption, reflection, or photoluminescence measurements and values between 1.3–2.1 eV are found for the optical gap [162, 165, 172, 184–186]. Experimental gap values are very scattered and may depend strongly on external influences.

As the screening in two-dimensional materials is typically quite low, excitonic effects are also very pronounced in phosphorene. This is the reason why the optical gap differs from the fundamental gap by the exciton binding energy. The binding energy in large-gap materials can be very large, on the order of several hundred meVs [180]. High-gap two-dimensional materials have smaller in-plane screening than low-gap materials. The lower the screening, the more localized is the exciton, which is typically found to be spread out in the nm range. The hydrogen atom is often taken as a model for Wannier–Mott excitons. In three dimensions and with the absence of screening one finds a radius of about 0.53 Å and a very strong binding energy of −13.6 eV. Comparing the spatial extents, the order of magnitude for the exciton binding energy of about 700–800 meV in phosphorene [167, 168, 181–183] is plausible, although excitons in two dimensions are fundamentally different from a simple 2D/3D hydrogenic model system [187].

Recently, it was established that a linear relationship,

$$\Delta_\mathrm{b} \approx 0.27\ \Delta_\mathrm{f}, \tag{6.1}$$

exists between the fundamental gap Δ_f and the binding energy of the exciton Δ_b [180], irrespective of atomic species and lattice arrangements in two-dimensional systems. This relationship can be used to express the optical gap ($\Delta_\mathrm{o} = \Delta_\mathrm{f} - \Delta_\mathrm{b}$) in terms of the fundamental gap by

$$\Delta_\mathrm{f} \approx \frac{1}{1 - 0.27}\Delta_\mathrm{o}. \tag{6.2}$$

Experimental measurements of the fundamental gap are rare. The fundamental gap of phosphorene was measured to be 2.05 eV with the help of scanning tunneling spectroscopy [177]. Another experiment [184] determined the fundamental gap of phosphorene to be 2.2 eV employing photoluminescence excitation spectroscopy. Theoretical predictions for the optical and fundamental gaps are within a broad range of values, see Tab. 6.1. The state-of-the-art theoretical method to determine fundamental band gaps is the *GW* approximation. It is a perturbative theory, which is based on DFT calculations to predict quasiparticle excitations. *GW* calculations usually reliably predict band gaps, but care needs to be taken to converge with respect to its parameters [188]. The *GW* predictions of the fundamental gap of monolayer black phosphorus range between 1.6 and 2.4 eV [167, 175–182], depending on the exchange-correlation functional used for the DFT calculation, the level of self-consistency, and on the convergence parameters.

Here, we carry out ground and excited state calculations of phosphorene, employing the quantum Monte Carlo (QMC) methods described in Sec. 2.5. QMC was already applied to phosphorene to study ground state properties of other 2D allotropes [189], as well as to determine the nature of interlayer interaction in bulk and few-layer black phosphorus [190]. The calculations revealed large differences between interlayer interaction energies and binding distances in bulk and bilayer black phosphorus, obtained by different DFT functionals and van der Waals correction schemes. Ground state diffusion Monte Carlo (DMC) calculations can provide a benchmark for these correction schemes.

In our study, we employ two different model systems to calculate the fundamental gap of free-standing phosphorene. We determine the fundamental gap for a system with periodic boundary conditions, as well as for a macroscopic molecule of phosphorene saturated with hydrogen atoms. Our starting point is a DFT calculation, where we use two different exchange-correlation functionals, namely the Perdew–Burke–Ernzerhof exchange-correlation functional (PBE) [28] and the Becke 3-parameter (exchange), Lee, Yang and Parr exchange-correlation functional (B3LYP) [30], to quantify the fixed-node dependency inherent in DMC calculations. We also determine the cohesive energy, which gives us a quantity to compare our ground state calculation to experiments.

This chapter is organized in the following way. We first introduce and discuss the fundamental gap and its relation to the optical gap in Sec. 6.2. In Sec. 6.3, the phosphorene lattice is defined and basic system properties are discussed. The DFT electronic structure is presented in Sec. 6.4 with focus on the band structure of two different exchange-correlation functionals and its basis set dependence. In Sec. 6.5, the QMC method is applied to phosphorene, showing which trial wave functions have been used and how they were optimized. After analyzing data correlations and errors, we discuss finite-size effects of the supercell calculations and determine the cohesive energy. In Sec. 6.6, we provide another approach to describe the system by finite phosphorene cluster QMC calculations. We present the obtained fundamental gaps for periodic and cluster calculations in Sec. 6.7, give an interpretation of our values with respect to experiments in Sec.6.8, and conclude in Sec. 6.9.

6.2 Fundamental gap

The fundamental gap Δ_f is one of the most important properties of matter. It characterizes a material as a metal or an insulator. The fundamental gap in a solid as well as in molecules is defined in terms of the energy difference of ionization potential E_I and electron affinity E_A [191] (the energy necessary to remove an electron from the system and the energy gained by adding an electron to the system, respectively),

$$\Delta_\mathrm{f} = E_\mathrm{I} - E_\mathrm{A} = (E_{N-1} - E_N) - (E_N - E_{N+1}). \tag{6.3}$$

The formula for the fundamental gap involves ground state energy differences of N- and $(N \pm 1)$-electron systems.

While being a many-body problem, effective noninteracting theory can give first in-

sights into the issue of calculating the fundamental gap. Within Hartree–Fock theory, the fundamental gap of Eq. (6.3) can be estimated by the Koopmans approximation [191, 192],

$$\Delta_{\mathrm{f}} \approx (E^{\mathrm{HF}}_{N-1} - E^{\mathrm{HF}}_{N}) - (E^{\mathrm{HF}}_{N} - E^{\mathrm{HF}}_{N+1}) \approx \varepsilon_{\mathrm{L}} - \varepsilon_{\mathrm{H}}. \tag{6.4}$$

This approximation evaluates the total energies of Hartree–Fock Slater determinants, which are built from single-particle orbitals ψ_i, obtained by a Hartree–Fock calculation of the N particle system with eigenvalues ε_i. For the $(N \pm 1)$ states, rows and columns of single-particle orbitals $\psi_{N+1}(\mathbf{r}_i) = \psi_{\mathrm{L}}(\mathbf{r}_i)$ $[\psi_N(\mathbf{r}_i) = \psi_{\mathrm{H}}(\mathbf{r}_i)]$ are added (removed) to (from) the determinant and evaluated on the $(N \pm 1)$-electron Hamiltonian. Assuming frozen orbitals (that is, no self-consistency in the orbitals for the charged systems), equality holds in Eq. (6.4) and the fundamental gap is given in terms of the difference of lowest unoccupied molecular orbital (LUMO) and highest occupied molecular orbital (HOMO) eigenvalues of the N-electron calculation. In a solid, instead of valence band maximum and conduction band minimum we refer to them still as HOMO and LUMO, respectively.

There is also a second interpretation of the fundamental gap. It can be regarded as the onset of the continuum for neutral excitations. With respect to this onset, excitations can be bound. This happens in the case of photon absorption, where the Coulomb interaction between the created electron and hole provides a binding energy Δ_{b}, and forms a bosonic quasiparticle, an exciton, such that the fundamental gap will be reduced to the optical gap,

$$\Delta_{\mathrm{o}} = \Delta_{\mathrm{f}} - \Delta_{\mathrm{b}}. \tag{6.5}$$

The optical gap can be measured for example by means of photoluminescence or optical absorption experiments, see Tab. 6.1.

Also Hartree–Fock theory provides direct access to such an interpretation [191]. In a vertical excitation, an electron is promoted from the HOMO into the LUMO. The ground state is represented by the Slater determinant $|\psi_1\psi_2\cdots\psi_{N-1}\psi_{\mathrm{H}}\rangle$ and the neutral excited state can be represented by the Slater determinant $|\psi_1\psi_2\cdots\psi_{N-1}\psi_{\mathrm{L}}\rangle$, where the HOMO orbital, $\psi_{\mathrm{H}}(\mathbf{r})$, was replaced by the LUMO orbital, $\psi_{\mathrm{L}}(\mathbf{r})$. Within Hartree–Fock, this leads to the excitation energy [191]

$$\begin{aligned}\Delta_{\mathrm{o}} &\approx \langle\psi_1\psi_2\cdots\psi_{\mathrm{L}}|\,\hat{H}^{\mathrm{HF}}\,|\psi_1\psi_2\cdots\psi_{\mathrm{L}}\rangle - \langle\psi_1\psi_2\cdots\psi_{\mathrm{H}}|\,\hat{H}^{\mathrm{HF}}\,|\psi_1\psi_2\cdots\psi_{\mathrm{H}}\rangle \\ &\approx \varepsilon_{\mathrm{L}} - \varepsilon_{\mathrm{H}} - J_{\mathrm{HL}} + K_{\mathrm{HL}},\end{aligned} \tag{6.6}$$

where

$$J_{\mathrm{HL}} = \int \mathrm{d}^3r \int \mathrm{d}^3r' \frac{|\psi_{\mathrm{H}}(\mathbf{r})|^2 |\psi_{\mathrm{L}}(\mathbf{r}')|^2}{|\mathbf{r}-\mathbf{r}'|} \tag{6.7}$$

is the Coulomb interaction and

$$K_{\mathrm{HL}} = \delta_{\sigma_{\mathrm{H}}\sigma_{\mathrm{L}}} \int \mathrm{d}^3r \int \mathrm{d}^3r' \frac{\psi^*_{\mathrm{L}}(\mathbf{r})\psi_{\mathrm{H}}(\mathbf{r})\psi^*_{\mathrm{H}}(\mathbf{r}')\psi_{\mathrm{L}}(\mathbf{r}')}{|\mathbf{r}-\mathbf{r}'|} \tag{6.8}$$

the exchange matrix element between HOMO and LUMO states. We again assumed

frozen orbitals. The leading term of Δ_o is the eigenvalue difference $\varepsilon_L - \varepsilon_H$, representing the fundamental gap as the onset of the continuum. The next leading term is the negative Coulomb interaction. Upon excitation, the electron and hole form a bound state. In this single-orbital excitation case, the value of J_{HL} will mainly depend on how spread the single-particle orbitals are, determining effectively if the electron and hole can be close to each other, or not. In small molecules, the orbitals are generally localized and there will occur a significant binding [191]. The more extended the orbitals $\psi_H(\mathbf{r})$ and $\psi_L(\mathbf{r})$, the smaller the Coulomb interaction will be. In the limit of infinitely extended orbitals, the Coulomb interaction goes to zero as, on average, the electron and hole do not interact. The last term in Eq. (6.6), the exchange energy K_{HL}, is diagonal in spin space. It is zero for exciting an up-electron to a down-electron ($\psi_L^\uparrow \to \psi_H^\downarrow$) and nonzero for exciting an up-electron to an up-electron ($\psi_L^\uparrow \to \psi_H^\uparrow$). This leads to a slightly increased Δ_o for the singlet-excitation compared to the triplet excitation. We will consider only same-spin excitations in this work.

A bound exciton will only be realized if the excited state wave function is localized such that the electron and hole can interact. In a solid, if only the HOMO and LUMO Bloch states at the Γ point are considered, the electron and hole wave functions will be extended infinitely throughout space and the Coulomb interaction is negligible. In this limit, Eqs. (6.3) and (6.6) are expected to give *the same result* [191]. In this work, we will exclusively use Eq. (6.6) for our QMC calculations, which is just an energy difference of two neutral states. We expect Eq. (6.3) to converge much slower with respect to system size as two of the three involved states represent two-dimensional charged states, which are expected to show large Coulomb finite-size errors due to the inefficient screening of the surrounding vacuum. By using Eq. (6.6) instead of Eq. (6.3) we also save one third of computational time, which is significant for the costly QMC calculations.

Within Hartree–Fock theory, the correlation energy is neglected and the fundamental gap will be greatly overestimated. One has to be careful in the interpretation of eigenvalue gaps resulting from single-particle theories. As exact Kohn–Sham theory provides the ground state energy, this theory is in principle able to evaluate Eq. (6.3) directly for nonperiodic systems. For small molecules, the *exact* Kohn–Sham gap also turns out to be very close to experimental optical gaps [191]. Neither in molecules nor in solids, is the exact Kohn–Sham HOMO–LUMO gap expected to give the real fundamental gap [191]. In calculations for *extended* systems, when dealing with approximate exchange-correlation functionals, for example LDA or GGA, as well as hybrid functionals, the HOMO–LUMO Kohn–Sham gap gives the same value as an evaluation of the fundamental gap with Eq. (6.3) [193]. The state-of-the-art approach to the calculation of the fundamental gap in solids is the *GW* formalism, which is a perturbative theory on DFT calculations, based on the quasiparticle Green's function G and the screened Coulomb interaction W. Within this method, one is able to determine the fundamental gap via the poles of the Green's function, which can be directly interpreted in terms of excitation energies of the many-body system. On top of *GW*, one may calculate the optical spectrum by solving the electron–hole Bethe–Salpeter equation [194]. Here, we try to evaluate the fundamental gap with the QMC approach by means of Eq. (6.6).

6.3 Phosphorene lattice

Similarly to graphene, which can be exfoliated from its parent material graphite, a monolayer of black phosphorus, phosphorene, can be extracted from its bulk counterpart [162]. A phosphorene sheet is shown from the side view in Fig. 6.1(a) and from top in Fig. 6.1(b). The lattice can be described by a rectangular unit cell with two lattice constants a_1 and a_2, containing four phosphorus atoms, see Fig. 6.1(b). The system shares some directional features with the graphene lattice and is a distorted hexagonal system. The phosphorene lattice can be thought of a two-layered system with repeated zigzag chains in the upper and lower layers, separated by a distance d_z [see Fig. 6.1(c) for the definition]. These zigzag chains of one layer are bonded to the other layer forming ridges with so-called armchair shape, see Fig. 6.1(a). Also, when viewed from top in Fig. 6.1(b), an armchair direction can be identified along the y-direction, similarly to the concept encountered in graphene. The lattice has a nonsymmorphic D_{2h} symmetry group [163], which includes inversion symmetry. The structure is rather complicated and symmetry-wise poses a severe test for *ab initio* codes. The atoms are found in a puckered sp^3-like bonding configuration with three neighboring phosphorus atoms. Together with the five valence electrons of a phosphorus atom this results in one lone-pair orbital per phosphorus atom, which makes it reactive to air and presumably favors this rippled appearance.

One consequence of this highly anisotropic system is that the $\mathbf{a}_2$ (armchair) direction is soft with respect to strain. A variation of $\Delta a_2 \leq 0.3$ Å results in only 5 meV change in energy per atom [190]. Such a behavior allows the system to withstand about 10% compressive/tensile in-plane strain [170]. The survey of predicted lattice constants in literature, see Tab. 6.1, reveals a large spread in DFT-optimized values of a_2, of about 4.50–4.63 Å [195], which is 3–6% larger than the experimentally reported value of 4.38 Å in the bulk system [196]. In the case of the a_1 direction, the variation is much smaller with 3.31–3.34 Å, agreeing also with the bulk value of 3.31 Å [196]. In the course of DMC studies of the interlayer binding of black phosphorus [190], also the a_2 lattice constant of monolayer phosphorene was calculated to be 4.32 Å, a *smaller* value compared to the bulk experimental one. Interestingly, this represents a compression rather than an expansion as predicted by DFT. As this value should be more accurate than the DFT ones and it is close to the experimental value of bulk black phosphorus, we take the measured bulk values to define our lattice [196]. The lattice constants are $a_1 = 3.3136$ Å, $a_2 = 4.3763$ Å, and $a_3 = 10.478$ Å with the Wyckoff position (0.00000, 0.08056, 0.10168) of the space group 64 Cmca. From this bulk system we cut out the monolayer (see also the `Crystal 14` input listing in App. D). With these lattice parameters, the inter-plane bond angle of $\theta_{\mathrm{P}} = 102.1^\circ$ and inter-plane bond length of $d_{\mathrm{P}} = 2.24$ Å can be extracted [see Fig. 6.1(c)].

In the quasi-2D calculations, the vacuum was formally set to 500 Å. For QMC calculations, we construct supercells of size $L \times L$, where L goes from 1 to 6, containing $N = 4L^2$ (4, 16, 36, 64, 100, and 144) atoms. The Γ points of their respective Brillouin zones fold back into the Brillouin zone of the 1×1 system as indicated in Fig. 6.1(d).

6.4 DFT electronic structure

Density functional theory, while reasonably accurate and relatively cheap in computational time, gives us a tool to study solids. As these calculations provide the starting point for our QMC calculations, we want to assess their quality. The calculations were carried out with the DFT code `Crystal 14` [53], which is able to deal with periodic calculations based on Gaussian basis sets. The choice of this code was necessary for a later conversion to the QMC code `qwalk` [44]. The phosphorus atom with electronic configuration [Ne] $3s^2\ 3p^3$ was modeled with five valence electrons by using a smooth scalar-relativistic pseudopotential, optimized for DMC calculations by Burkatzki et al. [197] (see App. D). Basis sets of VDZ (valence double-zeta) and VTZ (valence triple-zeta) quality, as well as the pseudopotential, were obtained from the website of Burkatzki[1]. Calculations were carried out with a minimal k point sampling of 12×12, such that the total energy was converged better than 10^{-4} Ha, leading to converged band gaps as well.

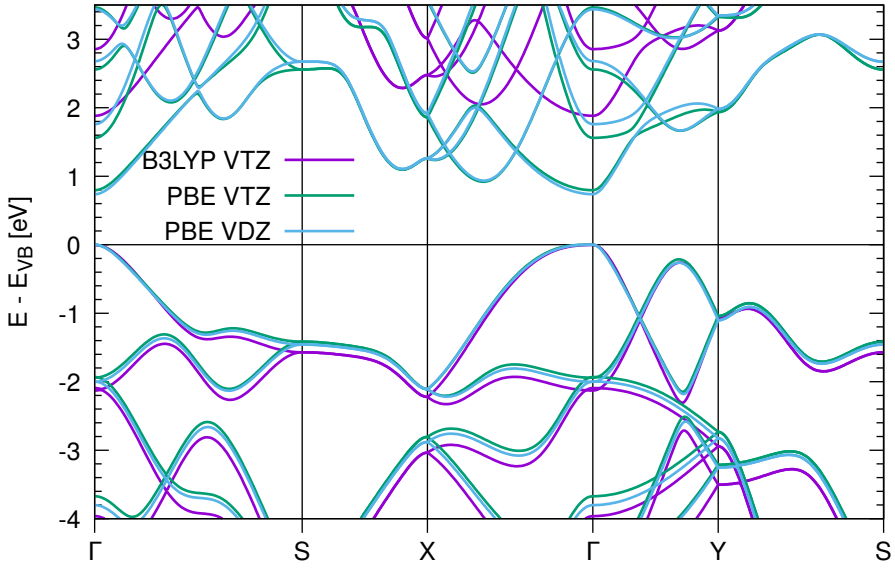

Figure 6.2: Band structure of phosphorene for different exchange-correlation functionals (PBE and B3LYP and basis sets (VDZ and VTZ) along high-symmetry lines [see Fig. 6.1(d)]. Energies are shifted with respect to the valence band maximum. The Kohn–Sham band gaps are 0.74 and 0.80 eV for PBE, and 1.88 eV for B3LYP.

In Fig. 6.2, we show the band structure of phosphorene along high-symmetry paths from the Brillouin zone in Fig. 6.1(d) for a hybrid functional B3LYP [30] (see Sec. 2.2.2), and a generalized gradient approximation functional PBE [28]. We find, in accordance with literature [163, 175], a very anisotropic band structure at the Γ point, reflecting the anisotropic shape of the lattice. We find a direct band gap at the Γ point with Kohn–Sham band gaps of 0.80 eV and 1.88 eV for calculations with PBE and

[1] http://www.burkatzki.com/pseudos/index.2.html

B3LYP, respectively. These values are similar to what is found in literature for PBE of 0.84 eV [174] or calculations based on the range-separated hybrid functional HSE06 of 1.52 eV [174]. The Kohn–Sham band gap changes from 0.74 eV to 0.80 eV, when increasing the basis set from VDZ to VTZ. The computationally most demanding part in later QMC calculations will be the evaluation of the wave function and its gradients. Therefore, due to computational limitations, the rest of the calculations are carried out with the VTZ basis set (instead of taking an even bigger one), observing an error of 0.05 eV in the Kohn–Sham band gap.

If one attempts to interpret the Kohn–Sham gap in terms of the fundamental gap of a solid, experimental gap values will be most commonly underestimated. The exact Kohn–Sham band gap is known to not equal the fundamental gap [191, 193] and, in general, LDA and GGA approximations to the exchange-correlation functionals give much lower values than experimentally measured. To give more empirical predictive power to band gap calculations of DFT, some fraction of exact-exchange from Hartree–Fock theory can be added, which often increases the band gap. This is also what can be seen here, when the PBE and B3LYP band gaps are compared. The two functionals give Kohn–Sham gap values differing by 1 eV. By using these very different inputs to our QMC calculations we can judge about the level of dependence on the DFT starting calculations.

6.5 QMC for periodic phosphorene

The methods of QMC have proven to be very accurate and are one of the most precise methods to calculate ground state properties for atoms, molecules, and solids [43]. In the two-dimensional realm, QMC was applied to theoretically verify the preferred AB stacking of bilayer graphene [198] and to determine its equilibrium van der Waals gap. In these calculations, van der Waals interactions are implicitly included in the full many-body Hamiltonian and therefore constitute benchmark results for dispersion correction schemes in DFT.

DMC works very well for systems involving phosphorus atoms, as fixed-node errors are typically rather small in second-row atoms [199]. Spin-orbit coupling effects, which are not accounted for in Hamiltonian (2.1), can also be neglected for phosphorus, which makes phosphorus-based solids ideal candidates to study with the QMC method.

QMC was already successfully applied to bulk and monolayer phosphorene [189, 190]. Similarly to the graphene bilayer calculations, the binding energy curve with respect to the sheet distances was determined for bulk and bilayer black phosphorus in AB stacking and compared to state-of-the-art dispersion-corrected DFT functionals [190]. Another important result was the determination of bulk and monolayer soft a_2 lattice constants of 4.40 Å and 4.32 Å, respectively. The result for the bulk lattice constant agrees to within half a percent with the experimental bulk value [196]. The same bulk value was measured also for the surface of a black phosphorus crystal by STM [200]. The value found by DMC calculations for the monolayer a_2 lattice constant is only 1.4% smaller than for bulk, reassuring our usage of the bulk lattice constant for a_2 and not using DFT optimized values.

In another work, DMC was applied to study a so-called martensitic (nondiffusive)

lattice phase transition from blue to black phosphorus [189]. Blue phosphorus has the same hexagonal lattice as graphene with the difference that A and B atoms are alternating in z height, which is very similar to silicene or germanene. In agreement with DFT calculations employing the PBE functional, the DMC calculations find that black and blue phosphorus are degenerate. The rather small barrier between the two allotropes of about 0.4 eV/atom is however underestimated by DFT by about 25%, even when a hybrid functional was used.

All of the previous works have in common that the solids were treated as periodic in two dimensions, where positions of electrons were periodically repeated in the form of Hamiltonian (2.1). The Coulomb energy between N periodically repeated pointlike charges q_i and q_j (representing electrons and ions) in the unit cell is given by

$$U = \frac{1}{2}\sum_{i=1}^{N}\sum_{j=1}^{N}{\sum_{\mathbf{R}}}' \frac{q_i q_j}{|\mathbf{r}_{ij}+\mathbf{R}|}. \tag{6.9}$$

The charges are separated by a distance $\mathbf{r}_{ij} = \mathbf{r}_j - \mathbf{r}_i$ plus a supercell lattice vector $\mathbf{R}$, where the term $i = j$ is excluded by the primed sum, when $\mathbf{R} = 0$ (excluding self-interaction of the charge). The sum in Eq. (6.9) does not converge absolutely, i.e., it diverges when summed over absolute values, and does so only slowly. This problem was solved for 3D periodic systems by Ewald [201–203], deriving the Ewald energy

$$\begin{aligned} U =& \frac{1}{2}\sum_{i=1}^{N}\sum_{j=1}^{N}{\sum_{|\mathbf{R}|=0}^{\infty}}' \frac{q_i q_j \mathrm{erfc}(\alpha|\mathbf{r}_{ij}+\mathbf{R}|)}{|\mathbf{r}_{ij}+\mathbf{R}|} \\ &+ \frac{1}{2\pi V}\sum_{i=1}^{N}\sum_{j=1}^{N}\sum_{\mathbf{G}\neq 0} q_i q_j \frac{4\pi^2}{G^2}\exp\left(-\frac{G^2}{4\alpha}\right)\cos(\mathbf{G}\cdot\mathbf{r}_{ij}) \\ &- \frac{\alpha}{\sqrt{\pi}}\sum_{i=1}^{N} q_i^2 \\ &+ J(\mathbf{M}, P). \end{aligned} \tag{6.10}$$

The main idea behind the Ewald method is to divide the charge density into a short-range and a long-range part, which also allows to divide the electrostatic potential and energy into short-range and long-range parts [203]. While not obvious at first, this can be achieved by addition and subtraction of Gaussian charge densities $G_\sigma(\mathbf{r})$, where each Gaussian charge density is centered at the point of the charges q_i with the same integrated charge of q_i and standard deviation of $\sigma = 1/(\sqrt{2}\alpha)$, such that the charge density of each particle becomes

$$\rho_i(\mathbf{r}) = \underbrace{q_i\delta(\mathbf{r}-\mathbf{r}_i) - q_i G_\sigma(\mathbf{r}-\mathbf{r}_i)}_{\text{short-range}} + \underbrace{q_i G_\sigma(\mathbf{r}-\mathbf{r}_i)}_{\text{long-range}}. \tag{6.11}$$

The long-rangedness of the Coulomb potential of the long-range charge density can be seen by integrating Poisson's equation for a Gaussian charge density [203]. It can

be found to be the Coulomb potential of a pointlike charge multiplied by the error function $\mathrm{erf}(r) = \frac{2}{\sqrt{\pi}} \int_0^r e^{-t^2}\, \mathrm{d}t$, which is small for small r, but gradually approaches unity for larger r and is thus long-ranged.

Due to the subtraction of the Gaussian charge density from the delta function, the solution of Poisson's equation for the short-range charge is proportional to the complementary error function $\mathrm{erfc}(r) = 1 - \mathrm{erf}(r)$. The short-ranged behavior of the complementary error function reflects the screening of the point-like charge by the superimposed Gaussian charge density with opposite charge. This leads to the first term in Eq. (6.10). From this term, one can see that in order to evaluate the short-range electrostatic energy, one only needs to sum over a few first images of the charges in real space. The **R**-cutoff is implicitly enforced by the complementary error function parameter α, which can be arbitrarily chosen such that the summation is computationally most efficient.

The long-ranged potential cannot be computed by real-space summation, but instead needs to be evaluated in reciprocal space. An expression for the reciprocal space evaluation can be obtained by Fourier transformation of the periodic array of Gaussian charges and solving Poisson's equation for the potential in reciprocal space [203]. Inverse Fourier transformation then leads to the real-space potential, which can be obtained by summing over reciprocal lattice vectors **G**, appearing in the second term of Eq. (6.10). It is apparent that this sum is short-ranged in reciprocal space due to the exponential function and can be evaluated efficiently. The third term in Eq. (6.10) is called self-energy and needs to be subtracted as it was already included in the reciprocal space part.

Care has to be taken with the summation order in the real-space sum, which here is summed over shells of $|\mathbf{R}|$ constituting a spherical summation order. Depending on the summation order, a surface correction term $J(\mathbf{M}, P)$ has to be added [202], which depends on the dipole moment $\mathbf{M}$ of the supercell and the summation geometry P. In the case of spherical summation ($P = S$), the surface correction term is

$$J(\mathbf{M}, S) = \frac{2\pi}{(2\varepsilon_\mathrm{s} + 1)V} |\mathbf{M}|^2, \tag{6.12}$$

which depends on the dielectric constant of the surrounding medium ε_s. Although the surface term is in general important, for three-dimensional systems the so-called "tinfoil" boundary condition is often applied, where $\varepsilon_\mathrm{s} \to \infty$ and $J(\mathbf{M}, S) = 0$ [202]. This is the Ewald energy currently implemented in `qwalk`.

For systems periodic in two dimensions and with a finite thickness in the third dimension, just as in phosphorene, the evaluation of the Ewald energy as in Eq. (6.10) is not appropriate and a quasi-two-dimensional analog has to be used [202]. This formulation is computationally much more demanding and requires a complete reimplementation in `qwalk`. Alternatively, it was shown that if one keeps the spherical summation order of real space terms in Eq. (6.10) and taking

$$J(\mathbf{M}, R) = \frac{2\pi}{V} M_z^2 \tag{6.13}$$

as the surface correction, the Ewald summation behaves effectively as if one sums

plane-wise in the periodic directions first and then sums in z-direction. This approach is commonly called EW3DC [202]. It was demonstrated that this approach can excellently reproduce results obtained by the costly quasi-2D Ewald formulation [202]. The surface term Eq. (6.13) was implemented and verified by Rene Derian in `qwalk` by the example of a 4×4 electron-ion configuration of an excited state, comparing it with the quasi-2D approach. The evaluation of the total Coulomb energy within EW3DC and quasi-2D Ewald summation techniques agreed better than 10^{-7} Ha and led to an energy correction of about 0.1 Ha compared to the tinfoil 3D Ewald energy.

With the implementation of periodic boundary conditions by means of the EW3DC technique, one achieves a quickly convergent evaluation of the Coulomb energy with respect to the lattice summation. Using the primitive unit cell of phosphorene as a repetition unit, the images of the electrons would be about 4 Å apart from each other. In a real crystal, such interactions are not present and the resulting Coulomb interaction is spurious. To reduce the interaction of the periodic images, one has to increase the simulation cell size, consisting out of $L \times L$ primitive cells and extrapolate, in order to remove these Coulomb finite-size effects. Several methods exist to correct finite-size effects in ground states, which go beyond this work [204–209].

6.5.1 Trial wave function

The accuracy of the trial wave function is of great importance to reduce the numerical costs of the DMC calculations by decreasing the fluctuations in the local energy (see Sec. 2.5). We employ trial wave functions of Slater–Jastrow type as introduced in Sec. 2.5.2. The Slater part of the ground state trial wave function,

$$\Psi_{\mathrm{T}}^{0} \propto \begin{vmatrix} \psi_1(\mathbf{r}_1) & \psi_1(\mathbf{r}_2) & \dots & \psi_1(\mathbf{r}_N) \\ \psi_2(\mathbf{r}_1) & \psi_2(\mathbf{r}_2) & \dots & \psi_2(\mathbf{r}_N) \\ \vdots & \vdots & \vdots & \vdots \\ \psi_{N-1}(\mathbf{r}_1) & \psi_{N-1}(\mathbf{r}_2) & \dots & \psi_{N-1}(\mathbf{r}_N) \\ \psi_N(\mathbf{r}_1) & \psi_N(\mathbf{r}_2) & \dots & \psi_N(\mathbf{r}_N) \end{vmatrix},$$

is approximated by a determinant built out of $N = L \times L \times 20$ Kohn–Sham orbitals ψ_i, which are obtained from PBE and B3LYP DFT calculations, taken from the Γ point of a periodic calculation. As our system is invariant with respect to time-reversal symmetry we can chose our trial wave function to be real-valued. This antisymmetric part of the wave function fixes the nodal surface (regions in $3N-1$ dimensional space, where the wave function is zero), as the Jastrow factor is positive definite. The determinant is therefore decisive for the magnitude of the fixed-node error in later DMC calculations for different functionals. We include electron–electron and electron–nucleon correlation terms in the Jastrow factor as described in Sec. 2.5.2. The electron–electron (same spin and opposite spin terms) and electron–nucleon terms are parametrized with ten Padé basis functions each, which together with the two γ curvature values (see Sec. 2.5.2) give a compact parametrization with only 32 variational parameters in the Jastrow function.

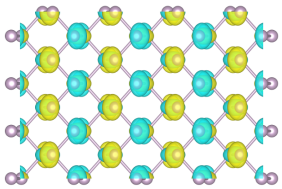

(a) HOMO top: periodic B3LYP

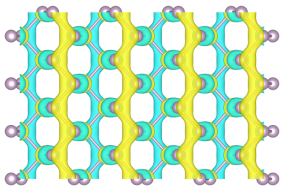

(b) LUMO top: periodic B3LYP

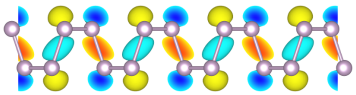

(c) HOMO side: periodic B3LYP

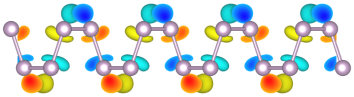

(d) LUMO side: periodic B3LYP

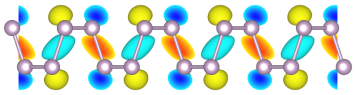

(e) HOMO side: periodic PBE

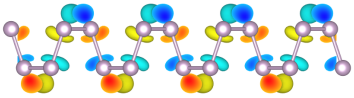

(f) LUMO side: periodic PBE

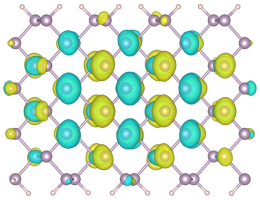

(g) HOMO top: cluster B3LYP

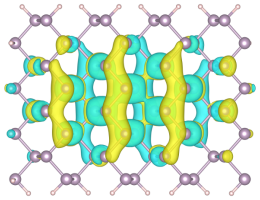

(h) LUMO top: cluster B3LYP

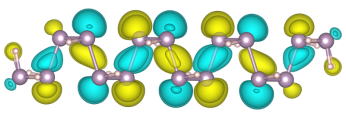

(i) HOMO side: cluster B3LYP

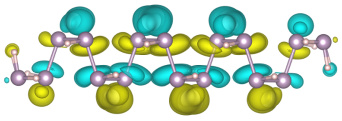

(j) LUMO side: cluster B3LYP

Figure 6.3: Top and side views of Kohn–Sham HOMO (left column) and LUMO (right column) orbitals for 4×4 periodic cells and cluster approximations. Larger spheres indicate phosphorus atoms, smaller spheres are hydrogen atoms. Colored surfaces represent the orbital's isosurfaces of values ± 0.279. Yellow surfaces represent positive valued parts of the orbitals, cyan colored the negative parts. In the side views, cuts through orbitals appear as color gradients, the darker the color, the higher is the orbital value.

For the excited state, we construct a trial wave function by the promotion of one electron from the highest spin-up occupied state (the $\mathbf{r}_i$ carry an implicit spin index)

to the lowest spin-up unoccupied state,

$$\Psi_{\mathrm{T}}^{\mathrm{e}} \propto \begin{vmatrix} \psi_1(\mathbf{r}_1) & \psi_1(\mathbf{r}_2) & \dots & \psi_1(\mathbf{r}_N) \\ \psi_2(\mathbf{r}_1) & \psi_2(\mathbf{r}_2) & \dots & \psi_2(\mathbf{r}_N) \\ \vdots & \vdots & \vdots & \vdots \\ \psi_{N-1}(\mathbf{r}_1) & \psi_{N-1}(\mathbf{r}_2) & \dots & \psi_{N-1}(\mathbf{r}_N) \\ \psi_{N+1}(\mathbf{r}_1) & \psi_{N+1}(\mathbf{r}_2) & \dots & \psi_{N+1}(\mathbf{r}_N) \end{vmatrix},$$

which corresponds to an excitation with spin $S_z = 0$. Once optimized for the ground state, we keep the Jastrow factor the same for the ground and the excited state trial wave functions.

In DMC, there exists only a variational principle for the ground state, even if the ground state is degenerate [210, 211]. For excited states, in general, no such variational principle holds within DMC. However, if the real-valued trial wave function transforms according to a one-dimensional irreducible representation of the symmetry group of the Hamiltonian, then a symmetry-constrained variational principle is available and the DMC algorithm gives an energy greater than or equal to the energy of the lowest exact eigenfunction with that symmetry [210]. The symmetries of the single-particle orbitals entering the excited state trial wave function are enforced by the DFT code and they will transform according to basis functions of irreducible representations of the phosphorene point group D_{2h}. This group only contains one-dimensional irreducible representations, which shows up also in the nondegenerate band structure of phosphorene at the Γ point, see Fig. 6.2. As our many-body trial wave function is composed of an antisymmetrized product of orbitals, which transform according to a real one-dimensional irreducible representation, also the many-body wave function has this transformation property. Therefore, we expect a variational principle to hold also for our excited state wave function.

To get a picture of low-energy single-particle orbitals, we compile in Figs. 6.3(a)–(f) a comparison of the HOMO and LUMO states obtained by B3LYP and PBE calculations. In the top and side views of the HOMO, Figs. 6.3 (a) and (c), we find a state which forms an inter-plane binding combination of p_z orbitals, where also small contributions of p_x and p_y orbitals are present [163]. The LUMO has an additional nodal plane between the phosphorus layers and represents the corresponding antibonding state. From the top view of the LUMO, Fig. 6.3(b) we also find extended stripes of binding orbitals along the zigzag direction. The comparison of side views of HOMO and LUMO states of PBE and B3LYP, Figs. 6.3(c)–(f), shows almost no differences of the orbitals, although one would expect a somewhat more diffusive behavior for the B3LYP LUMO due to exact-exchange [191]. A closer inspection reveals a slight contraction of the B3LYP HOMO with respect to the PBE HOMO and much smaller changes in the LUMOs. The close resemblance of the PBE and B3LYP orbitals are already surprising given the difference of 1 eV in the Kohn–Sham band gaps. It could indicate that fixed-node errors, which are second order in the error of the nodal surface [43], are small.

Single-particle finite-size effects Apart from the Coulomb finite-size effects discussed in the previous section we also encounter so-called single-particle or independent-particle finite-size errors. Our Slater determinant is built from the single-particle Kohn–Sham orbitals taken from the Γ point of a DFT supercell calculation. In independent-particle methods, such as in DFT, one employs Bloch's theorem to eliminate finite-size errors by obtaining the macroscopic limit via Brillouin zone integration [189]. By only taking the Γ point into account in our many-body wave function, we exclude orbitals with different crystal momentum. Due to backfolding of k points, we account for some of them by considering supercells including $N = L \times L \times 20$ electrons. When the real space supercell is doubled in each direction ($L = 2$), the reciprocal Brillouin zone simultaneously shrinks by a factor of two in each direction. In order for the new Brillouin zone to accommodate the $2 \times 2 \times 20$ electrons, the number of bands has to be multiplied by a factor of four with respect to the previous number of bands. In other words, the number of states below the Fermi energy is multiplied by a factor of four also at the Γ point. When the Γ point of the smaller Brillouin zone is periodically repeated, the points will fall also onto k points distinct from the Γ point of the original Brillouin zone, as shown in Fig. 6.1(d). In the 2×2 case for example, the Γ point will include information from the X, Y, and S points of the original band structure. The increase of the supercell size is analogous to the increase in k point sampling in a DFT calculation.

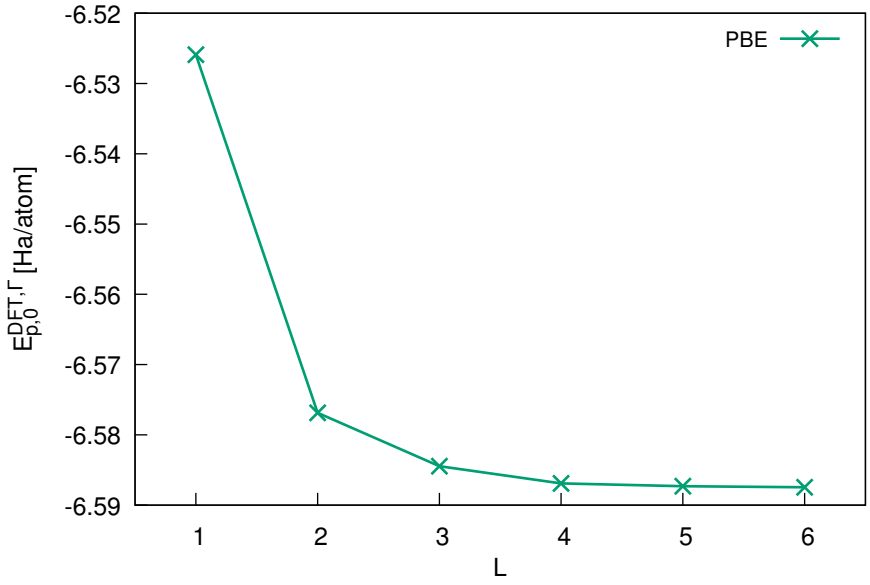

Figure 6.4: Independent-particle finite-size errors obtained from Γ-only single-shot DFT PBE calculations. The total energy per atom is shown for different supercell sizes $L \times L$. The energy difference between $L = 5$ and $L = 6$ supercells is 0.004 eV/atom. Single-particle finite-size errors are most pronounced for the first three supercell sizes.

To estimate the order of magnitude of the single-particle finite-size effects, we show the behavior of the total energy per atom with respect to the supercell size in Fig. 6.4. The data points are obtained from single-shot Γ point DFT PBE calculations, eval-

uating the total energy from a converged charge density. Finite-size effects are very pronounced in the range of 1×1 to 4×4, decreasing by about 0.061 Ha/atom, which is why we expect large single-particle finite-size errors in addition to the Coulomb finite-size effects for small cells. The convergence behavior of B3LYP calculations is very similar. The energy difference for the largest supercells is about $1.6 \cdot 10^{-4}$ Ha/atom or 4 meV/atom. Our preparatory DFT calculations for QMC are not Γ-only calculations, but have a k sampling of at least 6×6, which always includes the Γ point, such that these single-particle finite-size effects are absent in the orbitals at the DFT level, however, they will be present in the QMC calculations.

6.5.2 Trial wave function optimization

The cost of a DMC calculation is determined by the desired accuracy of the total energy. The standard error of the mean $\sigma = \sigma_E/\sqrt{M}$ of the energy depends on the local energy sample variance σ_E^2 [defined in Eq. (2.66)] and decreases only with the square root of statistically independent measurements $\sqrt{M}$ of the energy (see Sec. 2.5.1). In order to reduce the number of needed Monte Carlo steps, the autocorrelation time of the Monte Carlo steps has to be reduced, such that statistically independent measurements can be taken more frequently and/or the local energy variance σ_E^2 has to be reduced. The autocorrelation time can be indirectly reduced by optimizing the energy [212], which also reduces σ_E^2. Contrary to energy optimization, optimization of σ_E^2 is more stable [212], as it is bounded from below by zero. To combine the advantages of both types of optimizations, it was shown that optimizing a linear combination of total energy and variance with 0.95 energy and 0.05 variance is most effective [212]. This optimization method is also the path we follow.

A typical trial wave function optimization is shown in Fig. 6.5. One optimization step is composed out of two procedures. First, we generate a set of walker configurations, distributed according to the trial wave function of the previous optimization run (the parameters of the initial wave function are chosen from commonly observed values) via the VMC algorithm. Second, the set of configurations is used to minimize the parameters in the Jastrow factor with the help of a quasi-Newton algorithm, where the Hessians and gradients of the variance and energy are evaluated on the set of configurations. After a new optimal Jastrow parameter set has been found, the next optimization step is started.

In our scheme, the first optimization steps (in Fig. 6.5, nine of them) are optimizations with respect to variance. One can see that also the energy drops significantly when variance is optimized. For stable variance minimization we only need 2560 walkers, a reduced demand compared to the about 10,000 walkers needed for the refining mixed variance and energy optimization. After that, we switch to mixed minimization, where we can observe a rise in variance, but yet a decrease in energy by 0.1 Ha over the last 20 optimization steps. We consider our optimization converged if the energy does not change more than 0.3 mHa/atom over ten steps. Overall, here in the example of a 4×4 unit cell, the energy decreases by 8.994 Ha and the sample variance by 7.0225 Ha^2 (not shown in Fig. 6.5) with respect to the initial guess. In our calculations, the wave function optimization accounted for about 20% of the total computational cost and we could obtain about 92% of the DMC correlation energy.

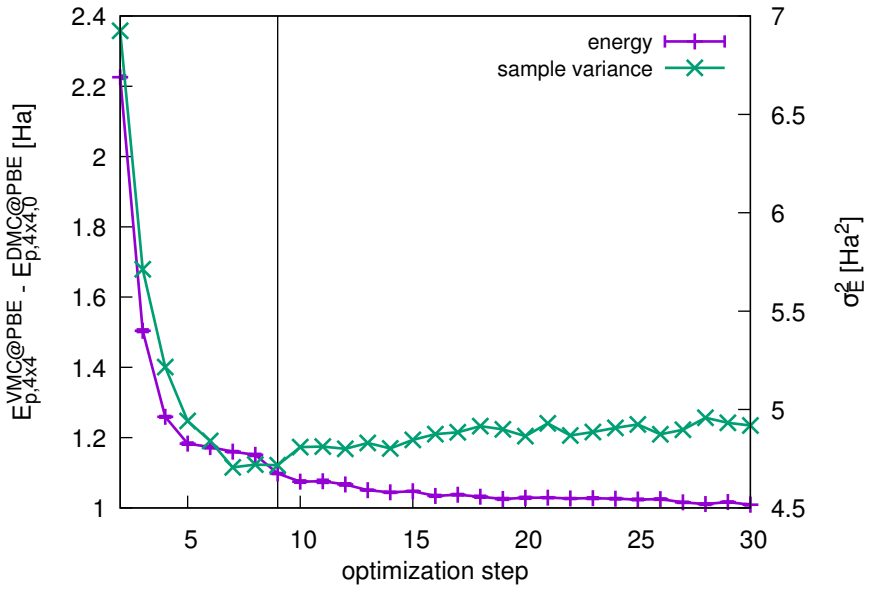

Figure 6.5: Evolution of the VMC energy (measured with respect to the DMC energy) and sample variance (σ_E^2) with respect to the number of optimization steps for the 4×4 supercell. We start with variance optimization; the vertical line indicates the switching to mixed energy and variance optimization. We only show data from the second step on for a better scale.

6.5.3 Data correlation and statistical error estimation

After optimization of the trial wave function, we employ the DMC method (see Sec. 2.5.3) to project out the ground state and cure possible local energy minima obtained by the VMC optimization. We chose a timestep of $\tau = 0.01$ (measured in Ha/$\hbar$), which was considered small enough by previous studies [189, 190] to decrease errors introduced by the small-time Trotter–Suzuki decomposition of the Green's function (see Sec. 2.5.3). The nonlocal pseudopotential was treated with the T-moves procedure to make the calculation variational [213].

A typical DMC trace of local energy measurements can be seen in Fig. 6.6. The calculation was carried out on 2560 cores with in total 23,040 independent walkers. One data point or *block* consists out of $M_{\mathrm{MC}} = 100$ measurements of local energy for each walker, taken after a collective advancement of the Monte Carlo walkers, which constitutes an average over 2,304,000 local energy values. From Fig. 6.6, we can see that the simulation equilibrates after about four blocks, or 400 Monte Carlo steps per walker, because the starting positions of the walkers were initialized with a VMC calculation involving the optimized wave function. The VMC generated positions already represent a good approximation to the ground state distribution.

Typically, subsequent steps of Monte Carlo simulations are correlated, because in a Monte Carlo step, walkers only move a bit away from their previous positions.

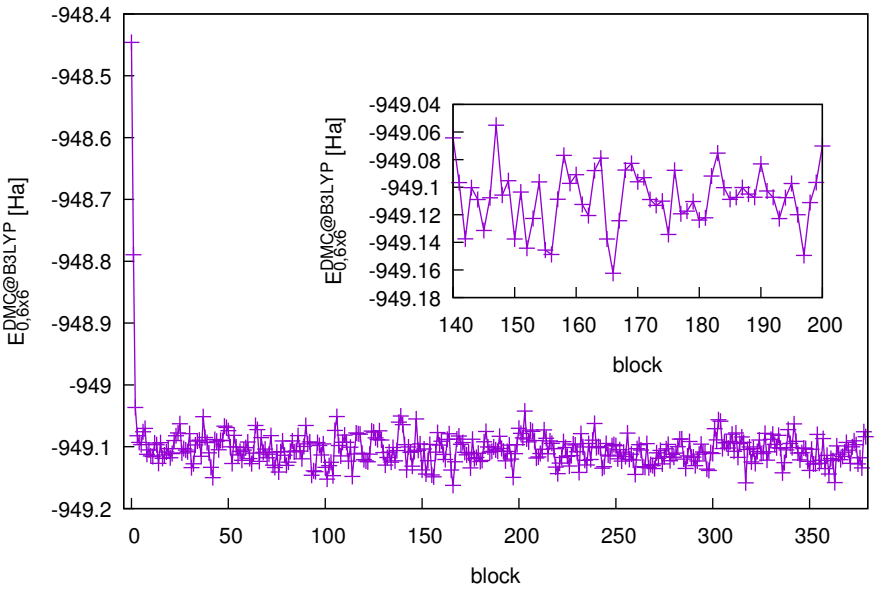

Figure 6.6: Data correlation in the measurement of the ground state DMC energy in the 6×6 periodic calculation. Each block contains 2,304,000 Monte Carlo steps. The inset shows a magnification of the data trace to see possible correlations.

Therefore, a simple estimation of the standard error of the mean, based on the formula

$$\sigma = \sqrt{\frac{\frac{1}{M_\mathrm{b}} \sum_i^{M_\mathrm{b}} (E_i - \bar{E})^2}{M_\mathrm{b} - 1}}, \tag{6.14}$$

where M_b is the number of blocks, E_i the average energy of the block, and $\bar{E}$ the average energy of all blocks, gives in general a biased result and typically underestimates the error [214]. During runtime, we estimate the error based on Eq. (6.14). This is justified by an empirical rule: if the Monte Carlo steps per block and walker, M_MC, multiplied by the timestep τ is about unity, blocks are approximately uncorrelated.

In our case, however, in the zoom-in of Fig. 6.6, one recognizes that data points still depend on each other, indicating presence of data correlation. We tried to evaluate the autocorrelation time based on the autocorrelation function, but the data is already too uncorrelated to do so accurately enough. Therefore, we employ the reblocking method [215] shown in Fig. 6.7. The error of the original data set with no reblocking is about 0.00108 Ha (30 meV). A reblocking transformation combines neighboring data points into a new data point by averaging, such that after the transformation only half of the initial number of data points is left [215]. A new estimate of the error is then carried out by application of Eq. (6.14) to the reblocked data. As soon as the curve in Fig. 6.7 assumes a within the error bars constant value, here after the third reblocking, a good estimate for the error is found [215]. In this case, the error was underestimated by Eq. (6.14) by about 0.0002 Ha or 5 meV by the original data set. A reblocking analysis was carried out for all our energy traces in this work.

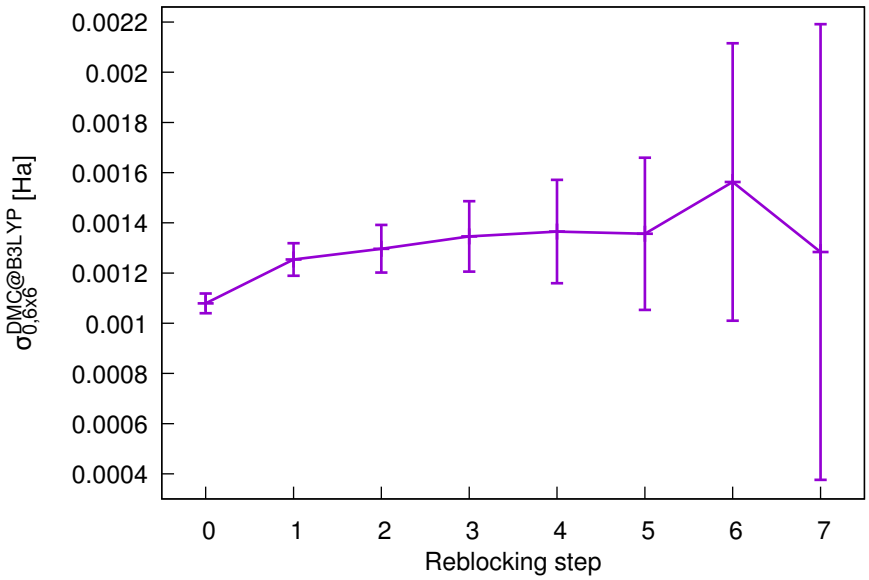

Figure 6.7: Reblocked standard error of mean of the energy data of Fig. 6.6. Error bars show the estimated error in the standard error.

6.5.4 Supercell dependence of the ground and excited state energy

Finite-size effects are present for periodic calculations, most pronounced for small unit cell sizes as discussed in the previous sections. Coulomb finite-size effects arise due to the artificial self-interaction of electrons with electrons in the neighboring supercells. We also expect to see single-particle finite-size effects, which originate from an insufficient number of k points that are effectively incorporated by the wave function. With increasing supercell size $L \times L$, we eventually expect the spurious Coulomb interaction between electron images to be screened away and that an increasing number of k points are incorporated into the wave function by reciprocal momentum backfolding, leading to a reduction of finite-size errors.

In Fig. 6.8, we show the dependence of the ground state total energy per atom versus the number of atoms per unit cell. This graph resembles the behavior of the Γ point DFT calculations in Fig. 6.4. Finite-size effects decrease by 0.059 Ha/atom, demonstrating the large single-particle finite-size effects for the evaluation of the total energy. By subtracting the Γ point DFT data from the DMC data, we find that Coulomb finite-size effects reduce by about 0.0027 Ha/atom (0.070 meV/atom) from 1×1 to the 6×6 supercell. For the evaluation of the ground state energy, this indicates that single-particle finite-size effects are dominant.

We now analyze the energy components of the energy per atom for the ground and excited states, obtained from B3LYP orbitals, versus the supercell size. One important energy component is the Hartree–Fock energy. The Hartree–Fock energy is defined as the evaluation of the many-body Slater determinant, constructed from orbitals of a Hartree–Fock calculation, on the many-body Hamiltonian. The VMC energy $E^{\mathrm{VMC-HF}}$ obtained by such a wave function would precisely recover the Hartree–Fock total energy. Hartree–Fock orbitals are not available to us, which is why we

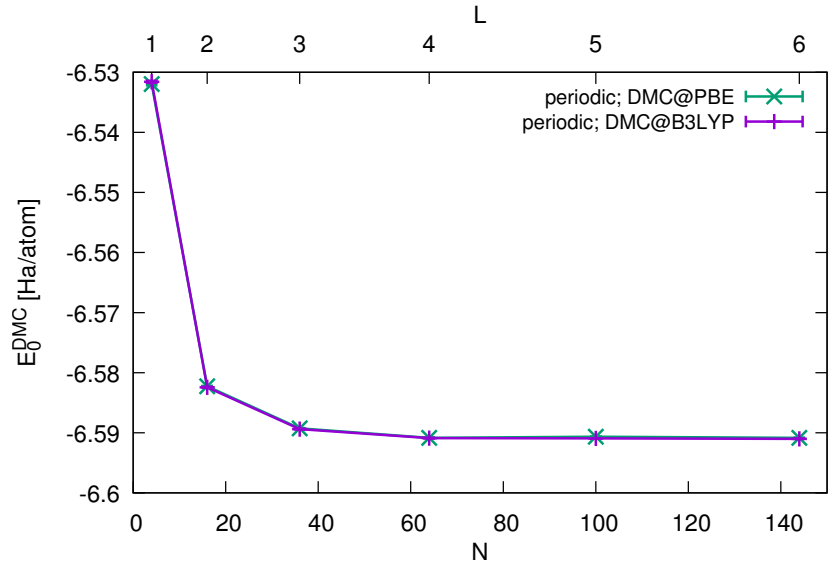

Figure 6.8: DMC energy per atom in the ground state versus the number of atoms, N, in the cell and supercell size, L, for the B3LYP and PBE periodic calculations. The energies for $L = 5$ and $L = 6$ differ by less than 0.005(1) eV/atom. Error bars are smaller than the data points.

approximate the Hartree–Fock energy by taking DFT orbitals instead (excluding any Jastrow factors), which gives an upper bound to the Hartree–Fock total energy. When referring to the Hartree–Fock energy in the following, it is meant as an approximation to the true Hartree–Fock energy. We define the correlation energy then to be the energy difference between the DMC energy and the approximate Hartree–Fock energy, $E^{\text{corr}} = E^{\text{DMC}} - E^{\text{VMC-HF}}$.

In Fig. 6.9, we show Hartree–Fock and correlation energies for ground and excited states with increasing supercell size for B3LYP orbitals. In both calculations, we recognize large finite-size effects in the cell sizes $L = 1 - 3$ for both energy components. From 1×1 to the 4×4 supercell, the Hartree–Fock energy has lowered by 0.066 Ha/atom for the ground state and 0.076 Ha/atom for the excited state. In this range, we see an opposite trend in the correlation energy: it raises by 0.007 Ha/atom and 0.011 Ha/atom for the ground and excited state, respectively. The insets of Figs. 6.9 indicate that convergence of finite-size effects is faster for the ground state than for the excited state. In the case of the Hartree–Fock energy, there is an order of magnitude difference in convergence behavior between the 6×6 ground and excited states. We find that the excited state DMC energy is stronger lowered by the correlation energy than the ground state energy.

The Hartree–Fock energy with -6.39463 Ha/atom in the 6×6 cell makes up for almost all the energy, where for comparison the Hartree–Fock energy for the phosphorus pseudoatom is -6.35908 Ha/atom [197]. Correlation energy accounts for about 3% of the total DMC energy throughout the series of supercells. In phosphorus atoms, the correlation energy was calculated to be -120 mHa/atom [216], which compared to the -197 mHa/atom we find in the solid, is quite smaller in magnitude, indicating a strong contribution to the binding energy of the correlation energy.

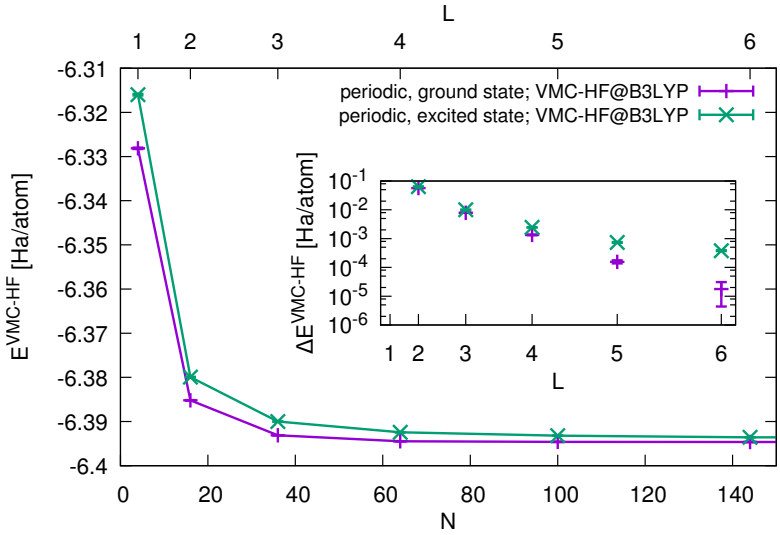

(a) Hartree–Fock energy per atom.

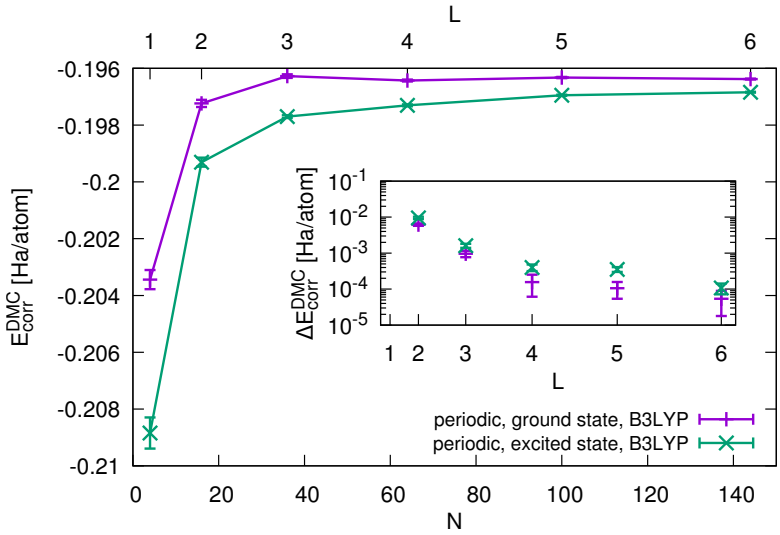

(b) Correlation energy per atom.

Figure 6.9: Hartree–Fock and correlation energy dependence of ground and excited states versus the supercell size. The insets show the convergence behavior of adjacent data points. The Hartree–Fock calculations are VMC calculations, evaluating the many-body Hamiltonian's energy with a Slater determinant based on B3LYP DFT orbitals. The correlation energy was obtained from $E^{\mathrm{DMC}} - E^{\mathrm{VMC-HF}}$.

6.5.5 Cohesive energy

One quantity to judge the quality of a DMC ground state calculation is to compare the calculated cohesive energy to the experimental value. The cohesive energy is the energy necessary to separate a solid into its noninteracting atomic constituents. Experimental cohesive energies for single layer phosphorene are not available. However, one can estimate the phosphorene cohesive energy by knowing the van der Waals binding

energy of black phosphorus (about 0.08 eV/atom [190]), which separates it into single sheets of phosphorene. Since the heat of sublimation for the transformation of black phosphorus into P_4 molecules and the P_4 molecules' cohesive energy is known, this thermodynamic path allows for an estimation of the cohesive energy of phosphorene. This estimation can be found in the supplemental material of Ref. [217] and the idea was given and carried out by Prof. Lubos Mitas. The estimated experimental cohesive energy of phosphorene is 3.29(9) eV/atom. The DFT values for the cohesive energy are 3.01 eV/atom and 3.49 eV/atom for B3LYP and PBE, respectively, which are off from the experimental estimate by −9% and +6%, respectively.

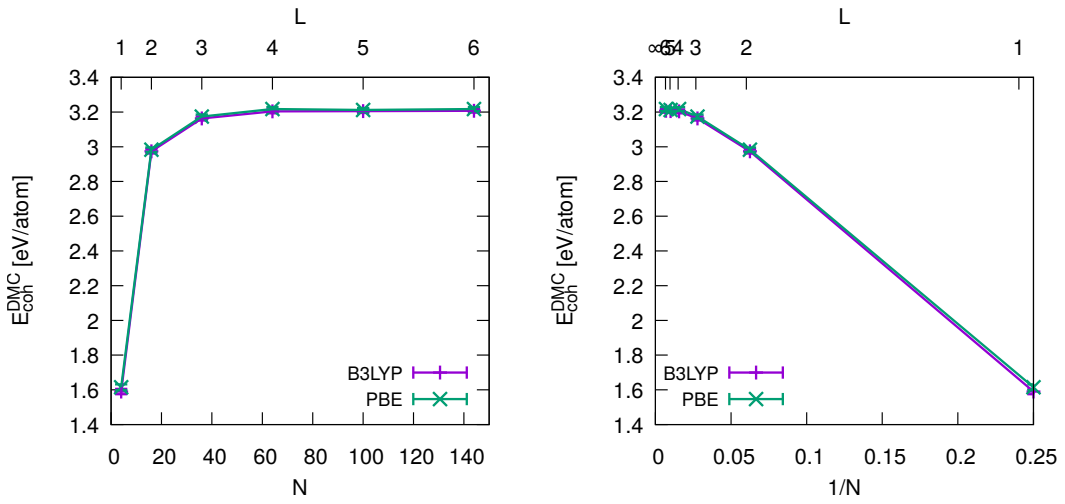

(a) (b)

Figure 6.10: Scaling of the cohesive energy E_{coh} versus the number of atoms in the supercell. The cohesive energy is obtained from $E^{\text{DMC}}_{0,\text{atom}} - E^{\text{DMC}}_{0,L\times L}/N$. In panel (a) the cohesive energy is plotted versus N and in (b) versus the inverse number of atoms $1/N$.

To determine the cohesive energy, also the DMC energy of a single phosphorus atom needs to be known. Our values for the atom are −6.4731(3) Ha and −6.4726(4) Ha for B3LYP and PBE, respectively. The values of cohesive energies $E^{\text{coh}}_{0,L\times L} = E^{\text{DMC}}_{0,\text{atom}} - E^{\text{DMC}}_{0,L\times L}/N$ versus supercell size for two different scalings can be seen in Fig. 6.10. The data is well saturated already at the 4×4 supercell size. From the values of the 6×6 ground state of −6.59101(1) Ha/atom for B3LYP and −6.59085(1) Ha/atom for PBE we estimate cohesive energies of 3.208(13) eV/atom and 3.216(13) eV/atom, respectively. The error bars here are due to the atomic calculation and the neglect of scaling extrapolation in L. Remarkably, the DMC values agree within the error bars and have corrected the DFT values quite significantly and in different directions. Both values underestimate the experimental value by 2.5%, which indicates that a large part of correlation energy has been restored and that the fixed-node errors are rather small and of similar size in both PBE and B3LYP calculations. In general, this leads us to the conclusion that the ground state is described very well.

6.6 QMC for phosphorene clusters

Periodic QMC calculations of solids require scaling with respect to system size as was seen in the previous sections. The Coulomb energy in periodic systems needs to be treated by an Ewald approach to make the Coulomb series convergent. An alternative to treat the solid is to cut out a piece of the crystal and terminate the dangling bonds with hydrogen atoms. We also consider this cluster approach as a control check for the periodic calculations, where we use a series of 4×4, 5×5, and 6×6 analogues of hydrogen-passivated supercells. The 4×4 cluster is shown in Fig. 6.3(g) as an example. The advantage of this approach is that the full many-body Hamiltonian, Eq. (2.1), can be used without replacement of the Coulomb energy by an Ewald sum on the one hand and an absence of periodic images of electrons on the other. However, due to the effective hard-wall boundaries, finite-size quantization is introduced and scaling with respect to system size $L \times L$ is still necessary.

The hydrogen atoms serve to saturate dangling bonds, which otherwise would produce low-energy states in the spectrum and in turn influence the determination of the electronic gap. This hinders us to determine the energy per phosphorus atom directly to compare to the periodic calculations. The number of phosphorus atoms in the simulation cell can be determined by the formula

$$N_{\mathrm{P}}(L) = 4L^2, \tag{6.15}$$

while the number of hydrogen atoms is given by

$$N_{\mathrm{H}}(L) = 4L + 2L = 6L. \tag{6.16}$$

The phosphorus atoms were placed in the same positions as in the periodic system. Outer phosphorus atoms were replaced by hydrogen pseudoatoms and their bonds to the inner phosphorus atoms were relaxed by Rene Derian. Wave functions were prepared in analogy to the periodic calculations, except for the additional electron-nucleon Jastrow degrees of freedom involving the hydrogen atoms. The QMC calculations with the same methodology as in the previous sections have been carried out and total DMC and VMC-HF energies were obtained.

Assuming that each phosphorus and hydrogen atom plays the same role in the bonding (which is not correct in general), we can attempt to decompose the total energy in terms of energy per phosphorus and hydrogen atom, E_{P} and E_{H}, respectively,

$$E(L) = N_{\mathrm{P}}(L)E_{\mathrm{P}} + N_{\mathrm{H}}(L)E_{\mathrm{H}}. \tag{6.17}$$

Assuming that the atomic energies do not change much going from one supercell size to the other, we can determine E_{P} and E_{H} by using the 4×4 and 5×5 energies. The same can be done for 5×5 and 6×6 to check, how well E_{P} and E_{H} are converged.

The solutions for the system of Eqs. (6.15), (6.16), and (6.17) for $L \neq L^2$ are

$$E_{\mathrm{P}} = \frac{1}{4}\left(\frac{E(L)}{L} - \frac{E(L-1)}{L-1}\right), \tag{6.18}$$

$$E_{\mathrm{H}} = \frac{E(L-1)L^2 - E(L)(L-1)^2}{6(L-1)L}. \tag{6.19}$$

This enables us to estimate $E_{\mathrm{P}} = -6.5906(1)$ Ha/atom and $E_{\mathrm{H}} = -0.5877(4)$ Ha/atom in the 4×4 and 5×5 combination, and $E_{\mathrm{P}} = -6.5916(1)$ Ha/atom and $E_{\mathrm{H}} = -0.5844(5)$ Ha/atom in the 5×5 and 6×6 combination. The estimated cohesive energy of $-3.225(11)$ eV is in agreement with the periodic calculations. We see a good convergence and agreement with the periodic result of $-6.59101(1)$ Ha/atom, which indicates that the cluster is a suitable representative of the crystal. The average hydrogen atom is bonded to black phosphorus with about 2.4 eV.

In the scenario of phosphorene clusters, we deal with finite size effects due to the effective hard-wall boundary conditions the hydrogen atoms impose on the structure. These boundary effects are also visible in the HOMO and LUMO of the 4×4 cluster, Figs. 6.3(g)–(j). The overall structure of the orbitals shares qualitative features with the HOMO/LUMO states from the periodic calculations. Compared to the density of the periodic orbitals, the orbitals carry more weight in the inner of the cluster and the wave functions are not localized on the hydrogen atoms and the outer rim of phosphorus atoms. For larger clusters, we find a similar behavior with a more appropriate periodic behavior of the orbitals within the macromolecules.

6.7 Fundamental gap from periodic and cluster QMC calculations

Although the diffusion Monte Carlo method was initially conceived to calculate the ground state of a system, it was already applied to determine the excitation energy of solids, clusters, and molecules [194, 218–222]. The method was employed for silicon [218] and diamond [221] to calculate the quasiparticle band structure, including the fundamental gap. Results were compared to *GW* calculations and experiments, and good agreement was found. In these studies, the excitation formula Eq. (6.6) was used to calculate the electronic gaps. The reason this formula got used instead of the fundamental gap formula, Eq. (6.3), was that exciton binding was deemed to be very small (about ten meV), which is smaller than the statistical error bars encountered in the mentioned works. The same methodology was also utilized to determine gaps of silicon and germanium nanoclusters [219, 220, 222], finding increased gaps with respect to the bulk limit due to quantum confinement effects. In a seminal work [194], many-body *GW* and QMC calculations were benchmarked against each other, determining the optical and fundamental gaps of SiH_4 and CH_4. Excellent agreement between the two very different methods was found.

In two-dimensional solids, the excitonic binding energy is not negligible and can be very large, as outlined in Sec. 6.2. The strong present Coulomb interactions introduce severe challenges for conventional single-particle theories like DFT. This physics may

also be reflected in the experimental and theoretical spreads of measured and predicted values of optical and fundamental gaps, see Tab. 6.1, of about 1 eV. State-of-the-art *GW* calculations [167, 168, 175–183] are not consistent with each other, giving values of the fundamental gap from 1.6 eV to 2.41 eV. *GW* calculations are typically known to lead to satisfactory results. However, in the case of phosphorene, there may be systematic errors, which still need to be explored. The discrepancy could come, for instance from using DFT-optimized lattice parameters, different levels of self-consistency in the Green's function, different exchange-correlation functionals within the DFT part, or the level of parameter convergence. A critical ingredient in 2D-periodic *GW* calculations was identified to be the Coulomb interaction cutoff in the vacuum direction [188]. It is therefore important to determine a fundamental gap value from an alternative theory in order to have a comparison. This is the QMC method in our case (see Sec. 2.5).

The procedure for calculating the fundamental gap for phosphorene is quickly summarized as follows. For each system size, after an initial DFT calculation with two different exchange-correlation functionals PBE and B3LYP (see Sec. 6.4), we construct a many-body trial wave function for the subsequent VMC and QMC computations from the DFT single-particle orbitals. The Slater determinant, which is multiplied by a variable Jastrow factor, contains the single-particle orbitals from the Γ point of the DFT calculation and constrains the nodal surface and symmetry of the trial wave function (see Secs. 2.5.2 and 6.5.1). The symmetry for the excited state is set by promoting the HOMO orbital to the LUMO orbital as outlined in Sec. 6.5.1. To make the DMC calculation more efficient, the initial VMC optimization is carried out to obtain a trial wave function via the variation of the Jastrow parameters. In the end, a DMC calculation is employed to find the energetically lowest state of the symmetry dictated by the nodal surface of the trial wave function [210]. The results can be used to evaluate the difference between the excited state energy $E_\mathrm{e}^{\mathrm{H}\to\mathrm{L}}$ and the ground state energy E_0,

$$\Delta_\mathrm{f} = E_\mathrm{e}^{\mathrm{H}\to\mathrm{L}} - E_0. \tag{6.20}$$

This equation, which formally is the one for the optical gap, is used instead of Eq. (6.3), because our extended HOMO and LUMO wave functions represent unbound excitations and therefore it is equivalent to the fundamental gap formula of Eq. (6.3) (as explained in Sec. 6.2). Furthermore, Eq. (6.20) has the advantage to involve only two states of one system instead of ground states of the neutral and two charged systems in Eq. (6.3). Equation (6.20) is also much easier to converge for finite size effects as it involves only charge-neutral states.

With Eq. (6.20), we try to resolve a fractional change in the energy due to an excitation, which is inversely proportional to the number of electrons in the simulation cell, a $1/N$ effect [218]. The precision of the calculation must therefore be sufficient to resolve this energy change amid the statistical noise. Together with the computationally intense DMC method and the finite-size scaling, we invested about 30 million core hours (of current architecture) into the calculation of the fundamental gap of phosphorene.

In Sec. 6.4, we have seen that the PBE and B3LYP calculations yield very different Kohn–Sham band gaps of 0.80 and 1.88 eV, respectively, due to the added

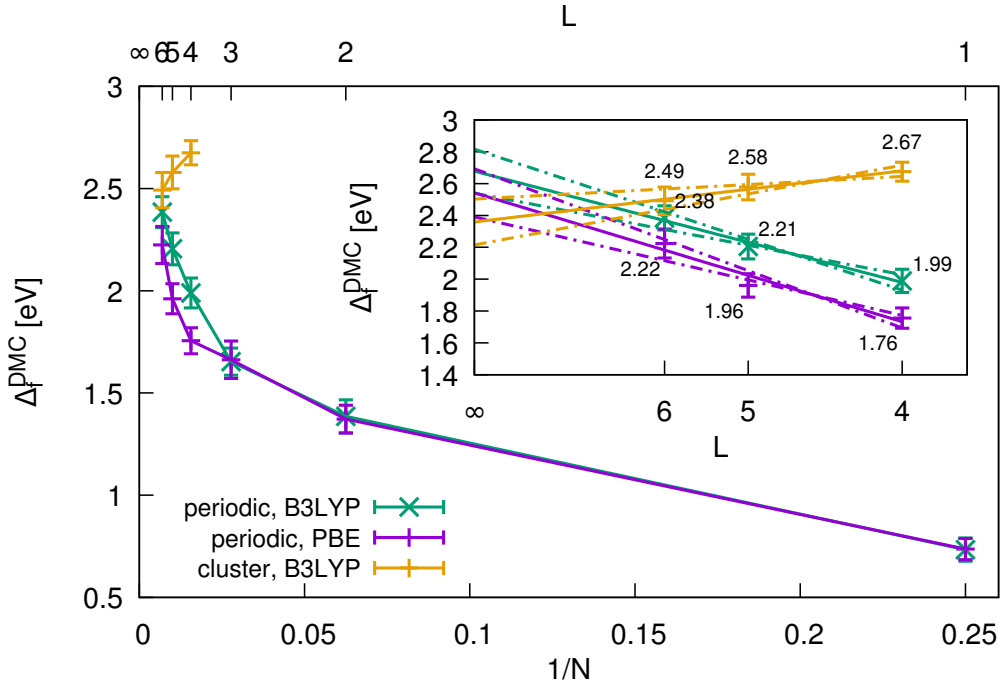

Figure 6.11: Scaling of the fundamental gap, comparing periodic with cluster calculations. For periodic calculations, the results for PBE and B3LYP exchange-correlation functionals are shown, whereas the cluster results are for B3LYP. Scaling with respect to the inverse number of atoms N is presented. The inset shows the extrapolation of the gap value, using the three largest supercell sizes $L = 4 - 6$. The extrapolated gap values are: $\Delta_f^{per,B3LYP} = 2.68(14)$ eV, $\Delta_f^{per,PBE} = 2.54(15)$ eV, and $\Delta_f^{clst,B3LYP} = 2.36(14)$ eV.

exact-exchange in B3LYP. This represents a very different starting point for our QMC calculations and fixed-node errors should appear if they are important here. In Fig. 6.11, we present the results from our fundamental gap calculations. Results are plotted with respect to the inverse number of electrons $1/N$. The periodic calculations reflect large finite-size effects for the 1×1 to 3×3 supercell sizes, where the gap is increasing monotonously. The values for 4×4 to 6×6 approximately indicate linear behavior versus $1/N$ scaling. An exact scaling law for the fundamental gap within this framework is unknown, which is the reason we extrapolate to an infinite system size with a $1/N$ extrapolation, displayed in the inset of Fig. 6.11. The fits were conducted by simulating three data points with normal distribution around their calculated mean value and standard error obtained from the DMC calculation. 100,000 linear fits were performed and the normally-distributed fit parameters statistically analyzed. This gives us the following fundamental gap values in the periodic case

$$\Delta_f^{per,PBE} = 2.54(15) \text{ eV}, \tag{6.21}$$

$$\Delta_f^{per,B3LYP} = 2.68(14) \text{ eV}. \tag{6.22}$$

Surprisingly, the two values are in quite good in agreement with each other, given the 1 eV difference in Kohn–Sham band gaps. This indicates, in combination with the cohesive energy results in Sec. 6.5.5, that fixed-node errors are indeed rather small. The largest uncertainty in these values comes from the unknown scaling dependency on the number of atoms in the system, which is usually the largest source of errors in periodic calculations [205].

To crosscheck our periodic calculations, we turned to clusters of phosphorene of different sizes, approximating the system as macromolecules, see Figs. 6.3(g) to 6.3(j). The clusters were passivated by hydrogen atoms to remove possible low-energy dangling bond states from the spectrum. Phosphorene clusters were prepared in the size of 4×4 to 6×6. The HOMO and LUMO orbitals from the 4×4 cluster are compared to the Γ point valence and conduction band single-particle wave functions in Fig. 6.3. Local features are recognized to be very similar. Due to the effective hard-wall boundary conditions, finite-size quantization effects are in general expected, which is also apparent from the cluster orbitals. Though, the types of finite-size effects are fundamentally different from the periodic calculations. In the cluster case, the results are not influenced by a periodic repetition of electrons. Indeed, we observe finite-size quantization in the fundamental gap scaling of the cluster, see Fig. 6.11. The gap values are larger for smaller clusters and become smaller for larger clusters. In this case we also plotted the gap values against $1/N$. The cluster values appear to have a much weaker dependence on the supercell size and can be extrapolated linearly to infinite system size. This leads to the infinite size result of

$$\Delta_{\mathrm{f}}^{\mathrm{clst,B3LYP}} = 2.36(14)\ \mathrm{eV}, \tag{6.23}$$

which is not far from the values obtained by the periodic calculations. For three reasons, we believe this is the more accurate result although the influence of the hydrogen edge might add complexity. Firstly, the Hamiltonian used for the cluster system is the pure Born–Oppenheimer one, without any uncertainties coming from a replacement of Coulomb interactions with the Ewald summation. Secondly, Coulomb finite-size effects are absent, which turn out to be intricate in quasi-2D systems [223]. Thirdly, the dependence of the fundamental gap is less pronounced with respect to the size of the cluster, which reduces errors in the infinite-size extrapolation. We expect the discrepancy with respect to the periodic system results to come from their excited states. Coulomb finite-size errors in quasi-2D systems mainly stem from situations when electrons leave the phosphorus plane, leading to an interaction of the electron with an extended associated exchange-correlation hole within the phosphorene sheet [223]. The exchange-correlation hole interacts with the adjacent supercells and finite-size errors are introduced. The excited state allows this situation to happen more frequently as the excited state wave function has a slower decay towards the vacuum. Therefore, the excited state is expected to be less well described than the ground state. Because both, ground state and excited state calculations are variational, with the excited state carrying a larger error, Eq. (6.20) represents just an upper bound for the fundamental gap and lies above the cluster result. Compared to *GW* values, our result of 2.36 eV is significantly larger than most of the theoretical values, see Tab. 6.1, but also consistent with 2.26 eV, 2.29 eV, and 2.41 eV of Refs. [138, 178, 182].

6.8 Interpretation in terms of experiments

Direct measurements [177, 184] of fundamental gaps in phosphorene are rare. Furthermore, the exciton binding energy and fundamental gap depend on the dielectric environments and are reduced on a substrate, compared to the free-standing material [224–226]. This complicates the comparison with experiments. The most direct measurement of the fundamental gap in phosphorene was conducted with the help of photoluminescence excitation spectroscopy (PLE) [184]. A tunable laser was used to excite the material in a range around the fundamental gap and the photoluminescence yield was analyzed. The exciton luminescence peak intensity can then be observed as a function of the excitation laser frequency. The onset of high exciton emission then marks the fundamental gap energy, determined as 2.26(10) eV. Phosphorene in this experiment was placed on SiO_2 with a dielectric constant of about $4\varepsilon_0$. The influence of the screening on the fundamental gap was estimated to be a reduction of about 0.1 eV to 0.2 eV, giving a rather good agreement with our cluster value. Another experiment measured a fundamental gap of 2.05 eV with the help of scanning tunneling spectroscopy (STS) [177]. This transport gap was measured not for a single phosphorene sheet, but for an in-situ cleaved black phosphorus crystal. The authors of the study attributed the rather high measured value to the surface sensitivity of the method [177]. The measured value is in contradiction with another measurement on the same material, where the fundamental gap was determined to be 0.3 eV [200], corresponding with the bulk number.

As the experimental situation is difficult, we ask the question: can we validate our free-standing phosphorene fundamental gap from optical gap measurements carried out on dielectric substrates? There are two aspects to answer this question with yes. First of all, via the linear relationship of the exciton binding energy and the fundamental gap [180], the latter can be expressed in terms of the optical gap for the free-standing system, see Eq. (6.2). Secondly, it was experimentally and theoretically established for other two-dimensional materials such as TMDCs that the optical gap peak barely changes with the dielectric environment [224–226]. When the material is placed on a substrate, one observes an equal reduction of the exciton binding energy and the fundamental gap, leading to an unchanged optical gap. This allows us to estimate the free-standing binding energy and the optical gap for arbitrary substrates as

$$\Delta_\mathrm{b} = 0.64(4)\ \mathrm{eV}, \tag{6.24}$$

$$\Delta_\mathrm{o} = 1.72(10)\ \mathrm{eV}, \tag{6.25}$$

which is in good agreement with two photoluminescence (PL) measurements, reporting 1.67 eV and 1.75 eV [165, 186]. We are also in good agreement with the optical absorption measurement of 1.73 eV [185]. The optical absorption measurement is in general more reliable than PL measurements, as the optical absorption is insensitive to the levels of defects and impurities, which complicate PL measurements [185]. The estimated binding energy is also in agreement with the Bethe–Salpeter equation (BSE) solutions based on *GW* [167, 180–182], as well as with predictions from effective electron-hole Hamiltonians [168, 183], see Tab. 6.1, although these values are mostly about 0.1 eV to 0.2 eV larger.

6.9 Summary and conclusions

In order to harvest the potential of black phosphorus with its layer-tunability of the direct band gap, we should understand the monolayer limit – phosphorene – first. Owing to the large discrepancy of fundamental and optical gaps within experiments and theory, a clarifying study for the free-standing monolayer phosphorene is needed. We employ systematic fixed-node quantum Monte Carlo (QMC) calculations, a method that exhibits benchmark character for ground state solid-state calculations. This is due to its ability to treat the full many-body Hamiltonian without severe approximations. This accuracy comes at the cost of high computational demand, which can be remedied by exploiting the method's good parallelizability, using a supercomputer. The computational expense of our study for example was 30 million core hours of today's computing architecture.

QMC was already used in the context of molecules and 3D solids to study their optical properties. In molecules, a formula devised for optical gaps gives good agreement with experimental optical gaps, whereas in 3D insulators the same formula predicts fundamental gaps. This is because excitonic effects are very small in the latter. In 2D, the screening behavior is significantly different than in 3D, leading to high exciton binding energies. In this work we show, that even though we use the optical gap formula for a 2D system, we obtain the fundamental gap as well, like in the 3D case. This is due to the delocalized nature of our considered electron-hole excitations and the consequent negligible Coulomb binding of electron-hole pairs.

We carried out systematic QMC calculations for periodic and cluster models of phosphorene, quantifying also fixed node errors by using two different exchange-correlation functionals for the preparatory DFT calculations. We determine the cohesive energy of the system to be 3.208(13) eV/atom (PBE) and 3.216(13) eV/atom (B3LYP) for periodic calculations and 3.224(13) eV/atom (B3LYP) for cluster calculations, indicating that the ground state is well described (comparing to indirect experimental estimation of the cohesive energy of 3.29(9) eV/atom [217]) and that fixed-node errors are small. Due to the agreement of periodic and cluster models, we are confident that clusters represent a good model for the bulk system.

Fundamental gaps were obtained by charge-neutral electron-hole excitations. Periodic calculations suffer from finite-size effects due to the treatment of the Hamiltonian with full Coulomb interactions, leading to unphysical self-interaction of electrons with their periodically repeated images. Finite-size effects are present for the clusters as well due to finite-size quantization. In both models, a system-size scaling was carried out. Extrapolation to infinite systems gives us values of 2.54(15) eV and 2.68(14) eV for the periodic calculations, using PBE and B3LYP nodal surfaces, respectively. This result is surprising given a 1 eV difference in Kohn–Sham band gaps of the input DFT calculations. This shows however, that fixed-node errors are also small for excited states. The cluster calculation leads to an extrapolated fundamental gap of 2.36(14) eV for B3LYP input. We find the cluster calculations to be more reliable, as no modifications are applied to the Hamiltonian, whereas in the periodic systems the Coulomb interaction needs to be replaced by the Ewald interaction. The cluster calculations represent real physical macromolecules without any errors other than fixed-node errors, whereas in the periodic case we attribute the higher fundamental

gap values to the overestimation of the excited state energy.

Although we calculated the fundamental gap for the free-standing system, our value can be directly related to optical measurements on substrates. Using the linear scaling law between the exciton binding energy and the fundamental gap in 2D materials [180], we can estimate the exciton binding energy of 0.64(6) eV and the optical gap of 1.72(10) eV, from the cluster calculations. Optical gaps are known to be independent on the dielectric environment, because the fundamental gap and exciton binding energy are reduced by the same amount upon screening [226]. Our value for the optical gap is in good agreement with recent optical absorption measurements and photoluminescence measurements of 1.67 eV [165], 1.73 eV [185], and 1.75 eV [186].

QMC calculations are very expensive and require human time [43] to carefully choose the basis set, special smooth pseudopotentials, as well as for wave function optimization. Nevertheless, we believe that QMC calculations will play a big role in future solid state calculations. Our calculations of the fundamental gap in phosphorene adds another number from an independent method and we hope to give a new reference ground for fundamental gap as a key input for more qualitative and approximate theories, such as tight-binding and $\mathbf{k} \cdot \mathbf{p}$, as well as for experimental interpretations. Our studies open up a way to explore the layer and strain dependence of the fundamental gap in black phosphorus. We expect to stimulate also QMC calculations for other 2D materials, where less severe but similar difficulties in the determination of the quasiparticle gaps exist [188].

A Numerical evaluation of the topological $\mathbb{Z}_2$ invariant with Z2Pack

The evaluation of topological invariants of solids sometimes turns out to be cumbersome, as these invariants are not necessarily eigenvalues of the Hamiltonian [58]. Here, the calculation of the $\mathbb{Z}_2$ invariant of a two-dimensional AII Hamiltonian is considered (see also App. B for a symmetry analysis). This topology class is solely based on the time-reversal symmetry and as long as this symmetry holds, the $\mathbb{Z}_2$ invariant is well defined [125].

If the system has a reflection symmetry in the plane, s_z is a good quantum number. In this case the $\mathbb{Z}_2$ invariant can be defined as the spin Chern number, $C_s = (C_\uparrow - C_\downarrow)/2$ [125], where for each electron species (spin-up and spin-down) a separate Chern number ($C_\uparrow$ and $C_\downarrow$) can be calculated by considering separately the block-diagonal parts of the Hamiltonian. However, in the case of systems where the z symmetry is broken, like for graphene on a substrate, s_z is not a good quantum number anymore. This is the case for Hamiltonian (4.1), where Rashba SOC mixes the spins. In this case one has to employ more sophisticated methods.

A.1 Hybrid Wannier functions and Wannier charge centers

To solve the problem of topological invariant calculation, here briefly a method based on hybrid Wannier charge centers [58, 227] is presented and its application to the case of SOC proximitized graphene is shown. The method is implemented in the python program `Z2Pack` [58], which is able to calculate the first Chern number, $\mathbb{Z}_2$ invariant, crystalline topological insulator invariants and is also suitable to study topological semimetal phases based on $\mathbf{k}\cdot\mathbf{p}$, tight-binding and *ab initio* calculations.

The principal quantities in this method are the so-called hybrid Wannier functions (HWFs)

$$|n, l_x, k_y, k_z\rangle = \frac{a_x}{2\pi}\int_{-\pi/a_x}^{\pi/a_x} \mathrm{d}k_x \; e^{ik_x l_x a_x}\,|\psi_{n\mathbf{k}}\rangle\,, \tag{A.1}$$

hybrid, because the Bloch wave function $|\psi_{n\mathbf{k}}\rangle$ is Fourier transformed only in one reciprocal space direction (here k_x). HWFs can be thought of localized wave functions in x (due to Fourier transform of extended Bloch wave functions) of a fictitious one-dimensional system, which is coupled to external parameters k_y and k_z [58]. l_x is an integer which labels the unit cell (of lattice constant a_x) in x direction, in which the HWF is localized.

The main interest lies in the spatial expectation value of the HWFs in the home unit cell ($l_x = 0$), called Wannier charge center (WCC)

$$\bar{x}_n(k_y, k_z) = \langle n, 0, k_y, k_z | x | n, 0, k_y, k_z \rangle \,. \tag{A.2}$$

It can be shown to be connected to the Berry potential $\mathcal{A}_n(\mathbf{k}) = i \langle u_{n\mathbf{k}} | \nabla_{\mathbf{k}} | u_{n\mathbf{k}} \rangle$ [58]:

$$\bar{x}_n(k_y, k_z) = \frac{a_x}{2\pi} \int_{-\pi/a_x}^{\pi/a_x} \mathrm{d}k_x \; \mathcal{A}_n^x(k_x, k_y, k_z). \tag{A.3}$$

The Berry curvature is the rotation of the Berry potential, $\mathbf{\Omega}_n(\mathbf{k}) = \nabla_{\mathbf{k}} \times \mathcal{A}_n(\mathbf{k})$, which, integrated over the Brillouin zone and summed over occupied bands, gives the first Chern number $C = \frac{1}{2\pi} \sum_n \int_{\mathrm{BZ}} \mathrm{d}^2k \; \Omega_n^z(\mathbf{k})$. It is then comprehensible, that the WCC can be used to calculate the first Chern number (also valid in the multiband case, details can be found in [58, 227])

$$C = \frac{1}{a_x} \left[\sum_n \bar{x}_n(k_y = 2\pi/a) - \sum_n \bar{x}_n(k_y = 0) \right], \tag{A.4}$$

here in two-dimensional systems (k_z is dropped) and n runs over bands in the manifold of interest (say valence bands).

For time-reversal symmetric cases, the Berry curvature is an odd quantity as a function of $\mathbf{k}$ which leads to a vanishing first Chern number. Therefore the first Chern number is of no use in the determination of the topological invariant. As mentioned in the beginning, to assign a $\mathbb{Z}_2$ invariant that in the limit of good s_z quantum number reduces to the spin Chern number, the Hilbert space has to be separated into different parts

$$\hat{\mathcal{H}} = \bigoplus_{i=1}^{N} \hat{\mathcal{H}}_i. \tag{A.5}$$

Each sub-Hilbert space can then be assigned an individual Chern number C_i,

$$C = \bigoplus_{i=1}^{N} C_i, \tag{A.6}$$

which sum to the first Chern number [in analogy to Eq. (A.4)]. The separation of the Hilbert space has to be carried out in a way, such that each individual Chern number is an integer [58]. In general the value of individual Chern numbers depend on how the Hilbert space is separated (depend on the gauge of projectors onto the subspaces) and unless other physical constraints are given, they have no physical meaning, only their sum has. In our case it is the time-reversal symmetry that is used to separate the Hilbert space ($N = 2$) and assign physical meaning in analogy to spin Chern numbers.

A.2 Examples of $\mathbb{Z}_2$ calculations of a nontrivial and trivial graphene system

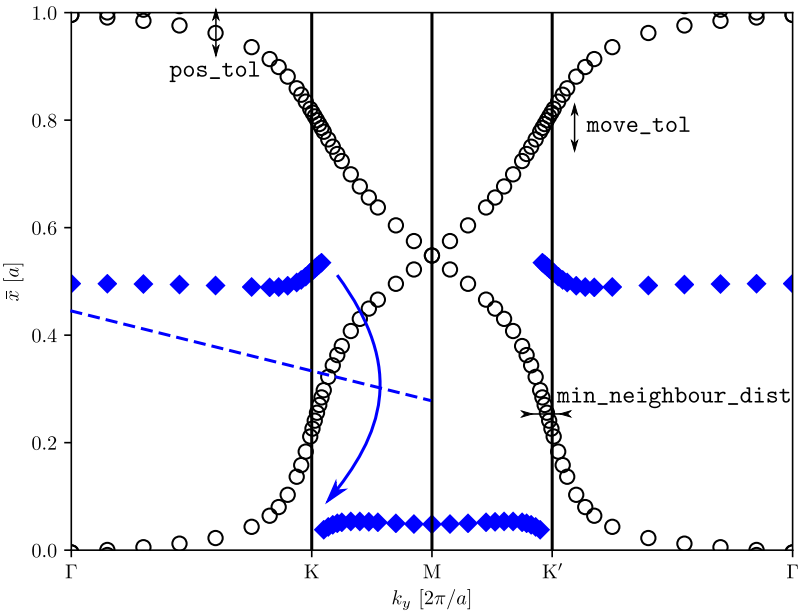

Figure A.1: Wannier charge center calculation (typical `Z2Pack` output with annotations added) in the case of uniform SOC along momenta on the straight k path ΓKMK′Γ. Empty dots indicate the expectation value of the x operator of the two hybrid Wannier functions resulting from the two occupied bands. Blue diamonds indicate where the largest gap between adjacent Wannier charge centers sits (the $\bar{x}$ axis has to be considered periodic). The blue arrow shows a single jump of the largest gap over one branch of Wannier charge center evolution in half of the Brillouin zone (ΓM), hence the state of the system is nontrivial. Blue dashed line denotes a continuous line from an arbitrary $\bar{x}(\Gamma)$ to an arbitrary $\bar{x}(\mathrm{M})$. Further indicated are convergence parameters (`pos_tol`, `move_tol`, `min_neighbour_dist`) explained in the text.

In Fig. A.1 the evolution of WCCs [Eq. (A.2)] of the occupied bands of a quantum spin Hall state [12] in momentum space is shown, with uniform intrinsic spin-orbit coupling as defined in Sec. 5.3.1 and values of the Hamiltonian as in Sec. 5.2. The k_y direction corresponds to the direction of ΓKMK′Γ and the Fourier transform, Eq. (A.1), was done in the orthogonal direction k_x. The WCCs are only well defined modulo a lattice constant [58] and therefore the graph has to be considered periodic in $\bar{x}$. Because only slight Rashba SOC is present here, s_z is still a relatively good quantum number (the figure doesn't change noticeably when Rashba SOC is turned off). Essentially then the two WCCs at each k_y can be assigned to spin-up and spin-down electrons. Time-reversal symmetry is present here, which is why the graph is

symmetric with respect to the time-reversal invariant point M. In analogy to Eq.(A.4) individual Chern numbers can be defined by $C_{\uparrow/\downarrow} = \frac{1}{a}[\bar{x}_{\uparrow/\downarrow}(k_y = 2\pi/a) - \bar{x}_{\uparrow/\downarrow}(k_y = 0)]$, which evaluates to about ± 1 (sightly decreased from 1 here due to Rashba SOC). The spin Chern number is then found to have the value $C_s = (C_\uparrow - C_\downarrow)/2 \approx 1$ and the system is in a quantum spin Hall state.

For larger Rashba values the Hilbert space division would not be well defined and values very different from $C_s = 1$ would be found. It turns out, that still a $\mathbb{Z}_2$ invariant can be defined by the number of times WCCs cross a continuous line drawn from an arbitrary $\bar{x}(\Gamma)$ to an arbitrary $\bar{x}(\mathrm{M})$ [227] as shown in Fig. A.1. The number of crossings indicates then the topological invariant, trivial if the number of crossings is even, nontrivial if the number of crossings is odd. In the case of Fig. A.1, exactly one crossing happens and therefore the system is topologically nontrivial.

For algorithmic reasons an equivalent method to counting the number of crossings is implemented in `Z2Pack`. In `Z2Pack` the position of the largest gap in $\bar{x}$ between WCCs is tracked, shown in Fig. A.1. It is then counted how many times WCCs are jumped over in half of the Brillouin zone by the largest gap and the invariant is determined. In Fig. A.2, the case of staggered intrinsic SOC is shown, where with two jumps an even number of hops occur and therefore the system is in a trivial state.

A.3 Workflow and convergence options

The convergence of a calculation of a binary number (the $\mathbb{Z}_2$ invariant) can be cumbersome. Therefore, a short description of the convergence options of `Z2Pack` is given (see code Listing A.1). After giving `Z2Pack` the Hamiltonian matrix as a function of $\mathbf{k}$ and defining a direction for the Fourier transform, the calculation has to be fine tuned. `Z2Pack` determines the invariant on its own, however one is advised to check the graph of WCCs manually.

```
z2_settings = {
    'num_lines': 21,
    'pos_tol': 1E-3,
    'iterator': range(10, 2000, 10)
    'move_tol': 0.05,
    'gap_tol': None,
    'min_neighbour_dist': 0.001,
}
```

Listing A.1: Python code for the `Z2Pack` settings.

The most important convergence option is the `pos_tol` option, which controls the convergence tolerance of the position of the WCC themselves (see Fig. A.1). If the convergence of `pos_tol` is not met, more and more k_x points are added to the Fourier transform (this is controlled by `iterator`) until it is.

The parameter `num_lines` sets the initial number of k_y points considered. In Figs. A.1 and A.2 more than 21 k_y points are visible (as defined in Listing A.1). `Z2Pack` dynamically inserts k_y points where WCCs are moving too fast, which is controlled by `move_tol`. In Figs. A.1 and A.2 this happens at the K points, because

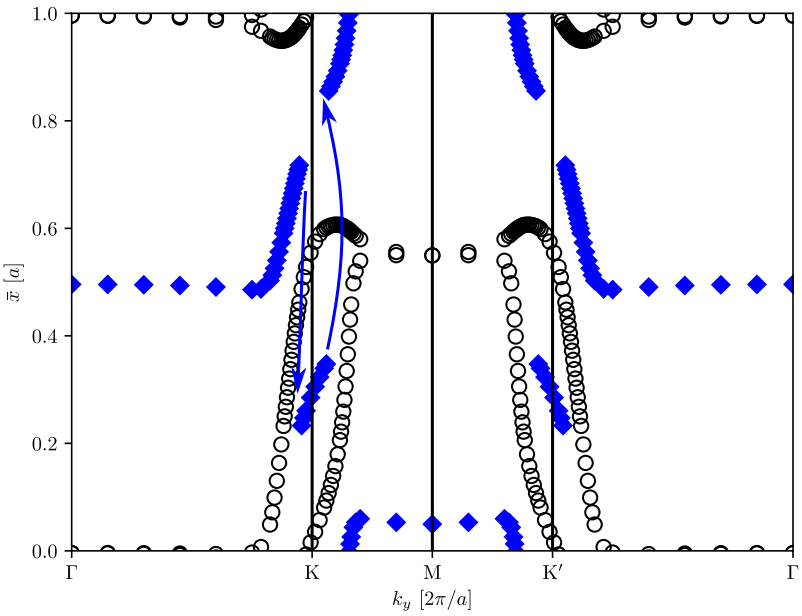

Figure A.2: Wannier charge center calculation (typical `Z2Pack` output with annotations added) in the case of staggered SOC along momenta on the straight k path ΓKMK′Γ. Empty dots indicate the expectation value of the x operator of the two hybrid Wannier functions resulting from the two occupied bands. Blue diamonds indicate where the largest gap between adjacent Wannier charge centers sits (the $\bar{x}$ axis has to be considered periodic). The blue arrows show two jumps of the largest gap over one branch of Wannier charge center evolution in half of the Brillouin zone (ΓM), hence the state of the system is trivial.

there the Berry curvature is largest and WCCs change the most. New k_y points are inserted until WCCs do not change more than `move_tol` from one k_y point to another. If an inserted k_y point is closer than `min_neighbor_dist` to an existing k_y point the insertion is stopped. `gap_tol` is very similar to `move_tol`, instead for WCCs it is the tolerance for movement of the largest gap.

In practical calculations, care has to be taken when gaps are small with respect to the largest energy scale, e.g., t. This happens in the case of staggered intrinsic SOC, for band structures similar as in Fig. 5.7(i). Nearby these small gaps, which are not lying directly at the K point, the Berry curvature can be strongly peaked (compare Fig. 5.8). In these regions WCCs can change quickly and can lead to problems in WCC convergence.

B Symmetry classification of graphene proximity Hamiltonians

Dimensionality and symmetries of Hamiltonians bear essential information to characterize their topological behavior [154]. Here we analyze Hamiltonian (4.1) concerning its generic symmetries (time-reversal, particle-hole, and sublattice symmetry) to see in which topology class it resides.

B.1 Generic symmetries of the Hamiltonian

The topological properties of a Hamiltonian are given by its symmetries, more precisely by generic symmetries as the time-reversal and particle-hole symmetries. These are anti-unitary symmetries represented by operators $\hat{\Theta}$

$$\hat{\Theta} = \hat{U}\hat{K} \tag{B.1}$$

$$\Leftrightarrow \hat{\Theta}^{-1} = \hat{K}^{-1}\hat{U}^{-1} = \hat{K}\hat{U}^{\dagger}, \tag{B.2}$$

which can be decomposed into unitary $\hat{U}$ and complex conjugation $\hat{K}$ parts.

B.1.1 Time-reversal symmetry

One of these fundamental symmetries is the time-reversal symmetry. A single-particle Hamiltonian is said to be time-reversal symmetric if there exists a symmetry operator $\hat{\Theta}_{\mathrm{T}}$ such that [154, 228]

$$\hat{\Theta}_{\mathrm{T}}\hat{H}\hat{\Theta}_{\mathrm{T}}^{-1} = \hat{H} \tag{B.3}$$

$$\Leftrightarrow \hat{U}_{\mathrm{T}}\hat{K}\hat{H}\hat{K}\hat{U}_{\mathrm{T}}^{\dagger} = \hat{H} \tag{B.4}$$

$$\Leftrightarrow \hat{U}_{\mathrm{T}}\hat{H}^{*}\hat{U}_{\mathrm{T}}^{\dagger} = \hat{H}. \tag{B.5}$$

The action of time-reversal symmetry in a lattice can be obtained in the following way [229]. Consider the one dimensional single-orbital spinless hopping Hamiltonian

$$\hat{H} = \sum_{nm} \hat{c}_n^{\dagger} H_{nm} \hat{c}_m, \tag{B.6}$$

with creation and annihilation operators $\hat{c}_n^\dagger$ and $\hat{c}_n$ on sites n and m and hopping matrix elements H_{nm}. The Fourier transform of operators is given by

$$\hat{c}_n = \frac{1}{\sqrt{N}} \sum_k e^{-ikn} \hat{c}_k, \tag{B.7}$$

where periodic boundary conditions are assumed and N is the number of unit cells, which limits the values for reciprocal lattice vectors $k = \frac{2n\pi}{N}$ with $n = 0, 1, \ldots, N-1$.

Using translational symmetry and inserting Eq. (B.7) into Eq. (B.6) one obtains

$$\hat{H} = \sum_k \hat{c}_k^\dagger \left(\sum_j e^{ikj} H_{0j} \right) \hat{c}_k = \sum_k \hat{c}_k^\dagger \hat{H}(k) \hat{c}_k. \tag{B.8}$$

The action of time-reversal symmetry on Hamiltonian (B.6) gives

$$\hat{\Theta}_\mathrm{T} \hat{H} \hat{\Theta}_\mathrm{T}^{-1} = \sum_k \hat{\Theta}_\mathrm{T} \hat{c}_k^\dagger \hat{\Theta}_\mathrm{T}^{-1} (\hat{\Theta}_\mathrm{T} \hat{H}(k) \hat{\Theta}_\mathrm{T}^{-1}) \hat{\Theta}_\mathrm{T} \hat{c}_k \hat{\Theta}_\mathrm{T}^{-1}. \tag{B.9}$$

Time-reversal in the spinless case decomposes as $\hat{U}_\mathrm{T} = 1$, $\hat{\Theta}_\mathrm{T} = \hat{K}$. It acts on the reciprocal momentum creation and annihilation operators as

$$\hat{\Theta}_\mathrm{T} \hat{c}_k \hat{\Theta}_\mathrm{T}^{-1} = \frac{1}{\sqrt{N}} \sum_n \hat{\Theta}_\mathrm{T} e^{ikn} \hat{\Theta}_\mathrm{T}^{-1} \hat{c}_n = \frac{1}{\sqrt{N}} \sum_n e^{-ikn} \hat{c}_n = \hat{c}_{-k}. \tag{B.10}$$

Eq. (B.9) together with Eq. (B.10) leads to

$$\hat{\Theta}_\mathrm{T} \hat{H} \hat{\Theta}_\mathrm{T}^{-1} = \sum_k \hat{c}_{-k}^\dagger \hat{H}(k)^* \hat{c}_{-k} = \sum_k \hat{c}_k^\dagger \hat{H}(-k)^* \hat{c}_k. \tag{B.11}$$

For time-reversal symmetric Hamiltonians this leads to

$$\hat{H} = \sum_k \hat{c}_{-k}^\dagger \hat{H}(-k) \hat{c}_{-k} \overset{!}{=} \hat{\Theta}_\mathrm{T} \hat{H} \hat{\Theta}_\mathrm{T}^{-1} = \sum_k \hat{c}_{-k}^\dagger (\hat{\Theta}_\mathrm{T} \hat{H}(k) \hat{\Theta}_\mathrm{T}^{-1}) \hat{c}_{-k}, \tag{B.12}$$

such that

$$\hat{H}(-k) = \hat{\Theta}_\mathrm{T} \hat{H}(k) \hat{\Theta}_\mathrm{T}^{-1} = \hat{H}(k)^*. \tag{B.13}$$

In the spinful case it can be shown that

$$\hat{H}(-k) = \hat{\Theta}_\mathrm{T} \hat{H}(k) \hat{\Theta}_\mathrm{T}^{-1} = \hat{U}_\mathrm{T} \hat{H}(k)^* \hat{U}_\mathrm{T}^\dagger, \tag{B.14}$$

or in more dimensions,

$$\hat{U}_\mathrm{T} \hat{H}(\mathbf{k})^* \hat{U}_\mathrm{T}^\dagger = \hat{H}(-\mathbf{k}). \tag{B.15}$$

The specific form of the $\hat{U}_\mathrm{T}$ part of the time-reversal symmetry (which is basis

dependent) for the Hamiltonian (4.2), such that Eq. (B.15) is fulfilled, reads

$$\hat{U}_{\mathrm{T}} = i\sigma_0 s_y = \begin{pmatrix} 0 & 1 & 0 & 0 \\ -1 & 0 & 0 & 0 \\ 0 & 0 & 0 & 1 \\ 0 & 0 & -1 & 0 \end{pmatrix}. \tag{B.16}$$

Let us emphasize that when $\mathbf{k} \to -\mathbf{k}$ in Hamiltonian (4.2), also the valley index κ has to change its sign. The unitary matrix in Eq. (B.16) is the expected symmetry holding for spin-1/2 particles. Here, σ describes the pseudospin (sublattice A and B of graphene) and s the real spin degree of freedom via Pauli matrices. $\hat{U}_{\mathrm{T}}$ is diagonal in sublattice space and converts spin-up to minus spin-down and spin-down to spin-up, and further has the property $\hat{\Theta}_{\mathrm{T}}^2 = -1$.

B.1.2 Particle-hole symmetry

A similar fundamental symmetry is the particle-hole (or charge-conjugation) symmetry, which anticommutes with the Hamiltonian:

$$\hat{\Theta}_{\mathrm{C}} \hat{H} \hat{\Theta}_{\mathrm{C}}^{-1} = -\hat{H} \tag{B.17}$$

$$\Rightarrow \hat{U}_{\mathrm{C}} \hat{K} \hat{H} \hat{K} \hat{U}_{\mathrm{C}}^{\dagger} = -\hat{H} \tag{B.18}$$

$$\Rightarrow \hat{U}_{\mathrm{C}} \hat{H}^{*} \hat{U}_{\mathrm{C}}^{\dagger} = -\hat{H}. \tag{B.19}$$

The condition for particle-hole symmetry for the k space Hamiltonian matrix can be obtained as

$$\hat{U}_{\mathrm{C}} \hat{H}(\mathbf{k})^{*} \hat{U}_{\mathrm{C}}^{\dagger} = -\hat{H}(-\mathbf{k}), \tag{B.20}$$

similarly as in the case of time-reversal symmetry.

Using the ansatz

$$\hat{U}_{\mathrm{C}} = i\sigma_i s_j, \tag{B.21}$$

with $i, j \in \{0, x, y, z\}$, such a symmetry cannot be found for Hamiltonian (4.2), where σ and s are Pauli matrices and zero labels the identity matrix.

In the case $\lambda_{\mathrm{I}}^{\mathrm{A}} = -\lambda_{\mathrm{I}}^{\mathrm{B}}$ the Hamiltonian has the following symmetry,

$$\hat{U}_{\mathrm{iC}} \hat{H}(\mathbf{k})^{*} \hat{U}_{\mathrm{iC}}^{\dagger} = -\hat{H}(\mathbf{k}). \tag{B.22}$$

first noticed by Denis Kochan [1] in terms of real-space hopping transformations. Here, the symmetry was found by using the ansatz (B.21) and testing all combinations of sign prefactors and argument signs of rhs. Eq. (B.20). The unitary matrix fulfilling Eq. (B.22) reads

$$\hat{U}_{\mathrm{iC}} = i\sigma_y s_x = \begin{pmatrix} 0 & 0 & 0 & 1 \\ 0 & 0 & 1 & 0 \\ 0 & -1 & 0 & 0 \\ -1 & 0 & 0 & 0 \end{pmatrix} \tag{B.23}$$

[1] Private communication (2017).

and squares to -1. The implications of this symmetry are most visible in the spectrum of a zigzag ribbons, color coded with spin, in the staggered SOC case Fig. 5.3(d). The symmetry Eq. (B.22) leads to an about $E = 0$ symmetric spectrum and flips spins and sublattices.

B.1.3 Sublattice symmetry

Time-reversal and particle-hole symmetries can be combined to give another generic, but unitary symmetry, the so-called sublattice (or chiral) symmetry $\hat{\Theta}_\mathrm{S}$

$$\hat{\Theta}_\mathrm{S} \equiv \hat{\Theta}_\mathrm{T}\hat{\Theta}_\mathrm{C} = \hat{U}_\mathrm{S} \tag{B.24}$$

$$\Rightarrow \hat{\Theta}_\mathrm{S}\hat{H}\hat{\Theta}_\mathrm{S}^{-1} = \hat{\Theta}_\mathrm{T}\hat{\Theta}_\mathrm{C}\hat{H}\hat{\Theta}_\mathrm{C}^{-1}\hat{\Theta}_\mathrm{T}^{-1} = -\hat{\Theta}_\mathrm{T}\hat{H}\hat{\Theta}_\mathrm{T}^{-1} = -\hat{H}. \tag{B.25}$$

The sublattice symmetry is given in k space by

$$\hat{U}_\mathrm{S}\hat{H}(\mathbf{k})\hat{U}_\mathrm{S}^\dagger = -\hat{H}(\mathbf{k}). \tag{B.26}$$

As time-reversal symmetry is present and particle-hole symmetry is absent, also the sublattice symmetry is absent here. As a remark [154], if both time-reversal symmetry and particle-hole symmetries are absent, sublattice symmetry could still be present.

Using ansatz (B.21) and testing all combinations of sign prefactors and argument signs of rhs. Eq. (B.26) in the case of $\lambda_\mathrm{I}^\mathrm{A} = -\lambda_\mathrm{I}^\mathrm{B}$, the following symmetry can be found

$$\hat{U}_\mathrm{iS}\hat{H}(\mathbf{k})\hat{U}_\mathrm{iS}^\dagger = -\hat{H}(-\mathbf{k}), \tag{B.27}$$

with

$$\hat{U}_\mathrm{iS} = i\sigma_y s_z = \begin{pmatrix} 0 & 0 & 1 & 0 \\ 0 & 0 & 0 & -1 \\ -1 & 0 & 0 & 0 \\ 0 & 1 & 0 & 0 \end{pmatrix}, \tag{B.28}$$

such that $\hat{U}_\mathrm{iS} = \hat{U}_\mathrm{T}\hat{U}_\mathrm{iC}$ and $\hat{U}_\mathrm{iS}^2 = -1$. This symmetry leads to an inversion center in the spectrum Fig. 5.3(d), located at $k = \pi/a$ and $E = 0$. It resembles a spectral symmetry known from particle-hole symmetric superconductors, however it is different since the spin channel is not changed under this transformation.

B.2 Classification

According to the tenfold way characterization of topological insulators and superconductors [154] we are now able to identify the symmetry class of Hamiltonian (4.1) or (4.2). In general, our system has only time-reversal symmetry, which squares to -1 ($T = -1$, $C = 0$, $S = 0$), which is why we are dealing with the case of an AII Hamiltonian. This means one can expect a $\mathbb{Z}_2$ classification in two dimensions.

As for the special symmetries $\hat{U}_\mathrm{iC}$ and $\hat{U}_\mathrm{iS}$ it is so far unknown, which implications they have for a topological subclassification. The symmetry properties resemble the CII class [154], where $T = -1$ and $C = -1$ and needs further investigation.

C Degeneracies of graphene proximity Hamiltonians at the K point

C.1 Eigenvalues

In the following, Hamiltonian (4.2) will be analyzed, to find analytical expressions when the spectrum at the K point of graphene is doubly degenerate. The eigenvalues of Hamiltonian at the K point ($k = 0$) can be found as

$$\begin{aligned}
\varepsilon_4 &= \frac{1}{2}(\lambda_\mathrm{I}^\mathrm{A} + \lambda_\mathrm{I}^\mathrm{B}) + \sqrt{[\Delta + \frac{1}{2}(\lambda_\mathrm{I}^\mathrm{A} - \lambda_\mathrm{I}^\mathrm{B})]^2 + 4\lambda_\mathrm{R}^2}, \\
\varepsilon_3 &= \Delta - \lambda_\mathrm{I}^\mathrm{A}, \\
\varepsilon_2 &= -\Delta - \lambda_\mathrm{I}^\mathrm{B}, \\
\varepsilon_1 &= \frac{1}{2}(\lambda_\mathrm{I}^\mathrm{A} + \lambda_\mathrm{I}^\mathrm{B}) - \sqrt{[\Delta + \frac{1}{2}(\lambda_\mathrm{I}^\mathrm{A} - \lambda_\mathrm{I}^\mathrm{B})]^2 + 4\lambda_\mathrm{R}^2}.
\end{aligned}$$

C.2 Triple degeneracies

Using the eigenvalues from the previous section and setting three of them equal $\varepsilon_1 = \varepsilon_2 = \varepsilon_3$, and solving for $\lambda_\mathrm{I}^\mathrm{A}/\lambda_\mathrm{I}^\mathrm{B}$ combinations, leads to the solutions

$$\begin{aligned}
\lambda_\mathrm{I}^\mathrm{A}(\Delta, \lambda_\mathrm{R}) &= \Delta - \sqrt{\Delta^2 + \lambda_\mathrm{R}^2}, \\
\lambda_\mathrm{I}^\mathrm{B}(\Delta, \lambda_\mathrm{R}) &= -\Delta - \sqrt{\Delta^2 + \lambda_\mathrm{R}^2},
\end{aligned} \tag{C.1}$$

and

$$\begin{aligned}
\lambda_\mathrm{I}^\mathrm{A}(\Delta, \lambda_\mathrm{R}) &= \Delta + \sqrt{\Delta^2 + \lambda_\mathrm{R}^2}, \\
\lambda_\mathrm{I}^\mathrm{B}(\Delta, \lambda_\mathrm{R}) &= -\Delta + \sqrt{\Delta^2 + \lambda_\mathrm{R}^2}.
\end{aligned} \tag{C.2}$$

These represent points in $\lambda_\mathrm{I}^\mathrm{A} - \lambda_\mathrm{I}^\mathrm{B}$ space, where three bands touch each other, see also Fig. 5.7(h), where such a case is shown. The two triple points can be seen in Fig. C.1, where three lines intersect.

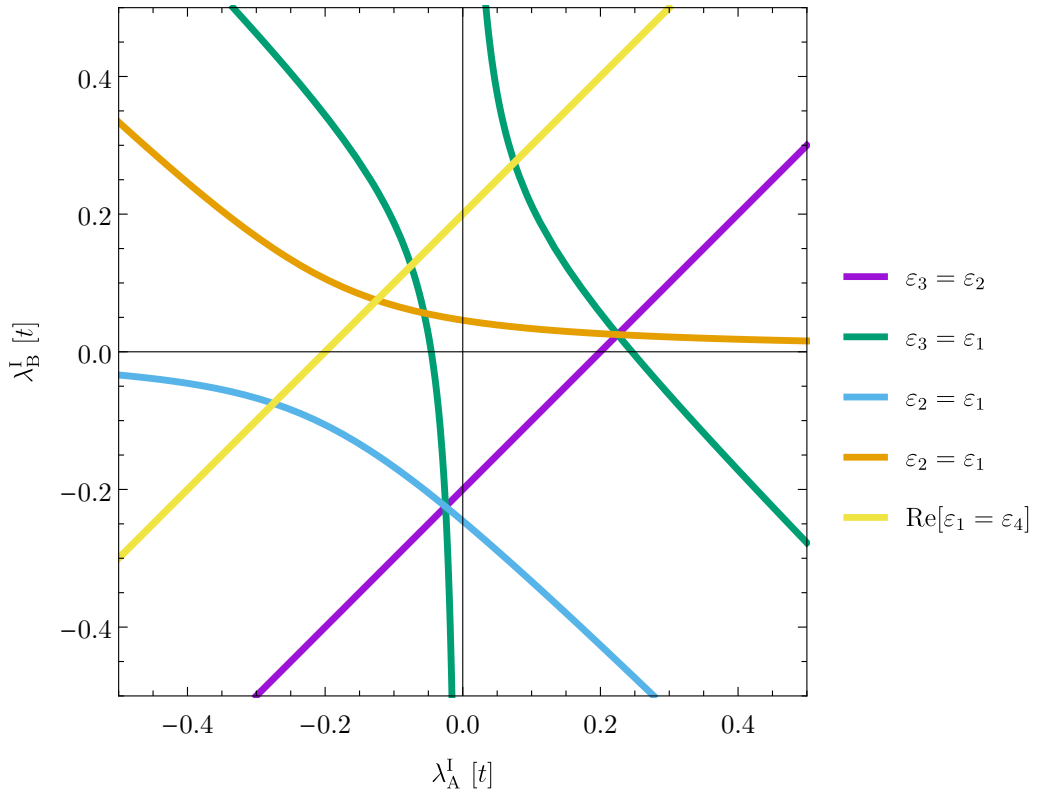

Figure C.1: Double degeneracies in the spin-orbit coupling proximitized graphene spectrum. Solid lines represent points in $\lambda_I^A - \lambda_I^B$ phase space, where the spectrum at the K point is doubly degenerate. This includes also points in which the valence and conduction bands touch and therefore the global graphene gap closes, compare Sec. 5.4. Hamiltonian parameters were chosen as $\Delta = 0.1\ t$, $\lambda_R = 0.075\ t$.

C.3 Double degeneracies

To get more insight into the global graphene gap closings we derived analytic conditions for when the graphene spectrum is at least doubly degenerate at the K point. These can be obtained by setting pairs of eigenvalues equal and solving for λ_I^B as a function of λ_I^A.

If we choose two different eigenvalues out of four to be equal, we have $\binom{4}{2} = \frac{4!}{2!(4-2)!} = 6$ combinations, which are:

$$\varepsilon_3 = \varepsilon_2 :$$
$$\lambda_{\mathrm{I}}^{\mathrm{B}}(\Delta, \lambda_{\mathrm{R}}, \lambda_{\mathrm{I}}^{\mathrm{A}}) = -2\Delta + \lambda_{\mathrm{I}}^{\mathrm{A}} \tag{C.3}$$
$$\varepsilon_3 = \varepsilon_1 :$$
$$\lambda_{\mathrm{I}}^{\mathrm{B}}(\Delta, \lambda_{\mathrm{R}}, \lambda_{\mathrm{I}}^{\mathrm{A}}) = 2\Delta - \lambda_{\mathrm{I}}^{\mathrm{A}} + \frac{2\lambda_{\mathrm{R}}^2}{\lambda_{\mathrm{I}}^{\mathrm{A}}} \tag{C.4}$$
$$\varepsilon_3 = \varepsilon_4 :$$
$$\lambda_{\mathrm{I}}^{\mathrm{B}}(\Delta, \lambda_{\mathrm{R}}, \lambda_{\mathrm{I}}^{\mathrm{A}}) = 2\Delta - \lambda_{\mathrm{I}}^{\mathrm{A}} + \frac{2\lambda_{\mathrm{R}}^2}{\lambda_{\mathrm{I}}^{\mathrm{A}}} \tag{C.5}$$
$$\varepsilon_2 = \varepsilon_1 :$$
$$\lambda_{\mathrm{I}}^{\mathrm{B}}(\Delta, \lambda_{\mathrm{R}}, \lambda_{\mathrm{I}}^{\mathrm{A}}) = -\Delta - \frac{\lambda_{\mathrm{I}}^{\mathrm{A}}}{2} \pm \sqrt{\left(\Delta + \frac{\lambda_{\mathrm{I}}^{\mathrm{A}}}{2}\right)^2 + 2\lambda_{\mathrm{R}}} \tag{C.6}$$
$$\varepsilon_2 = \varepsilon_4 :$$
$$\lambda_{\mathrm{I}}^{\mathrm{B}}(\Delta, \lambda_{\mathrm{R}}, \lambda_{\mathrm{I}}^{\mathrm{A}}) = -\Delta - \frac{\lambda_{\mathrm{I}}^{\mathrm{A}}}{2} \pm \sqrt{\left(\Delta + \frac{\lambda_{\mathrm{I}}^{\mathrm{A}}}{2}\right)^2 + 2\lambda_{\mathrm{R}}} \tag{C.7}$$
$$\varepsilon_1 = \varepsilon_4 :$$
$$\lambda_{\mathrm{I}}^{\mathrm{B}}(\Delta, \lambda_{\mathrm{R}}, \lambda_{\mathrm{I}}^{\mathrm{A}}) = 2\Delta + \lambda_{\mathrm{I}}^{\mathrm{A}} \pm 4i\lambda_{\mathrm{R}} \tag{C.8}$$

Out of the nine solutions, only six are unique. The last one, Eq. (C.8) in general is complex valued. In Fig. C.1 we show the real part of condition C.8 and the other conditions, which are in total five functions $\lambda_{\mathrm{I}}^{\mathrm{B}}(\lambda_{\mathrm{I}}^{\mathrm{A}})$. Exemplary band structures of different points in $\lambda_{\mathrm{I}}^{\mathrm{A}} - \lambda_{\mathrm{I}}^{\mathrm{B}}$ space can be found in Fig. 5.7.

Lines in Fig. C.1 indicate points in $\lambda_{\mathrm{I}}^{\mathrm{A}} - \lambda_{\mathrm{I}}^{\mathrm{B}}$ space where the spectrum is doubly degenerate for a choice of two bands. These two bands can be either the pair of valence states, the pair of conduction states or the higher valence and lower conduction bands. This last combination gives the positions where a global graphene band gap closing happens and nicely coincides with data in Fig. 5.5a.

Phenomenologically, the line representing the real part of condition Eq. C.8 represents cases with maximal s_z mixture of a pair of bands, which do not have to be necessarily degenerate. An example for this case with additional degeneracy is shown in Fig. 5.7(d).

D Listings of QMC input and data sets

For future reproducibility we give the input for `Crystal 14` used to carry out our DFT calculations of phosphorene in listing D.1. In the next subsections, the pseudopotential and basis set are explained.

Listing D.1: `Crystal 14` phosphorene input.

```
PHOSPHORENE
CRYSTAL
0 0 0
64
3.3136 10.478 4.3763
1
215 0.00000 0.10168 0.08056
SLABCUT
0 1 0
2
2
ENDgeom
215 8
INPUT
5. 3 1 1 0 0 0
 2.02622810 5.00000000 -1
 9.95970113 10.13114051 1
 2.74841795 -14.94375088 0
 2.60470698 23.62479480 0
 2.54957900 18.18547203 0
0 0 5 0 1.0
 1.604109 -0.284591
 3.452917 0.024766
 7.432561 0.001798
 15.998924 -0.000314
 34.438408 0.000088
0 0 1 2 1.0
   0.29355283 1.00000
0 0 1 0 1.0
   0.08881117 1.00000
0 2 5 0 1.0
 0.866651 0.091727
 1.766191 -0.057060
 3.599410 -0.005103
```

```
 7.335418 0.000328
 14.949217 -0.000046
0 2 1 3 1.0
   0.3563131 1.00000
0 2 1 0 1.0
   0.12452536 1.00000
0 3 1 0 1.0
   1.26060912 1.00000
0 3 1 0 1.0
   0.32280258 1.00000
99 0
ENDbasis
PRINTOUT
EIGENVAL
-1
EIGENVEC
-999
END
DFT
B3LYP
ENDDFT
SHRINK
6 6
FMIXING
80
NOSYMADA
SAVEWF
END
```

D.1 Pseudopotential

For QMC applications special smoothened pseudopotentials are needed in order to reduce the fluctuation of the local energy due to the divergent behavior of the Coulomb energy near the nuclei. We employ here an energy-consistent Hartree–Fock scalar-relativistic pseudopotential [197], which was specifically generated for DMC and can be obtained from the website in the footnote[1].

The effective core potential V_{ps} consists out of (see user manual of `Crystal 14` [53])

$$V_{\mathrm{ps}} = V_{\mathrm{Coulomb}} + V_{\mathrm{local}} + V_{\mathrm{semilocal}} \tag{D.1}$$

$$= -\frac{Z}{r} + \sum_{k=1}^{M} r^{n_k} C_k e^{-\alpha_k r^2} + \sum_{l=0}^{4} \left[\sum_{k=1}^{M_l} r^{n_{kl}} C_{kl} e^{-\alpha_{kl} r^2} \right] |l\rangle \langle l| \ , \tag{D.2}$$

[1] http://www.burkatzki.com/pseudos/index.2.html

which are the Coulomb term of the pseudoatom, with charge $Z = 5$ in our case. The other terms are expressed in terms of Gaussian functions. The local potential in our case is given by three summands, with powers -1, 1 and 0 of r, see listing D.2. The exponents α are given in the first column of the listed pseudopotential and the coefficients C can be found in the second row. The term with r^{-1} has the property that it cancels exactly the Coulomb term divergence, which is a desired property for DMC calculations [43, 197]. The last term of the pseudopotential is the nonlocal term, which involves projectors onto angular momentum eigenstates. The phosphorene pseudopotential contains s and p nonlocal channels.

Listing D.2: Phosphorus pseudopotential input.

```
Z  M M0 M1 M2 M3 M4
5  3  1  1  0  0  0
alpha       C             n
2.02622810  5.00000000   -1
9.95970113  10.13114051    1
2.74841795  -14.94375088   0
2.60470698  23.62479480    0
2.54957900  18.18547203    0
```

D.2 Basis Set

The basis set employed in our calculations is given in listing D.3 in `Crystal 14` form. The basis set is of VTZ (valence triple-zeta) quality with two contracted Gaussian type orbitals for angular momenta s and p, consisting out of five Gaussian primitives and two uncontracted primitives per angular momentum. Two polarization functions are added with d symmetry. All the uncontracted primitive parameters were optimized to produce minimal energy in the B3LYP-based DFT calculation of phosphorene (carried out by Rene Derian).

Listing D.3: Phosphorus basis set input.

```
---- s ----
0 0 5 0 1.0
 alpha        C
 1.604109    -0.284591
 3.452917     0.024766
 7.432561     0.001798
 15.998924   -0.000314
 34.438408    0.000088
0 0 1 2 1.0
   0.29355283   1.00000
0 0 1 0 1.0
   0.08881117   1.00000
---- p ----
0 2 5 0 1.0
```

```
 0.866651      0.091727
 1.766191     -0.057060
 3.599410     -0.005103
 7.335418      0.000328
 14.949217    -0.000046
0 2 1 3 1.0
   0.3563131     1.00000
0 2 1 0 1.0
   0.12452536    1.00000
---- d ----
0 3 1 0 1.0
   1.26060912    1.00000
0 3 1 0 1.0
   0.32280258    1.00000
```

Bibliography

[1] A. K. Geim and I. V. Grigorieva, *Van der Waals heterostructures.* Nature **499**, 419 (2013). (Cited on pages 1 and 2.)

[2] K. S. Novoselov, *Electric Field Effect in Atomically Thin Carbon Films.* Science **306**, 666 (2004). (Cited on pages 1, 81, and 82.)

[3] K. F. Mak, C. Lee, J. Hone, J. Shan, and T. F. Heinz, *Atomically Thin MoS2: A New Direct-Gap Semiconductor.* Phys. Rev. Lett. **105**, 136805 (2010). (Cited on pages 1 and 105.)

[4] A. H. Castro Neto, F. Guinea, N. M. R. Peres, K. S. Novoselov, and A. K. Geim, *The electronic properties of graphene.* Rev. Mod. Phys. **81**, 109 (2009). (Cited on pages 1, 35, 52, 69, and 81.)

[5] L. Banszerus, M. Schmitz, S. Engels, J. Dauber, M. Oellers, F. Haupt, K. Watanabe, T. Taniguchi, B. Beschoten, and C. Stampfer, *Ultrahigh-mobility graphene devices from chemical vapor deposition on reusable copper.* Sci. Adv. **1**, e1500222 (2015). (Cited on pages 1, 59, 81, and 105.)

[6] I. Žutić, J. Fabian, and S. Das Sarma, *Spintronics: Fundamentals and applications.* Rev. Mod. Phys. **76**, 323 (2004). (Cited on pages 1, 35, 59, and 82.)

[7] J. Fabian, A. Matos-Abiague, C. Ertler, P. Stano, and I. Zutic, *Semiconductor Spintronics.* Acta Phys. Slovaca **57**, 565 (2007). (Cited on page 1.)

[8] W. Han, R. K. Kawakami, M. Gmitra, and J. Fabian, *Graphene spintronics.* Nat. Nanotechnol. **9**, 794 (2014). (Cited on pages 1, 35, 59, and 82.)

[9] I. Žutić, A. Matos-Abiague, B. Scharf, H. Dery, and K. Belashchenko, *Proximitized materials.* arXiv:1805.07942 (2018). (Cited on page 1.)

[10] M. Gmitra and J. Fabian, *Graphene on transition-metal dichalcogenides: A platform for proximity spin-orbit physics and optospintronics.* Phys. Rev. B **92**, 155403 (2015). (Cited on pages 1, 66, 71, 82, 83, 84, and 105.)

[11] M. Gmitra, D. Kochan, P. Högl, and J. Fabian, *Trivial and inverted Dirac bands and the emergence of quantum spin Hall states in graphene on transition-metal dichalcogenides.* Phys. Rev. B **93**, 155104 (2016). (Cited on pages 1, 66, 67, 73, 74, 83, 84, 85, 95, 99, 100, 103, and 105.)

[12] C. L. Kane and E. J. Mele, *Quantum Spin Hall Effect in Graphene.* Phys. Rev. Lett. **95**, 226801 (2005). (Cited on pages 1, 75, 82, 84, 85, 89, and 139.)

[13] D. Kochan, S. Irmer, and J. Fabian, *Model spin-orbit coupling Hamiltonians for graphene systems.* Phys. Rev. B **95**, 165415 (2017). (Cited on pages 2, 52, 53, 56, 66, 67, 69, 84, and 85.)

[14] X. Ling, H. Wang, S. Huang, F. Xia, and M. S. Dresselhaus, *The renaissance of black phosphorus.* Proc. Natl. Acad. Sci. **112**, 4523 (2015). (Cited on pages 2, 105, and 106.)

[15] L. Li, Y. Yu, G. J. Ye, Q. Ge, X. Ou, H. Wu, D. Feng, X. H. Chen, and Y. Zhang, *Black phosphorus field-effect transistors.* Nat. Nanotechnol. **9**, 372 (2014). (Cited on pages 2 and 105.)

[16] A. Castellanos-Gomez, *Black Phosphorus: Narrow Gap, Wide Applications.* J. Phys. Chem. Lett. **6**, 4280 (2015). (Cited on pages 2, 105, and 106.)

[17] P. Hohenberg and W. Kohn, *Inhomogeneous Electron Gas.* Phys. Rev. **136**, B864 (1964). (Cited on pages 3 and 6.)

[18] W. Kohn and L. J. Sham, *Self-Consistent Equations Including Exchange and Correlation Effects.* Phys. Rev. **140**, A1133 (1965). (Cited on pages 3, 6, and 7.)

[19] A. K. Rajagopal and J. Callaway, *Inhomogeneous Electron Gas.* Phys. Rev. B **7**, 1912 (1973). (Cited on pages 3 and 21.)

[20] A. H. MacDonald and S. H. Vosko, *A relativistic density functional formalism.* J. Phys. C Solid State Phys. **12**, 2977 (1979). (Cited on pages 3 and 21.)

[21] P. E. Blöchl, *Projector augmented-wave method.* Phys. Rev. B **50**, 17953 (1994). (Cited on pages 3, 9, 13, 14, 16, and 17.)

[22] A. Dal Corso, *Projector augmented-wave method: Application to relativistic spin-density functional theory.* Phys. Rev. B **82**, 075116 (2010). (Cited on pages 3, 21, 22, and 38.)

[23] W. Kohn, *Nobel Lecture: Electronic structure of matter - wave functions and density functionals.* Rev. Mod. Phys. **71**, 1253 (1999). (Cited on page 6.)

[24] R. M. Martin, *Electronic Structure: Basic Theory and Practical Methods.* Cambridge: Cambridge University Press (2004). (Cited on pages 6, 7, and 8.)

[25] A. Postnikov, *Lectures on the Density Functional Theory: 3 Total energy as functional of electron density.* Osnabrück: Universität Osnabrück (2009). (Cited on page 7.)

[26] K. Burke, *Perspective on density functional theory.* J. Chem. Phys. **136**, 150901 (2012). (Cited on pages 9 and 10.)

[27] D. M. Ceperley and B. J. Alder, *Ground state of the electron gas by a stochastic model.* Phys. Rev. Lett. **45**, 566 (1980). (Cited on pages 10 and 23.)

[28] J. P. Perdew, K. Burke, and M. Ernzerhof, *Generalized gradient approximation made simple.* Phys. Rev. Lett. **77**, 3865 (1996). (Cited on pages 10, 38, 60, 109, and 113.)

[29] A. J. Cohen, P. Mori-Sánchez, and W. Yang, *Challenges for density functional theory.* Chem. Rev. **112**, 289 (2012). (Cited on page 10.)

[30] A. D. Becke, *Density-functional thermochemistry. III. The role of exact exchange.* J. Chem. Phys. **98**, 5648 (1993). (Cited on pages 10, 109, and 113.)

[31] A. J. Garza and G. E. Scuseria, *Predicting Band Gaps with Hybrid Density Functionals.* J. Phys. Chem. Lett. **7**, 4165 (2016). (Cited on page 11.)

[32] V. I. Anisimov, J. Zaanen, and O. K. Andersen, *Band theory and Mott insulators: Hubbard U instead of Stoner I.* Phys. Rev. B **44**, 943 (1991). (Cited on pages 11, 38, 47, and 60.)

[33] M. Cococcioni and S. de Gironcoli, *A linear response approach to the calculation of the effective interaction parameters in the LDA+U method.* Phys. Rev. B **71**, 035105 (2005). (Cited on pages 11, 38, 61, 63, and 71.)

[34] S. Grimme, *Semiempirical GGA-type density functional constructed with a long-range dispersion correction.* J. Comp. Chem. **27**, 1787 (2006). (Cited on pages 12, 38, 60, and 62.)

[35] S. Cottenier, *Density Functional Theory and the Family of (L)APW-methods: a step-by-step introduction.* Leuven: KU Leuven, Belgium: Instituut voor Kern-en Stralingsfysica (2013). (Cited on page 13.)

[36] R. Schade, *Relativistische Effekte in der PAW-Methode jenseits der skalaren Approximation.* Master's thesis, Georg-August-Universität Göttingen, 2012. (Cited on pages 13, 14, and 21.)

[37] P. E. Blöchl, C. J. Först, and J. Schimpl, *Projector augmented wave method: ab initio molecular dynamics with full wave functions.* Bull. Mat. Sci. **26**, 33 (2003). (Cited on pages 13, 14, 15, and 17.)

[38] S. Louie, S. Froyen, and L. Cohen, *Nonlinear ionic pseudopotentials in spin-density-functional calculations.* Phys. Rev. B **26**, 1738 (1982). (Cited on page 17.)

[39] P. Pyykkö, *Relativistic Effects in Structural Chemistry.* Chem. Rev. **88**, 563 (1988). (Cited on page 18.)

[40] M. Weissbluth, *Atoms and Molecules.* New York: Academic Press (1978). (Cited on pages 18 and 20.)

[41] P. A. M. Dirac, *The Quantum Theory of the Electron.* Proc. Roy. Soc. Lond. A **117**, 610 (1928). (Cited on page 18.)

[42] B. H. Bransden and C. J. Joachain, *Physics of atoms and molecules.* New York: Longman Scientific & Technical / Wiley (1987). (Cited on page 18.)

[43] W. Foulkes, L. Mitas, R. Needs, and G. Rajagopal, *Quantum Monte Carlo simulations of solids.* Rev. Mod. Phys. **73**, 33 (2001). (Cited on pages 23, 24, 25, 26, 27, 28, 29, 31, 32, 114, 119, 135, and 153.)

[44] L. K. Wagner, M. Bajdich, and L. Mitas, *QWalk: A quantum Monte Carlo program for electronic structure.* J. Comp. Phys. **228**, 3390 (2009). (Cited on pages 23, 28, 33, and 113.)

[45] N. Nemec, M. D. Towler, and R. J. Needs, *Benchmark all-electron ab initio quantum Monte Carlo calculations for small molecules.* J. Comp. Phys. **132**, 034111 (2010). (Cited on page 23.)

[46] N. Metropolis, A. W. Rosenbluth, M. N. Rosenbluth, A. H. Teller, and E. Teller, *Equation of state calculations by fast computing machines.* J. Chem. Phys. **21**, 1087 (1953). (Cited on page 25.)

[47] R. Jastrow, *Many-Body Problem with Strong Forces.* Phys. Rev. **98**, 1479 (1955). (Cited on page 26.)

[48] T. Kato, *On the eigenfunctions of many-particle systems in quantum mechanics.* Commun. Pure Appl. Math. **10**, 151 (1957). (Cited on page 27.)

[49] M. Bajdich and L. Mitas, *Electronic Structure Quantum Monte Carlo.* Acta Phys. Slovaca **59**, 81 (2009). (Cited on pages 27 and 28.)

[50] R. C. Grimm and R. G. Storer, *Monte-Carlo solution of Schrödinger's equation.* J. Comp. Phys. **7**, 134 (1971). (Cited on page 28.)

[51] J. B. Anderson, *A random-walk simulation of the Schrödinger equation: H3+.* J. Chem. Phys. **63**, 1499 (1975). (Cited on page 28.)

[52] S. R. Bahn and K. W. Jacobsen, *An object-oriented scripting interface to a legacy electronic structure code.* Comput. Sci. Eng. **4**, 56 (2002). (Cited on pages 33 and 61.)

[53] R. Dovesi, R. Orlando, A. Erba, C. M. Zicovich-Wilson, B. Civalleri, S. Casassa, L. Maschio, M. Ferrabone, M. De La Pierre, P. D'Arco, Y. Noël, M. Causà, M. Rérat, and B. Kirtman, *CRYSTAL14: A program for the ab initio investigation of crystalline solids.* Int. J. Quant. Chem. **114**, 1287 (2014). (Cited on pages 33, 113, and 152.)

[54] P. Giannozzi, S. Baroni, N. Bonini, M. Calandra, R. Car, C. Cavazzoni, D. Ceresoli, G. L. Chiarotti, M. Cococcioni, I. Dabo, A. Dal Corso, S. De Gironcoli, S. Fabris, G. Fratesi, R. Gebauer, U. Gerstmann, C. Gougoussis, A. Kokalj, M. Lazzeri, L. Martin-Samos, N. Marzari, F. Mauri, R. Mazzarello, S. Paolini, A. Pasquarello, L. Paulatto, C. Sbraccia, S. Scandolo, G. Sclauzero, A. P. Seitsonen, A. Smogunov, P. Umari, and R. M. Wentzcovitch, *QUANTUM ESPRESSO:*

A modular and open-source software project for quantum simulations of materials. J. Phys. Condens. Matter **21**, 395502 (2009). (Cited on pages 33, 38, 39, and 60.)

[55] K. Momma and F. Izumi, *VESTA 3 for three-dimensional visualization of crystal, volumetric and morphology data.* J. Appl. Cryst. **44**, 1272 (2011). (Cited on page 33.)

[56] K. Schwarz and P. Blaha, *Solid state calculations using WIEN2k.* Comput. Mat. Sci. **28**, 259 (2003). (Cited on pages 33 and 61.)

[57] A. Kokalj, *XCrySDen - a new program for displaying crystalline structures and electron densities.* J. Mol. Graph. Model. **17**, 176 (2000). (Cited on page 33.)

[58] D. Gresch, G. Autès, O. V. Yazyev, M. Troyer, D. Vanderbilt, B. A. Bernevig, and A. A. Soluyanov, *Z2Pack: Numerical Implementation of Hybrid Wannier Centers for Identifying Topological Materials.* Phys. Rev. B **95**, 075146 (2017). (Cited on pages 33, 91, 137, 138, and 139.)

[59] M. Gmitra, S. Konschuh, C. Ertler, C. Ambrosch-Draxl, and J. Fabian, *Band-structure topologies of graphene: Spin-orbit coupling effects from first principles.* Phys. Rev. B **80**, 235431 (2009). (Cited on pages 35, 52, 67, 69, and 82.)

[60] A. H. Castro Neto and F. Guinea, *Impurity-Induced Spin-Orbit Coupling in Graphene.* Phys. Rev. Lett. **103**, 026804 (2009). (Cited on pages 35, 36, and 47.)

[61] M. Gmitra, D. Kochan, and J. Fabian, *Spin-Orbit Coupling in Hydrogenated Graphene.* Phys. Rev. Lett. **110**, 246602 (2013). (Cited on pages 35, 36, 37, 39, 41, 46, 47, 52, 53, 54, 55, 58, 66, 71, 83, and 84.)

[62] J. Balakrishnan, G. Kok Wai Koon, M. Jaiswal, a. H. Castro Neto, and B. Özyilmaz, *Colossal enhancement of spin–orbit coupling in weakly hydrogenated graphene.* Nat. Phys. **9**, 284 (2013). (Cited on pages 35 and 36.)

[63] O. V. Yazyev and L. Helm, *Defect-induced magnetism in graphene.* Phys. Rev. B **75**, 125408 (2007). (Cited on pages 35 and 103.)

[64] H. González-Herrero, J. M. Gómez-Rodríguez, P. Mallet, M. Moaied, J. J. Palacios, C. Salgado, M. M. Ugeda, J.-Y. Veuillen, F. Yndurain, and I. Brihuega, *Atomic-scale control of graphene magnetism by using hydrogen atoms.* Science **352**, 437 (2016). (Cited on page 35.)

[65] D. Kochan, M. Gmitra, and J. Fabian, *Spin Relaxation Mechanism in Graphene: Resonant Scattering by Magnetic Impurities.* Phys. Rev. Lett. **112**, 116602 (2014). (Cited on pages 35, 36, 37, and 41.)

[66] A. Kramida, Yu. Ralchenko, and J. Reader, *Atomic Spectra Database (ver. 5.5.2).* [Online]. Available: https://physics.nist.gov/asd [2018, March 2]. Gaithersburg, MD (2018). (Cited on pages 35 and 40.)

[67] S. Irmer, T. Frank, S. Putz, M. Gmitra, D. Kochan, and J. Fabian, *Spin-orbit coupling in fluorinated graphene.* Phys. Rev. B **91**, 115141 (2015). (Cited on pages 36, 37, 39, 46, 52, 53, 54, 55, and 71.)

[68] K. Zollner, T. Frank, S. Irmer, M. Gmitra, D. Kochan, and J. Fabian, *Spin-orbit coupling in methyl functionalized graphene.* Phys. Rev. B **93**, 045423 (2016). (Cited on pages 36, 37, 52, 53, 54, 55, and 82.)

[69] L. Huai, W. Qingwei, and L. Lixin, *An improvement on the formula for group electronegativity.* J. Chem. Educ. **69**, 783 (1992). (Cited on page 36.)

[70] J. T. Robinson, J. S. Burgess, C. E. Junkermeier, S. C. Badescu, T. L. Reinecke, F. K. Perkins, M. K. Zalalutdniov, J. W. Baldwin, J. C. Culbertson, P. E. Sheehan, and E. S. Snow, *Properties of Fluorinated Graphene Films.* Nano Lett. **10**, 3001 (2010). (Cited on page 36.)

[71] R. M. Guzmán-Arellano, A. D. Hernández-Nieves, C. A. Balseiro, and G. Usaj, *Gate-induced enhancement of spin-orbit coupling in dilute fluorinated graphene.* Phys. Rev. B **91**, 195408 (2015). (Cited on page 36.)

[72] J. Hu, J. Alicea, R. Wu, and M. Franz, *Giant Topological Insulator Gap in Graphene with 5d Adatoms.* Phys. Rev. Lett. **109**, 266801 (2012). (Cited on pages 36 and 76.)

[73] D. Ma, Z. Li, and Z. Yang, *Strong spin–orbit splitting in graphene with adsorbed Au atoms.* Carbon N. Y. **50**, 297 (2012). (Cited on page 36.)

[74] C. Weeks, J. Hu, J. Alicea, M. Franz, and R. Wu, *Engineering a Robust Quantum Spin Hall State in Graphene via Adatom Deposition.* Phys. Rev. X **1**, 021001 (2011). (Cited on pages 36 and 76.)

[75] H. Jiang, Z. Qiao, H. Liu, J. Shi, and Q. Niu, *Stabilizing Topological Phases in Graphene via Random Adsorption.* Phys. Rev. Lett. **109**, 116803 (2012). (Cited on page 36.)

[76] T. O. Wehling, S. Yuan, A. I. Lichtenstein, A. K. Geim, and M. I. Katsnelson, *Resonant Scattering by Realistic Impurities in Graphene.* Phys. Rev. Lett. **105**, 056802 (2010). (Cited on page 36.)

[77] X. Hong, S.-H. Cheng, C. Herding, and J. Zhu, *Colossal negative magnetoresistance in dilute fluorinated graphene.* Phys. Rev. B **83**, 085410 (2011).

[78] A. Ferreira, T. G. Rappoport, M. A. Cazalilla, and A. H. Castro Neto, *Extrinsic Spin Hall Effect Induced by Resonant Skew Scattering in Graphene.* Phys. Rev. Lett. **112**, 066601 (2014). (Cited on page 58.)

[79] D. V. Tuan, F. Ortmann, D. Soriano, S. O. Valenzuela, and S. Roche, *Pseudospin-driven spin relaxation mechanism in graphene.* Nat. Phys. **10**, 857 (2014). (Cited on pages 36 and 58.)

[80] K. T. Chan, J. B. Neaton, and M. L. Cohen, *First-principles study of metal adatom adsorption on graphene.* Phys. Rev. B **77**, 235430 (2008). (Cited on page 36.)

[81] C. Mattevi, H. Kim, and M. Chhowalla, *A review of chemical vapour deposition of graphene on copper.* J. Mater. Chem. **21**, 3324 (2011). (Cited on page 36.)

[82] J. Balakrishnan, G. K. W. Koon, A. Avsar, Y. Ho, J. H. Lee, M. Jaiswal, S.-J. Baeck, J.-H. Ahn, A. Ferreira, M. A. Cazalilla, A. H. C. Neto, and B. Özyilmaz, *Giant spin Hall effect in graphene grown by chemical vapour deposition.* Nat. Commun. **5**, 4748 (2014). (Cited on pages 36, 57, 58, and 59.)

[83] G. Kresse and D. Joubert, *From ultrasoft pseudopotentials to the projector augmented-wave method.* Phys. Rev. B **59**, 1758 (1999). (Cited on pages 38 and 60.)

[84] J. E. Dennis Jr. and J. J. Morée, *Quasi-Newton Methods, Motivation and Theory.* SIAM Rev. **19**, 46 (1977). (Cited on page 38.)

[85] M. Amft, S. Lebègue, O. Eriksson, and N. V. Skorodumova, *Adsorption of Cu, Ag, and Au atoms on graphene including van der Waals interactions.* J. Phys. Condens. Matter **23**, 395001 (2011). (Cited on page 39.)

[86] J. Sugar and A. Musgrove, *Energy Levels of Copper, Cu I through Cu XXIX.* J. Phys. Chem. Ref. Data **19**, 527 (1990). (Cited on pages 40 and 42.)

[87] A. Dal Corso, *Pseudopotentials periodic table: From H to Pu.* Comput. Mater. Sci. **95**, 337 (2014). (Cited on page 39.)

[88] P.-O. Löwdin, *On the Non-Orthogonality Problem Connected with the Use of Atomic Wave Functions in the Theory of Molecules and Crystals.* J. Chem. Phys. **18**, 365 (1950). (Cited on page 41.)

[89] R. F. W. Bader, *Atoms in Molecules: A Quantum Theory.* Oxford, U.K.: Oxford University Press (1990). (Cited on page 41.)

[90] C. Cao, M. Wu, J. Jiang, and H.-P. Cheng, *Transition metal adatom and dimer adsorbed on graphene: Induced magnetization and electronic structures.* Phys. Rev. B **81**, 205424 (2010). (Cited on page 41.)

[91] M. Wu, E.-Z. Liu, M. Y. Ge, and J. Z. Jiang, *Stability, electronic, and magnetic behaviors of Cu adsorbed graphene: A first-principles study.* Appl. Phys. Lett. **94**, 102505 (2009). (Cited on page 41.)

[92] E. H. Lieb, *Two theorems on the Hubbard model.* Phys. Rev. Lett. **62**, 1201 (1989). (Cited on page 41.)

[93] T. Frank, S. Irmer, M. Gmitra, D. Kochan, and J. Fabian, *Copper adatoms on graphene: Theory of orbital and spin-orbital effects.* Phys. Rev. B **95**, 035402 (2017). (Cited on pages 42, 44, 50, 53, 54, 55, 57, and 58.)

[94] P. R. Wallace, *The Band Theory of Graphite.* Phys. Rev. **71**, 622 (1947). (Cited on page 52.)

[95] J. W. McClure and Y. Yafet, Theory of the g-factor of the current carriers in graphite single crystals. in *Proc. Fifth Conf. Carbon*, 22–28, Elsevier (1962). (Cited on pages 52 and 84.)

[96] J. Bundesmann, D. Kochan, F. Tkatschenko, J. Fabian, and K. Richter, *Theory of spin-orbit-induced spin relaxation in functionalized graphene.* Phys. Rev. B **92**, 081403 (2015). (Cited on page 58.)

[97] G. Giovannetti, P. A. Khomyakov, G. Brocks, V. M. Karpan, J. van den Brink, and P. J. Kelly, *Doping Graphene with Metal Contacts.* Phys. Rev. Lett. **101**, 026803 (2008). (Cited on pages 59, 61, 62, 64, 71, and 82.)

[98] P. A. Khomyakov, G. Giovannetti, P. C. Rusu, G. Brocks, J. van den Brink, and P. J. Kelly, *First-principles study of the interaction and charge transfer between graphene and metals.* Phys. Rev. B **79**, 195425 (2009). (Cited on pages 59, 61, 64, and 73.)

[99] V. G. Kravets, R. Jalil, Y.-J. Kim, D. Ansell, D. E. Aznakayeva, B. Thackray, L. Britnell, B. D. Belle, F. Withers, I. P. Radko, Z. Han, S. I. Bozhevolnyi, K. S. Novoselov, A. K. Geim, and A. N. Grigorenko, *Graphene-protected copper and silver plasmonics.* Sci. Rep. **4**, 5517 (2015). (Cited on page 59.)

[100] X. Xu, D. Yi, Z. Wang, J. Yu, Z. Zhang, R. Qiao, Z. Sun, Z. Hu, P. Gao, H. Peng, Z. Liu, D. Yu, E. Wang, Y. Jiang, F. Ding, and K. Liu, *Greatly Enhanced Anti-corrosion of Cu by Commensurate Graphene Coating.* Adv. Mater. **30**, 1702944 (2018). (Cited on page 59.)

[101] L. Gao, J. R. Guest, and N. P. Guisinger, *Epitaxial Graphene on Cu(111).* Nano Lett. **10**, 3512 (2010). (Cited on pages 59, 61, and 65.)

[102] Z. Yan, Z. Peng, and J. M. Tour, *Chemical Vapor Deposition of Graphene Single Crystals.* Acc. Chem. Res. **47**, 1327 (2014). (Cited on page 59.)

[103] D. Boyd, W.-H. Lin, C.-C. Hsu, M. Teague, C.-C. Chen, Y.-Y. Lo, W.-Y. Chan, W.-B. Su, T.-C. Cheng, C.-S. Chang, C.-I. Wu, and N.-C. Yeh, *Single-step deposition of high-mobility graphene at reduced temperatures.* Nat. Commun. **6**, 6620 (2015). (Cited on page 59.)

[104] J. Avila, I. Razado, S. Lorcy, R. Fleurier, E. Pichonat, D. Vignaud, X. Wallart, and M. C. Asensio, *Exploring electronic structure of one-atom thick polycrystalline graphene films: A nano angle resolved photoemission study.* Sci. Rep. **3**, 2439 (2013). (Cited on pages 59, 61, 63, 64, and 65.)

[105] C. Jeon, H.-N. Hwang, W.-G. Lee, Y. G. Jung, K. S. Kim, C.-Y. Park, and C.-C. Hwang, *Rotated domains in chemical vapor deposition-grown monolayer graphene on Cu(111): an angle-resolved photoemission study.* Nanoscale **5**, 8210 (2013). (Cited on pages 64 and 65.)

[106] A. J. Marsden, M.-C. Asensio, J. Avila, P. Dudin, A. Barinov, P. Moras, P. M. Sheverdyaeva, T. W. White, I. Maskery, G. Costantini, N. R. Wilson, and G. R. Bell, *Is graphene on copper doped?.* Phys. status solidi - Rapid Res. Lett. **7**, 643 (2013). (Cited on pages 59 and 64.)

[107] A. M. Shikin, A. G. Rybkin, D. Marchenko, A. a. Rybkina, M. R. Scholz, O. Rader, and A. Varykhalov, *Induced spin–orbit splitting in graphene: the role of atomic number of the intercalated metal and π–d hybridization.* New J. Phys. **15**, 013016 (2013). (Cited on pages 59, 60, and 64.)

[108] A. Varykhalov, M. R. Scholz, T. K. Kim, and O. Rader, *Effect of noble-metal contacts on doping and band gap of graphene.* Phys. Rev. B **82**, 121101(R) (2010). (Cited on page 64.)

[109] H. Vita, S. Böttcher, K. Horn, E. N. Voloshina, R. E. Ovcharenko, T. Kampen, A. Thissen, and Y. S. Dedkov, *Understanding the origin of band gap formation in graphene on metals: graphene on Cu/Ir(111).* Sci. Rep. **4**, 5704 (2015). (Cited on page 64.)

[110] A. L. Walter, S. Nie, A. Bostwick, K. S. Kim, L. Moreschini, Y. J. Chang, D. Innocenti, K. Horn, K. F. McCarty, and E. Rotenberg, *Electronic structure of graphene on single-crystal copper substrates.* Phys. Rev. B **84**, 195443 (2011). (Cited on pages 59, 61, and 64.)

[111] S. Abdelouahed, A. Ernst, J. Henk, I. V. Maznichenko, and I. Mertig, *Spin-split electronic states in graphene: Effects due to lattice deformation, Rashba effect, and adatoms by first principles.* Phys. Rev. B **82**, 125424 (2010). (Cited on page 59.)

[112] Z. Y. Li, Z. Q. Yang, S. Qiao, J. Hu, and R. Q. Wu, *Spin–orbit splitting in graphene on metallic substrates.* J. Phys. Condens. Matter **23**, 225502 (2011). (Cited on page 59.)

[113] O. Rader, A. Varykhalov, J. Sánchez-Barriga, D. Marchenko, A. Rybkin, and A. M. Shikin, *Is There a Rashba Effect in Graphene on 3d Ferromagnets?.* Phys. Rev. Lett. **102**, 057602 (2009). (Cited on page 59.)

[114] D. Marchenko, A. Varykhalov, M. Scholz, G. Bihlmayer, E. Rashba, A. Rybkin, A. Shikin, and O. Rader, *Giant Rashba splitting in graphene due to hybridization with gold.* Nat. Commun. **3**, 1232 (2012). (Cited on page 59.)

[115] T. Olsen and K. S. Thygesen, *Random phase approximation applied to solids, molecules, and graphene-metal interfaces: From van der Waals to covalent bonding.* Phys. Rev. B **87**, 075111 (2013). (Cited on pages 60, 62, 71, and 72.)

[116] M. Vanin, J. J. Mortensen, A. K. Kelkkanen, J. M. Garcia-Lastra, K. S. Thygesen, and K. W. Jacobsen, *Graphene on metals: A van der Waals density functional study.* Phys. Rev. B **81**, 081408 (2010).

[117] M. Andersen, L. Hornekær, and B. Hammer, *Graphene on metal surfaces and its hydrogen adsorption: A meta-GGA functional study.* Phys. Rev. B **86**, 085405 (2012). (Cited on pages 60, 62, 71, and 72.)

[118] M. E. Straumanis and L. S. Yu, *Lattice parameters, densities, expansion coefficients and perfection of structure of Cu and of Cu–In α phase.* Acta Crystallogr. Sect. A **25**, 676–682 (1969). (Cited on pages 61 and 62.)

[119] F. D. M. Haldane, *Model for a Quantum Hall Effect without Landau Levels: Condensed-Matter Realization of the "Parity Anomaly".* Phys. Rev. Lett. **61**, 2015 (1988). (Cited on pages 67, 81, 84, 86, and 88.)

[120] Y. A. Bychkov, V. Mel'nikov, and E. I. Rashba, *Effect of spin-orbit coupling on the energy spectrum of a 2D electron system in a tilted magnetic field.* Sov. Phys. JETP **71**, 401–405 (1990). (Cited on page 67.)

[121] T. Frank, M. Gmitra, and J. Fabian, *Theory of electronic and spin-orbit proximity effects in graphene on Cu(111).* Phys. Rev. B **93**, 155142 (2016). (Cited on pages 67 and 84.)

[122] F. Cardarelli, Properties of Materials. in *Mater. Handb.*, 1–99, Cham: Springer International Publishing (2018). (Cited on page 73.)

[123] S. Konschuh, M. Gmitra, and J. Fabian, *Tight-binding theory of the spin-orbit coupling in graphene.* Phys. Rev. B **82**, 245412 (2010). (Cited on page 74.)

[124] C. L. Kane and E. J. Mele, *Z2 Topological Order and the Quantum Spin Hall Effect.* Phys. Rev. Lett. **95**, 146802 (2005). (Cited on pages 78, 82, 84, and 89.)

[125] Y. Ren, Z. Qiao, and Q. Niu, *Topological phases in two-dimensional materials: A review.* Rep. Prog. Phys. **79**, 066501 (2016). (Cited on pages 78, 81, 93, 94, 95, and 137.)

[126] G. W. Semenoff, V. Semenoff, and F. Zhou, *Domain Walls in Gapped Graphene.* Phys. Rev. Lett. **101**, 087204 (2008). (Cited on page 78.)

[127] W. Yao, S. A. Yang, and Q. Niu, *Edge States in Graphene: From Gapped Flat-Band to Gapless Chiral Modes.* Phys. Rev. Lett. **102**, 096801 (2009).

[128] X. Bi, J. Jung, and Z. Qiao, *Role of geometry and topological defects in the one-dimensional zero-line modes of graphene.* Phys. Rev. B **92**, 235421 (2015). (Cited on page 78.)

[129] Y. Zhang, Y.-W. Tan, H. L. Stormer, and P. Kim, *Experimental observation of the quantum Hall effect and Berry's phase in graphene.* Nature **438**, 201 (2005). (Cited on page 81.)

[130] K. V. Klitzing, G. Dorda, and M. Pepper, *New Method for High-Accuracy Determination of the Fine-Structure Constant Based on Quantized Hall Resistance.* Phys. Rev. Lett. **45**, 494 (1980). (Cited on page 81.)

[131] D. J. Thouless, M. Kohmoto, M. P. Nightingale, and M. den Nijs, *Quantized Hall Conductance in a Two-Dimensional Periodic Potential.* Phys. Rev. Lett. **49**, 405 (1982). (Cited on page 81.)

[132] K. S. Novoselov, A. Mishchenko, A. Carvalho, and A. H. Castro Neto, *2D materials and van der Waals heterostructures.* Science **353**, aac9439 (2016). (Cited on page 82.)

[133] Z. Wang, C. Tang, R. Sachs, Y. Barlas, and J. Shi, *Proximity-Induced Ferromagnetism in Graphene Revealed by the Anomalous Hall Effect.* Phys. Rev. Lett. **114**, 016603 (2015). (Cited on page 82.)

[134] H. B. Heersche, P. Jarillo-Herrero, J. B. Oostinga, L. M. K. Vandersypen, and A. F. Morpurgo, *Bipolar supercurrent in graphene.* Nature **446**, 56 (2007). (Cited on page 82.)

[135] A. Avsar, J. Y. Tan, T. Taychatanapat, J. Balakrishnan, G. Koon, Y. Yeo, J. Lahiri, A. Carvalho, A. S. Rodin, E. O'Farrell, G. Eda, A. H. Castro Neto, and B. Özyilmaz, *Spin–orbit proximity effect in graphene.* Nat. Commun. **5**, 4875 (2014). (Cited on page 82.)

[136] C.-P. Lu, G. Li, K. Watanabe, T. Taniguchi, and E. Andrei, *MoS2: Choice Substrate for Accessing and Tuning the Electronic Properties of Graphene.* Phys. Rev. Lett. **113**, 156804 (2014).

[137] S. Larentis, J. R. Tolsma, B. Fallahazad, D. C. Dillen, K. Kim, A. H. MacDonald, and E. Tutuc, *Band Offset and Negative Compressibility in Graphene-MoS2 Heterostructures.* Nano Lett. **14**, 2039 (2014).

[138] Z. Wang, D.-K. Ki, H. Chen, H. Berger, A. H. MacDonald, and A. F. Morpurgo, *Strong interface-induced spin-orbit interaction in graphene on WS2.* Nat. Commun. **6**, 8339 (2015). (Cited on pages 83, 84, 103, and 132.)

[139] Z. Wang, D.-K. Ki, J. Y. Khoo, D. Mauro, H. Berger, L. S. Levitov, and A. F. Morpurgo, *Origin and Magnitude of 'Designer' Spin-Orbit Interaction in Graphene on Semiconducting Transition Metal Dichalcogenides.* Phys. Rev. X **6**, 041020 (2016).

[140] B. Yang, M.-F. Tu, J. Kim, Y. Wu, H. Wang, J. Alicea, R. Wu, M. Bockrath, and J. Shi, *Tunable spin–orbit coupling and symmetry-protected edge states in graphene/WS2.* 2D Mater. **3**, 031012 (2016). (Cited on pages 84, 85, 91, and 103.)

[141] S. Omar and B. J. van Wees, *Graphene-WS2 heterostructures for tunable spin injection and spin transport.* Phys. Rev. B **95**, 081404(R) (2017). (Cited on page 82.)

[142] T. Völkl, T. Rockinger, M. Drienovsky, K. Watanabe, T. Taniguchi, D. Weiss, and J. Eroms, *Magnetotransport in heterostructures of transition metal dichalcogenides and graphene.* Phys. Rev. B **96**, 125405 (2017). (Cited on page 82.)

[143] A. Dankert and S. P. Dash, *Electrical gate control of spin current in van der Waals heterostructures at room temperature.* Nat. Commun. **8**, 16093 (2017). (Cited on page 82.)

[144] A. W. Cummings, J. H. Garcia, J. Fabian, and S. Roche, *Giant Spin Lifetime Anisotropy in Graphene Induced by Proximity Effects.* Phys. Rev. Lett. **119**, 206601 (2017). (Cited on pages 83, 85, and 103.)

[145] T. S. Ghiasi, J. Ingla-Aynés, A. A. Kaverzin, and B. J. van Wees, *Large Proximity-Induced Spin Lifetime Anisotropy in Transition-Metal Dichalcogenide/Graphene Heterostructures.* Nano Lett. **17**, 7528 (2017). (Cited on page 103.)

[146] L. A. Benítez, J. F. Sierra, W. Savero Torres, A. Arrighi, F. Bonell, M. V. Costache, and S. O. Valenzuela, *Strongly anisotropic spin relaxation in graphene–transition metal dichalcogenide heterostructures at room temperature.* Nat. Phys. **14**, 303 (2018). (Cited on page 83.)

[147] Y. K. Luo, J. Xu, T. Zhu, G. Wu, E. J. McCormick, W. Zhan, M. R. Neupane, and R. K. Kawakami, *Opto-Valleytronic Spin Injection in Monolayer MoS2/Few-Layer Graphene Hybrid Spin Valves.* Nano Lett. **17**, 3877 (2017). (Cited on page 83.)

[148] A. Avsar, D. Unuchek, J. Liu, O. L. Sanchez, K. Watanabe, T. Taniguchi, B. Özyilmaz, and A. Kis, *Optospintronics in Graphene via Proximity Coupling.* ACS Nano **11**, 11678 (2017). (Cited on page 83.)

[149] M. Offidani, M. Milletarì, R. Raimondi, and A. Ferreira, *Optimal Charge-to-Spin Conversion in Graphene on Transition-Metal Dichalcogenides.* Phys. Rev. Lett. **119**, 196801 (2017). (Cited on page 83.)

[150] T. P. Kaloni, L. Kou, T. Frauenheim, and U. Schwingenschlögl, *Quantum spin Hall states in graphene interacting with WS2 or WSe2.* Appl. Phys. Lett. **105**, 233112 (2014). (Cited on page 84.)

[151] A. M. Alsharari, M. M. Asmar, and S. E. Ulloa, *Mass inversion in graphene by proximity to dichalcogenide monolayer.* Phys. Rev. B **94**, 241106 (2016). (Cited on pages 84, 92, and 94.)

[152] S. F. Islam and C. Benjamin, *A scheme to realize the quantum spin-valley Hall effect in monolayer graphene.* Carbon N. Y. **110**, 304 (2016). (Cited on page 89.)

[153] Y. Hatsugai, *Chern number and edge states in the integer quantum Hall effect.* Phys. Rev. Lett. **71**, 3697 (1993). (Cited on page 89.)

[154] S. Ryu, A. P. Schnyder, A. Furusaki, and A. W. W. Ludwig, *Topological insulators and superconductors: tenfold way and dimensional hierarchy.* New J. Phys. **12**, 065010 (2010). (Cited on pages 91, 143, and 146.)

[155] Z. Qiao, W.-K. Tse, H. Jiang, Y. Yao, and Q. Niu, *Two-Dimensional Topological Insulator State and Topological Phase Transition in Bilayer Graphene.* Phys. Rev. Lett. **107**, 256801 (2011). (Cited on page 94.)

[156] T. B. Boykin, M. Luisier, and G. Klimeck, *Current density and continuity in discretized models.* Eur. J. Phys. **31**, 1077 (2010). (Cited on page 96.)

[157] G. Rosenberg, H.-M. Guo, and M. Franz, *Wormhole effect in a strong topological insulator.* Phys. Rev. B **82**, 041104(R) (2010). (Cited on page 98.)

[158] Y.-M. Lin, V. Perebeinos, Z. Chen, and P. Avouris, *Electrical observation of subband formation in graphene nanoribbons.* Phys. Rev. B **78**, 161409 (2008). (Cited on page 99.)

[159] P. Ruffieux, S. Wang, B. Yang, C. Sánchez-Sánchez, J. Liu, T. Dienel, L. Talirz, P. Shinde, C. A. Pignedoli, D. Passerone, T. Dumslaff, X. Feng, K. Müllen, and R. Fasel, *On-surface synthesis of graphene nanoribbons with zigzag edge topology.* Nature **531**, 489 (2016). (Cited on page 103.)

[160] G. Z. Magda, X. Jin, I. Hagymási, P. Vancsó, Z. Osváth, P. Nemes-Incze, C. Hwang, L. P. Biró, and L. Tapasztó, *Room-temperature magnetic order on zigzag edges of narrow graphene nanoribbons.* Nature **514**, 608 (2014). (Cited on page 103.)

[161] K. Watanabe, T. Taniguchi, and H. Kanda, *Direct-bandgap properties and evidence for ultraviolet lasing of hexagonal boron nitride single crystal.* Nat. Mater. **3**, 404 (2004). (Cited on page 105.)

[162] H. Liu, A. T. Neal, Z. Zhu, Z. Luo, X. Xu, D. Tománek, and P. D. Ye, *Phosphorene: An Unexplored 2D Semiconductor with a High Hole Mobility.* ACS Nano **8**, 4033 (2014). (Cited on pages 105, 106, 107, 108, and 112.)

[163] M. Kurpas, M. Gmitra, and J. Fabian, *Spin-orbit coupling and spin relaxation in phosphorene: Intrinsic versus extrinsic effects.* Phys. Rev. B **94**, 155423 (2016). (Cited on pages 105, 112, 113, and 119.)

[164] M. A. Huber, F. Mooshammer, M. Plankl, L. Viti, F. Sandner, L. Z. Kastner, T. Frank, J. Fabian, M. S. Vitiello, T. L. Cocker, and R. Huber, *Femtosecond photo-switching of interface polaritons in black phosphorus heterostructures.* Nat. Nanotechnol. **12**, 207 (2017). (Cited on page 105.)

[165] G. Zhang, S. Huang, A. Chaves, C. Song, V. O. Özçelik, T. Low, and H. Yan, *Infrared fingerprints of few-layer black phosphorus.* Nat. Commun. **8**, 14071 (2017). (Cited on pages 106, 107, 108, 133, and 135.)

[166] G. Zhang, A. Chaves, S. Huang, F. Wang, Q. Xing, T. Low, and H. Yan, *Determination of layer-dependent exciton binding energies in few-layer black phosphorus.* Sci. Adv. **4**, eaap9977 (2018). (Cited on page 106.)

[167] V. Tran, R. Soklaski, Y. Liang, and L. Yang, *Layer-controlled band gap and anisotropic excitons in few-layer black phosphorus.* Phys. Rev. B **89**, 235319 (2014). (Cited on pages 106, 107, 108, 130, and 133.)

[168] A. S. Rodin, A. Carvalho, and A. H. Castro Neto, *Excitons in anisotropic two-dimensional semiconducting crystals.* Phys. Rev. B **90**, 075429 (2014). (Cited on pages 106, 107, 108, 130, and 133.)

[169] J. Guan, W. Song, L. Yang, and D. Tománek, *Strain-controlled fundamental gap and structure of bulk black phosphorus.* Phys. Rev. B **94**, 045414 (2016). (Cited on page 106.)

[170] R. Roldán, A. Castellanos-Gomez, E. Cappelluti, and F. Guinea, *Strain engineering in semiconducting two-dimensional crystals.* J. Phys. Condens. Matter **27**, 313201 (2015). (Cited on pages 106 and 112.)

[171] K. Tokár, R. Derian, J. Brndiar, and I. Štich, *Strain control of vibrational properties of few layer phosphorene.* J. Appl. Phys. **120**, 194305 (2016). (Cited on page 106.)

[172] A. Surrente, A. A. Mitioglu, K. Galkowski, W. Tabis, D. K. Maude, and P. Plochocka, *Excitons in atomically thin black phosphorus.* Phys. Rev. B **93**, 121405 (2016). (Cited on pages 106, 107, and 108.)

[173] L. Li, J. Kim, C. Jin, G. J. Ye, D. Y. Qiu, F. H. da Jornada, Z. Shi, L. Chen, Z. Zhang, F. Yang, K. Watanabe, T. Taniguchi, W. Ren, S. G. Louie, X. H. Chen, Y. Zhang, and F. Wang, *Direct observation of the layer-dependent electronic structure in phosphorene.* Nat. Nanotechnol. **12**, 21 (2016). (Cited on page 106.)

[174] Y. Cai, G. Zhang, and Y.-W. Zhang, *Layer-dependent Band Alignment and Work Function of Few-Layer Phosphorene.* Sci. Rep. **4**, 6677 (2015). (Cited on pages 107 and 114.)

[175] A. N. Rudenko and M. I. Katsnelson, *Quasiparticle band structure and tight-binding model for single- and bilayer black phosphorus.* Phys. Rev. B **89**, 201408 (2014). (Cited on pages 107, 108, 113, and 130.)

[176] A. N. Rudenko, S. Yuan, and M. I. Katsnelson, *Toward a realistic description of multilayer black phosphorus: From GW approximation to large-scale tight-binding simulations.* Phys. Rev. B **92**, 085419 (2015). (Cited on page 107.)

[177] L. Liang, J. Wang, W. Lin, B. G. Sumpter, V. Meunier, and M. Pan, *Electronic Bandgap and Edge Reconstruction in Phosphorene Materials.* Nano Lett. **14**, 6400 (2014). (Cited on pages 107, 108, and 133.)

[178] F. A. Rasmussen, P. S. Schmidt, K. T. Winther, and K. S. Thygesen, *Efficient many-body calculations for two-dimensional materials using exact limits for the screened potential: Band gaps of MoS2, h-BN, and phosphorene.* Phys. Rev. B **94**, 155406 (2016). (Cited on pages 107 and 132.)

[179] V. Wang, Y. Kawazoe, and W. T. Geng, *Native point defects in few-layer phosphorene.* Phys. Rev. B **91**, 045433 (2015). (Cited on page 107.)

[180] Z. Jiang, Z. Liu, Y. Li, and W. Duan, *Scaling Universality between Band Gap and Exciton Binding Energy of Two-Dimensional Semiconductors.* Phys. Rev. Lett. **118**, 266401 (2017). (Cited on pages 107, 108, 133, and 135.)

[181] F. Ferreira and R. M. Ribeiro, *Improvements in the GW and Bethe-Salpeter-equation calculations on phosphorene.* Phys. Rev. B **96**, 115431 (2017). (Cited on pages 107 and 108.)

[182] J.-H. Choi, P. Cui, H. Lan, and Z. Zhang, *Linear Scaling of the Exciton Binding Energy versus the Band Gap of Two-Dimensional Materials.* Phys. Rev. Lett. **115**, 066403 (2015). (Cited on pages 107, 108, 132, and 133.)

[183] A. Chaves, M. Z. Mayers, F. M. Peeters, and D. R. Reichman, *Theoretical investigation of electron-hole complexes in anisotropic two-dimensional materials.* Phys. Rev. B **93**, 115314 (2016). (Cited on pages 107, 108, 130, and 133.)

[184] X. Wang, A. M. Jones, K. L. Seyler, V. Tran, Y. Jia, H. Zhao, H. Wang, L. Yang, X. Xu, and F. Xia, *Highly anisotropic and robust excitons in monolayer black phosphorus.* Nat. Nanotechnol. **10**, 517 (2015). (Cited on pages 107, 108, and 133.)

[185] L. Li, J. Kim, C. Jin, G. J. Ye, D. Y. Qiu, F. H. da Jornada, Z. Shi, L. Chen, Z. Zhang, F. Yang, K. Watanabe, T. Taniguchi, W. Ren, S. G. Louie, X. H. Chen, Y. Zhang, and F. Wang, *Direct observation of the layer-dependent electronic structure in phosphorene.* Nat. Nanotechnol. **12**, 21 (2016). (Cited on pages 107, 133, and 135.)

[186] J. Yang, R. Xu, J. Pei, Y. W. Myint, F. Wang, Z. Wang, S. Zhang, Z. Yu, and Y. Lu, *Optical tuning of exciton and trion emissions in monolayer phosphorene.* Light Sci. Appl. **4**, e312 (2015). (Cited on pages 107, 108, 133, and 135.)

[187] A. Chernikov, T. C. Berkelbach, H. M. Hill, A. Rigosi, Y. Li, O. B. Aslan, D. R. Reichman, M. S. Hybertsen, and T. F. Heinz, *Exciton Binding Energy and Nonhydrogenic Rydberg Series in Monolayer WS2.* Phys. Rev. Lett. **113**, 076802 (2014). (Cited on page 108.)

[188] D. Y. Qiu, F. H. da Jornada, and S. G. Louie, *Screening and many-body effects in two-dimensional crystals: Monolayer MoS2.* Phys. Rev. B **93**, 235435 (2016). (Cited on pages 108, 130, and 135.)

[189] K. G. Reeves, Y. Yao, and Y. Kanai, *Diffusion quantum Monte Carlo study of martensitic phase transition energetics: The case of phosphorene.* J. Chem. Phys. **145**, 124705 (2016). (Cited on pages 109, 114, 115, 120, and 122.)

[190] L. Shulenburger, A. Baczewski, Z. Zhu, J. Guan, and D. Tománek, *The Nature of the Interlayer Interaction in Bulk and Few-Layer Phosphorus.* Nano Lett. **15**, 8170 (2015). (Cited on pages 109, 112, 114, 122, and 127.)

[191] E. J. Baerends, O. V. Gritsenko, and R. van Meer, *The Kohn–Sham gap, the fundamental gap and the optical gap: the physical meaning of occupied and virtual Kohn–Sham orbital energies.* Phys. Chem. Chem. Phys. **15**, 16408 (2013). (Cited on pages 109, 110, 111, 114, and 119.)

[192] T. Koopmans, *Über die Zuordnung von Wellenfunktionen und Eigenwerten zu den Einzelnen Elektronen Eines Atoms.* Physica **1**, 104 (1934). (Cited on page 110.)

[193] J. P. Perdew, W. Yang, K. Burke, Z. Yang, E. K. U. Gross, M. Scheffler, G. E. Scuseria, T. M. Henderson, I. Y. Zhang, A. Ruzsinszky, H. Peng, J. Sun, E. Trushin, and A. Görling, *Understanding band gaps of solids in generalized Kohn–Sham theory.* Proc. Natl. Acad. Sci. **114**, 2801 (2017). (Cited on pages 111 and 114.)

[194] J. C. Grossman, M. Rohlfing, L. Mitas, S. G. Louie, and M. L. Cohen, *High Accuracy Many-Body Calculational Approaches for Excitations in Molecules.* Phys. Rev. Lett. **86**, 472 (2001). (Cited on pages 111 and 129.)

[195] V. Wang, Y. C. Liu, Y. Kawazoe, and W. T. Geng, *Role of Interlayer Coupling on the Evolution of Band Edges in Few-Layer Phosphorene.* J. Phys. Chem. Lett. **6**, 4876 (2015). (Cited on page 112.)

[196] A. Brown and S. Rundqvist, *Refinement of the crystal structure of black phosphorus.* Acta Crystallogr. **19**, 684 (1965). (Cited on pages 112 and 114.)

[197] M. Burkatzki, C. Filippi, and M. Dolg, *Energy-consistent pseudopotentials for quantum Monte Carlo calculations.* J. Chem. Phys. **126**, 234105 (2007). (Cited on pages 113, 125, 152, and 153.)

[198] E. Mostaani, N. D. Drummond, and V. I. Fal'ko, *Quantum Monte Carlo Calculation of the Binding Energy of Bilayer Graphene.* Phys. Rev. Lett. **115**, 115501 (2015). (Cited on page 114.)

[199] K. M. Rasch and L. Mitas, *Fixed-node diffusion Monte Carlo method for lithium systems.* Phys. Rev. B **92**, 045122 (2015). (Cited on page 114.)

[200] B. Kiraly, N. Hauptmann, A. N. Rudenko, M. I. Katsnelson, and A. A. Khajetoorians, *Probing Single Vacancies in Black Phosphorus at the Atomic Level.* Nano Lett. **17**, 3607 (2017). (Cited on pages 114 and 133.)

[201] P. P. Ewald, *Die Berechnung optischer und elektrostatischer Gitterpotentiale.* Ann. Phys. **369**, 253 (1921). (Cited on page 115.)

[202] I.-C. Yeh and M. L. Berkowitz, *Ewald summation for systems with slab geometry.* J. Chem. Phys. **111**, 3155 (1999). (Cited on pages 116 and 117.)

[203] H. Lee and W. Cai, *Ewald summation for Coulomb interactions in a periodic supercell*, vol. 3. Stanford, CA: Stanford University (2009). (Cited on pages 115 and 116.)

[204] L. M. Fraser, W. M. C. Foulkes, G. Rajagopal, R. J. Needs, S. D. Kenny, and a. J. Williamson, *Finite-size effects and Coulomb interactions in quantum Monte Carlo calculations for homogeneous systems with periodic boundary conditions.* Phys. Rev. B **53**, 1814 (1996). (Cited on page 117.)

[205] N. D. Drummond, R. J. Needs, A. Sorouri, and W. M. C. Foulkes, *Finite-size errors in continuum quantum Monte Carlo calculations.* Phys. Rev. B **78**, 125106 (2008). (Cited on page 132.)

[206] A. J. Williamson, G. Rajagopal, R. J. Needs, L. M. Fraser, W. M. C. Foulkes, Y. Wang, and M.-Y. Chou, *Elimination of Coulomb finite-size effects in quantum many-body simulations.* Phys. Rev. B **55**, R4851 (1997).

[207] P. R. C. Kent, R. Q. Hood, A. J. Williamson, R. J. Needs, W. M. C. Foulkes, and G. Rajagopal, *Finite-size errors in quantum many-body simulations of extended systems.* Phys. Rev. B **59**, 1917 (1999).

[208] S. Chiesa, D. M. Ceperley, R. M. Martin, and M. Holzmann, *Finite-Size Error in Many-Body Simulations with Long-Range Interactions.* Phys. Rev. Lett. **97**, 076404 (2006).

[209] H. Kwee, S. Zhang, and H. Krakauer, *Finite-Size Correction in Many-Body Electronic Structure Calculations.* Phys. Rev. Lett. **100**, 126404 (2008). (Cited on page 117.)

[210] W. M. C. Foulkes, R. Q. Hood, and R. J. Needs, *Symmetry constraints and variational principles in diffusion quantum Monte Carlo calculations of excited-state energies.* Phys. Rev. B **60**, 4558 (1999). (Cited on pages 119 and 130.)

[211] P. J. Reynolds, D. M. Ceperley, B. J. Alder, and W. A. Lester, *Fixed-node quantum Monte Carlo for molecules.* J. Chem. Phys. **77**, 5593 (1982). (Cited on page 119.)

[212] C. J. Umrigar and C. Filippi, *Energy and Variance Optimization of Many-Body Wave Functions.* Phys. Rev. Lett. **94**, 150201 (2005). (Cited on page 121.)

[213] M. Casula, *Beyond the locality approximation in the standard diffusion Monte Carlo method.* Phys. Rev. B **74**, 161102 (2006). (Cited on page 122.)

[214] M. E. J. Newman and G. T. Barkema, *Monte carlo methods in statistical physics chapter 1-4.* Oxford: Oxford University Press (1999). (Cited on page 123.)

[215] H. Flyvbjerg and H. G. Petersen, *Error estimates on averages of correlated data.* J. Chem. Phys. **91**, 461 (1989). (Cited on page 123.)

[216] K. M. Rasch, S. Hu, and L. Mitas, *Communication: Fixed-node errors in quantum Monte Carlo: Interplay of electron density and node nonlinearities.* J. Chem. Phys. **140**, 041102 (2014). (Cited on page 125.)

[217] T. Frank, R. Derian, L. Mitas, J. Fabian, and I. Stich, *Many-body quantum Monte Carlo study of 2D materials: cohesion and band gap in single-layer phosphorene.* arXiv:1805.10823 (2018). (Cited on pages 127 and 134.)

[218] A. Williamson, R. Hood, R. Needs, and G. Rajagopal, *Diffusion quantum Monte Carlo calculations of the excited states of silicon.* Phys. Rev. B **57**, 12140 (1998). (Cited on pages 129 and 130.)

[219] A. R. Porter, M. D. Towler, and R. J. Needs, *Excitons in small hydrogenated Si clusters.* Phys. Rev. B **64**, 035320 (2001). (Cited on page 129.)

[220] A. J. Williamson, J. C. Grossman, R. Q. Hood, A. Puzder, and G. Galli, *Quantum Monte Carlo Calculations of Nanostructure Optical Gaps: Application to Silicon Quantum Dots.* Phys. Rev. Lett. **89**, 196803 (2002). (Cited on page 129.)

[221] M. D. Towler, R. Q. Hood, and R. J. Needs, *Minimum principles and level splitting in quantum Monte Carlo excitation energies: Application to diamond.* Phys. Rev. B **62**, 2330 (2000). (Cited on page 129.)

[222] J. E. Vincent, J. Kim, and R. M. Martin, *Quantum Monte Carlo calculations of the optical gaps of Ge nanoclusters using core-polarization potentials.* Phys. Rev. B **75**, 045302 (2007). (Cited on page 129.)

[223] B. Wood, W. M. C. Foulkes, M. D. Towler, and N. D. Drummond, *Coulomb finite-size effects in quasi-two-dimensional systems.* J. Phys. Condens. Matter **16**, 891 (2004). (Cited on page 132.)

[224] A. Raja, A. Chaves, J. Yu, G. Arefe, H. M. Hill, A. F. Rigosi, T. C. Berkelbach, P. Nagler, C. Schüller, T. Korn, C. Nuckolls, J. Hone, L. E. Brus, T. F. Heinz, D. R. Reichman, and A. Chernikov, *Coulomb engineering of the bandgap and excitons in two-dimensional materials.* Nat. Commun. **8**, 15251 (2017). (Cited on page 133.)

[225] A. V. Stier, N. P. Wilson, G. Clark, X. Xu, and S. A. Crooker, *Probing the Influence of Dielectric Environment on Excitons in Monolayer WSe 2 : Insight from High Magnetic Fields.* Nano Lett. **16**, 7054 (2016).

[226] Y. Cho and T. C. Berkelbach, *Environmentally sensitive theory of electronic and optical transitions in atomically thin semiconductors.* Phys. Rev. B **97**, 041409 (2018). (Cited on pages 133 and 135.)

[227] A. A. Soluyanov and D. Vanderbilt, *Computing topological invariants without inversion symmetry.* Phys. Rev. B **83**, 235401 (2011). (Cited on pages 137, 138, and 140.)

[228] A. Altland, *Lecture on Symmetries and Topology in Non-Interacting Fermion Systems.* San Sebastian: Topological Matter School (2016). (Cited on page 143.)

[229] C. D. Beule, *Time reversal on a lattice.* Talk at University of Antwerp (Cited on page 143.)

List of Publications

- *Spin-orbit coupling in fluorinated graphene*,
  S. Irmer, T. Frank, S. Putz, M. Gmitra, D. Kochan, and J. Fabian,
  Phys. Rev. B **91**, 115141 (2015)

- *Spin-orbit coupling in methyl functionalized graphene*,
  K. Zollner, T. Frank, S. Irmer, M. Gmitra, D. Kochan, and J. Fabian,
  Phys. Rev. B **92**, 045423 (2016)

- *Theory of electronic and spin-orbit proximity effects in graphene on Cu (111)*,
  T. Frank, M. Gmitra, and J. Fabian,
  Phys. Rev. B **93**, 155142 (2016)

- *Theory of proximity-induced exchange coupling in graphene on hBN/(Co, Ni)*,
  K. Zollner, M. Gmitra, T. Frank, and J. Fabian,
  Phys. Rev. B **94**, 155441 (2016)

- *Excitonic valley effects in monolayer WS_2 under high magnetic fields*,
  G. Plechinger, Ph. Nagler, A. Arora, A. G. Águila, M. V. Ballottin, T. Frank,
  Ph. Steinleitner, M. Gmitra, J. Fabian, P. C. M. Christianen, R. Bratschitsch,
  Ch. Schüller, and T. Korn,
  Nano Lett. **16**, 7899 (2016)

- *Excitonic Stark effect in MoS_2 monolayers*,
  B. Scharf, T. Frank, M. Gmitra, J. Fabian, I. Žutić, and V. Perebeinos,
  Phys. Rev. B **94**, 245434 (2016)

- *Copper adatoms on graphene: Theory of orbital and spin-orbital effects*,
  T. Frank, S. Irmer, M. Gmitra, D. Kochan, and J. Fabian,
  Phys. Rev. B **95**, 035402 (2017)

- *Femtosecond photo-switching of interface polaritons in black phosphorus heterostructures*,
  M. A. Huber, F. Mooshammer, M. Plankl, L. Viti, F. Sandner, L. Z. Kastner,
  T. Frank, J. Fabian, M. S. Vitiello, T. L. Cocker, and R. Huber,
  Nat. Nanotechnol. **12**, 207 (2017)

- *Protected pseudohelical edge states in $\mathbb{Z}_2$-trivial proximitized graphene*,
  T. Frank, P. Högl, M. Gmitra, D. Kochan, and J. Fabian,
  Phys. Rev. Lett. **97**, 156402 (2018)

- *Many-body quantum Monte Carlo study of 2D materials: cohesion and band gap in single-layer phosphorene*,
  T. Frank, R. Derian, K. Tokár, L. Mitas, J. Fabian, and I. Štich,
  Phys. Rev. X **9**, 011018 (2019)

Acknowledgments

I would like to thank my professor Jaroslav Fabian for giving me the opportunity to work in his group. I am deeply grateful for his scientific and human guidance. His door was always open for spontaneous questions and discussions, which was very generous. Thank you!

I am grateful to have profited from mentoring by Martin Gmitra. His guidance and sharing of experience was exceptional. During my studies he always supported me, also with non-scientific advice. Without Rene Derian, the chapter on phosphorene would not have been possible. I would like to thank him and Ivan Štich to teach me about quantum Monte Carlo. Furthermore, I would like to thank all other scientific collaborators for their efforts.

I thank Andreas Costa, Daniel Hernangómez-Pérez, Susanne Irmer, Denis Kochan, Marta Pelc, Phillipp Reck, and Klaus Zollner for proofreading.

My thank goes to everybody from the chair of Klaus Richter and from the Fabian group for making the PhD time so enjoyable.

Last but not least, I would like to thank my loved ones for their constant support and understanding!

Finally, I acknowledge GRK Grant No. 1570, the International Doctorate Program Topological Insulators of the Elite Network of Bavaria, and SFB 1277 (B07) for funding.